

THE QUASI-DIABATIC HAMILTONIAN APPROACH
TO ACCURATE AND EFFICIENT NON-ADIABATIC DYNAMICS
WITH CORRECT TREATMENT OF CONICAL INTERSECTION SEAMS

By
Xiaolei Zhu

A dissertation submitted to Johns Hopkins University in conformity with the
requirements for the degree of Doctor of Philosophy

Baltimore, Maryland

January 22, 2014

© 2014 Xiaolei Zhu
All Rights Reserved

Abstract

A method to simulate photoelectron spectra using quadratic local quasi-diabatic Hamiltonians (\mathbf{H}^d) is generalized and augmented to enable high accuracy dynamics simulations of nonadiabatic processes that involve large amplitude motions, including dissociation. The improvement is achieved by using a flexible symmetry adapted analytical expansion to approximate the representation of electronic Hamiltonian operator in a quasi-diabatic basis, the diabaticity of which is achieved by minimization of residual coupling between quasi-diabatic states.

Although previous theoretical treatments have been used to treat adiabatic dissociation and rearrangement processes with success, difficulties have been encountered in systems complicated by seams of conical intersections. Existing methods are either too expensive to be applied, or could not provide sufficient accuracy. Even for nonadiabatic reactions of very small systems, such as photodissociation of NH_3 , all previous theoretical treatments have been unable to accurately reproduce experimental measurements.

In this work, inspired by the success of bound-state \mathbf{H}^d approach, a rigorous and flexible framework is established to create a more robust method for accurate and efficient nonadiabatic dynamics simulations, through the construction of quasi-diabatic Hamiltonians(\mathbf{H}^d) that correctly describes reactions. This new method requires no assumption on the properties of individual systems. The application of local intersection adapted representations and partially diagonalized representations enabled entire seams of conical intersections as well as the nearby regions to be accurately described. No *ad hoc* approximation is made in the diabatization procedure, and the residual coupling of

the underlying quasi-diabatic representation is minimized in a least squares sense and can be exactly quantified. Polynomials of arbitrary functions of internal coordinates are used to construct an extremely flexible basis for \mathbf{H}^d , and generic symmetry treatment allows incorporation of arbitrary point group or Complete Nuclear Permutation Inversion (CNPI) group symmetry¹.

With the \mathbf{H}^d constructed from the new approach, the $\tilde{A} \leftarrow \tilde{X}$ photodissociation process of NH_3 was simulated. New results, obtained using \mathbf{H}^d constructed with the method described in this work, accurately reproduce experimental measurements, illustrating its promising potential.

The method is then further enhanced to allow application to much larger systems, with the coupled potential energy surfaces of the $1,2,3^1A$ states for the photodissociation of phenol used as an example. A partially diagonalized representation approach is developed to accurately treat near degenerate points, and a null-space analysis procedure is added to guide the selection of monomial basis and to remove linear dependencies in the fitting procedure. Coupled potential energy surfaces that fully incorporate all 33 degrees of freedom, many different large amplitude motions, and multiple seams of conical intersections, are successfully constructed from *ab initio* data.

Thesis Advisor:

Professor David R. Yarkony, Johns Hopkins University

Additional Readers:

Professor Paul J. Dagdigian, Johns Hopkins University

Professor Harris J Silverstone, Johns Hopkins University

¹ P. R. Bunker, *Molecular Symmetry and Spectroscopy*. (Academic Press, New York, 1979)

This dissertation is dedicated to my dear wife Jin Yang.

Acknowledgement

My deepest gratitude is to my advisor, Dr. David R. Yarkony for granting me the opportunity to work in his research group. His guidance made the journey to Ph.D. rewarding and stimulating. His experience and expertise in the area is unparalleled and was indispensable during the course of every research project. Most of all, I sincerely appreciate him for being extraordinarily kind and patient to always support me to pursue my ideas, even after repeated mistakes and failures and periods of frustration.

I would like to thank Dr. Michael Schuurman and Dr. Joseph Dillion for their help and friendship. Not only did they teach me all they know without reservation about research in the group, they also helped me to adapt to life in graduate school, and in a foreign country. A great many ideas incorporated in this dissertation are results of discussions with them.

I would like to thank current and former members of the group, Christopher Malbon, Sara Marquez and Nathan Kopf, along with Joseph and Michael, for countless inspiring conversations both during group meetings and in private. Special thanks to Chris for sharing a cheerful office with me.

I would like to express my gratitude to our collaborator, Dr. Hua Guo, Dr. Jianyi Ma and Dr. Changjian Xie, for performing full quantum dynamics simulations on our constructed Hamiltonians. It was an incredible learning experience to work with Dr Guo's research group. It is their state-of-the art quantum dynamics simulations that served as the verification of the quality of our constructed coupled potential energy surfaces. As the first users of our code outside our group, they also served as the beta

tester of our program and their feedbacks resulted in a number of improvement and bug fixes. Thank you for bearing with us through the bugs and problems!

I would like to say thank you to all my friends and colleagues at Hopkins for their friendship and company, especially Xin Tang, Ting Zhang, Yao Li, Yuqi Li, Dr. Yang Li, Man Li, Jing Chen, Dr. Xiang Li, Xuan Li, Xinxing Zhang, Jing Li, Ying Zhang and Yuchong Shao. I would like to thank Jin Yang, whom I met and married during the years of my Ph.D. studies. She is the source of my passion and confidence, and is the main reason I had a life outside of research lab.

Copyright and Permission Notices:

This dissertation contains the following original papers that have been previously published in peer-reviewed journals:

Chapter	Reprint with Permission from	Copyright
Chapter 2	X. Zhu, D.R. Yarkony, The Journal of Chemical Physics 132 , 104101 (2010)	©2010, AIP Publishing LLC.
Chapter 3	X. Zhu, D.R. Yarkony, The Journal of Chemical Physics 137 , 22A511 (2012)	©2012, AIP Publishing LLC.
Chapter 4	X. Zhu, J. Ma, D.R. Yarknony, H. Guo, The Journal of Chemical Physics 136 , 234301 (2012) J. Ma, X. Zhu, H. Guo, D.R. Yarkony, The Journal of Chemical Physics 137 , 22A541 (2012)	©2012, AIP Publishing LLC.
Chapter 5	X. Zhu, D.R. Yarknony, The Journal of Chemical Physics 140 , 024112 (2014)	©2014, AIP Publishing LLC.

The work presented in Chapter 2 was supported by NSF grant CHE-0513952 to DRY. The work presented in Chapter 3 was supported by NSF grant CHE-1010644 to D.R.Y. The portion of work presented in Chapter 4 that involve construction of \mathbf{H}^d was supported by NSF grant CHE-1010644 to DRY. JYM and HG, who performed the 6-dimensional quantum mechanical calculations, acknowledge the support of the NSF grant CHE-0910828 to HG. The work presented in Chapter 5 was supported by NSF grant CHE-1010644 to D.R.Y.

Table of Contents

ABSTRACT.....	II
ACKNOWLEDGEMENT.....	V
LIST OF TABLES	XIV
LIST OF FIGURES	XVII
CHAPTER 1 INTRODUCTION.....	1
1.1 CHEMISTRY BEYOND THE BORN-OPPENHEIMER APPROXIMATION	1
1.2 ELIMINATING THE COMPUTATIONAL BOTTLENECK WITH ANALYTICAL APPROXIMATION.....	3
1.3 INADEQUACIES OF EXISTING METHODS	4
1.4 THE NON-LOCAL QUASI-DIABATIC HAMILTONIAN (H^D) APPROACH	5
REFERENCES	8
CHAPTER 2 TOWARD HIGHLY EFFICIENT NONADIABATIC DYNAMICS ON THE FLY: AN ALGORITHM TO FIT NON-LOCAL QUASI-DIABATIC, COUPLED ELECTRONIC STATE HAMILTONIANS BASED ON <i>AB INITIO</i> ELECTRONIC STRUCTURE DATA.....	10
2.1 ABSTRACT.....	10
2.2 INTRODUCTION.....	11
2.3 THE QUASI-DIABATIC HAMILTONIAN AND ITS DETERMINATION	14
2.3.1 <i>The Quasi-Diabatic Hamiltonian</i>	14
2.3.2 <i>Equations defining H^d</i>	14
2.3.3 <i>Constrained Pseudo Normal Equations</i>	16

2.3.4 Advantages of the Pseudo Constrained Normal Equations Approach	18
2.3.5 Nuclear Coordinates.....	19
2.3.6 Global Symmetry of H^d	21
2.4 H^D FOR THE $1,2^1A$ ELECTRONIC STATES OF NH_3	22
2.4.1 Electronic Structure description of NH_3	23
2.4.2 Symmetry-adapted internal coordinates	23
2.4.3 Construction of H^d	25
2.4.4 Accuracy of H^d	26
2.5 SUMMARY AND CONCLUSIONS.....	44
2.6 APPENDICES	45
2.6.1 Complete Nuclear Permutation Inversion Group of NH_3	45
2.6.2 Transformation Properties of Dot-Cross-Product Function	46
2.6.3 CNPI Irreducible Representations of Electronic States	47
2.6.4 Ab Initio and H^d Predicted Energies of All Data Points	48
2.6.5 Geometries of All Data Points	55
REFERENCES	63

CHAPTER 3 QUASI-DIABATIC REPRESENTATIONS OF ADIABATIC POTENTIAL ENERGY SURFACES COUPLED BY CONICAL INTERSECTIONS INCLUDING BOND BREAKING: A MORE GENERAL CONSTRUCTION PROCEDURE AND AN ANALYSIS OF THE DIABATIC REPRESENTATION	68
3.1 ABSTRACT.....	68
3.2 INTRODUCTION.....	69

3.3 THE ALGORITHM.....	73
3.3.1 <i>General Definitions</i>	73
3.3.2 <i>Defining equations</i>	74
3.3.3 <i>Original Algorithm</i>	78
3.3.4 <i>Newton Raphson equations</i>	78
3.4 COMPUTATIONAL RESULTS.....	79
3.4.1 <i>Derivative Couplings</i>	81
3.4.2 <i>Newton-Raphson equations</i>	83
3.4.3 <i>The Diabatic Character of the Representation</i>	88
3.5 SUMMARY AND CONCLUSIONS.....	94
3.6 APPENDICES.....	94
3.6.1 <i>Form of Singule Coordinate Functions Used to Construct H^d</i>	94
3.6.2 <i>Second derivatives of Unknown Coefficients</i>	96
3.6.3 <i>Evaluation of $\frac{\partial \mathbf{d}^l(\mathbf{R}_n)}{\partial z_k}$</i>	98
3.6.4 <i>Formulation and solution of Eq. (3-23)</i>	100
REFERENCES.....	104

CHAPTER 4 COMPUTATIONAL DETERMINATION OF THE $\tilde{A} \leftarrow \tilde{X}$	
ABSORPTION SPECTRA AND PHOTODISSOCIATION PRODUCT	
BRANCHING RATIOS OF NH₃ AND OF ND₃ USING H^D AND FULL SIX	
DIMENSIONAL QUANTUM DYNAMICS	112
4.1 ABSTRACT.....	112
4.2 INTRODUCTION.....	112

4.3 THEORETICAL APPROACH	117
4.3.1 <i>Diabatic Representations</i>	117
4.3.2 <i>Quantum Dynamics</i>	124
4.4 ANALYSIS OF H ^D : ELECTRONIC STRUCTURE	129
4.4.1 <i>Electronic Structure: ab initio treatment</i>	129
4.4.2 <i>Electronic Structure: Spectroscopic constants</i>	129
4.4.3 <i>Electronic Structure: Conical intersection seam</i>	134
4.5 ANALYSIS OF H ^D : VIBRATIONAL SPECTRA.....	136
4.5.1 <i>The \tilde{X}^1A_1 State</i>	136
4.5.2 <i>The \tilde{A}^1A_2 State</i>	137
4.6 ANALYSIS OF H ^D : NON-ADIABATIC DYNAMICS	142
4.7 SUMMARY AND CONCLUSION	144
REFERENCES	145

CHAPTER 5 FITTING COUPLED POTENTIAL ENERGY SURFACES FOR LARGE SYSTEMS: METHOD AND CONSTRUCTION OF A 3-STATE REPRESENTATION FOR PHENOL PHOTODISSOCIATION IN THE FULL 33 INTERNAL DEGREES OF FREEDOM	157
5.1 ABSTRACT.....	157
5.2 INTRODUCTION.....	158
5.3 THE ALGORITHM	161
5.3.1 <i>Definitions</i>	161
5.3.2 <i>Defining equations</i>	162
5.4 TREATING LARGER MOLECULES	165

5.4.1 Enhanced Methodology: Reduction of N^c - Preconditioning.....	166
5.4.2 Redundant coordinates	168
5.4.3 The diabatic representation and CNPI group symmetry.....	170
5.4.4 Description near Conical Intersections.....	171
5.5 1,2,3 ¹ A STATES OF PHENOL.....	174
5.5.1 Electronic Structure Description.....	175
5.5.2 Summary of the H^d	176
5.5.3 Quality of Fit: Coarse Assays.....	180
5.5.4 Quality of Fit: Detailed Assays.....	184
5.5.5 Determining the Domain of Definition of H^d	187
5.5.6 Extent of the Domain of Definition.....	192
5.5.7 Automatic Smoothing of Discontinuities in Ab Initio Data.....	194
5.5.8 Treatment of Conical Intersections.....	196
5.6 SUMMARY AND CONCLUSIONS.....	197
5.7 APPENDICES.....	199
5.7.1 Partial diagonalization of $H^d(\mathbb{R}^n)$	199
5.7.2 Calculating $\nabla \mathbf{d}^J$ for an arbitrary number of degeneracy groups composed of an arbitrary number of degenerate states.....	206
5.7.3 Extending the Skeletal Data.....	208
5.7.4 Improved Least Squares Algorithm for Handling Large Systems.....	209
5.7.5 Geometries of Ab Initio and Fit Critical Points.....	212
5.7.6 Harmonic Frequencies of Ab Initio and Fit Critical Points.....	226
REFERENCES.....	229

CURRICULUM VITAE..... 240

List of Tables

TABLE 2-1. LOCATION OF CRITICAL POINTS. $\phi=0$ EXCEPT AT $MINIC_{3v}$ WHERE $\phi=22.44$	25
TABLE 2-2. QUALITY OF FITS. FIT1-FIT3 CONSTRUCTED FROM THE 239 POINT FIT DATA SET WITH 48 INTERPOLATION (INTER) POINTS. FIT4 INCLUDES ALL 287 POINTS IN FIT SET. FIT3 USES $T = 0$.	29
TABLE 2-3. COMPARISON OF FIT2 AND <i>AB INITIO</i> RESULTS FOR INTERPOLATION POINTS ALONG PATHS DESCRIBED IN TEXT. NODES ARE IN BOLD FACE. ENERGIES IN cm^{-1} . $E_j = E_j(\mathbf{H}^D) - E_j(\text{AB INITIO})$.	30
TABLE 2-4 COMPARISON OF FIT2 AND <i>AB INITIO</i> HARMONIC FREQUENCIES (IN cm^{-1}).	38
TABLE 2-5. CHARACTER TABLE OF S_3 .	46
TABLE 2-6. <i>AB INITIO</i> AND \mathbf{H}^D PREDICTED ENERGIES USING FIT2 FOR ALL DATA POINTS. ENERGIES IN cm^{-1} , NUMBERING OF NODES REFERS TO TABLE 2-1.	48
TABLE 2-7. INTERNAL GEOMETRY OF ALL NODES, FIT AND INTERPOLATION POINTS. BOND LENGTHS ARE PRESENTED IN \AA , ANGLES IN DEGREES.	55
TABLE 3-1. RMS ERRORS FOR \mathbf{H}^D DETERMINED FROM EQS. (3-22) AND (3-23).	85
TABLE 3-2 \mathbf{H}^D AND <i>AB INITIO</i> DETERMINED FREQUENCIES AND THEIR UNSIGNED ERRORS (UERROR) AT EXTREMA. ERR IS THE MAGNITUDE OF THE DIFFERENCE BETWEEN THE \mathbf{H}^D AND <i>AB INITIO</i> DETERMINED QUANTITY. ALL QUANTITIES IN cm^{-1} .	87
TABLE 4-1. PARAMETERS FOR G_L .	121
TABLE 4-2. NUMERICAL PARAMETERS (IN A.U.) USED IN WAVE PACKET CALCULATIONS.	128
TABLE 4-3. SPECTROSCOPIC CONSTANTS AND RELATED DATA FOR \tilde{X}^1A_1 AND \tilde{A}^1A_2'' STATES OF NH_3 .	131

TABLE 4-4. SPECTROSCOPIC CONSTANTS AND RELATED DATA FOR \tilde{X} AND STATES OF NH_2 . ENERGIES IN cm^{-1} , DISTANCES IN \AA AND ANGLES IN DEGREES. ORDERING OF HARMONIC FREQUENCIES IS THAT OF REF. ⁹⁴	133
TABLE 4-5. CONICAL INTERSECTION SEAM FOR $1,2^1\text{A}$ STATES OF NH_3	135
TABLE 4-6. LOW-LYING VIBRATIONAL LEVELS OF $\text{NH}_3(\tilde{X})$ OBTAINED USING THE LVT \mathbf{H}^{P} AND THE PRESENT WORK (PW). ENERGIES IN cm^{-1} RELATIVE TO CORRESPONDING ZERO-POINT ENERGY.	138
TABLE 4-7. LINEWIDTH (cm^{-1}) OF NH_3 FROM EXPERIMENT AND COMPUTATIONS BASED ON \mathbf{H}^{D} OBTAINED IN THE PRESENT WORK (PW) AND \mathbf{H}^{D} FROM LVT, AS REPORTED IN REF. ³⁵ . EXPERIMENTAL VALUES TAKEN FROM REF. ⁶ EXCEPT FOR $\nu_2 \leq 3$ FOR NH_3 AND $\nu_2 \leq 2$ FOR ND_3 WHERE VALUES FROM REF. ⁷ , WHICH ARE MORE CONSISTENT WITH THE AVAILABLE EXPERIMENTAL DATA ARE USED. THE $E(N)$ EXHIBIT A SYSTEMATIC ERROR OWING TO THE ERROR IN T_e REPORTED IN TABLE 4-3.	141
TABLE 5-1. IMPORTANT PARAMETERS OF FITTING PROCEDURE	177
TABLE 5-2. COORDINATE FUNCTIONS USED TO CONSTRUCT \mathbf{H}^{P}	178
TABLE 5-3. RMS ERROR OF FIT CRITICAL POINT GEOMETRIES FROM <i>AB INITIO</i> VALUES	185
TABLE 5-4. ENERGETICS OF CRITICAL POINTS IN cm^{-1}	186
TABLE 5-5. ERROR IN HARMONIC FREQUENCIES AND ZERO POINT ENERGIES	187
TABLE 5-6. DYNAMICS SUMMARY ASSAY	189
TABLE 5-7: FITTING ERROR FROM RANDOMLY SELECTED TRAJECTORIES.....	191
TABLE 5-8. BOND LENGTHS OF CRITICAL POINTS. “ <i>AB INITIO</i> ” REFERS TO THE VALUE OF INTERNAL COORDINATES ON <i>AB INITIO</i> POTENTIAL ENERGY SURFACES, AND “ERROR”	

REFERS TO THE DIFFERENCE BETWEEN FIT AND <i>AB INITIO</i> INTERNAL COORDINATES (FIT MINUS <i>AB INITIO</i> COORDINATE VALUE).	212
TABLE 5-9. BOND ANGLES OF CRITICAL POINTS. ALL THE BENDING ANGLES OF THE BENZENE RING AND ONE ANGLE FOR EACH ATOM OUTSIDE THE BENZENE CARBONS ARE INCLUDED. THE SECOND ATOM INDEX IN THE ATOM LIST CORRESPOND TO THE VERTEX OF THE BOND ANGLE.	214
TABLE 5-10. DIHEDRAL ANGLES OF PHENOL OH-TORSIONAL SADDLE POINT. THE POINT REPORTED HERE, THE OH-TORSIONAL SADDLE POINT ON THE GROUND STATE, IS THE ONLY NON-PLANAR CRITICAL POINT. ALL THE PLANAR CRITICAL POINTS ON <i>AB INITIO</i> SURFACES ARE ALSO EXACTLY PLANAR IN THE FIT DUE TO SYMMETRY CONSTRAINS.	216
TABLE 5-11. CARTESIAN GEOMETRIES OF <i>AB INITIO</i> AND FIT CRITICAL POINTS.	217

List of Figures

FIGURE 2-1. PROJECTION OF DATA POINT GEOMETRIES ON G-H PLANE.....	28
FIGURE 2-2. COMPARISON OF $H^{(D)}$ AND <i>AB INITIO</i> AT INTERPOLATED POINTS ALONG A SEMICIRCLE WITH RADIUS 0.015 AU ON <i>G-H</i> PLANE NEAR $MEXC_{2V}$. RIGHT HAND ORDINATE REFERS TO DASHED CURVES.	32
FIGURE 2-3. LINEAR SYNCHRONOUS TRANSIT PATH $MIN2D_{3H} \rightarrow SAD2C_{2V} \rightarrow MEXC_{2V}$. RIGHT HAND ORDINATE REFERS TO DASHED CURVES. LEFT: E_1 PANEL; RIGHT: E_2 PANEL ...	33
FIGURE 2-4. LINEAR SYNCHRONOUS TRANSIT PATH $SAD2C_{2V} \rightarrow ASYM1C_{2V}$ (BYPASSING $MEXC_{2V}$). RIGHT HAND ORDINATE REFERS TO DASHED CURVES. LEFT: E_1 PANEL ; RIGHT: E_2 PANEL.....	33
FIGURE 2-5. NH BOND LENGTH DISPLACEMENTS FROM $MEXC_{2V}$. RIGHT HAND ORDINATE REFERS TO DASHED CURVES. LEFT: E_1 PANEL; RIGHT: E_2 PANEL.....	34
FIGURE 2-6. LINEAR SYNCHRONOUS TRANSIT PATH $MEXC_{2V} \rightarrow MINIC_{3V}$. RIGHT HAND ORDINATE REFERS TO DASHED CURVES. LEFT: E_1 PANEL; RIGHT: E_2 PANEL.....	34
FIGURE 2-7. COMPARISON OF <i>AB INITIO</i> AND H^D DETERMINED DERIVATIVE COUPLINGS FOR DATA POINTS INCLUDED IN THE FIT. <i>X</i> -AXIS IS THE <i>AB INITIO</i> VALUE, <i>Y</i> -AXIS IS THE H^D DETERMINED VALUE OF A COMPONENT OF A NONZERO VALUED OF THE DERIVATIVE COUPLING. TOP: FIT1; BOTTOM: FIT2.....	40
FIGURE 2-8. COMPARISON OF <i>AB INITIO</i> AND H^D DETERMINED DERIVATIVE COUPLINGS FOR INTERPOLATED POINTS. <i>X</i> -AXIS IS THE <i>AB INITIO</i> VALUE, <i>Y</i> -AXIS IS THE H^D DETERMINED VALUE OF A COMPONENT OF A NONZERO VALUED OF THE DERIVATIVE COUPLING. TOP: FIT1; BOTTOM: FIT2.....	40

FIGURE 2-9 COMPARISON OF *AB INITIO* AND H^D DETERMINED ENERGY GRADIENTS FOR POINTS INCLUDED IN THE FIT. X-AXIS IS THE *AB INITIO* VALUE, Y-AXIS IS THE H^D DETERMINED VALUE OF A COMPONENT OF A NONZERO VALUE OF AN ENERGY GRADIENT. LEFT: FIT1; RIGHT: FIT2..... 41

FIGURE 2-10 COMPARISON OF *AB INITIO* AND H^D DETERMINED ENERGY GRADIENTS FOR INTERPOLATED POINTS. X-AXIS IS THE *AB INITIO* VALUE, Y-AXIS IS THE H^D DETERMINED VALUE OF A COMPONENT OF A NONZERO VALUE OF AN ENERGY GRADIENT. LEFT: FIT1;RIGHT: FIT2. 41

FIGURE 2-11. 3D PLOT OF $H^{(D)}$ DETERMINED ADIABATIC ENERGIES ON G-H PLANE 42

FIGURE 3-1. PLOT OF $1,2^1A$ ADIABATIC POTENTIAL ENERGY SURFACES OF NH_3 AS A FUNCTION OF $R(N-H)$ AND OUT OF PLANE ANGLE($^\circ$). THE OUT OF PLANE ANGLE ϕ , ($0 < \phi < 90^\circ$) SATISFIES $\sin \phi = \frac{\vec{d}_{N-H1} \times \vec{d}_{N-H2} \cdot \vec{d}_{N-H3}}{\|\vec{d}_{N-H1} \times \vec{d}_{N-H2} + \vec{d}_{N-H2} \times \vec{d}_{N-H3} + \vec{d}_{N-H3} \times \vec{d}_{N-H1}\|}$ WHERE

$$\vec{d}_{N-Hn} = \vec{r}_{N-Hn} / r_{N-Hn} \dots\dots\dots 72$$

FIGURE 3-2. PLOT COMPARING THE ACCURACY OF H^D CONSTRUCTED FROM EQ. (3-22), BLACK DOT AND EQ. (3-23), RED DOTS. MAGNITUDE OF RESIDUAL ENERGY GRADIENT PLOTTED AGAINST THE MAGNITUDE OF THE ENERGY GRADIENT. THESE TWO FIGURE ARE PLOTTED FROM THE SAME DATA. LEFT: RED ON TOP; RIGHT: BLACK ON TOP..... 85

FIGURE 3-3. PLOT COMPARING THE ACCURACY OF H^D CONSTRUCTED FROM EQ. (3-22), BLACK DOT AND EQ. (3-23), RED DOTS. MAGNITUDE OF RESIDUAL DERIVATIVE COUPLING PLOTTED AGAINST THE MAGNITUDE OF THE DERIVATIVE COUPLING. 86

FIGURE 3-4. PLOT OF ENERGIES $E^{a,I,(ab)}$, $E^{a,J,(ab)}$ (BLACK, SOLID LINES) $E^{a,I,(m)}$, $E^{a,J,(m)}$ (BLACK DASHED LINES) DERIVATIVE COUPLINGS $\| \| \|$ (DARK BLUE, SOLID LINES) AND RESIDUAL COUPLING $\| \delta \mathbf{f}^{a,I,J} \|$ (LIGHT BLUE, DASHED LINES) AS A FUNCTION OF R(N-H) ALONG A DISSOCIATIVE PATH WHICH IS THE UNION OF POINTS CONNECTING THE \tilde{A} STATE MINIMUM TO THE \tilde{A} STATE SADDLE POINT; THE \tilde{A} STATE SADDLE POINT TO THE MINIMUM ENERGY CROSSING (MEX) POINT; AND THE MEX POINT TOWARD THE ASYMPTOTE. PLATE (A) REPORTS THE GLOBAL PATH. PLATES (B) AND (C) REPORT RESTRICTIONS OF THAT PATH TO: (B) A PATH FROM THE \tilde{A} STATE MINIMUM TO THE \tilde{A} STATE SADDLE POINT AND (C) A PATH NEAR THE MEX. FILLED (OPEN) CIRCLES POINTS INCLUDED (NOT INCLUDED) IN THE FIT DATA SET. 89

FIGURE 3-5. PLOT OF ENERGIES $E^{a,I,(ab)}$, $E^{a,J,(ab)}$ (BLACK, SOLID LINES) $E^{a,I,(m)}$, $E^{a,J,(m)}$ (BLACK DASHED LINES), DERIVATIVE COUPLINGS $\| \| \|$ (DARK BLUE, SOLID LINE) AND RESIDUAL COUPLING $\| \delta \mathbf{f}^{a,I,J} \|$ (LIGHT BLUE, DASHED LINE) ALONG A PATH CENTERED AT THE MINIMUM ENERGY CONICAL INTERSECTION AS A FUNCTION AS A FUNCTION OF THE OUT OF PLANE ANGLE. FILLED (OPEN) CIRCLES ARE POINTS INCLUDED (NOT INCLUDED) IN THE FIT DATA SET..... 90

FIGURE 3-6. PLOT OF ENERGIES $E^{a,I,(ab)}$, $E^{a,J,(ab)}$ (BLACK SOLID LINES), $E^{a,I,(m)}$, $E^{a,J,(m)}$ (BLACK DASHED LINES), DERIVATIVE COUPLINGS $\| \| \|$ (DARK BLUE SOLID LINE) AND RESIDUAL COUPLING $\| \delta \mathbf{f}^{a,I,J} \|$ (LIGHT BLUE, DASHED LINES) AS A FUNCTION OF THE OUT OF PLANE ANGLE FROM THE PLANAR SADDLE POINT ON THE 1^1A POTENTIAL ENERGY SURFACE TO THE GROUND STATE MINIMUM. FILLED CIRCLES POINTS INCLUDED IN THE FIT DATA SET. 91

FIGURE 3-7. PLOT OF ENERGIES $E^{a,I,(ab)}$, $E^{a,J,(ab)}$ (BLACK, SOLID LINES) $E^{a,I,(m)}$, $E^{a,J,(m)}$ (BLACK DASHED LINES), DERIVATIVE COUPLINGS $\| \dot{\mathbf{f}} \|$ (DARK BLUE, SOLID LINE) AND RESIDUAL COUPLING $\| \delta \mathbf{f}^{a,I,J} \|$ (LIGHT BLUE DASHED LINES) ALONG A PATH STARTING FROM THE MEX TO A DISTINCT LOCAL MINIMUM ENERGY CONICAL INTERSECTION, MEX-L WITH A SIGNIFICANTLY DIFFERENT MOLECULAR STRUCTURE. FILLED (OPEN) CIRCLES POINTS INCLUDED (NOT INCLUDED) IN THE FIT DATA SET. THE PATH IS PREDOMINATELY ALONG THE OUT-OF-PLANE ANGLE, ALONG WHICH DIRECTION THE DIABATIC STATES ARE COUPLED. NOTE THAT BY MOVING ALONG THE MIRROR IMAGE OF THIS PATH ONE CAN ACHIEVE A FULL ROTATION AND RETURN TO THE MEX 91

FIGURE 3-8. DIABATIC REPRESENTATION AS A FUNCTION OF R(N-H) AND OUT-OF-PLANE ANGLE. TOP: $H_{1,1}^d$ AND $H_{2,2}^d$; BOTTOM: $H_{1,2}^d$ 94

FIGURE 4-1. THREE DIMENSIONAL PLOT OF ADIABATIC POTENTIAL ENERGY SURFACES SHOWING: (I) MINIMA ON GROUND STATE AND EXCITED STATES, (II) A SADDLE POINTS ON THE 1^1A AND 2^1A POTENTIAL ENERGY SURFACES AND (III) THE MINIMUM ENERGY CROSSING ON THE $1,2^1A$ SEAM OF CONICAL INTERSECTIONS. 136

FIGURE 4-2. $E^{\text{exp}}(n)$, $E_{\text{shift}}^m(n) = E^m(n) - [E^m(0) - E^{\text{exp}}(0)]$ AND $\delta E^m(n) = E^{\text{exp}}(n) - E_{\text{shift}}^m(n)$ FOR $M = \text{PW}$ AND LVT FOR N QUANTA IN ν_2 MODE OF \tilde{A} STATE OF NH_3 AND ND_3 . 138

FIGURE 4-3. INTENSITIES OF TRANSITIONS FROM THE GROUND VIBRATIONAL LEVEL OF NH_3 (\tilde{X}) TO THE 2^N LEVEL OF THE \tilde{A} STATE, COMPARED WITH MEASURED SPECTRA FROM REF. ⁶ LEFT: NH_3 . RIGHT: ND_3 139

FIGURE 4-4. CALCULATED LIFETIMES OF 2^N LEVELS OF NH_3 AND ND_3 USING THE \mathbf{H}^p BY LVT AND PRESENT WORK (PW) COMPARED WITH THE EXPERIMENTAL NH_3 VALUES OF

REF. ⁷ $0 \leq N \leq 3$ AND REF. ⁴ $3 < N \leq 6$ BASED ON THE COMPILATION OF REF. ⁸ AND
 THE EXPERIMENTAL ND₃ VALUES OF REF. ⁷ $0 \leq N \leq 2$. LEFT: NH₃; RIGHT: ND₃ 140

FIGURE 4-5 PERCENTAGE OF NH₂(\tilde{X}) AS A FUNCTION OF THE TOTAL ENERGY, RELATIVE TO
 THE \tilde{X} STATE MINIMUM. THE EVEN AND ODD PARITIES ARE REPRESENTED BY RED
 AND BLUE, RESPECTIVELY. THE OPENING OF THE NH₂(\tilde{X}) CHANNEL IS INDICATED IN THE
 FIGURE BY A ARROW. THE EXPERIMENTAL ESTIMATES¹⁰² ARE GIVEN AS BLACK
 CIRCLES. 143

FIGURE 4-6. THE FRACTION OF ND₂(\tilde{X}) AS A FUNCTION OF THE TOTAL ENERGY, RELATIVE TO
 THE \tilde{X} STATE MINIMUM. THE EVEN AND ODD PARITIES ARE REPRESENTED BY RED
 AND BLUE, RESPECTIVELY. THE OPENING OF THE ND₂(\tilde{X}) CHANNEL IS INDICATED IN THE
 FIGURE BY A ARROW. THE EXPERIMENTAL ESTIMATES¹⁰² ARE GIVEN AS BLACK
 CIRCLES. 144

FIGURE 5-1. PHENOL SHOWING ATOM NUMBERING USED IN THIS WORK..... 175

FIGURE 5-2. RMS ENERGY ERROR FOR 1,2,3¹A STATES AND THE TOTAL. 181

FIGURE 5-3. SCATTER PLOT FOR ENERGY GRADIENTS. GRADIENT NORMS ARE GIVEN IN
 ATOMIC UNIT. NORM OF RESIDUAL GRADIENT, $\|\nabla(E^{a,J,(ab)} - E^{a,J,(m)})\|$ (ORDINATE)
 PLOTTED AGAINST THE MAGNITUDE OF THE *AB INITIO* ENERGY GRADIENT (ABSCISSA).
 182

FIGURE 5-4. SCATTER PLOTS FOR DERIVATIVE COUPLINGS. COUPLING NORMS ARE GIVEN IN
 ATOMIC UNIT. NORM OF RESIDUAL COUPLING $\|\mathbf{f}^{a,J,I,(ab)} - \mathbf{f}^{a,J,I,(m)}\|$ (ORDINATE) PLOTTED
 AGAINST THE MAGNITUDE OF THE *AB INITIO* DERIVATIVE COUPLING (ABSCISSA). 182

FIGURE 5-5. PATH FROM GROUND STATE EQUILIBRIUM TO LARGE R(O-H). DERIVATIVE COUPLINGS NEAR THE 1^1A-2^1A MINIMUM ENERGY CONICAL INTERSECTION ARE ALSO SHOWN.....	183
FIGURE 5-6. DERIVATIVE COUPLINGS NEAR THE 2^1A-3^1A CONICAL INTERSECTION.	183
FIGURE 5-7. TOTAL ENERGY DISTRIBUTION OF 1000 TEST QUASI-CLASSICAL TRAJECTORIES	189
FIGURE 5-8. ENERGY PROFILE OF TWO SAMPLE TRAJECTORIES THAT DISSOCIATE ON 1^1A , 2^1A POTENTIAL ENERGY SURFACES. BLACK MARKERS DENOTE RANDOMLY CHOSEN POINTS FOR WHICH ENERGIES ARE COMPARED WITH <i>AB INITIO</i> RESULTS. SEE TABLES VIIA-B. LEFT: 1^1A CHANNEL; RIGHT: 2^1A CHANNEL.....	190
FIGURE 5-9. LARGE AMPLITUDE MOTION. HISTOGRAM SHOWING DISPLACEMENTS ALONG BOND DISTANCES, BOND ANGLES AND DIHEDRAL ANGLES FOR ALL DATA POINTS USED IN THE FIT.....	193
FIGURE 5-10. LARGE AMPLITUDE MOTION USED TO CONFIRM DOMAIN OF DEFINITION. PICTURES OF PHENOL SHOWING LARGEST DISPLACEMENTS ALONG 9 INTERNAL COORDINATES FOR \mathbf{R}^N WITH ENERGY $<50,000\text{cm}^{-1}$. BOND STRETCHES, BOND ANGLES AND DIHEDRAL ANGLES EXCEPT THOSE INVOLVED IN THE DISSOCIATION OF O-H BOND ARE INCLUDED.	193
FIGURE 5-11. QUALITY OF FIT ENERGY AND COUPLING ON PATH TO PREFULVENIC INTERSECTION.....	194
FIGURE 5-12. ANALYSIS OF A DISCONTINUITY IN THE <i>AB INITIO</i> DATA CAUSED BY A CHANGE FROM RYDBERG TO VALENCE CHARACTER OF AN ORBITAL IN THE ACTIVE SPACE. DISCONTINUITY OCCURS FOR R(OH) $\sim 1.185 \text{ \AA}$	196

Chapter 1 Introduction

1.1 Chemistry beyond the Born-Oppenheimer Approximation

It has been long established that almost all the desired knowledge about a chemical process rests in the wave function of the chemical system, obtained by solving quantum mechanical equations, in the case of a non-relativistic molecular system, the Schrödinger equation. However, solving such equations for even a moderately sized molecule is a formidable, if not impossible, task.

The Born-Oppenheimer(BO) Approximation, also referred to as the adiabatic approximation, significantly alleviates such difficulties by allowing separation of nuclear and electronic motions in molecular systems. This converts the impractical task of the solution of the molecular Schrödinger equation into two more practical steps: generation of potential energy surface(PES) by solving electronic Schrödinger equation at various geometries, and nuclear dynamics on the PES. The BO Approximation is extremely powerful and often also accurate enough for most chemical processes. As a result, it is almost ubiquitously applied throughout chemistry.

Despite its utility in quantum mechanical calculations, this indispensable approximation is not always valid. When a reaction takes place at high energy, usually through high temperature or by photoexcitation, or when electronic degeneracy is present at low energy, multiple electronic states can become involved, making the process non-adiabatic. The family of non-adiabatic processes encompasses many important reactions. In reactions in extreme temperature or pressure, including many processes involved in ignition, combustion and explosion, are non-adiabatic because of the large amount of

available energy. BO Approximation is also violated in photochemical processes, where absorption of a photon causes the system to be electronically excited, including vital biochemical processes such as vision, photosynthesis, and the UV resistency of DNA; valuable industrial processes such as the photovoltaic effect and solar energy conversion; as well as many astronomical and atmospheric reactions; and many more.

To facilitate calculations of non-adiabatic processes, the total wave function has to be expanded with more than one adiabatic state. Instead of a single PES, a set of coupled PESs and interstate couplings have to be provided. Alternatively, the simulation can be performed in a diabatic representation where interstate couplings are ignorable, but the electronic Hamiltonian is not diagonal.

In the recent years, much progress has been made to allow very high accuracy dynamics simulations for adiabatic processes. Adiabatic PES can be built with permutationally invariant polynomials^{1,2}, Shepard interpolation³ or moving least squares technique⁴. However, nonadiabatic processes are more challenging to describe. Experimental observations are usually indirect and can be difficult to interpret. Discrepancies between theoretical predictions and experimental results are common. Fit diabatic potential energy surfaces⁵⁻⁷ usually cannot achieve sufficient accuracy and employ tricks to construct diabatic states that are difficult to verify. Direct dynamics methods⁸⁻¹⁰ on the other hand are extremely expensive, often requiring less expensive but also less accurate wave functions and limiting dynamics simulation to a very small number of trajectories. New theoretical methods that can achieve high accuracy at acceptable cost are therefore highly desired.

1.2 Eliminating the Computational Bottleneck with Analytical Approximation

Accurate non-adiabatic calculations often require very expensive multireference electronic structure calculations, which can take hours or even days even when executed in parallel. The nuclear dynamics step also requires the PESs and derivative couplings to be evaluated over large number of points, sometimes several million. As a result, the electronic structure step becomes the computational bottleneck and makes high precision simulation extremely difficult.

Direct non-adiabatic simulations with highly accurate wave functions that can achieve chemical accuracy are still impractical for most molecules and will remain so in the near future. Approximate methods are therefore desired to accelerate the data generation procedure by making a (hopefully) small compromise in their precision.

In this work, the approximation is accomplished by constructing analytical functions, which can reliably generate high precision energy and derivative coupling data with significantly reduced cost. Because of the smoothness of potential energy surfaces, the number of data point needed to construct an analytical approximation for the relevant region is many magnitudes smaller than the number of points needed in the simulation procedure, resulting in significant acceleration of the overall process. For example, dynamics with quasi-classical surface hopping trajectories usually require millions of evaluations of the PESs, which can be built from only a few thousand data points. A quasi-diabatic representation is used because the smoothness and absence of singularity in such representations is crucial for a correct description of the vicinity of conical intersection seams.

1.3 Inadequacies of Existing Methods

In the past few years, many successful dynamics simulations were reported for adiabatic processes by fitting ab initio data to analytical functions^{1,2}. However, at the vicinity of conical intersections, potential energies become discontinuous and the derivative couplings approach infinity, complicating the fitting procedure. On the other hand, nonadiabatic interactions are most prominent near such singularities, making their description a crucial task for nonadiabatic dynamic simulations. Therefore, special treatment is necessary for the seam of conical intersections.

This usually means working in diabatic representations, the definition of which varies among authors. “Diabatization by ansatz” method^{11,12} fits adiabatic energy data to a diabatic Hamiltonian and assume that a smooth fit that reproduce these energies should be diabatic. Various methods also exist to construct diabatic states by referencing the continuity of electronic wave functions, such as orbital overlap based method¹³ or approaches based on four-fold-way¹⁴. Numerous other methods also use molecular properties to construct diabatic representation.

However, constructing diabatic states with these methods can cause potential problems in the ensuing simulations. When solving nuclear dynamics in a diabatic representation the residual couplings, the derivative couplings between diabatic states, are ignored. Above-mentioned methods define diabatic states with other perceived properties and the residual couplings are not necessarily small.

It is therefore necessary to work in a method where residual couplings are quantified. The quasi-diabatic Hamiltonian(\mathbf{H}^d) approach previously developed in our group¹⁵⁻¹⁷ achieves this by utilizing derivative coupling data for the adiabatic states.

Although derived from “diabatization-by-ansatz” methods, the explicit fit of derivative couplings allows the fitting program to actively search for representations where residual couplings are small, rather than relying on the smoothness of fitting functions to do so.

The advantages of the \mathbf{H}^d method were evident in my previous project on the photoelectron spectroscopy of pyrrolide anion^{16,17}, where the spectrum was strongly perturbed by a conical intersection. Residual couplings completely vanish at the minimum energy crossing point and were kept minimal throughout the relevant region. Quantitative agreement with experimental measurements was observed.

However, that method is limited to bound-state problems that are confined around a fixed origin point. The ansatz does not possess the flexibility to describe more complex features of the potential energy surfaces, and the point group symmetry treatments break down when large amplitude motions take place. Large amplitude motions also make large portions of the seam of conical intersections accessible to nuclear wave functions. However, the method in its present form is not capable of describing large portions of the seam that contain regions with qualitatively different characters.

1.4 The Non-local Quasi-diabatic Hamiltonian (\mathbf{H}^d) Approach

It has been made clear that enhancement and generalization of the previous \mathbf{H}^d approach is desired so that the new method can be applied to more complex nonadiabatic processes such as photodissociation, while retaining the excellent treatment of conical intersections.

To expand the domain of applicability of local expansions, one either must change the form of the expansion to allow the description of regions further away, or interpolations have to be made between multiple centers. For the interpolation methods,

Shepard interpolation methods and modified Shepard interpolation methods¹⁸⁻²⁰ have been developed for the construction of both adiabatic and diabatic surfaces. However, locally constructed diabatic representations are subject to one arbitrary constant rotation, no matter which type of diabatization technique is used. Such constant rotation cannot be determined unless the center of the expansion point possesses symmetry and the off-diagonal block carry nonsymmetric representation. The derivative couplings between the interpolation centers are affected by the choice of this arbitrary rotation, making it unreliable for strongly nonadiabatic regions.

In Chapter 2, the local quadratic \mathbf{H}^d method is generalized so that it is applicable to dissociative systems without the need of interpolations. Globally well-behaved functions are used as coordinates to obtain the correct behavior upon dissociation. Polynomials of these coordinates are used as a flexible basis, and Lagrange multipliers in combination with intersection adapted coordinates are used to treat arbitrary number of points of conical intersections. A projection operator technique is also developed to handle CNPI instead of point group symmetry. $1,2^1A$ states of NH_3 is used as an example.

In Chapter 3, the theory is reformulated in more general terms, starting slightly differently by searching for the most diabatic representation in a least-squares sense and at the same time trying to reproduce energies and energy gradients. Method to quantify residual coupling between quasi-diabatic states is also established. The notion of origin, which was a relic of the local method, is abolished, resulting in a very flexible method that can describe multiple regions accurately on an equal footing. The exact formula of the gradient of the Lagrangian is also derived, and a modified Gauss-Newton procedure is

used to facilitate better convergence. A trajectory-guided point sampling approach is also adopted to saturate data in dynamically relevant regions. The algorithm is applied to NH_3 system, and is able to describe significantly larger region of the nuclear configuration space with drastically improved accuracy. Residual couplings between quasi-diabatic states are also quantitatively calculated, verifying the diabaticity of the constructed representation.

In Chapter 4, the \mathbf{H}^d for $1,2^1\text{A}$ states of NH_3 is put to test in the simulation of the photodissociation absorption spectra of NH_3 and ND_3 . Experimental measurement is very precisely reproduced, and significant improvement over the previous treatments is achieved. In other work not present in this dissertation²¹, \mathbf{H}^d is also used to simulate branching ratios and kinetic energy release profile of the same reaction, which provide more dynamical information, both with very good agreement with experimental measurements. These simulations evince the high quality of the representation, both in terms of reproduction of potential energy surfaces, and in the correct treatment of non-adiabatic interactions.

In Chapter 5, the method is further enhanced with new features to enable description of much larger systems. A partially diagonalized representation approach enables the correct treatment of conical intersection or near degeneracy points without the need to exactly reproduce *ab initio* data, enabling the description of a seam space with much larger dimensionality. A null-space analysis procedure is adopted to help determine the most efficient polynomial basis, as well as to remove linear dependencies from the fitting equations. The fitting procedure is also improved to run faster and use fewer resources, so that larger system can be handled. The $1,2,3^1\text{A}$ coupled potential

energy surfaces are constructed for the photodissociation process of phenol as an example. All 33 degrees of freedom are fully incorporated, which describes many different large amplitude motions. The fit can also correctly reproduce multiple seams of conical intersections.

References

- 1 J. M. Bowman, G. Czako, B. Fu, *Phys. Chem. Chem. Phys.* **13**, 8094 (2011).
- 2 C. Chen, B. Braams, D.Y. Lee, J.M. Bowman, P.L. Houston, D. Stranges, *J. Phys. Chem. A* **115**, 6797 (2011).
- 3 O. Godsi, M. A. Collins, and U. Peskin, *J. Chem. Phys.* **132**, 124106(2010).
- 4 R. Dawes, D. L. Thompson, A. F. Wagner, and M. Minkoff, *J. Chem. Phys.* **128**, Thompson, *J. Chem. Phys.* **130**, 144107(2009)
- 5 W. Lai, S.Y. Lin, D. Xie, H. Guo, *J. Chem. Phys.* **129**, 154311(2008).
- 6 D. Bonhommeau, R. Valero, D.G. Truhlar, A.W. Jasper, *J. Chem. Phys.* **130**, 234303(2009).
- 7 W. Lai, S.Y. Lin, D. Xie, H. Guo, *J. Phys. Chem. A* **114**, 3121(2010).
- 8 G. A. Worth, M. A. Robb, and B. Lasorne, *Mol. Phys.* **106**, 2077(2008).
- 9 M. Barbatti, A. J. A. Aquino, J. Szymczak, D. Nachtigallova, and H. Lischka, *Phys. Chem. Chem. Phys.* **13**, 6145(2011).
- 10 A. F. Izmaylov, *J. Chem. Phys.* **138**, 104115(2013).
- 11 W. Eisfeld, A. Viel, *J. Chem. Phys.* **122**, 204317 (2005).
- 12 A. Viel, W. Eisfeld, C.R. Evenhuis, U. Manthe, *Chem Phys* **347**, 331(2008).
- 13 T. Ichino, A.J. Gianola, W.C. Lineberger, J.F. Stanton, *J. Chem. Phys.* **125**, 084312 (2006).
- 14 S. Nangia, D.G. Truhlar, *J. Chem. Phys.* **124**, 124309 (2006).

- 15 M.S. Schuurman, D.R. Yarkony, J. Chem. Phys. **127**, 094104 (2007).
- 16 X. Zhu, D. R. Yarkony, J. Chem. Phys. **130**, 234108 (2009).
- 17 X. Zhu, D. R. Yarkony, J. Phys. Chem. C **114**, 5312 (2010).
- 18 C.R. Evenhuis, M.A. Collins, J. Chem. Phys. **121**, 2515 (2004).
- 19 C.R. Evenhuis, X. Lin, D.H. Zhang, D.R. Yarkony, M.A. Collins, J. Chem. Phys. **123**, 134110 (2005).
- 20 O. Godsi, C.R. Evenhuis, M.A. Collins, J. Chem. Phys. **125**, 104105 (2006).
- 21 J. Ma, X. Zhu, H. Guo, and D. R. Yarkony, J. Chem. Phys. **137**, 22A541(2012).

Chapter 2 Toward Highly Efficient Nonadiabatic Dynamics on the Fly: An Algorithm to Fit Non-local Quasi-Diabatic, Coupled Electronic State Hamiltonians based on *ab initio* Electronic Structure Data

2.1 Abstract

An algorithm for constructing a quasi-diabatic, coupled electronic state Hamiltonian, in a localized region of nuclear coordinate space, suitable for determining bound state spectra, is generalized to determine a non-local Hamiltonian capable of describing, for example, multichannel nonadiabatic photodissociation. For N^{state} coupled electronic states, the Hamiltonian, \mathbf{H}^d , is a symmetric $N^{state} \times N^{state}$ matrix whose elements are polynomials involving: decaying exponentials $\exp(-ar_{i,j}^n)$ $n = 1,2$ where $\mathbf{r}_{i,j} = \mathbf{R}^i - \mathbf{R}^j$, $r_{i,j} = \|\mathbf{r}_{i,j}\|$, \mathbf{R}^j locates the j^{th} nucleus; and scaled dot-cross product coordinates, proportional to $\mathbf{r}_{i,j} \times \mathbf{r}_{i,k} \cdot \mathbf{r}_{i,l}$. The constructed Hamiltonian is constrained to reproduce, exactly, the *ab initio* data, energies, gradients and derivative coupling at selected points, or nodes, in nuclear coordinate space. The remainder of the *ab initio* data is approximated in a least squares sense using a normal equations approach. The fitting procedure includes a damping term that precludes oscillations due to the nodal constraints or local excesses of parameters. To illustrate the potential of the fitting procedure an \mathbf{H}^d is constructed, with the full nuclear permutation-inversion symmetry, which describes portions of the $1,2^1A$ potential energy surfaces of NH_3 , including the minimum energy point on the $1,2^1A$ seam of conical intersection and the NH_2+H asymptote. *Ab initio* data at 239 nuclear configurations was used in the construction, which was tested at forty-eight additional nuclear configurations. While the energy range on the ground and excited potential energy surface are each individually $\sim 45,000 \text{ cm}^{-1}$, the root mean square error for the energies at all points is only 93.6 cm^{-1} . The location and local conical topography of the minimum energy conical intersection is exactly reproduced. The derivative couplings are shown to be well reproduced, justifying the attribute quasi-diabatic.

2.2 Introduction

The representation of PESs and their interstate interactions has long been a goal of computational quantum chemistry.¹⁻² Recently several approaches to fitting coupled state potential energy surfaces have been reported, including a generally applicable approach based on Shepard interpolation,³⁻⁵ an approach specifically oriented toward triatomics with some point group symmetry,⁶ an approach based on the "diabatization by ansatz" technique² and an approach based on the four-fold way.⁷ In each of these approaches the coupled adiabatic potential energy surfaces are obtained from a quasi-diabatic Hamiltonian, \mathbf{H}^d , an $N^{state} \times N^{state}$ matrix whose matrix elements are polynomials in a set of nuclear coordinates. In this work we introduce a new method for obtaining this \mathbf{H}^d . In our approach \mathbf{H}^d is based on, *ab initio* derivative couplings, $\mathbf{f}^{I,J}(\mathbf{Q}) = \left\langle \Psi_I^a(\mathbf{q};\mathbf{Q}) \left| \nabla \Psi_J^a(\mathbf{q};\mathbf{Q}) \right\rangle_{\mathbf{q}}$ as well as adiabatic energies, $E_I(\mathbf{Q})$, $I = 1 - N^{state}$, and energy gradients $\nabla E_I(\mathbf{Q})$, obtained over a wide range of nuclear configurations. Here $\Psi_I^a(\mathbf{q};\mathbf{Q})$ is a high level, multireference configuration interaction (MRCI), adiabatic electronic state wave function with energy $E_I(\mathbf{Q})$, \mathbf{Q} is a set of at least, (since we will be using over complete bases) $N^{int} = 3N^{at} - 6$ internal coordinates for the N^{at} nuclei and \mathbf{q} are the coordinates of the N^{el} electrons. In this work we will refer to an \mathbf{H}^d , determined using data over a wide range of nuclear configurations including dissociated configurations, as non-locally defined. Advantages of the proposed approach, attributable in part to the use of derivative coupling data and in part to algorithmic innovation, include the following. (a) No *a priori* knowledge of the locus of conical intersection seams is required and yet the local topography of a conical intersection is reproduced exactly. (b) No preliminary diabaticization of the *ab initio* data is required and since derivative coupling data is used in

constructing the fit, the residual derivative coupling is minimized in a least squares sense. (c) High level MRCI wave functions is used from which derivative coupling and energy gradient data are readily determine,⁸ but does not require second derivatives which are quite costly to obtain. With regard to point (b), we note that it is not possible to remove all the residual derivative coupling since it has been shown by Baer, Mead and others that in general rigorous diabatic electronic states do not exist.^{9,10,11}

Section 2.3 describes the algorithm used to construct \mathbf{H}^d , a generalization of our pseudo normal equations method for determining \mathbf{H}^d (Ref. ^{12,13}) for bound electronic states which uses natural internal coordinates.¹⁴ Four key aspects of our algorithm will be discussed, constraints, nuclear coordinates, damping and symmetry. Constraints are imposed, through the use of Lagrange multipliers, at points in nuclear coordinate space called "nodes". At nodes, some or all of the electronic structure data, energy, energy gradients and derivative couplings are reproduced exactly by \mathbf{H}^d . The second issue is the choice of internal coordinates. We cannot use bond distances as we did in determining the bound \mathbf{H}^d since bond distances go to $+\infty$ as the molecule dissociates, which is an anathema to our polynomial form of \mathbf{H}^d . In addition, local internal coordinates for one geometrical isomer are in general ill-suited for use at a distinct geometrical isomer. Instead we use a generalization of the approach developed by Braams, Bowman and co-workers¹⁵ who used functions of the form $\exp(-\alpha |\mathbf{R}^i - \mathbf{R}^j|)$, where $\mathbf{R}^j = (R_x^j, R_y^j, R_z^j)$ locates the j^{th} nucleus, to successfully fit ground state global adiabatic potential energy surfaces, for molecules including protonated water dimer¹⁶ and hydroxycarbene.¹⁷ The third issue, referred to as damping, represents the fact that for higher order polynomials, with many parameters, although the defining equations are technically over determined,

data from locally poorly defined regions may lead to parametrizations which interpolate poorly, or even oscillate, between data points. To avoid this situation a damping or smoothing term is introduced into the fitting procedure which eliminates this deficiency. Finally for truly global representations, extensions of the non-local representations emphasized in this work, there is the issue of the non-rigid molecule¹⁸ or CNPI symmetry,¹⁹ the symmetry induced by interchange of identical nuclei and inversion of the entire molecule, nuclei and electrons. We explain how, in the case considered here, projection operators are used to incorporate this symmetry. See also Refs. ^{15,5}.

Section 2.4 addresses the computational issues involved in the fitting procedure. We seek to establish that algorithm reported in section 2.3 is a viable tool for fitting coupled potential energy surfaces, exhibiting conical intersections, for dissociative systems, over a wide range of nuclear configurations. The $1,2^1A$ states of NH_3 are used as an example. This system, whose photodissociation has been the subject of considerable experimental²⁰⁻²² and theoretical^{7, 23-25} interest, was chosen because it exhibits the key challenge encountered in constructing a non-local H^d , a conical intersection well removed from the origin of the coordinate system, which leads to a dissociation channel. We demonstrate the accuracy of the fit and the use of the damping or smoothing function to eliminate inter data point oscillations. We show that as a consequence of the use of nodes not only does H^d have the correct topographical features, minima, saddle points, conical intersections and dissociation asymptotes but it has them in precisely the same location in nuclear coordinate space and at the same energy as the *ab initio* data from which it is derived. We demonstrate how use of nodes also enables us to precisely reproduce the conical topography obtained from *ab initio* data at a point of

conical intersection. We further demonstrate how over complete bases can be used to systematically improve the accuracy of the fit. Finally we show that the *ab initio* derivative couplings are well reproduced by \mathbf{H}^d justifying the attribute quasi-diabatic. Section 2.5 summarizes the research in this chapter.

2.3 The Quasi-diabatic Hamiltonian and its Determination

The quasi-diabatic representation, \mathbf{H}^d , is intended to approximate the *ab initio* energies $E_I(\mathbf{Q})$, the energy gradients $\nabla E_I(\mathbf{Q})$, and the derivative couplings $\mathbf{f}^{IJ}(\mathbf{Q})$ for N^{state} adiabatic electronic states, over a wide range of \mathbf{Q} . Here \mathbf{Q} is a set of, N^{rc} , internal coordinates that may be overcomplete.

2.3.1 The Quasi-Diabatic Hamiltonian

\mathbf{H}^d is a symmetric $N^{\text{state}} \times N^{\text{state}}$ matrix whose elements are polynomials in the internal coordinates:

$$H_{\alpha,\beta}^d(\mathbf{Q}) \square \langle \Psi_{\alpha}^d(\mathbf{q};\mathbf{Q}) | H^e(\mathbf{q};\mathbf{Q}) | \Psi_{\beta}^d(\mathbf{q};\mathbf{Q}) \rangle_{\mathbf{q}}$$

$$= E_{\alpha}(\mathbf{Q}^0) \delta_{\alpha,\beta} + \sum_{k=1}^{N^{rc}} V_k^{(1),\alpha,\beta} Q_k + 1/2 \sum_{k,l=1}^{N^{rc}} V_{k,l}^{(2),\alpha,\beta} Q_k Q_l + 1/3 \sum_{k,l,m=1}^{N^{rc}} V_{k,l,m}^{(3),\alpha,\beta} Q_k Q_l Q_m \quad (2-1)$$

Here H^e is the electronic Hamiltonian in the Coulomb approximation and $\Psi_{\alpha}^d(\mathbf{q};\mathbf{Q})$, $\alpha = 1 - N^{\text{state}}$ are the quasi-diabatic electronic states. The eigenvectors of \mathbf{H}^d satisfy the electronic Schrödinger equation:

$$[\mathbf{H}^d(\mathbf{Q}) - \mathbf{I}E_I^{(d)}(\mathbf{Q})] \mathbf{d}^I(\mathbf{Q}) = \mathbf{0} \quad (2-2)$$

2.3.2 Equations defining \mathbf{H}^d

The equations defining \mathbf{H}^d are obtained by differentiating eq. (2-2) and using the derivative of eq. (2-1). However, because of the over completeness of \mathbf{Q} , care must be

exercised when taking the requisite partial derivatives. For example while

$(\partial H_{\alpha,\beta}^d / \partial Q_m)_{Q_k \neq Q_m}$ makes mathematical sense in terms of eq.(2-1), it makes no sense in

nuclear coordinate space since it is not be possible to change Q_m while holding all

remaining Q_k constant. On the other hand $(\partial H_{\alpha,\beta}^d / \partial R_s^m)_{R_s^m \neq R_s^m}$ is not a problem. In what

follows we will use $\nabla^R = (\frac{\partial}{\partial R_x^1}, \frac{\partial}{\partial R_y^1}, \frac{\partial}{\partial R_z^1}, \frac{\partial}{\partial R_x^2}, \dots)$ and when the superscript on ∇ is

suppressed, ∇^R is assumed. Thus, from eqs. (2-2) and (2-1) and their derivatives with

respect to R_s^n we obtain:

$$\nabla E_I^{(d)} = \mathbf{d}^{I\dagger} (\nabla \mathbf{H}^d) \mathbf{d}^I \equiv \mathbf{M}^{I,J,(d)} \quad (2-3)$$

and

$$(E_J^{(d)} - E_I^{(d)}) \mathbf{f}^{I,J,(d)} \equiv (E_J^{(d)} - E_I^{(d)}) \mathbf{d}^{I\dagger} \nabla \mathbf{d}^J = \mathbf{d}^{I\dagger} (\nabla \mathbf{H}^d) \mathbf{d}^J \equiv \mathbf{M}^{I,J,(d)} \quad (2-4)$$

Given the form of eq. (2-1), the gradient $\nabla \mathbf{H}^{(d)}$ is readily evaluated as

$$\frac{\partial H_{\alpha,\beta}^d}{\partial R_s^n} = \sum_{k=1}^{N^{rc}} V_k^{(1),\alpha,\beta} \frac{\partial Q_k}{\partial R_s^n} + \sum_{k,l=1}^{N^{rc}} V_{k,l}^{(2),\alpha,\beta} \frac{\partial Q_k}{\partial R_s^n} Q_l + \sum_{k,l,m=1}^{N^{rc}} V_{k,l,m}^{(3),\alpha,\beta} \frac{\partial Q_k}{\partial R_s^n} Q_l Q_m + \dots \quad (2-5)$$

Inserting Eq. (2-5) into eqs. (2-3), (2-4) yields

$$\begin{aligned} M_{n,s}^{I,J,(d)}(\mathbf{Q}) &= \sum_{\alpha,\beta,k} [d_\alpha^I d_\beta^J \frac{\partial Q_k}{\partial R_s^n}] V_k^{(1),\alpha,\beta} + \sum_{\alpha,\beta,k,l} [d_\alpha^I d_\beta^J \frac{\partial Q_k}{\partial R_s^n} Q_l] V_{k,l}^{(2),\alpha,\beta} \\ &+ \sum_{\alpha,\beta,k,l,m} [d_\alpha^I d_\beta^J \frac{\partial Q_k}{\partial R_s^n} Q_l Q_m] V_{k,l,m}^{(3),\alpha,\beta} + \dots \end{aligned} \quad (2-6)$$

while inserting eq. (2-1) into eq. (2-2) gives:

$$\begin{aligned} M_0^{I,I,(d)}(\mathbf{Q}) &= \sum_{\alpha,\beta,k} [d_\alpha^I d_\beta^I Q_k] V_k^{\alpha,\beta} + \\ &1/2 \sum_{\alpha,\beta,k,l} [d_\alpha^I d_\beta^I Q_k Q_l] V_{k,l}^{(2),\alpha,\beta} + 1/3 \sum_{\alpha,\beta,k,l,m} [d_\alpha^I d_\beta^I Q_k Q_l Q_m] V_{k,l,m}^{(3)\alpha,\beta} + \dots \end{aligned} \quad (2-7)$$

and

$$M_0^{I,I,(d)}(\mathbf{Q}) = E_I^{(d)}(\mathbf{Q}) - E_I^{(d)}(\mathbf{Q}^0) \quad (2-8)$$

Below we will see that the Q_k are known analytically so that ∇Q_k is readily determined in closed form. It is possible to determine the $V_k^{(1),\alpha,\beta}$ using analytic gradient techniques⁸ provided the origin \mathbf{Q}^0 is conveniently located but we do not use that observation in this work. If the $\mathbf{M}^{I,J,(d)}$ are replaced by the corresponding *ab initio* determined values, $\mathbf{M}^{I,J}$, eq. (2-6) for $I=J$ [for $I \neq J$] asserts that an \mathbf{H}^d determined energy gradient [derivative coupling times an energy difference] is equal to the corresponding *ab initio* quantity. Similarly eq. (2-7) asserts the equality of an \mathbf{H}^d determined and an *ab initio* determined energy. In this manner, eqs. (2-6) and (2-7) relate the unknown coefficients $V_{k, \dots}^{(j),\alpha,\beta}$ to *ab initio* energies, energy gradients and interstate coupling gradients, the later being defined as the derivative coupling multiplied by the energy difference.

2.3.3 Constrained Pseudo Normal Equations

We now choose $\mathbf{Q} = \mathbf{Q}(m)$ for $1 \leq m \leq N^{\text{point}}$. Then, with the left hand side of eqs. (2-6) and (2-7), $M_{n,s}^{I,J}(\mathbf{Q}(m))$ viewed as a vector \mathbf{M} of length $N^{\text{eq,t}} = [(N^{\text{state}}(N^{\text{state}}+1)/2)(3N^{\text{int}}) + N^{\text{state}}]N^{\text{point}}$ and indexing the N^{uniq} unique elements of $V_{k, \dots}^{(j),\alpha,\beta}$ as a vector \mathbf{V} , eqs. (2-6) and (2-7) can be rewritten as

$$\mathbf{WV} = \mathbf{M} \quad (2-9)$$

where \mathbf{W} is a matrix of dimension $N^{\text{eq,t}} \times N^{\text{uniq}}$, constructed from the factors in the square brackets on the right hand side of eqs. (2-6) and (2-7).

Several points concerning eq. (2-9) are germane. Note that at each $\mathbf{Q}(m)$ only $(N^{\text{state}}(N^{\text{state}}+1)/2)N^{\text{int}} + N^{\text{state}}$ of the $(N^{\text{state}}(N^{\text{state}}+1)/2)(3N^{\text{int}}) + N^{\text{state}}$ equations are linearly independent since \mathbf{H}^d is expressed in internal coordinates. Therefore ignoring "accidental" linear dependencies, the total number of linearly independent equations is

$N^{eq} = [(N^{state}(N^{state}+1)/2)N^{int} + N^{state}]N^{point}$. As was done in Ref. ¹², it is straightforward to include only the nonzero by symmetry combinations of coefficients in $V_{k,m,\dots}^{(i),\alpha,\beta}$. This will enable us to include CNPI symmetry into eq. (2-9) using projection operators. Finally, note that $N^{uniq} \neq N^{eq}$, so that eq. (2-9) is not solvable as written. N^{point} is chosen so that $N^{eq} > N^{uniq}$, that is, eq. (2-9) is over determined. Consequently we partition eq. (2-9) into two sets of equations. The first N^{lsq} equations, which are to be solved in a least squares sense, will be denoted below by the superscript *lsq*. The remaining $N^{eq} - N^{lsq} = N^{nodes}$ equations, which are to be solved exactly, are the equations for the nodes, and will be denoted below by the superscript *node*. Then the desired solution of the equations that comprise eq. (2-9) is obtained by minimizing the Lagangian:

$$L(\mathbf{V}, \boldsymbol{\lambda}) = 1/2 \sum_{j=1}^{N^{lsq}} (M_j - \sum_{i=1}^{N^{unk}} W_{j,i} V_i)^2 + \sum_{j=N^{lsq}+1}^{N^{eq}} \lambda_j (M_j - \sum_{i=1}^{N^{unk}} W_{j,i} V_i) + 1/2 \mathbf{V}^\dagger \mathbf{t} \mathbf{V} \quad (2-10)$$

with respect to both the parameters V_j , and the Lagrange multipliers λ_j which gives

$$\begin{pmatrix} \mathbf{W}^{lsq\dagger} \mathbf{W}^{lsq} + \mathbf{t} & -\mathbf{W}^{node\dagger} \\ \mathbf{W}^{node} & \mathbf{0} \end{pmatrix} \begin{pmatrix} \mathbf{V} \\ \boldsymbol{\lambda} \end{pmatrix} = \begin{pmatrix} \mathbf{W}^{lsq\dagger} \mathbf{M}^{lsq} \\ \mathbf{M}^{node} \end{pmatrix} \quad (2-11)$$

Here the user chosen \mathbf{t} is a positive definite diagonal matrix with $t_{j,j}$ small, usually $< 10^{-5}$. The $\mathbf{V}^\dagger \mathbf{t} \mathbf{V}$ term is the damping or smoothing term noted in the Introduction. It serves to preclude inadequately defined parameters from becoming large, producing modest improvements in the root mean square error, but producing fits that do not interpolate well, (*i.e.* produce inter point oscillations). This point is discussed from a numerical perspective in Section 2.4. Since they cannot be described by a Hamiltonian based exclusively on internal coordinates, derivative couplings due to translations and rotations are removed from the *ab initio* data prior to fitting.

Equation (2-11) and its defining equations, eqs. (2-6) and (2-7) and (2-8), are the key results of this section. In the absence of the Lagrange multipliers and damping term, the (1,1) block of eq. (2-11) represents a system of normal equations²⁶ for the V . The system of constrained normal equations that constitute eq. (2-11) is not truly linear since the correct \mathbf{d}^I are not known until the V are determined. This issue is resolved by determining the V and the \mathbf{d}^I self-consistently. As a consequence eq. (2-11) is referred to as a system of pseudo constrained normal equations.

2.3.4 Advantages of the Pseudo Constrained Normal Equations Approach

The use of gradient and derivative coupling information reduces the number of points, nuclear configurations, at which *ab initio* data is required to determine the unknown coefficients compared to energy based determinations. Further energy gradients and derivative couplings are obtained at limited additional cost from MRCI wave functions once the energies have been determined.^{8, 27} However these are not the principal advantages of present combined energy and gradient based approach. Using the energy and energy gradient constraints we can require that an \mathbf{H}^d determined potential energy surface have an extremum at precisely the same point and energy as the *ab initio* results. Using the energy gradient, interstate coupling gradient and energy constraints it is possible to require the \mathbf{H}^d determined potential energy surfaces to exhibit a conical intersection at the same point as in the *ab initio* treatment and with the same local conical topography. This is possible since the local topography of a conical intersection is defined by three gradient vectors, the average energy gradient, $\mathbf{s} = (\mathbf{M}^{I,I} + \mathbf{M}^{J,J})/2$, the energy difference gradient, $\mathbf{g} = (\mathbf{M}^{I,I} - \mathbf{M}^{J,J})/2$, and the interstate coupling gradient, $\mathbf{h} =$

$\mathbf{M}^{I,J}$ vectors.²⁸ In section 2.4, we show how an \mathbf{H}^d with the above noted properties can be obtained for the lowest two electronic states of NH_3 .

2.3.5 Nuclear Coordinates.

Natural internal coordinates, which are appropriate for a single equilibrium or reference structure, are not well-suited for a non-local \mathbf{H}^d . In addition, since \mathbf{H}^d is a polynomial in the coordinates, it is desirable that the Q_j are in the range $-1 < Q_j \leq 1$. Internuclear distance coordinates, $r_{ij} = |\mathbf{R}^i - \mathbf{R}^j|$, $1 \leq i < j \leq N^{\text{at}}$ avoid the limitations of a single set of natural internal coordinates, in that they can describe any requisite reference structure. However nuclear distance coordinates may approach infinity as the molecule dissociates. As a result, any polynomial defined in such a coordinate system will also approach infinity, which is an anathema for the molecular Hamiltonian. Following Braams and Bowman,¹⁵⁻¹⁶ to describe molecular fragmentation in a general manner, exponential transformations are used to compress the r_{ij} into the interval $[-1, 1]$ during fragmentation.

(i) Exponential Functions of interatomic distances

In this work two exponential transformations are employed. The first set of transformed coordinates, follows closely those of Braams and Bowman. To succinctly define these coordinates we introduce the single index notation $r_k \equiv r_{i_k, j_k}$ where $k = 1 - N^{\text{at}}(N^{\text{at}}-1)/2$, $1 \leq i < j \leq N^{\text{at}}$, and $r_k = |\mathbf{R}^{i_k} - \mathbf{R}^{j_k}|$. The exponentials

$$\bar{Q}_k / S_k = (1 - e^{-\alpha_k r_k}) \quad (2-12)$$

are contained in the interval $[0,1]$. Then we define the first set of bounded internal coordinates,

$$Q_k^{(1)}/S_k = [\bar{Q}_k(r_k) - \bar{Q}_k(r_k^{(0)})]/S_k = (1 - e^{-\alpha_k \Delta r_k}) e^{-\alpha_k r_k^{(0)}} \quad (2-13)$$

where, $\Delta r_k \equiv r_k - r_k^{(0)}$, and $r_k^{(0)}$ is evaluated at \mathbf{Q}^0 , the origin of the coordinates. S_k is an arbitrary parameter that defines the scaling of the terms of the polynomial with respect to their order. When $t=0$ in equation (2-10), this parameter does not have any effect. Here, we let $S_k = e^{\alpha_k r_k^{(0)}}$, so that $Q_k^{(1)} \rightarrow 1$ when $\Delta r_k \rightarrow +\infty$. For $N^{at} > 4$, the $N^{at}(N^{at} - 1)/2$ dimensional set $\mathbf{Q}^{(1)}$ is over complete, that is $N^{at}(N^{at} - 1)/2 > N^{int}$. Despite the over completeness of the $Q_k^{(1)}$, we found the size of the polynomial basis required to reproduce the *ab initio* data can be reduced considerably by adding a second set of exponential coordinates defined as

$$Q_k^{(2)}/S_k' = Q_k^{(2)}(r_k)/S_k' = (1 - \exp[-\beta_k(r_k - r_k^{(0)})^2]) \quad (2-14)$$

where $S_k' = 1$, so that $Q_k^{(2)} \rightarrow 1$ when $\Delta r_k \rightarrow +\infty$. The only requirement on α_k , β_k is that they be invariant under the CNPI group discussed below. Note that the second order terms of $Q_k^{(1)}$, $Q_k^{(1)2}$, have the form of a Morse potential, which gives the qualitatively correct dissociation behavior.

(ii) Inversion symmetry and "dot-cross product" functions⁵

The electronic Hamiltonian is invariant under the operation, inversion of the nuclei and the electrons through the origin (a subgroup of order 2 of the CNPI group). Nuclear distances, r_k , are invariant under this inversion operation. As a consequence, the transformed functions of these coordinates are necessarily symmetric with respect to this inversion operation. Therefore, when an internal coordinate that is antisymmetric with respect to inversion is required internuclear separation coordinates alone are inadequate. To handle this, a third type of internal coordinate is introduced, the scaled dot-cross product coordinate⁵

$$Q_{i,j,k,l}^{(3)} = \frac{(\mathbf{R}^i - \mathbf{R}^j) \cdot (\mathbf{R}^i - \mathbf{R}^k) \times (\mathbf{R}^i - \mathbf{R}^l)}{(r_{i,j} r_{i,k} r_{i,l} r_{j,k} r_{j,l} r_{k,l})^\gamma} \quad (2-15)$$

where γ is determined as part of the fitting procedure. This coordinate is either symmetric or anti-symmetric with respect to any permutation of the four vertices. It is readily seen that under the inversion operation where $\mathbf{R}^k \rightarrow -\mathbf{R}^k$, for all k , $Q_{i,j,k,l}^{(3)} \rightarrow -Q_{i,j,k,l}^{(3)}$. It will be shown in section 2.4, that $Q_{i,j,k,l}^{(3)}$ are required for $H_{1,2}^d$ block of ammonia.

2.3.6 Global Symmetry of \mathbf{H}^d

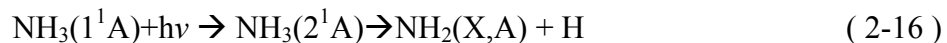
Because \mathbf{H}^d must be valid around many different conformations having distinct point group symmetry, point groups do not describe the full symmetry of a global Hamiltonian. To address the global symmetry of \mathbf{H}^d , non-rigid group symmetry,¹⁸ also known as complete nuclear permutation inversion (CNPI) group symmetry,¹⁹ is employed. This analysis is not essential to our non-local fitting algorithm but is certainly quite useful. The theory is a consequence of the invariance of the electronic Hamiltonian under a subset of the non-rigid group operations given by Longuet-Higgins.¹⁸ Because we are working with a non-relativistic Born-Oppenheimer Hamiltonian expanded in internal coordinate space, only two types of non-rigid group operations are relevant: (i) any permutation of same type nuclei (isotopes are considered identical); and (ii) the simultaneous inversion of all particles, electrons and nuclei, through the origin, as noted above.

At geometries where the electronic states are non-degenerate, the adiabatic states always carry one-dimensional irreducible representations of the CNPI group. In the current approach the adiabatic states are expanded in terms of quasi-diabatic states, Ψ_α^d ,

chosen to agree with the adiabatic states at the origin.^{12, 29} Thus these quasi-diabatic states carry the same irreducible representations as the adiabatic states. Hence near the origin and in the absence of crossings with additional quasi-diabatic states the individual blocks of \mathbf{H}^d carry the irreducible representation corresponding to $irred(\Psi_\alpha^d) \times irred(\Psi_\beta^d)$ where *irred* denotes "the irreducible representation carried by". To enforce the global symmetry, for each block of \mathbf{H}^d , we use the corresponding CNPI group projection operators on each of the terms of the polynomial of a particular order. This projection procedure requires some of the $V_{k, \dots}^{(m), \alpha, \beta}$ to have a fixed relation to others of the same order. Operationally this is equivalent to the procedure for constraining symmetry related coefficients for non-abelian point groups used in our algorithm to construct bound \mathbf{H}^d (Ref. ¹²) and our implementation reflects this. Further discussion of this issue is presented in section 2.4.

2.4 \mathbf{H}^d for the $1,2^1A$ Electronic States of NH_3

In this section the computational issues associated with the construction of a non-local \mathbf{H}^d using eq. (2-11) are addressed, using portions of the $1,2^1A$ coupled potential energy surfaces of NH_3 , which are relevant to the photodissociation reaction,



as an example. This system was chosen since it embodies, as described below, key challenges encountered in dealing with strongly coupled dissociative potential energy surfaces. The following regions are explicitly considered: (i) the equilibrium geometry of the 1^1A_1 state of NH_3 which has C_{3v} symmetry, denoted *min1C_{3v}*; (ii) the equilibrium geometry of the 2^1A state which has D_{3h} symmetry, denoted *min2D_{3h}*; (iii) the minimum energy $1^1A - 2^1A$ conical intersection which has C_{2v} symmetry, denoted *mexC_{2v}*; (iv) the

saddle point separating $min2D_{3h}$ and $mexC_{2v}$, denoted $sad2C_{2v}$; (v) the ground state inversion saddle point, denoted $sad1C_{2v}$; and (vi) the ground and excited states in the dissociation channel $NH_3 \rightarrow NH_2 + H(^2S)$. The origin of the internal coordinate system is taken as $min2D_{3h}$ and the zero of energy is E_1 at that point.

2.4.1 Electronic Structure description of NH_3 .

The molecular orbitals were obtained from a state averaged multiconfiguration self consistent field treatment that averaged two states with equal weights and used wave functions obtained from a 8 electron in 9 orbital, complete active space expansion. The atomic orbital basis consisted of Dunning's aug-cc-pVTZ basis plus an extra Rydberg s-function on nitrogen and Dunning's aug-cc-pVTZ basis on the hydrogens. Dynamic correlation was incorporated at the second order configuration interaction level, with the interacting space restrictions. The resulting MRCI expansion consisted of 33.9 million configuration state functions (CSFs). All electronic structure calculations reported in this work employed the COLUMBUS suite of electronic structure codes.^{30,8} It is important to emphasize that these are not low-level calculations of convenience.

2.4.2 Symmetry-adapted internal coordinates

The coordinates are comprised of twelve compressed internuclear distance coordinates, six $Q^{(1)}$ from eq. (2-13), and six $Q^{(2)}$ from eq. (2-14) and a thirteenth coordinate $Q_{NH\bar{H}\bar{H}}^{(3)} = Q_{N,H^1,H^2,H^3}^{(3)}$, from eq. (2-15), is also included. It will also be convenient, when specifying geometries, to use the out of plane angle ϕ , defined as:

$$\phi = \text{ArcSin} \left[\frac{\mathbf{e}_{N,H^1} \cdot (\mathbf{e}_{N,H^2} - \mathbf{e}_{N,H^1}) \times (\mathbf{e}_{N,H^3} - \mathbf{e}_{N,H^1})}{|(\mathbf{e}_{N,H^2} - \mathbf{e}_{N,H^1}) \times (\mathbf{e}_{N,H^3} - \mathbf{e}_{N,H^1})|} \right] \quad (2-17)$$

where $\mathbf{e}_{N,H^j} = \mathbf{r}_{N,H^j} / r_{N,H^j}$, although it must be emphasized that this coordinate is not used in the construction of \mathbf{H}^d .

The first 12 coordinates would be adequate for $H_{1,1}^d$ and $H_{2,2}^d$, but not for $H_{1,2}^d$. To address this issue and the global symmetry of the molecule, the CNPI group of ammonia is used. This group is generated by the permutation of the hydrogen nuclei and inversion of electrons and nuclei. It is isomorphic to the point group D_{3h} and will be denoted $D_{3h}(\text{CNPI})$. A brief discussion of this group and its character table are found in Appendix 2.6.1. In Appendix 2.6.2 it is shown that $Q_{NHHH}^{(3)}$ transforms as the A_2'' representation of the CNPI group of ammonia, denoted $A_2''(\text{CNPI})$. In Appendix 2.6.3 the symmetry of the electronic states is addressed. It is shown that, on the basis of the discussion in section 2.3.6, functions that transform as A_2'' (CNPI) are required for $H_{1,2}^d$ while for the $H_{1,1}^d$ and $H_{2,2}^d$ blocks functions that transform as A_1' (CNPI) are required.

Thus to impose CNPI symmetry on the polynomials appearing in \mathbf{H}^d two sets of polynomials are required, one transforming as $A_1'(\text{CNPI})$ and one transforming as $A_2''(\text{CNPI})$. These polynomials are constructed by applying the projection operators to each and everyone of the monomials of a particular order and then retaining only the unique non-zero functions, which as noted in section 2.3 are fixed linear combinations of the monomials in eq (2-1). We note that these polynomials are all symmetric sums over hydrogen permutations. The A_1' projector selects terms which are even order in $Q_{NHHH}^{(3)}$, while A_2'' projector selects terms which are odd order in $Q_{NHHH}^{(3)}$.

The term definitions of monomials, (from which the symmetry adapted polynomials are constructed) available to construct the matrix elements of \mathbf{H}^d , are

expressed in terms of ordered triples $(l,n,m)^k$. The ordered triple $(l,n,m)^k$ includes $\mathbf{Q}^{(1)}$ through order l , $\mathbf{Q}^{(2)}$ through order n , and $\mathbf{Q}^{(3)}$ through order m , with total order not exceeding k . Only polynomials of even (odd) order in $\mathbf{Q}^{(3)}$ contribute to the diagonal (off diagonal) blocks of \mathbf{H}^d .

2.4.3 Construction of \mathbf{H}^d

Nine points were chosen as nodes. These points include *min1C_{3v}*, *sad1D_{3h}*, *min2D_{3h}*, *sad2C_{2v}*, *mexC_{2v}*, two points in the NH₂ + H exit channel corresponding to optimized ground and excited state geometries with the third r_{NH} restricted to be 3.5Å, denoted *asym1C_{2v}*, *asym2C_{2v}*, and two points optimized on the same two electronic states with the molecule almost completely dissociated, denoted *dis1C_{2v}*, *dis2C_{2v}*. Table 2-1 reports the coordinates of these points. For all the nodes energies and energy gradients are fit exactly. Interstate coupling gradients at C_{2v} geometries are also fit exactly. At the other nodes the interstate coupling gradients are included in the least squares block to allow relaxation of eigenvectors \mathbf{d}^l throughout the iterative procedure.

Table 2-1. Location of Critical Points. $\phi=0$ except at *min1C_{3v}* where $\phi=22.44$

Node	NH ¹	NH ²	NH ³	$\angle_{\text{H}_1\text{NH}_2}$	$\angle_{\text{H}_1\text{NH}_3}$
<i>min2D_{3h}</i>	1.0485	1.0485	1.0485	60.00	60.00
<i>min1C_{3v}</i>	1.0154	1.0154	1.0154	73.65	73.65
<i>sad1D_{3h}</i>	0.9979	0.9979	0.9979	60.00	60.00
<i>sad2C_{2v}</i>	1.3054	1.0408	1.0408	56.23	56.23
<i>mexC_{2v}</i>	1.9689	1.0222	1.0222	54.60	54.60
<i>asym1C_{2v}</i>	3.5099	1.0283	1.0283	51.39	51.39
<i>asym2C_{2v}</i>	11.4476	1.0283	1.0283	51.39	51.39
<i>dis1C_{2v}</i>	3.5099	0.9986	0.9986	72.61	72.61
<i>dis2C_{2v}</i>	6.1558	0.9986	0.9986	72.61	72.61

The exception is a conical intersection, here $mexC_{2v}$. There, regardless of symmetry, the energies, energy gradients and interstate coupling gradients are constrained to reproduce the *ab initio* data, so that the structure of the conical intersection is preserved. To accomplish this the orthogonalized³¹ form of the \mathbf{g} (energy difference gradient) and \mathbf{h} (interstate coupling gradient) vectors²⁸ are used. At $mexC_{2v}$ \mathbf{g} is largely an N-H stretch, an approximate reaction coordinate for reaction (2-16), and \mathbf{h} is proportional to $Q_{NHHH}^{(3)}$. The smoothing factor $t_{i,i}$ was chosen as $t_{i,i} = t = 3 \times 10^{-6}$. This was the lowest value that makes the number of remaining linear dependencies equal to the theoretical number of linear dependencies caused by translation and rotation components of gradients and couplings that are included in the Lagrange multiplier block. The scale factors were chosen as $\alpha_k = 0.75$ and $\beta_k = 0.5$ after some trial and error optimization.

2.4.4 Accuracy of H^d

Here we demonstrate five key properties of the fit: (i) it reproduces the energies, energy gradients and derivative couplings at the nodes exactly, and provides a good overall fit to the remaining data; (ii) it interpolates reliably, avoiding inter point oscillations; (iii) it correctly locates and describes conical intersections; (iv) it describes molecular dissociation; and (v) it reproduces the derivative couplings, particularly the larger couplings, over the entire region considered, quite well, justifying the attribute quasi-diabatic.

a. Data Used

Ab initio electronic structure data was obtained at 287 nuclear configurations, which were partitioned into two sets. The first data set, comprised of 239 points, includes groups of points near each of the nodes; points along a linear synchronous transit path

between nodes, which resembles a reaction path; and a grid of points on the g - h ²⁸ or branching³² plane of $mexC_{2v}$ which spans as large an area as the *ab initio* method permits (that is, in some high energy regions the two quasi-diabatic state approximation breaks down). On this grid, the NH distance in approximately the \mathbf{g} direction, ranges from 0.74Å to ~10Å, thereby spanning from the inner potential wall to the asymptote. The displacement along ϕ , which coincides with \mathbf{h} direction, ranges from 0° to 40°. Beyond 40°, the 2-state *ab initio* description starts to deteriorate as the molecule approaches a seam of intersection between the second and third states. This set of points is referred to as the fit points. Energy, energy gradient and interstate coupling gradient information obtained from these points results in $N^{eq} = 4582$. These equations are used to fit approximately 2160 unknown coefficients.

Ab initio calculations are also performed at 48 geometries referred to as interpolation points. The resulting *ab initio* data were excluded from all but one of the fitting sets. For reasons discussed below, we will construct one fit in which all the available data is included in the fitting procedure. These points will enable us to examine the quality/smoothness of a fit at geometries not directly included in the fitting procedure. Except for a 7 point loop in the g - h plane of $mexC_{2v}$, the interpolation points are defined in terms of linear synchronous transit paths connecting nodes or paths originating at nodes. All these paths either include or pass near the conical intersection, $mexC_{2v}$, the most challenging region of nuclear coordinate space to describe. One set of interpolation points, that connecting nodes $minIC_{3v}$ and $mexC_{2v}$, does not pass near any of the fit points, other than its endpoints. Along this path the angle ϕ increases from 0° to 22.44°, whereas in the remaining cases $\phi = 0$, reflecting the importance of planar nuclear

configurations on the 2^1A potential energy surface. To put these points in context, Figure 2-1 reports the projections of all points considered onto the g - h plane of $mexC_{2v}$.

Energies and geometries of the data points are provided in Table 2-6 and Table 2-7 in appendices 2.6.4. Table 2-6 provides a comparison of the final fit FIT2 (see section 2.4.4-b) and *ab initio* (MRCI) energies at all 287 nuclear configurations which includes 9 nodes and 230 other points that are used to construct the final fit, and 48 additional interpolation points. Table 2-7 gives the internal coordinates of each of these points.

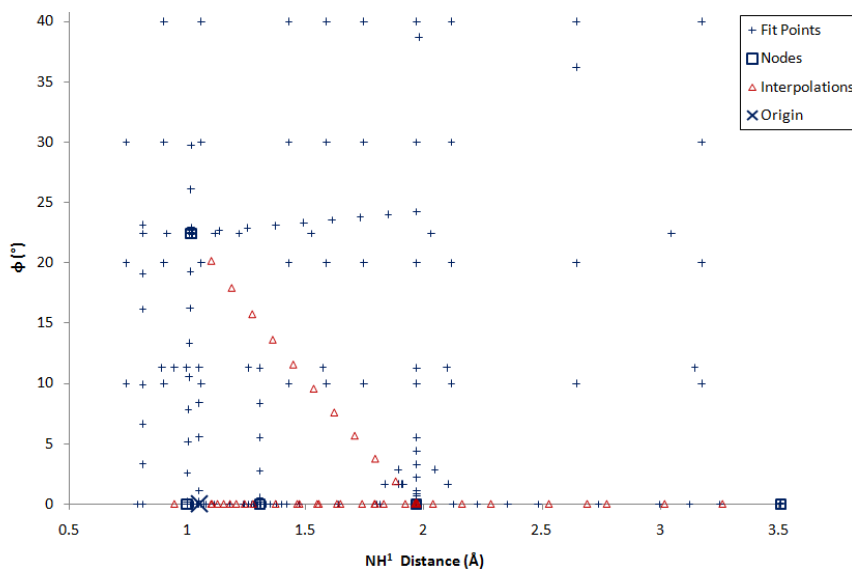


Figure 2-1. Projection of Data Point Geometries on g - h Plane

b. Importance of $Q^{(2)}$ Terms and Damping Factor

Four different fits, denoted FIT k , $k = 1-4$, were obtained, providing insights into the choice of term definitions and the use of the damping function. FIT k , $k = 1 - 3$, are based on *ab initio* data at the (239) fit points, while FIT4 is based on data at all the data points. These fits are summarized in Table 2-2 which reports the term definitions, number of coefficients, N^{coef} , size of a term t , and root mean square error for the energies (RMSEE). The RMSEE depend on the data included in the sum and Table 2-2 provides

three partitionings. Below when no qualifier is expressed the all data RMSEE is assumed. Fit1 has no $\mathbf{Q}^{(2)}$ terms, while FIT k , $k=2,3$ include $\mathbf{Q}^{(2)}$ through first order. Comparing FIT1 and FIT2 in Table 2-2 clearly evinces the importance of $\mathbf{Q}^{(2)}$ terms. The RMSEE for FIT2 is 94 cm^{-1} while that for FIT1 is 303 cm^{-1} , with both fits having similar N^{coef} .

Comparing the RMSEE for FIT2 and FIT3 illustrates the role of the damping term. FIT3 has exactly the same polynomial expansion as FIT2. FIT2 has a damping term $t = 3 \times 10^{-5}$ whereas in FIT3 $t = 0$. FIT3 is found to have a very large number of local minima, solutions to eq. (2-11) with distinct V and the final converged fit depends strongly on which points are included in the fit data set. Further, for FIT3, in some regions the fit is oscillatory. Shown in Table 2-2 are the RMSEE for the FIT3 (a local minimum) obtained using the converged FIT2 as the starting guess. The RMSEE for FIT3 is slightly smaller than for FIT2, as expected, but FIT3 has much larger V in all orders, implying that FIT3 is more oscillatory. As a result of including the damping term, FIT2 has no singularities from the least square block, as determined by singular valued decomposition. On the other hand, FIT3 has 1680 singularities removed from least square block by singular value decomposition. Therefore, except when noted otherwise, for the remainder of this section we restrict our attention to FIT2.

Table 2-2. Quality of Fits. FIT1-FIT3 constructed from the 239 point fit data set with 48 interpolation (Inter) points. FIT4 includes all 287 points in fit set. FIT3 uses $t = 0$.

	Term Def	N^{Coef}	RMSEE		
			Fit Pts	Inter Pts	All Pts
FIT1	$(8,0,8)^8$	2169	329.08	102.60	302.76
FIT2	$(6,1,6)^6$	2163	100.42	47.14	93.64
FIT3	$(6,1,6)^6$	2163	99.76	45.61	92.92
FIT4	$(6,1,6)^6$	2163	101.70	46.55	94.74

Table 2-3. Comparison of FIT2 and *ab initio* results for interpolation points along paths described in text. Nodes are in bold face. Energies in cm^{-1} . $\Delta E_j = E_j(\mathbf{H}^d) - E_j(\textit{ab initio})$. (a) Semicircle with radius 0.015 au in g-h plane around *mexC*_{2v}. θ is the angle relative to **g** in degrees.

θ	r_{NH^1}	ϕ	$E_1(\textit{ab initio})$	ΔE_1	$E_2(\textit{ab initio})$	ΔE_2
0	3.7109	0.00	38919.47	-0.01	39116.84	0.05
30	3.7122	0.05	38935.04	-0.01	39116.77	0.03
60	3.7158	0.10	38974.28	0.00	39119.91	0.00
90	3.7206	0.11	39014.19	0.00	39137.86	0.00
120	3.7255	0.10	39032.42	0.01	39177.46	0.00
150	3.7291	0.05	39035.94	0.03	39216.28	-0.01
180	3.7304	0.00	39036.07	0.05	39231.64	-0.01

(b) *min2D*_{3h} → *sad2C*_{2v} → *mexC*_{2v}

	r_{NH^1}	ϕ	$E_1(\textit{ab initio})$	ΔE_1	$E_2(\textit{ab initio})$	ΔE_2
<i>min2D</i>_{3h}	1.9814	0.00	0.00	0.00	43884.72	0.00
	2.0819	0.00	1230.57	1.04	44163.19	-27.67
	2.1321	0.00	2090.11	1.87	44450.09	-44.62
	2.1823	0.00	3078.45	2.50	44783.94	-52.43
	2.2325	0.00	4174.36	2.71	45128.41	-48.68
	2.2828	0.00	5359.47	2.41	45449.71	-35.91
	2.3497	0.00	7051.31	1.40	45792.16	-15.05
	2.4167	0.00	8842.12	0.32	45992.65	-2.13
<i>sad2C</i>_{2v}	2.4669	0.00	10234.18	0.00	46037.70	0.01
	2.5966	0.00	13754.30	1.39	45801.46	-7.66
	2.7695	0.00	18442.80	-8.40	44917.94	-9.02
	2.9424	0.00	22955.01	-21.65	43692.31	-4.41
	3.1154	0.00	27186.55	-23.80	42435.64	19.72
	3.2883	0.00	31071.39	-16.79	41286.07	30.91
	3.4612	0.00	34572.72	-7.19	40287.08	19.32
	3.6342	0.00	37674.92	-0.86	39443.05	2.86
<i>mexC</i>_{2v}	3.7206	0.00	39075.99	0.00	39075.99	0.00

Table 2-3. Comparison of FIT2 and *ab initio* results for interpolation points along paths described in text. Nodes are in bold face. Energies in cm^{-1} . $\Delta E_j = E_j(\mathbf{H}^d) - E_j(\textit{ab initio})$.
(Continued)

(c) $sad2C_{2v} \rightarrow asym1C_{2v}$

	r_{NH^1}	ϕ	$E_1(\textit{ab initio})$	ΔE_1	$E_2(\textit{ab initio})$	ΔE_2
<i>sad2C_{2v}</i>	1.3054	0.00	10234.18	0.00	46037.70	0.01
	1.5504	0.00	22740.91	-20.02	43814.37	-15.32
	1.7953	0.00	33388.62	-9.38	40717.27	17.26
	2.0403	0.00	38614.22	9.97	41213.67	-2.30
	2.2852	0.00	37352.76	112.26	46310.35	-28.68
	2.5301	0.00	36637.38	167.06	49310.12	-43.59
	2.7751	0.00	36251.23	114.81	50992.24	-31.58
	3.0200	0.00	36053.66	44.29	51966.40	-12.95
	3.2650	0.00	35960.79	7.87	52597.20	-2.46
<i>asym1C_{2v}</i>	3.5099	0.00	35926.06	-0.02	53072.27	0.00

(d) NH Displacements from *mexC_{2v}*

Point Type	r_{NH^1}	ϕ	$E_1(\textit{ab initio})$	ΔE_1	$E_2(\textit{ab initio})$	ΔE_2
	0.9459	0.00	-6.74	0.01	46280.23	-10.00
	1.1046	0.00	1389.43	8.65	44827.84	-242.76
	1.4750	0.00	19044.85	-11.30	44756.55	56.60
	1.6338	0.00	26671.79	-25.16	42563.94	65.12
	1.7925	0.00	33236.50	-11.31	40653.25	38.74
<i>mexC_{2v}</i>	1.9689^a	0.00	39075.99	0.00	39075.99	0.00
	2.1630	0.00	37903.36	57.48	43756.07	-13.11
	2.6921	0.00	36491.39	143.86	49616.67	-39.80
	5.3380	0.00	36141.06	18.17	51254.41	-3.52
	10.6298	0.00	36146.37	12.55	51258.56	-2.03

Table 2-3. (Continued)

(e) $mexC_{2v} \rightarrow minIC_{3v}$

Point Type	r_{NH^1}	ϕ	$E_1(ab\ initio)$	ΔE_1	$E_2(ab\ initio)$	ΔE_2
$mexC_{2v}$	1.9689	0	39075.99	0.00	39075.99	0.00
	1.8822	1.87	36094.58	1.31	40127.85	6.94
	1.7955	3.75	32678.53	11.36	41374.19	12.63
	1.7088	5.65	28840.34	34.03	42812.96	-2.46
	1.6222	7.57	24611.82	61.98	44417.10	-34.41
	1.5355	9.54	20049.96	76.90	46104.93	-44.45
	1.4488	11.54	15244.29	58.52	47669.96	-10.70
	1.3621	13.60	10322.29	-6.78	48760.76	9.05
	1.2754	15.71	5532.85	-63.78	49136.07	1.51
	1.1888	17.88	1252.02	-59.61	48777.90	-107.47
	1.1021	20.12	-1977.99	-19.63	48533.29	-83.94
$minIC_{3v}$	1.0154	22.44	-3314.10	0.00	49682.59	0.00

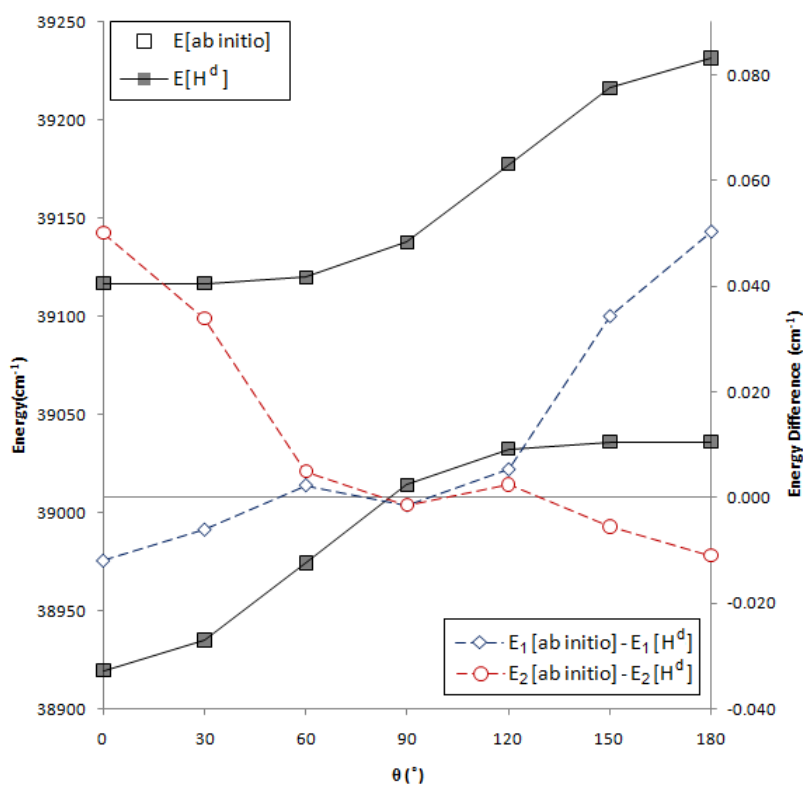


Figure 2-2. Comparison of $H^{(d)}$ and $ab\ initio$ at interpolated points along a semicircle with radius 0.015 au on $g-h$ plane near $mexC_{2v}$. Right hand ordinate refers to dashed curves.

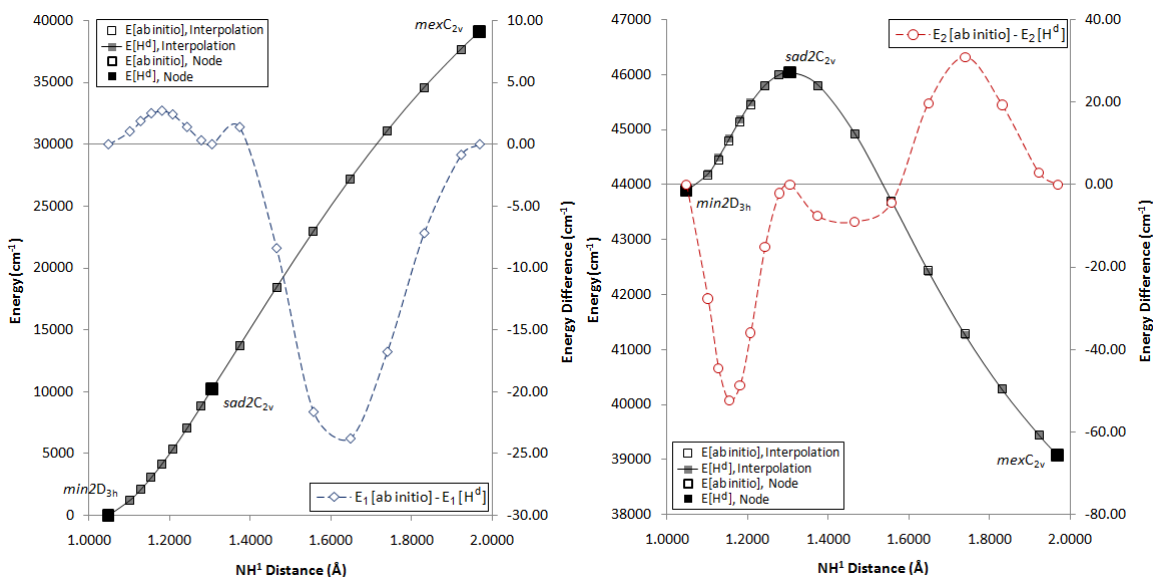


Figure 2-3. Linear Synchronous Transit Path $min2D_{3h} \rightarrow sad2C_{2v} \rightarrow mexC_{2v}$. Right hand ordinate refers to dashed curves. Left: E_1 panel; Right: E_2 panel

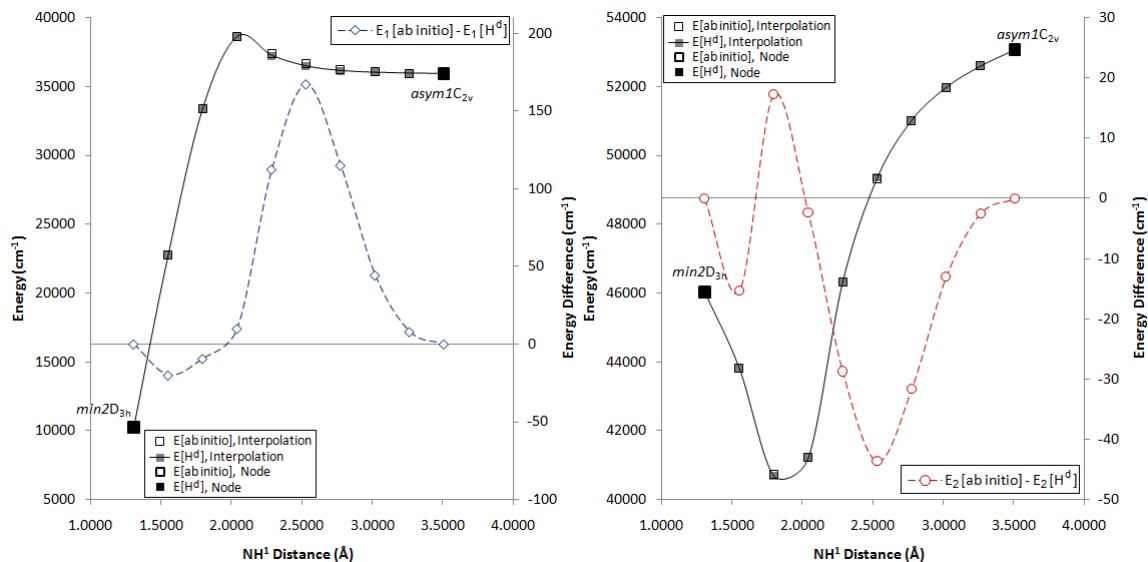


Figure 2-4. Linear Synchronous Transit Path $sad2C_{2v} \rightarrow asym1C_{2v}$ (bypassing $mexC_{2v}$). Right hand ordinate refers to dashed curves. Left: E_1 panel ; Right: E_2 panel

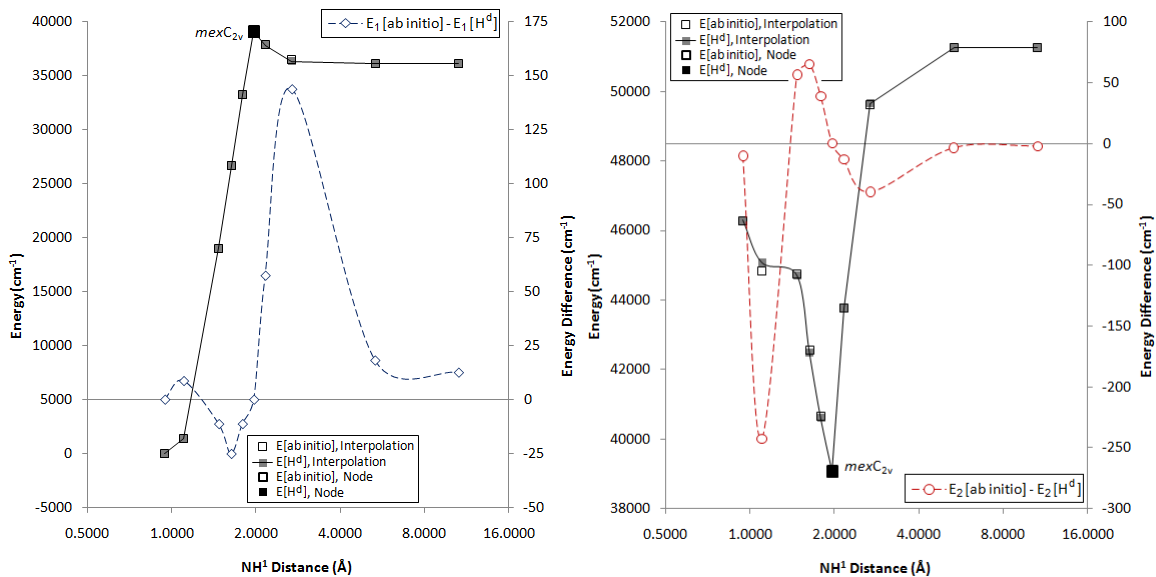


Figure 2-5. NH Bond Length Displacements from *mexC*_{2v}. Right hand ordinate refers to dashed curves. Left: E₁ panel; Right: E₂ panel

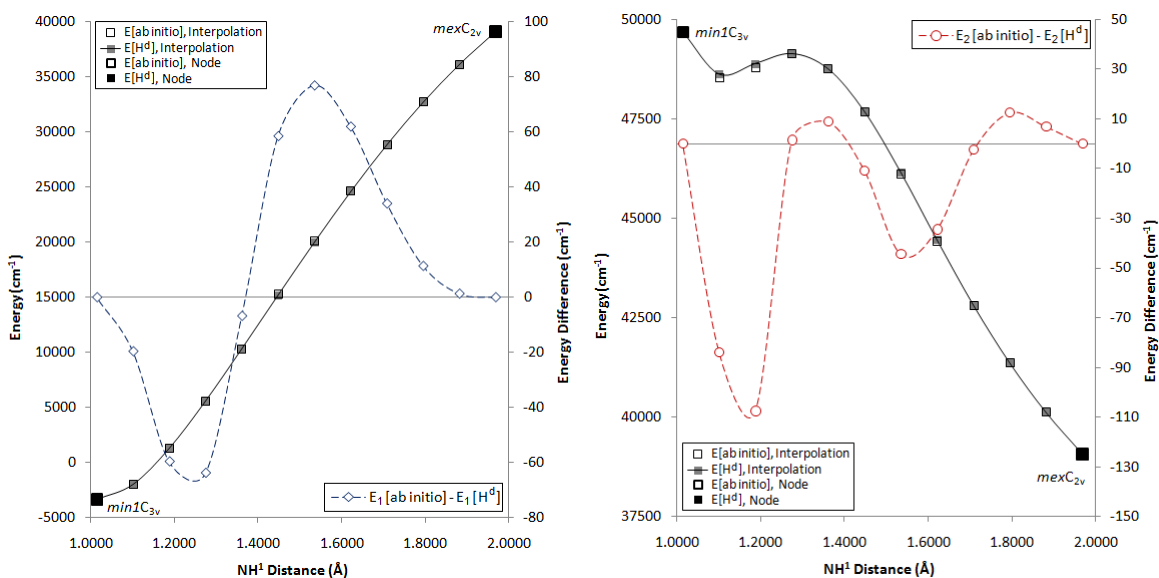


Figure 2-6. Linear Synchronous Transit Path *mexC*_{2v} → *min1C*_{3v}. Right hand ordinate refers to dashed curves. Left: E₁ panel; Right: E₂ panel

c. Fit at and near the nodes.

As can be seen from Table 2-6 and Table 2-3(b–e), (discussed in detail in the following section) at the nodes the \mathbf{H}^d determined energies agree with the *ab initio* results to within 0.02 cm^{-1} , except for the ground state energies at *asym2C_{2v}* and *dis2C_{2v}*, which have an error of 0.10 cm^{-1} . This is expected but reassuring. The node at *mexC_{2v}* requires additional discussion. Since it is a conical intersection, the description of its local topography is a key issue for the constructed \mathbf{H}^d . In this regard the algorithm performs flawlessly as is demonstrated in Figure 2-2 and Table 2-3a, which compare the *ab initio* and \mathbf{H}^d determined energies evaluated at 7 interpolation points along a semicircle on the *g-h* plane with radius 0.015 au centered at *mexC_{2v}*. Note that a larger loop of points with a radius of 0.3 au in the *g-h* plane is included in the fit to ensure the correct description of higher order effects near the intersection. The RMSEE was found to be 0.024 cm^{-1} for the small loop and 19 cm^{-1} for the large loop. Again the small error for the small loop, is not unexpected since the \mathbf{H}^d determined \mathbf{g} and \mathbf{h} vectors are constrained to agree with the *ab initio* results. The small error on the large loop, which has an energetic range of $\sim 4000 \text{ cm}^{-1}$, is quite encouraging.

d. Energy Interpolation

Table 2-3(b-e) and the associated figures, Figure 2-3 to Figure 2-6, denoted FTb – FTc below, consider the ability of FIT2 to interpolate energies, that is predict energies of points not in the data set. In a subsequent section the ability to interpolate energy gradients and derivative couplings is considered. The figures and tables report two quantities $E_i(\textit{ab initio})$ the *ab initio* determined energy of the i^{th} state, and the interpolations errors, $\Delta E_i = E_i(\mathbf{H}^d) - E_i(\textit{ab initio})$, for $i=1, 2$, where $E_i(\mathbf{H}^d)$ is the \mathbf{H}^d

determined energy of the i^{th} state. In addition, the figures report $E_i(\mathbf{H}^{\text{d}})$. $E_i(\text{ab initio})$ and ΔE_i are reported at 41 interpolation points, in addition to the 7 points reported in Table 2-3(a) and discussed above. In these figures, the energy scales for E_1 are, in general, quite large spanning 30,000 – 40,000 cm^{-1} . The scales for E_2 are much smaller spanning 7,000 – 13,000 cm^{-1} . ΔE_i scales are tiny by comparison, ranging from $\pm 60 \text{ cm}^{-1}$, to $\pm 200 \text{ cm}^{-1}$.

Comparing the $E_i(\text{ab initio})$ and $E_i(\mathbf{H}^{\text{d}})$ in Figure 2-3 to Figure 2-6 demonstrates the general agreement of the shapes of the *ab initio* and \mathbf{H}^{d} determined energy curves, with deviations of the *ab initio* and \mathbf{H}^{d} determined energies, evident at only very few points. A comparison based on the much finer ΔE_i scale follows. The FTb (14 interpolation points) describes a path connecting *minD*_{3h} to *mexC*_{2v} to via *sad2C*_{2v}. On this path the ΔE_i must be considered very small, never exceeding 52.43 cm^{-1} along a path on which the energy changes by tens of thousands of wave numbers. FTc (8 interpolation points) represents a path connecting *sad2C*_{2v} to *asym1C*_{2v} passing near but not through *mexC*_{2v}. Although the maximum ΔE_i gets somewhat larger here, 167 cm^{-1} , the point to point change the ΔE_i is, in general, less than 10% of the corresponding change in the $E_i(\text{ab initio})$, so that the shape of the curves are very well reproduced. The situation for FTe, which describes a path connecting *mexC*_{2v} to *min1C*_{3v} using 10 interpolation points, is similar to that for FTc, except going from the 8th to the 9th interpolation point, where ΔE_2 increases by -109 cm^{-1} compared to a change in $E_2(\text{ab initio})$ of -359 cm^{-1} . Still, as Figure 2-6 indicates, the shape of the E_2 potential is well reproduced. Recall that along this path there are no fit points in the immediate vicinity of the interpolation points. See Figure 2-1. Finally FTd reports energetics, at 10 interpolation points, based on changes in the NH bond distance of the unique hydrogen, centered at *mexC*_{2v}. Here the

preponderance of the interpolations exhibit modest errors, $< 65 \text{ cm}^{-1}$, with the exception of the point with $\Delta E_2 = -242.76 \text{ cm}^{-1}$. Note that in this region the *ab initio* energies for the second state exhibit a dramatic dependence on the NH bond distance indicating the need more *ab initio* data in this region. Still viewed on the scale of E_2 for the first three points in FTd, the described error is quite modest.

Further analysis of FTb-e shows that the errors reflect more than anything else the proximity to the nodes. The error is pushed down toward zero near any node, and remains very small in the region close to it. Further away from nodes, the worse the fit gets. However it must be emphasized that even when the molecule went through very large displacements from a node, where the energy has changed on the scale of $\sim 10,000 \text{ cm}^{-1}$, the surface still interpolates quite well, producing an error not to exceeding 242 cm^{-1} . It is possible to improve the quality of the fit at a certain region by making one point near the region a node or simply including more data near the region. Indeed the simple expedient of including the interpolation points in the fit data set, producing FIT4, improves the quality of the fit at those points, with the RMSEE of these points decreased from 47.14 cm^{-1} to 46.55 cm^{-1} , and the largest error decreased from -242.76 cm^{-1} to -180.40 cm^{-1} . For FIT4, the RMSEE of the fit data increased from 100.42 cm^{-1} to 101.70 cm^{-1} , and RMSEE of all points increased from 93.64 cm^{-1} to 94.74 cm^{-1} . Thus in this case, with the addition of new data into the fit set, the RMSEE of the interpolations, the fit data set and total data set remained largely unchanged. This is an indicator that the original data set is adequate for the representation of the region where the interpolations are made. It is also clear that including a point with large error into the fit set will significantly improve the fit of that point, whereas adding a point that is already well fit

will most likely have an insignificant effect. Methods to use quasi-classical trajectories to guide the selection of data points will be introduced in the next chapter.

e. Harmonic Frequencies, Energy Gradients and Derivative Couplings

In the present approach while the locus of single surface extrema are constrained to agree with *ab initio* results, the local curvature is not. Instead the energy gradients (and interstate coupling gradients) are computed near each extrema and included in the least squares fit. The harmonic frequencies are a measure of the accuracy with which these energy gradients are reproduced. Table 2-4 compares the \mathbf{H}^d and *ab initio* determined frequencies at three extrema *min1C_{3v}*, *min2D_{3h}* and *sad2C_{2v}*. The agreement is seen to be good. The root mean square relative error of these frequencies is 8%.

Table 2-4 Comparison of FIT2 and *ab initio* harmonic frequencies (in cm^{-1}).

<i>Min1C_{3v}</i>		<i>Min2D_{3h}</i>		<i>Sad2C_{2v}</i>	
<i>ab initio</i>	\mathbf{H}^d	<i>ab initio</i>	\mathbf{H}^d	<i>ab initio</i>	\mathbf{H}^d
3584.10	3441.79	2957.67	2910.71	3334.14	3235.47
3584.10	3441.79	2957.67	2910.71	3244.70	2985.71
3456.26	3423.32	2800.76	2773.89	1434.95	1276.66
1674.48	1647.70	1333.65	1481.83	961.53	894.42
1674.48	1647.70	1333.65	1481.83	475.34	531.63
1066.24	978.90	762.18	702.66	-2005.01	-1890.08

Figure 2-7 and Figure 2-8 consider the accuracy of the derivative couplings (not the coupling gradients) for FIT1 and FIT2 at the fit and interpolation points respectively. Figure 2-9 and Figure 2-10 do the same for the energy gradients. In each of these figures, for each datum, the \mathbf{H}^d determined value is plotted on the ordinate against the *ab initio* determined value on the abscissa. For both plots a logarithmic scale was used. If agreement for a particular datum is exact the point falls on the diagonal. We focus initially on the data included in the fit and then turn to the interpolation points. From these figures it is clearly shown that for regions where gradients or derivative couplings are significant, *ab initio* values are very well reproduced by both FIT1 and FIT2. For smaller values of the gradients or derivative couplings, both fits deteriorate somewhat. This deterioration is a result the least square fitting procedure which minimizes the total error, leaving smaller data with larger relative errors, but still small absolute errors. It is clear from these figures that FIT2 is far better than FIT1 for small gradients and derivative couplings. The number of outliers for the derivative couplings near the origin are reduced for FIT2 compared to FIT1 while for the energy gradients a general reduction of the scatter (size of error) is evident. These comparisons demonstrate once again the value of the $\mathbf{Q}^{(2)}$ terms. In terms of the absolute errors, generally speaking, FIT2 reliably reproduces the energy gradients with magnitudes $>10^{-3}$ and derivative couplings with magnitudes $> 10^{-2}$. This good reproduction of the derivative coupling justifies the attribute quasi-diabatic. It should also be noted that almost all the points that have largest relative errors are from the border of the grid where data points are relatively sparse, which is to be expected.

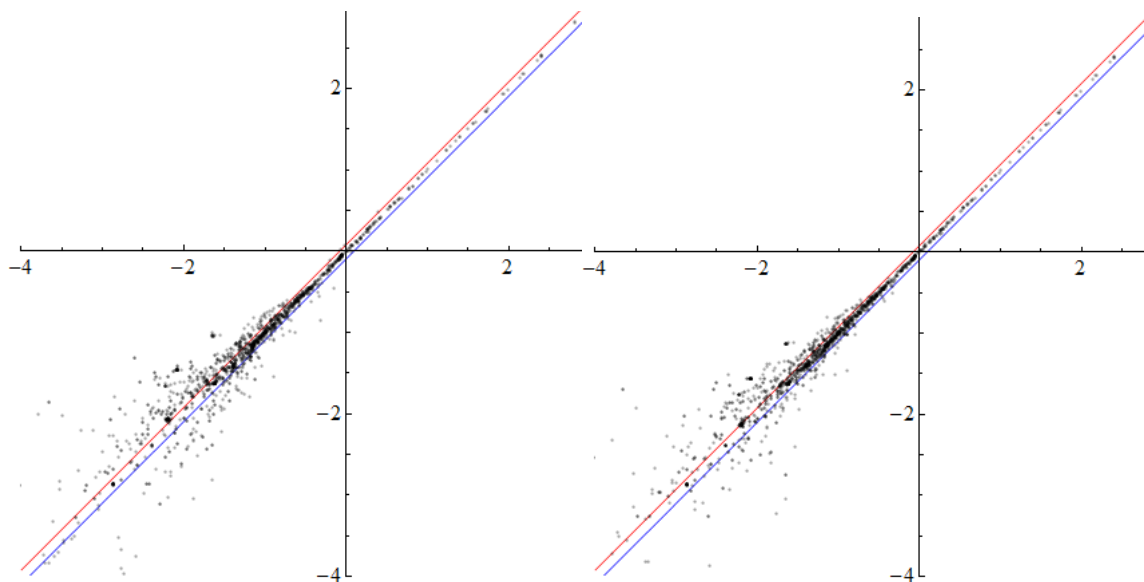


Figure 2-7. Comparison of *ab initio* and H^d determined derivative couplings for data points included in the fit. *x*-axis is the *ab initio* value, *y*-axis is the H^d determined value of a component of a nonzero valued of the derivative coupling. Left: FIT1; Right: FIT2.

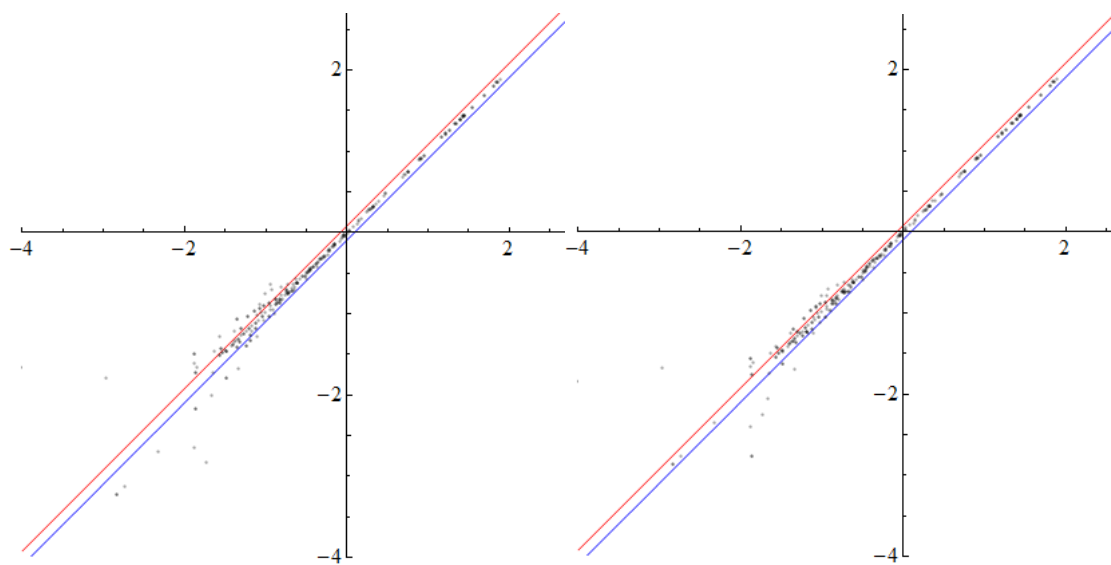


Figure 2-8. Comparison of *ab initio* and H^d determined derivative couplings for interpolated points. *x*-axis is the *ab initio* value, *y*-axis is the H^d determined value of a component of a nonzero valued of the derivative coupling. Left: FIT1; Right: FIT2.

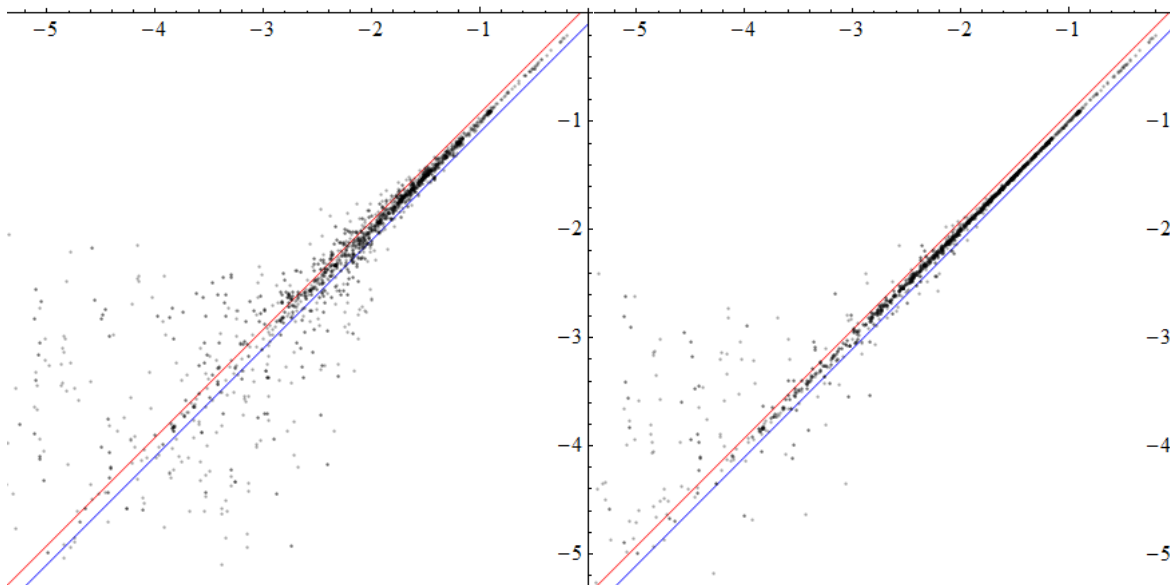


Figure 2-9 Comparison of *ab initio* and H^d determined energy gradients for points included in the fit. *x*-axis is the *ab initio* value, *y*-axis is the H^d determined value of a component of a nonzero value of an energy gradient. Left: FIT1; Right: FIT2

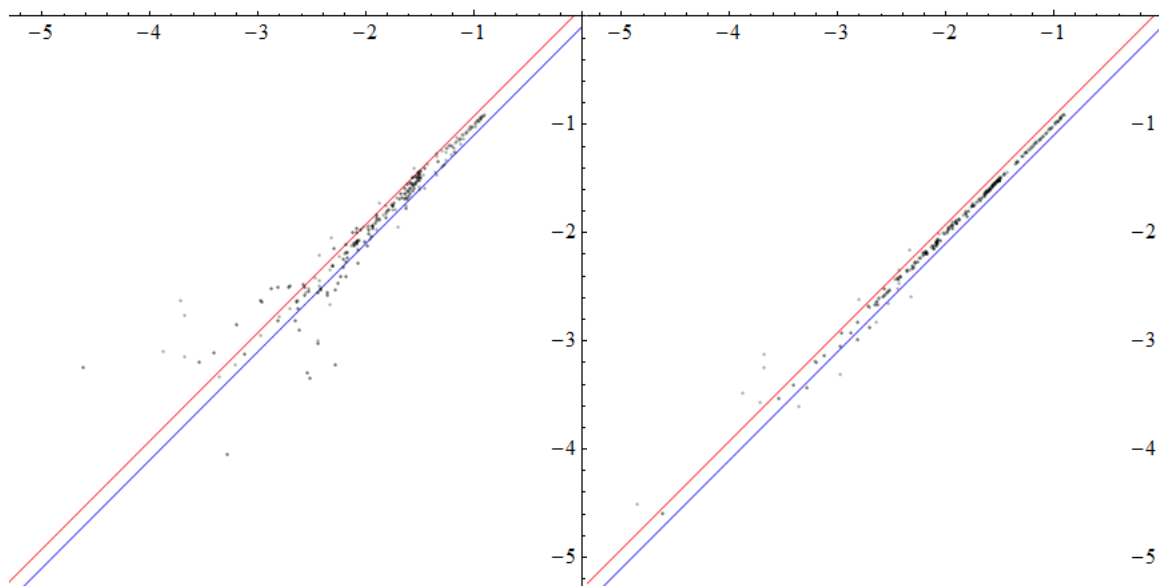


Figure 2-10 Comparison of *ab initio* and H^d determined energy gradients for interpolated points. *x*-axis is the *ab initio* value, *y*-axis is the H^d determined value of a component of a nonzero value of an energy gradient. Left: FIT1; Right: FIT2.

The data for the interpolation points recapitulate the trends observed for the points included in the fit with the additional observation that the errors for the interpolated points are less significant than for the fit data results. This observation, which was also found for the energies, see Table 2-2, reflects the choice of interpolation points. The interpolation points were chosen in the energetically important regions where the concentration of data points is larger. Hence we find that \mathbf{H}^d performs better than average in these regions.

Figure 2-11 summarizes the fit, and emphasizes its smoothness, providing a three dimensional plot of the the \mathbf{H}^d determined adiabatic energies. Key nodes are identified.

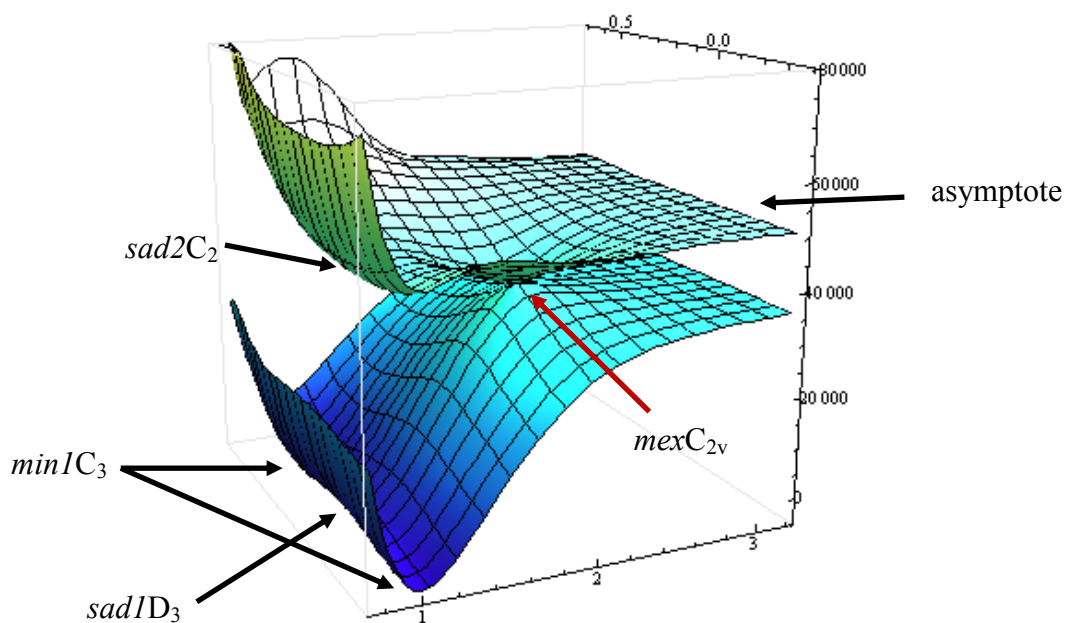


Figure 2-11. 3D Plot of $\mathbf{H}^{(d)}$ Determined Adiabatic Energies on g-h Plane

f. Improving the fit and outliers

Note that most of the energy errors discussed above are considerably less than the RMSEE errors in Table 2-2. Thus it is not surprising that in Table 2-6, there are 8 points, (points numbered 166-172, 178 in that table) with larger errors, errors in E_2 , in the range $400 \text{ cm}^{-1} - 531 \text{ cm}^{-1}$. The 531 cm^{-1} error is the maximum error in the data set. The energy range for E_2 is over $45,000 \text{ cm}^{-1}$. Here $E_2 = \sim 57,000 \text{ cm}^{-1}$, well above the energy needed to describe reaction (2-16). The maximum error for E_1 is 323 cm^{-1} , at point 179 in Table 2-6, where $E_1 = \sim 36,000 \text{ cm}^{-1}$. For these points, the relative energetics are quite reasonable, which we attribute to the inclusion of energy gradient data. In the vicinity of these outliers the energy gradients are large so that the errors represent relatively modest overshooting. The previous discussion concerning FTe is an example of this situation. In general, we find that even for the outlier points the fit is good.

Although the fit described here is quite good, there are factors that can lead to problems in constructing an \mathbf{H}^d in a particular region of nuclear coordinate space, including: (i) intruder states where the N^{state} approximation becomes inadequate, and (ii) the functional form becomes inadequate, and/or there is insufficient *ab initio* data or it is improperly used. There is little one can do about the failure of the N^{state} approximation, except avoid that region if feasible or increase N^{state} if the region in question is important. For (ii) the use of over complete bases allows us to include additional, localized, functions to improve the fit in the problematic region, and it is straightforward to introduce more electronic structure data or additional nodes, in that region to define the new parameters.

2.5 Summary and Conclusions

An approach is introduced for constructing a non-locally defined quasi-diabatic, coupled electronic state Hamiltonian, \mathbf{H}^d , which can supply electronic structure data to diabatic or adiabatic state based, dynamics on the fly algorithms.³³⁻³⁴ \mathbf{H}^d is constructed from high level MRCI wave functions from which derivative coupling and energy gradient data are readily obtained.⁸ Advantages of the proposed approach are attributable in part to the use of derivative coupling data and in part to algorithmic innovation. Using the concept of nodes, the algorithm reproduces the local topography of a conical intersection exactly. The location and energies of selected single surface extrema are also reproduced exactly. Since derivative coupling data is used in constructing the Hamiltonian, it is maximally quasi-diabatic in a least squares sense. The coordinate system includes exponentially decaying functions of the internuclear distances, following Braams and Bowman,¹⁵⁻¹⁶ and dot-cross product functions of Collins and coworkers.^{5, 35} The algorithm takes advantage of the flexibility offered by an over complete set of nuclear coordinates and incorporates a damping function to effectively mitigate fitting problems associated with the use of such coordinate systems.

The potential of this approach was illustrated by constructing an \mathbf{H}^d with the full permutational symmetry for portions of the ground and first excited state potential energy surfaces of NH_3 , relevant to its photodissociation to $\text{NH}_2 + \text{H}$. The analysis presented here is very encouraging. Although the energy range on each potential energy surface is $\sim 45,000 \text{ cm}^{-1}$ the RMS energy error is less than 100 cm^{-1} . Also gratifying is the excellent reproduction of the derivative coupling, particularly in, but not limited to, the vicinity of the conical intersection. justifying the attribute quasi-diabatic for \mathbf{H}^d .

In this report we have focused on the ability of \mathbf{H}^d to reproduce the *ab initio* data regardless of its quality, although high quality *ab initio* data were used. Later in this dissertation, a detailed analysis of the accuracy of an \mathbf{H}^d , designed to describe the photodissociation process, $\text{NH}_3(\text{X}) + h\nu \rightarrow \text{NH}_3(\text{A}) \rightarrow \text{NH}_2(\text{X,A}) + \text{H}$, in the context of the available experimentally measured²⁰⁻²¹ and computationally determined results²⁴⁻²⁵ will be provided.

2.6 Appendices

2.6.1 Complete Nuclear Permutation Inversion Group of NH_3

The CNPI symmetry group for NH_3 , denoted $D_{3h}(\text{CNPI})$ is generated by the permutations of hydrogen nuclei and the inversion of all particles. Since inversion of all particles commutes with all permutations, the $D_{3h}(\text{CNPI})$ group is the direct product of S_3 and C_{E^*} , where S_3 is the permutation group of the three identical nuclei, the hydrogen atoms and C_{E^*} is the inversion group of order 2. Here we have denoted the inversion operation as E^* so as not to confuse it with the point group inversion, i . A permutation, p , of three objects will be denoted by $\begin{pmatrix} 1 & 2 & 3 \\ p(1) & p(2) & p(3) \end{pmatrix}$ and abbreviated $(p(1), p(2), p(3))$. Then using standard group theoretical techniques for constructing classes, S_3 is found to have three classes, $(1,2,3)$; $(2,3,1)$, $(3,1,2)$; and $(1,3,2)$, $(3,2,1)$, $(2, 1,3)$ and is isomorphic to the point group C_{3v} . The character table for S_3 is given in Table 2-5 and is seen to be the character table for C_{3v} with the identifications

$$\begin{aligned} (1,2,3) &\leftrightarrow E && \text{A 2-1} \\ (2,3,1), (3,1,2) &\leftrightarrow C_3, C_3^2 && \text{A 2-2} \end{aligned}$$

$$(1,3,2), (3,2,1), (2,1,3) \leftrightarrow \sigma'_v, \sigma''_v, \sigma'''_v \quad \text{A 2-3}$$

It is important to observe that the isomorphism is group theoretical, the actual operations are unrelated *except* at specific geometries as discussed below. The full $D_{3h}(\text{CNPI})$ character table is just the direct product of the S_3 and C_{E^*} character tables. In the text, the superscripts ' and '' are introduced to the irreducible representation labels to denote the symmetric and antisymmetric representation of C_{E^*} respectively.

Table 2-5. Character Table of S_3

	E	(231), (312)	(213), (321), (132)
A_1	1	1	1
A_2	1	1	-1
E	2	-1	0

2.6.2 Transformation Properties of Dot-Cross-Product Function

We are concerned with the transformation properties of $Q_{N,H^1,H^2,H^3}^{(3)} \equiv Q_{NHHH}^{(3)}$ (see eq. (2-15)) under the operations of $D_{3h}(\text{CNPI})$. It is sufficient to determine the transformation properties of the generators of this group, E^* , (2,3,1) and (2,1,3). We find

$$\begin{aligned}
 P_{(2,3,1)} Q_{NHHH}^{(3)} &= P_{(2,3,1)} \frac{(\mathbf{R}^N - \mathbf{R}^{H^1}) \cdot (\mathbf{R}^N - \mathbf{R}^{H^2}) \times (\mathbf{R}^N - \mathbf{R}^{H^3})}{(r_{N,H^1} r_{N,H^2} r_{N,H^3} r_{H^1,H^2} r_{H^1,H^3} r_{H^2,H^3})^\gamma} \\
 &= \frac{(\mathbf{R}^N - \mathbf{R}^{H^2}) \cdot (\mathbf{R}^N - \mathbf{R}^{H^3}) \times (\mathbf{R}^N - \mathbf{R}^{H^1})}{(r_{N,H^2} r_{N,H^3} r_{N,H^1} r_{H^2,H^3} r_{H^2,H^1} r_{H^3,H^1})^\gamma} = Q_{NHHH}^{(3)} \quad \text{A 2-4}
 \end{aligned}$$

$$P_{(2,1,3)} Q_{NHHH}^{(3)} = \frac{(\mathbf{R}^N - \mathbf{R}^{H^2}) \cdot (\mathbf{R}^N - \mathbf{R}^{H^1}) \times (\mathbf{R}^N - \mathbf{R}^{H^3})}{(r_{N,H^2} r_{N,H^1} r_{N,H^3} r_{H^2,H^1} r_{H^2,H^3} r_{H^1,H^3})^\gamma} = -Q_{NHHH}^{(3)} \quad \text{A 2-5}$$

$$\begin{aligned}
P_E \cdot Q_{NHHH}^{(3)} &= P_E \cdot \frac{(\mathbf{R}^N - \mathbf{R}^{H^1}) \cdot (\mathbf{R}^N - \mathbf{R}^{H^2}) \times (\mathbf{R}^N - \mathbf{R}^{H^3})}{(r_{N,H^1} r_{N,H^2} r_{N,H^3} r_{H^1,H^2} r_{H^1,H^3} r_{H^2,H^3})^\gamma} \\
&= \frac{-(\mathbf{R}^N - \mathbf{R}^{H^1}) \cdot (\mathbf{R}^N - \mathbf{R}^{H^2}) \times (\mathbf{R}^N - \mathbf{R}^{H^3})}{(r_{N,H^1} r_{N,H^2} r_{N,H^3} r_{H^1,H^2} r_{H^1,H^3} r_{H^2,H^3})^\gamma} = -Q_{NHHH}^{(3)}
\end{aligned}
\tag{A 2-6}$$

Here we have used the identities $\mathbf{a} \times \mathbf{b} \cdot \mathbf{c} = \mathbf{c} \times \mathbf{a} \cdot \mathbf{b}$ and $\mathbf{a} \times \mathbf{b} = -\mathbf{b} \times \mathbf{a}$. From the character table, Table 2-5, it is seen that $Q_{NHHH}^{(3)}$ carries the A_2'' irreducible representation of $D_{3h}(\text{CNPI})$.

2.6.3 CNPI Irreducible Representations of Electronic States

Non-rigid group symmetry and point group symmetry of electronic states have fundamentally different physical meanings.¹⁹ However, at geometries that are invariant under non-rigid group operations, the CNPI characters of electronic wave functions can be determined from their point group symmetry. In this molecule, the D_{3h} equilibrium geometry of the ${}^1A_2''$ excited state is invariant under any non-rigid group operations and thus it is chosen to calculate the character. In order to determine the CNPI characters from the point group characters the correspondence of the CNPI and point group operations is required. It is readily seen that the group theoretical isomorphism in eqs. (A 2-1, A 2-2, A 2-3) plus the mapping $i \longleftrightarrow E^*$ is the appropriate identification. Thus the point group labels for the electronic states at the D_{3h} reference geometry are the same as the $D_{3h}(\text{CNPI})$ designations. The ground electronic state is a totally symmetric ${}^1A_1'$ state and therefore carries the ${}^1A_1'$ irreducible representation of the . The first excited state of ammonia is a ${}^1A_2''$ state³⁶ and hence has that symmetry in the CNPI group.

2.6.4 *Ab Initio* and H^d Predicted Energies of All Data Points

Table 2-6. *Ab initio* and H^d Predicted Energies using FIT2 for All Data Points. Energies in cm⁻¹, numbering of nodes refers to Table 2-1.

GEOM	E ₁ (<i>ab initio</i>)	E ₁ (FIT2)	ΔE ₁	E ₂ (<i>ab initio</i>)	E ₂ (FIT2)	ΔE ₂
Nodes						
1	0.00	0.00	0.00	43884.72	43884.72	0.00
2	-3314.10	-3314.10	0.00	49682.59	49682.59	0.00
3	-1356.88	-1356.87	0.00	44925.87	44925.86	0.01
4	10234.18	10234.18	0.00	46037.70	46037.70	0.01
5	39075.99	39075.99	0.00	39075.99	39075.99	0.00
6	35926.06	35926.08	-0.02	53072.27	53072.27	0.00
7	35937.98	35937.95	0.02	53218.25	53218.25	0.00
8	42718.16	42718.25	-0.09	46960.33	46960.32	0.01
9	42715.48	42715.39	0.10	47119.22	47119.23	0.00
Fit Points						
10	325.90	325.89	0.02	43897.70	43897.69	0.01
11	15.97	15.95	0.01	43897.58	43898.62	-1.04
12	16.12	16.11	0.01	43897.77	43898.87	-1.10
13	-0.53	-0.51	-0.02	43885.06	43885.08	-0.02
14	4.29	4.19	0.09	43888.31	43889.58	-1.27
15	4.30	4.22	0.09	43888.33	43889.57	-1.25
16	-1129.16	-1129.21	0.05	44241.48	44241.42	0.06
17	404.64	404.25	0.38	44212.12	44238.89	-26.77
18	385.59	384.94	0.65	44187.12	44207.54	-20.41
19	107.60	105.29	2.31	43974.77	44005.75	-30.98
20	105.62	102.50	3.12	43972.83	44006.55	-33.72
21	-13.27	-12.71	-0.56	43893.28	43893.68	-0.40
22	1920.45	1919.70	0.75	44183.56	44182.93	0.64
23	423.69	423.57	0.12	44237.13	44270.25	-33.12
24	-323.05	-311.42	-11.63	44110.03	44118.37	-8.34
25	-702.28	-681.46	-20.83	44424.16	44439.62	-15.46
26	-1187.29	-1160.40	-26.90	44923.45	44945.54	-22.09
27	-3309.04	-3308.99	-0.05	49582.21	49582.48	-0.27
28	-3308.76	-3308.71	-0.04	49685.08	49685.38	-0.29
29	-3308.69	-3308.65	-0.04	49686.35	49686.65	-0.30
30	-3312.71	-3312.65	-0.06	49732.93	49733.43	-0.51
31	-3312.78	-3312.72	-0.06	49655.90	49656.38	-0.48
32	-3313.25	-3313.24	-0.01	49828.92	49828.97	-0.05
33	-3294.88	-3294.70	-0.18	49511.29	49512.27	-0.98
34	-3294.32	-3294.21	-0.12	49700.29	49701.26	-0.97
35	-3294.14	-3294.03	-0.11	49700.50	49701.47	-0.97

Table 2-6. *Ab initio* and H^d Predicted Energies using FIT2 for All Data Points. Energies in cm⁻¹, numbering of nodes refers to Table 2-1. (Continued)

GEOM	E₁(<i>ab initio</i>)	E₁(FIT2)	ΔE₁	E₂(<i>ab initio</i>)	E₂(FIT2)	ΔE₂
36	-3307.27	-3306.94	-0.33	49692.11	49694.76	-2.65
37	-3306.55	-3306.21	-0.34	49819.24	49821.73	-2.49
38	-3310.68	-3310.64	-0.04	49978.42	49978.61	-0.18
39	-3083.85	-3083.07	-0.78	52271.19	52287.87	-16.68
40	-2357.96	-2362.09	4.13	55399.93	55460.87	-60.94
53	-1357.18	-1357.17	-0.01	44926.13	44926.14	0.00
54	1569.78	1568.43	1.35	44274.01	44308.49	-34.48
55	3980.43	3977.77	2.66	45070.68	45119.31	-48.64
56	6937.33	6935.88	1.45	45774.04	45789.64	-15.60
57	10499.08	10499.04	0.04	46038.26	46038.53	-0.27
58	10238.12	10238.09	0.03	46041.06	46041.17	-0.11
59	10238.65	10238.64	0.00	46041.82	46041.94	-0.12
60	10275.91	10275.90	0.00	46038.34	46038.25	0.10
61	10211.50	10211.51	-0.01	46038.03	46038.04	-0.01
62	10233.53	10233.52	0.01	46038.25	46038.27	-0.03
63	11586.77	11586.38	0.40	46001.75	46005.17	-3.42
64	11185.00	11183.82	1.18	46147.86	46144.27	3.59
65	10340.86	10341.03	-0.18	46136.15	46143.11	-6.96
66	10255.40	10255.80	-0.40	46042.17	46044.03	-1.86
67	9982.13	9981.83	0.30	46067.41	46062.23	5.18
68	10228.54	10228.45	0.09	46041.63	46041.86	-0.23
69	19020.05	19019.65	0.39	46099.38	46017.75	81.62
70	12148.80	12140.98	7.82	47539.01	47578.18	-39.17
71	12970.11	12971.22	-1.11	48558.33	48630.68	-72.35
72	10764.98	10771.67	-6.69	46150.70	46201.15	-50.46
73	9680.42	9677.49	2.93	46861.26	46741.82	119.44
74	10093.98	10091.89	2.09	46136.20	46141.48	-5.28
75	7461.26	7459.39	1.87	45967.81	45992.24	-24.43
76	10601.50	10600.61	0.89	46348.89	46362.26	-13.37
77	10576.85	10577.63	-0.78	46072.62	46074.13	-1.51
78	9780.44	9774.76	5.68	46437.61	46455.15	-17.53
79	9243.46	9239.71	3.75	46956.33	46982.95	-26.62
80	8548.79	8559.12	-10.32	47718.79	47742.38	-23.59
81	9766.24	9766.21	0.04	46032.69	46032.85	-0.17
82	9302.10	9301.96	0.14	46017.72	46018.55	-0.82
83	8842.12	8841.80	0.32	45992.65	45994.78	-2.13
84	8386.65	8386.11	0.54	45957.40	45961.60	-4.20
85	11398.60	11398.32	0.29	46009.41	46011.62	-2.20
86	12573.78	12572.83	0.95	45928.39	45934.29	-5.91
87	13754.30	13752.92	1.39	45801.46	45809.11	-7.66

Table 2-6. *Ab initio* and H^d Predicted Energies using FIT2 for All Data Points. Energies in cm⁻¹, numbering of nodes refers to Table 2-1. (Continued)

GEOM	E₁(<i>ab initio</i>)	E₁(FIT2)	ΔE₁	E₂(<i>ab initio</i>)	E₂(FIT2)	ΔE₂
88	14935.12	14934.34	0.78	45633.32	45640.49	-7.17
89	18731.05	18740.45	-9.41	44847.31	44856.78	-9.47
90	26675.17	26699.31	-24.14	42588.58	42571.83	16.75
91	33520.75	33530.81	-10.07	40582.48	40557.88	24.59
92	38964.76	38964.76	0.00	39107.84	39107.78	0.06
93	38997.23	38997.19	0.04	39097.19	39097.30	-0.11
94	39062.63	39062.63	0.00	39083.83	39083.78	0.05
95	39063.10	39063.09	0.00	39083.94	39083.94	0.00
96	39027.52	39027.46	0.06	39089.37	39089.42	-0.05
97	38985.96	38985.97	-0.01	39155.40	39155.39	0.01
98	34008.29	34017.33	-9.03	40733.20	40694.61	38.59
99	34564.99	34568.06	-3.08	40638.90	40613.94	24.96
100	35923.53	35920.37	3.17	40552.06	40549.70	2.36
101	37249.86	37253.73	-3.87	40965.00	40963.99	1.01
102	37917.07	37910.05	7.03	42019.17	42019.70	-0.53
103	38175.90	38144.01	31.89	43001.82	43009.54	-7.72
104	38252.52	38210.24	42.28	43375.22	43384.71	-9.49
105	39824.48	39826.52	-2.04	43399.59	43450.06	-50.47
106	39724.90	39727.93	-3.04	43335.99	43388.44	-52.45
107	38284.80	38278.38	6.43	40425.78	40425.60	0.18
108	35637.92	35633.69	4.22	40338.57	40362.53	-23.96
109	38952.33	38952.34	-0.01	39199.68	39199.68	-0.01
110	38828.70	38828.73	-0.03	39323.40	39323.42	-0.02
111	38705.09	38705.16	-0.07	39447.16	39447.20	-0.04
112	38581.51	38581.65	-0.14	39570.95	39571.02	-0.07
113	38457.95	38458.18	-0.23	39694.78	39694.87	-0.09
114	38457.95	38458.18	-0.23	39694.78	39694.87	-0.09
115	37840.45	37841.66	-1.21	40314.59	40314.67	-0.08
116	37223.37	37226.67	-3.30	40935.73	40935.24	0.49
117	36606.71	36613.54	-6.83	41558.51	41556.45	2.06
118	35990.60	36002.66	-12.06	42183.23	42178.19	5.04
119	32936.83	33003.83	-67.00	45342.17	45290.43	51.74
120	27672.95	27811.07	-138.12	51680.94	51535.13	145.81
121	29083.82	29177.02	-93.20	60055.87	60031.28	24.59
122	37095.54	36949.28	146.26	47133.52	47169.44	-35.92
123	36309.42	36181.22	128.20	50507.26	50543.18	-35.92
124	36030.33	36005.89	24.44	51843.03	51851.59	-8.57
125	35941.32	35940.08	1.23	52505.40	52505.82	-0.42
126	38017.68	37919.81	97.87	43858.16	43873.95	-15.79
127	37871.44	37687.96	183.47	46119.49	46151.92	-32.43

Table 2-6. *Ab initio* and H^d Predicted Energies using FIT2 for All Data Points. Energies in cm⁻¹, numbering of nodes refers to Table 2-1. (Continued)

GEOM	$E_1(\textit{ab initio})$	$E_1(\text{FIT2})$	ΔE_1	$E_2(\textit{ab initio})$	$E_2(\text{FIT2})$	ΔE_2
128	38371.00	38227.45	143.55	46897.93	46919.77	-21.85
129	39373.56	39304.60	68.97	47012.74	47016.41	-3.66
130	40822.02	40803.13	18.88	46946.70	46944.36	2.33
131	35931.19	35931.07	0.12	52872.10	52872.15	-0.06
132	35926.39	35926.40	-0.02	53072.58	53072.58	0.00
133	35930.62	35930.51	0.11	53077.00	53076.97	0.03
134	35926.06	35926.07	-0.01	53072.27	53072.25	0.03
135	35927.27	35927.18	0.09	52915.41	52915.44	-0.03
136	35926.05	35926.05	0.00	53072.27	53072.29	-0.02
137	35918.88	35911.42	7.46	53180.51	53182.72	-2.21
138	35925.92	35917.30	8.62	53205.32	53208.05	-2.73
139	35931.14	35925.67	5.47	53212.57	53214.60	-2.03
140	35934.10	35931.39	2.71	53215.28	53216.67	-1.39
141	43066.72	43066.58	0.14	46968.40	46967.84	0.56
142	42715.89	42715.98	-0.09	46958.04	46958.03	0.01
143	42723.75	42723.67	0.08	46966.03	46966.02	0.00
144	42718.15	42718.25	-0.10	46960.33	46960.32	0.01
145	42959.77	42959.51	0.26	46962.35	46962.24	0.11
146	42718.15	42718.20	-0.05	46960.34	46960.37	-0.03
147	42701.05	42690.80	10.25	47078.17	47078.82	-0.64
148	42705.88	42694.21	11.67	47106.72	47107.03	-0.32
149	42710.74	42703.95	6.78	47114.93	47115.05	-0.12
150	42713.83	42711.20	2.63	47117.94	47117.95	-0.01
151	24910.81	25032.22	-121.40	52023.06	51850.64	172.41
152	21515.31	21619.07	-103.76	52513.40	52344.86	168.54
153	17483.20	17578.27	-95.06	53123.32	52963.36	159.96
154	12880.30	12966.55	-86.25	53609.31	53454.78	154.53
155	7854.37	7946.12	-91.76	53423.12	53333.83	89.29
156	2836.96	2902.51	-65.55	52182.45	52163.13	19.32
157	-1381.04	-1361.55	-19.49	50238.78	50292.94	-54.16
158	8258.99	8259.55	-0.56	62956.02	62920.15	35.87
159	-1047.03	-1040.67	-6.36	52879.58	52940.45	-60.87
160	-1844.90	-1829.73	-15.17	49910.31	49963.08	-52.78
161	1518.43	1573.50	-55.06	51423.99	51447.88	-23.90
162	14468.16	14547.30	-79.14	53040.03	52868.07	171.96
163	29534.97	29699.27	-164.30	51213.44	51039.21	174.23
164	35678.92	35806.50	-127.58	51912.90	51783.60	129.30
165	36032.28	36044.40	-12.11	52027.20	52032.65	-5.45
166	10242.32	10242.67	-0.34	57234.81	57765.93	-531.12
167	10171.48	10173.72	-2.25	57320.97	57852.08	-531.12

Table 2-6. *Ab initio* and H^d Predicted Energies using FIT2 for All Data Points. Energies in cm⁻¹, numbering of nodes refers to Table 2-1. (Continued)

GEOM	E ₁ (<i>ab initio</i>)	E ₁ (FIT2)	ΔE ₁	E ₂ (<i>ab initio</i>)	E ₂ (FIT2)	ΔE ₂
168	9984.70	9990.77	-6.08	57597.01	58123.09	-526.08
169	9753.67	9762.64	-8.97	58110.33	58616.44	-506.11
170	9610.11	9618.94	-8.83	60119.50	60541.54	-422.04
171	9969.18	9975.77	-6.59	61754.10	62154.70	-400.60
172	11432.08	11437.34	-5.25	65129.72	65557.74	-428.01
173	35931.69	35926.70	5.00	53213.13	53215.06	-1.93
174	35931.88	35861.10	70.78	53212.79	53287.20	-74.42
175	35932.33	35938.63	-6.31	53212.30	53242.64	-30.34
176	35932.62	35746.63	185.99	53212.32	53419.10	-206.78
177	35932.46	36097.61	-165.15	53212.47	52872.48	339.99
178	35932.08	35959.13	-27.05	53212.16	52747.77	464.39
179	35931.88	35609.25	322.62	53211.88	52991.68	220.20
180	1523.12	1534.41	-11.29	49578.68	49876.66	-297.98
181	-771.13	-755.89	-15.24	46704.73	46845.67	-140.95
182	-1531.79	-1511.18	-20.61	45304.37	45347.90	-43.54
183	5993.68	6025.06	-31.39	47344.60	47301.13	43.47
184	20602.76	20539.07	63.69	46988.64	47138.97	-150.34
185	34858.15	34893.62	-35.48	45844.93	45820.49	24.45
186	37003.67	36990.56	13.11	49800.85	49756.23	44.63
187	37068.10	37025.19	42.92	50099.42	50109.87	-10.45
188	22616.28	22624.66	-8.38	72710.42	72963.44	-253.02
189	22214.77	22238.86	-24.09	76128.57	76086.18	42.39
190	24351.29	24325.35	25.94	83824.09	83499.47	324.62
191	1043.11	1053.04	-9.92	49437.22	49507.20	-69.98
192	134.43	154.87	-20.44	52706.58	52806.22	-99.64
193	1546.63	1559.88	-13.25	60160.37	60476.75	-316.37
194	8156.75	8293.48	-136.73	73655.73	73632.00	23.73
195	-750.51	-726.50	-24.01	45389.82	45585.33	-195.51
196	-2246.53	-2218.31	-28.22	48591.68	48728.37	-136.68
197	-1624.63	-1599.98	-24.65	55774.12	55827.94	-53.82
198	3936.12	3968.57	-32.45	68639.08	68283.42	355.66
199	15018.55	14960.15	58.39	47222.72	47224.10	-1.38
200	12018.45	12058.59	-40.14	52286.14	52168.70	117.43
201	10987.00	11123.41	-136.41	60199.68	60012.52	187.17
202	14394.62	14447.09	-52.47	71757.22	72006.74	-249.53
203	33778.62	33838.64	-60.02	44913.42	44870.01	43.41
204	29800.17	29977.77	-177.60	51305.27	51131.57	173.69
205	28336.53	28467.25	-130.73	58890.97	58775.12	115.85
206	30558.13	30632.13	-74.00	68528.82	68486.81	42.00
207	22352.76	22266.89	85.87	45815.99	45866.59	-50.60

Table 2-6. *Ab initio* and H^d Predicted Energies using FIT2 for All Data Points. Energies in cm⁻¹, numbering of nodes refers to Table 2-1. (Continued)

GEOM	E ₁ (<i>ab initio</i>)	E ₁ (FIT2)	ΔE ₁	E ₂ (<i>ab initio</i>)	E ₂ (FIT2)	ΔE ₂
208	28406.93	28361.36	45.58	44707.39	44742.83	-35.44
209	35292.43	35292.34	0.09	46185.74	46167.37	18.38
210	36038.21	35786.03	252.18	50423.34	50578.55	-155.21
211	35990.28	35925.24	65.04	51612.60	51652.60	-40.00
212	36004.41	35943.81	60.60	51905.49	51938.37	-32.88
213	36017.49	35955.57	61.92	51924.51	51983.49	-58.98
214	36022.97	35976.40	46.57	51929.23	51979.14	-49.90
215	18720.46	18732.23	-11.78	51864.31	51794.38	69.92
216	24289.17	24365.45	-76.29	51297.93	51241.34	56.60
217	32089.16	32199.06	-109.90	51740.28	51571.99	168.29
218	35238.10	35137.50	100.59	53447.81	53504.58	-56.77
219	35813.19	36004.15	-190.96	54004.41	53782.03	222.38
220	35977.93	36054.19	-76.26	54150.14	54023.28	126.87
221	35995.71	35983.08	12.63	54165.47	54207.13	-41.66
222	36000.99	35928.55	72.43	54170.84	54274.44	-103.61
223	17254.22	17373.62	-119.41	60261.35	59990.85	270.50
224	22614.77	22750.80	-136.03	59542.63	59463.41	79.22
225	31011.05	31118.51	-107.46	58697.09	58483.88	213.21
226	38389.94	38576.90	-186.96	66249.47	66185.26	64.20
227	36630.81	36900.12	-269.31	58568.19	58250.58	317.61
228	36932.30	36908.86	23.45	58570.23	58429.45	140.78
229	36954.56	36852.54	102.01	58581.13	58708.81	-127.68
230	36959.75	36906.93	52.82	58586.96	58680.20	-93.24
231	20040.30	20112.97	-72.66	71316.45	71307.70	8.75
232	25026.16	25144.74	-118.58	70040.22	69957.42	82.80
233	33274.96	33344.29	-69.33	67811.02	67756.55	54.47
234	38270.93	38490.72	-219.79	66478.32	66387.82	90.50
235	39584.20	39447.82	136.37	66092.15	66246.30	-154.15
236	39960.54	39809.67	150.88	65998.62	65815.29	183.34
237	39986.11	39766.52	219.59	66006.41	66266.34	-259.93
238	39991.67	40021.02	-29.36	66012.55	66109.85	-97.29
239	13513.36	13509.09	4.27	61758.48	62071.00	-312.52
Interpolation Points						
240	38919.47	38919.48	-0.01	39116.84	39116.79	0.05
241	38935.04	38935.05	-0.01	39116.77	39116.74	0.03
242	38974.28	38974.28	0.00	39119.91	39119.90	0.00
243	39014.19	39014.19	0.00	39137.86	39137.86	0.00
244	39032.42	39032.42	0.01	39177.46	39177.46	0.00
245	39035.94	39035.90	0.03	39216.28	39216.29	-0.01
246	39036.07	39036.02	0.05	39231.64	39231.66	-0.01

Table 2-6 (Continued)

GEOM	$E_1(ab\ initio)$	$E_1(FIT2)$	ΔE_1	$E_2(ab\ initio)$	$E_2(FIT2)$	ΔE_2
247	8842.12	8841.80	0.32	45992.65	45994.78	-2.13
248	7051.31	7049.91	1.40	45792.16	45807.21	-15.05
249	5359.47	5357.05	2.41	45449.71	45485.62	-35.91
250	4174.36	4171.64	2.71	45128.41	45177.09	-48.68
251	3078.45	3075.95	2.50	44783.94	44836.38	-52.43
252	2090.11	2088.24	1.87	44450.09	44494.71	-44.62
253	1230.57	1229.53	1.04	44163.19	44190.86	-27.67
254	13754.30	13752.92	1.39	45801.46	45809.11	-7.66
255	18442.80	18451.20	-8.40	44917.94	44926.96	-9.02
256	22955.01	22976.65	-21.65	43692.31	43696.72	-4.41
257	27186.55	27210.35	-23.80	42435.64	42415.92	19.72
258	31071.39	31088.18	-16.79	41286.07	41255.16	30.91
259	34572.72	34579.91	-7.19	40287.08	40267.76	19.32
260	37674.92	37675.79	-0.86	39443.05	39440.20	2.86
261	22740.91	22760.93	-20.02	43814.37	43829.69	-15.32
262	33388.62	33398.01	-9.38	40717.27	40700.02	17.26
263	38614.22	38604.25	9.97	41213.67	41215.97	-2.30
264	37352.76	37240.50	112.26	46310.35	46339.04	-28.68
265	36637.38	36470.33	167.06	49310.12	49353.71	-43.59
266	36251.23	36136.43	114.81	50992.24	51023.82	-31.58
267	36053.66	36009.38	44.29	51966.40	51979.35	-12.95
268	35960.79	35952.92	7.87	52597.20	52599.66	-2.46
269	-6.74	-6.75	0.01	46280.23	46290.23	-10.00
270	1389.43	1380.77	8.65	44827.84	45070.60	-242.76
271	19044.85	19056.15	-11.30	44756.55	44699.95	56.60
272	26671.79	26696.94	-25.16	42563.94	42498.82	65.12
273	33236.50	33247.81	-11.31	40653.25	40614.51	38.74
274	37903.36	37845.89	57.48	43756.07	43769.18	-13.11
275	36491.39	36347.53	143.86	49616.67	49656.47	-39.80
276	36141.06	36122.89	18.17	51254.41	51257.93	-3.52
277	36146.37	36133.82	12.55	51258.56	51260.59	-2.03
278	36094.58	36093.27	1.31	40127.85	40120.91	6.94
279	32678.53	32667.17	11.36	41374.19	41361.56	12.63
280	28840.34	28806.31	34.03	42812.96	42815.42	-2.46
281	24611.82	24549.84	61.98	44417.10	44451.51	-34.41
282	20049.96	19973.06	76.90	46104.93	46149.38	-44.45
283	15244.29	15185.77	58.52	47669.96	47680.66	-10.70
284	10322.29	10329.08	-6.78	48760.76	48751.71	9.05
285	5532.85	5596.63	-63.78	49136.07	49134.56	1.51
286	1252.02	1311.64	-59.61	48777.90	48885.37	-107.47
287	-1977.99	-1958.36	-19.63	48533.29	48617.23	-83.94

2.6.5 Geometries of All Data Points

Table 2-7. Internal Geometry of All Nodes, Fit and Interpolation Points. Bond lengths are presented in Å, angles in degrees.

GEOM	NH¹	NH²	NH³	∠H¹NH²	∠H¹NH³	ϕ
Nodes						
1	1.0485	1.0485	1.0485	60.00	60.00	0.00
2	1.0154	1.0154	1.0154	73.65	73.65	22.44
3	0.9979	0.9979	0.9979	60.00	60.00	0.00
4	1.3054	1.0408	1.0408	56.23	56.23	0.00
5	1.9689	1.0222	1.0222	54.60	54.60	0.00
6	3.5099	1.0283	1.0283	51.39	51.39	0.00
7	11.4476	1.0283	1.0283	51.39	51.39	0.00
8	3.5099	0.9986	0.9986	72.61	72.61	0.00
9	6.1558	0.9986	0.9986	72.61	72.61	0.00
Fit Points						
10	1.0547	1.0547	1.0547	60.00	60.00	0.00
11	1.0442	1.0572	1.0442	60.00	60.00	0.00
12	1.0411	1.0485	1.0560	60.00	60.00	0.00
13	1.0485	1.0485	1.0485	60.00	60.00	0.22
14	1.0485	1.0485	1.0485	60.47	60.47	0.00
15	1.0485	1.0485	1.0485	60.81	59.19	0.00
16	1.0180	1.0180	1.0180	60.00	60.00	0.00
17	1.0111	1.0860	1.0485	60.00	60.00	0.00
18	1.0269	1.0269	1.0917	60.00	60.00	0.00
19	1.0485	1.0485	1.0485	60.00	64.05	0.00
20	1.0485	1.0485	1.0485	55.32	62.34	0.00
21	1.0485	1.0485	1.0485	60.04	60.04	-1.10
22	1.0791	1.0791	1.0791	60.00	60.00	0.00
23	1.0701	1.0701	1.0053	60.00	60.00	0.00
24	1.0485	1.0485	1.0485	60.92	60.92	-5.55
25	1.0485	1.0485	1.0485	62.09	62.09	-8.38
26	1.0485	1.0485	1.0485	63.74	63.74	-11.30
27	1.0199	1.0173	1.0173	73.68	73.68	22.41
28	1.0177	1.0107	1.0147	73.56	73.86	22.38
29	1.0168	1.0168	1.0105	73.93	73.45	22.40
30	1.0154	1.0154	1.0154	73.74	73.39	22.52
31	1.0154	1.0154	1.0154	74.01	73.40	22.39
32	1.0154	1.0154	1.0154	73.91	73.91	22.68
33	1.0215	1.0215	1.0215	73.65	73.65	22.44
34	1.0154	1.0079	1.0229	73.65	73.65	22.44

Table 2-7. Internal Geometry of All Nodes, Fit and Interpolation Points.(Continued)

GEOM	NH ¹	NH ²	NH ³	$\angle H^1NH^2$	$\angle H^1NH^3$	ϕ
35	1.0068	1.0197	1.0197	73.65	73.65	22.44
36	1.0154	1.0154	1.0154	74.47	72.85	22.44
37	1.0154	1.0154	1.0154	73.42	73.42	22.65
38	1.0154	1.0154	1.0154	74.18	74.18	22.92
39	1.0133	1.0133	1.0133	77.88	77.88	26.08
40	1.0154	1.0154	1.0154	82.47	82.47	29.73
41	1.0132	1.0132	1.0132	69.46	69.46	19.27
42	1.0110	1.0110	1.0110	66.03	66.03	16.25
43	1.0088	1.0088	1.0088	63.32	63.32	13.35
44	1.0066	1.0066	1.0066	61.33	61.33	10.55
45	1.0045	1.0045	1.0045	60.01	60.01	7.84
46	1.0023	1.0023	1.0023	59.36	59.36	5.19
47	1.0001	1.0001	1.0001	59.36	59.36	2.59
48	1.0009	1.0009	1.0009	60.00	60.00	0.00
49	1.0016	0.9941	0.9979	60.00	60.37	0.00
50	1.0000	1.0000	0.9936	60.43	59.79	0.00
51	0.9979	0.9979	0.9979	60.00	59.57	0.00
52	0.9979	0.9979	0.9979	60.50	59.75	0.00
53	0.9979	0.9979	0.9979	60.00	60.00	0.19
54	1.1128	1.0466	1.0466	59.06	59.06	0.00
55	1.1770	1.0447	1.0447	58.12	58.12	0.00
56	1.2412	1.0428	1.0428	57.18	57.18	0.00
57	1.3101	1.0426	1.0426	56.33	56.33	0.00
58	1.3075	1.0360	1.0401	56.19	56.56	0.00
59	1.3067	1.0422	1.0359	56.60	56.04	0.00
60	1.3054	1.0408	1.0408	56.24	55.85	0.00
61	1.3054	1.0408	1.0408	56.68	56.00	0.00
62	1.3054	1.0408	1.0408	56.24	56.24	0.20
63	1.3319	1.0408	1.0408	56.23	56.23	0.00
64	1.3054	1.0596	1.0596	54.75	54.75	0.00
65	1.3054	1.0596	1.0221	56.23	56.23	0.00
66	1.3054	1.0408	1.0408	54.21	58.26	0.00
67	1.3054	1.0408	1.0408	57.57	57.57	0.00
68	1.3054	1.0408	1.0408	56.25	56.25	0.55
69	1.4179	1.0900	1.0900	52.54	52.54	0.00
70	1.2359	1.1204	1.1204	50.56	50.56	0.00
71	1.3054	1.1344	0.9473	56.08	56.08	0.00

Table 2-7. Internal Geometry of All Nodes, Fit and Interpolation Points.(Continued)

GEOM	NH¹	NH²	NH³	$\angle H^1NH^2$	$\angle H^1NH^3$	ϕ
72	1.3054	1.0408	1.0408	46.11	66.36	0.00
73	1.3054	1.0408	1.0408	63.49	63.49	0.00
74	1.3054	1.0408	1.0408	56.58	56.58	2.75
75	1.2558	1.0278	1.0278	56.23	56.23	0.00
76	1.2949	1.0303	1.0916	56.23	56.23	0.00
77	1.3054	1.0408	1.0408	51.56	58.57	0.00
78	1.3054	1.0408	1.0408	57.16	57.16	-5.53
79	1.3054	1.0408	1.0408	58.33	58.33	-8.37
80	1.3054	1.0408	1.0408	60.00	60.00	-11.28
81	1.2966	1.0411	1.0411	56.36	56.36	0.00
82	1.2877	1.0414	1.0414	56.48	56.48	0.00
83	1.2788	1.0416	1.0416	56.61	56.61	0.00
84	1.2700	1.0419	1.0419	56.73	56.73	0.00
85	1.3283	1.0402	1.0402	56.18	56.18	0.00
86	1.3512	1.0396	1.0396	56.12	56.12	0.00
87	1.3741	1.0389	1.0389	56.06	56.06	0.00
88	1.3969	1.0383	1.0383	56.01	56.01	0.00
89	1.4713	1.0362	1.0362	55.83	55.83	0.00
90	1.6371	1.0315	1.0315	55.42	55.42	0.00
91	1.8030	1.0269	1.0269	55.01	55.01	0.00
92	1.9651	1.0196	1.0196	54.55	54.55	0.00
93	1.9689	1.0222	1.0222	54.60	54.95	0.00
94	1.9693	1.0180	1.0206	54.58	54.61	0.00
95	1.9683	1.0223	1.0177	54.81	54.29	0.00
96	1.9670	1.0209	1.0209	54.86	54.25	0.00
97	1.9670	1.0209	1.0209	54.57	54.40	0.15
98	1.8143	0.9966	0.9966	54.60	54.60	0.00
99	1.8350	1.0000	1.0000	54.68	54.68	-1.65
100	1.8916	1.0094	1.0094	54.85	54.85	-2.86
101	1.9689	1.0222	1.0222	54.93	54.93	-3.30
102	2.0461	1.0351	1.0351	54.85	54.85	-2.86
103	2.1027	1.0445	1.0445	54.68	54.68	-1.65
104	2.1234	1.0479	1.0479	54.60	54.60	0.00
105	1.9119	0.8997	0.9967	54.68	54.68	-1.65
106	1.9073	1.0251	0.8994	54.68	54.68	-1.65
107	1.8916	1.0094	1.0094	54.68	46.09	-1.63
108	1.8916	1.0094	1.0094	64.61	49.72	-1.64

Table 2-7. Internal Geometry of All Nodes, Fit and Interpolation Points.(Continued)

GEOM	NH¹	NH²	NH³	∠H¹NH²	∠H¹NH³	ϕ
109	1.9689	1.0222	1.0222	54.60	54.60	-0.22
110	1.9689	1.0222	1.0222	54.61	54.61	-0.44
111	1.9689	1.0222	1.0222	54.62	54.62	-0.66
112	1.9689	1.0222	1.0222	54.63	54.63	-0.88
113	1.9689	1.0222	1.0222	54.65	54.65	-1.10
114	1.9689	1.0222	1.0222	54.65	54.65	-1.10
115	1.9689	1.0222	1.0222	54.82	54.82	-2.20
116	1.9689	1.0222	1.0222	55.10	55.10	-3.30
117	1.9689	1.0222	1.0222	55.49	55.49	-4.41
118	1.9689	1.0222	1.0222	55.99	55.99	-5.53
119	1.9689	1.0222	1.0222	60.24	60.24	-11.28
120	1.9689	1.0222	1.0222	78.23	78.23	-24.25
121	1.9794	1.1075	1.1075	103.20	103.20	-38.69
122	2.3541	1.0233	1.0233	54.00	54.00	0.00
123	2.7394	1.0244	1.0244	53.40	53.40	0.00
124	3.1247	1.0255	1.0255	52.82	52.82	0.00
125	3.5099	1.0266	1.0266	52.25	52.25	0.00
126	2.2257	1.0183	1.0183	56.91	56.91	0.00
127	2.4826	1.0144	1.0144	59.41	59.41	0.00
128	2.7394	1.0104	1.0104	62.12	62.12	0.00
129	2.9962	1.0065	1.0065	65.12	65.12	0.00
130	3.2531	1.0026	1.0026	68.54	68.54	0.00
131	3.5098	1.0246	1.0246	51.66	51.66	0.00
132	3.5046	1.0284	1.0284	51.39	51.39	0.00
133	3.5099	1.0321	1.0246	51.39	51.39	0.00
134	3.5099	1.0283	1.0283	50.99	51.80	0.00
135	3.5099	1.0283	1.0283	51.63	51.63	0.00
136	3.5099	1.0283	1.0283	51.39	51.39	0.11
137	4.0391	1.0283	1.0283	51.39	51.39	0.00
138	4.5683	1.0283	1.0283	51.39	51.39	0.00
139	5.0974	1.0283	1.0283	51.39	51.39	0.00
140	5.6266	1.0283	1.0283	51.39	51.39	0.00
141	3.5099	0.9949	0.9949	73.31	73.31	0.00
142	3.5046	0.9987	0.9987	72.61	72.61	0.00
143	3.5099	1.0024	0.9949	72.61	72.61	0.00
144	3.5099	0.9986	0.9986	72.21	73.02	0.00
145	3.5099	0.9986	0.9986	73.13	73.13	0.00

Table 2-7. Internal Geometry of All Nodes, Fit and Interpolation Points.(Continued)

GEOM	NH¹	NH²	NH³	∠H¹NH²	∠H¹NH³	ϕ
146	3.5099	0.9986	0.9986	72.61	72.61	0.10
147	4.0391	0.9986	0.9986	72.61	72.61	0.00
148	4.5683	0.9986	0.9986	72.61	72.61	0.00
149	5.0974	0.9986	0.9986	72.61	72.61	0.00
150	5.6266	0.9986	0.9986	72.61	72.61	0.00
151	1.8497	1.0214	1.0214	77.62	77.62	-24.01
152	1.7305	1.0205	1.0205	77.02	77.02	-23.78
153	1.6113	1.0197	1.0197	76.44	76.44	-23.55
154	1.4921	1.0188	1.0188	75.86	75.86	-23.32
155	1.3729	1.0180	1.0180	75.30	75.30	-23.10
156	1.2538	1.0171	1.0171	74.74	74.74	-22.88
157	1.1346	1.0163	1.0163	74.19	74.19	-22.65
158	0.8123	1.0154	1.0154	73.65	73.65	22.44
159	0.9139	1.0154	1.0154	73.65	73.65	22.44
160	1.1169	1.0154	1.0154	73.65	73.65	22.44
161	1.2185	1.0154	1.0154	73.65	73.65	22.44
162	1.5231	1.0154	1.0154	73.65	73.65	22.44
163	2.0308	1.0154	1.0154	73.65	73.65	22.44
164	3.0462	1.0154	1.0154	73.65	73.65	22.44
165	5.0770	1.0154	1.0154	73.65	73.65	22.44
166	0.8104	1.0485	1.0485	60.00	60.00	0.00
167	0.8104	1.0485	1.0485	60.50	60.50	3.33
168	0.8104	1.0485	1.0485	61.98	61.98	6.64
169	0.8104	1.0485	1.0485	64.34	64.34	9.90
170	0.8104	1.0485	1.0485	71.25	71.25	16.16
171	0.8104	1.0485	1.0485	75.52	75.52	19.11
172	0.8104	1.0485	1.0485	82.56	82.56	23.15
173	5.1752	1.0283	1.0283	51.39	51.39	0.00
174	5.1911	1.0283	1.0283	57.53	57.53	-11.69
175	5.2344	1.0283	1.0283	72.45	72.45	-22.77
176	5.2931	1.0283	1.0283	90.79	90.79	-32.31
177	5.3510	1.0283	1.0283	108.79	108.79	-38.25
178	5.3931	1.0283	1.0283	122.94	122.94	-33.86
179	5.4084	1.0283	1.0283	128.61	128.61	0.00
180	0.8913	1.0485	1.0485	63.74	63.74	-11.30
181	0.9437	1.0485	1.0485	63.74	63.74	-11.30
182	0.9961	1.0485	1.0485	63.74	63.74	-11.30

Table 2-7. Internal Geometry of All Nodes, Fit and Interpolation Points.(Continued)

GEOM	NH¹	NH²	NH³	$\angle H^1NH^2$	$\angle H^1NH^3$	ϕ
183	1.2582	1.0485	1.0485	63.74	63.74	-11.30
184	1.5728	1.0485	1.0485	63.74	63.74	-11.30
185	2.0971	1.0485	1.0485	63.74	63.74	-11.30
186	3.1456	1.0485	1.0485	63.74	63.74	-11.30
187	5.2427	1.0485	1.0485	63.74	63.74	-11.30
188	0.7408	1.0222	1.0222	57.88	57.88	10.00
189	0.7408	1.0222	1.0222	66.76	66.76	20.00
190	0.7408	1.0222	1.0222	79.37	79.37	30.00
191	0.8996	1.0222	1.0222	57.88	57.88	10.00
192	0.8996	1.0222	1.0222	66.76	66.76	20.00
193	0.8996	1.0222	1.0222	79.37	79.37	30.00
194	0.8996	1.0222	1.0222	94.20	94.20	40.00
195	1.0584	1.0222	1.0222	57.88	57.88	10.00
196	1.0584	1.0222	1.0222	66.76	66.76	20.00
197	1.0584	1.0222	1.0222	79.37	79.37	30.00
198	1.0584	1.0222	1.0222	94.20	94.20	40.00
199	1.4288	1.0222	1.0222	57.88	57.88	10.00
200	1.4288	1.0222	1.0222	66.76	66.76	20.00
201	1.4288	1.0222	1.0222	79.37	79.37	30.00
202	1.4288	1.0222	1.0222	94.20	94.20	40.00
203	1.9689	1.0222	1.0222	57.88	57.88	10.00
204	1.9689	1.0222	1.0222	66.76	66.76	20.00
205	1.9689	1.0222	1.0222	79.37	79.37	30.00
206	1.9689	1.0222	1.0222	94.20	94.20	40.00
207	1.5875	1.0222	1.0222	57.88	57.88	10.00
208	1.7463	1.0222	1.0222	57.88	57.88	10.00
209	2.1167	1.0222	1.0222	57.88	57.88	10.00
210	2.6459	1.0222	1.0222	57.88	57.88	10.00
211	3.1751	1.0222	1.0222	57.88	57.88	10.00
212	4.2334	1.0222	1.0222	57.88	57.88	10.00
213	5.2918	1.0222	1.0222	57.88	57.88	10.00
214	10.5835	1.0222	1.0222	57.88	57.88	10.00
215	1.5875	1.0222	1.0222	66.76	66.76	20.00
216	1.7463	1.0222	1.0222	66.76	66.76	20.00
217	2.1167	1.0222	1.0222	66.76	66.76	20.00
218	2.6459	1.0222	1.0222	66.76	66.76	20.00
219	3.1751	1.0222	1.0222	66.76	66.76	20.00

Table 2-7. Internal Geometry of All Nodes, Fit and Interpolation Points.(Continued)

GEOM	NH¹	NH²	NH³	∠H¹NH²	∠H¹NH³	ϕ
220	4.2334	1.0222	1.0222	66.76	66.76	20.00
221	5.2918	1.0222	1.0222	66.76	66.76	20.00
222	10.5835	1.0222	1.0222	66.76	66.76	20.00
223	1.5875	1.0222	1.0222	79.37	79.37	30.00
224	1.7463	1.0222	1.0222	79.37	79.37	30.00
225	2.1167	1.0222	1.0222	79.37	79.37	30.00
226	2.6459	1.0222	1.0222	86.39	86.39	36.22
227	3.1751	1.0222	1.0222	79.37	79.37	30.00
228	4.2334	1.0222	1.0222	79.37	79.37	30.00
229	5.2918	1.0222	1.0222	79.37	79.37	30.00
230	10.5835	1.0222	1.0222	79.37	79.37	30.00
231	1.5875	1.0222	1.0222	94.20	94.20	40.00
232	1.7463	1.0222	1.0222	94.20	94.20	40.00
233	2.1167	1.0222	1.0222	94.20	94.20	40.00
234	2.6459	1.0222	1.0222	94.20	94.20	40.00
235	3.1751	1.0222	1.0222	94.20	94.20	40.00
236	4.2334	1.0222	1.0222	94.20	94.20	40.00
237	5.2918	1.0222	1.0222	94.20	94.20	40.00
238	10.5835	1.0222	1.0222	94.20	94.20	40.00
239	0.7871	1.0222	1.0222	54.60	54.60	0.00
Interpolation Points						
240	1.9637	1.0214	1.0214	54.60	54.60	0.00
241	1.9644	1.0215	1.0215	54.60	54.60	0.05
242	1.9663	1.0218	1.0218	54.60	54.60	0.10
243	1.9689	1.0222	1.0222	54.60	54.60	0.11
244	1.9714	1.0227	1.0227	54.60	54.60	0.10
245	1.9733	1.0230	1.0230	54.60	54.60	0.05
246	1.9740	1.0231	1.0231	54.60	54.60	0.00
247	1.2788	1.0416	1.0416	56.61	56.61	0.00
248	1.2434	1.0427	1.0427	57.11	57.11	0.00
249	1.2080	1.0438	1.0438	57.62	57.62	0.00
250	1.1814	1.0446	1.0446	58.01	58.01	0.00
251	1.1548	1.0454	1.0454	58.40	58.40	0.00
252	1.1283	1.0462	1.0462	58.79	58.79	0.00
253	1.1017	1.0469	1.0469	59.19	59.19	0.00
254	1.3741	1.0389	1.0389	56.06	56.06	0.00
255	1.4656	1.0364	1.0364	55.84	55.84	0.00

Table 2-7. Internal Geometry of All Nodes, Fit and Interpolation Points.(Continued)

GEOM	NH¹	NH²	NH³	∠H¹NH²	∠H¹NH³	ϕ
256	1.5571	1.0338	1.0338	55.61	55.61	0.00
257	1.6486	1.0312	1.0312	55.39	55.39	0.00
258	1.7401	1.0287	1.0287	55.16	55.16	0.00
259	1.8316	1.0261	1.0261	54.94	54.94	0.00
260	1.9231	1.0235	1.0235	54.71	54.71	0.00
261	1.5504	1.0395	1.0395	55.67	55.67	0.00
262	1.7953	1.0381	1.0381	55.12	55.12	0.00
263	2.0403	1.0367	1.0367	54.57	54.57	0.00
264	2.2852	1.0353	1.0353	54.03	54.03	0.00
265	2.5301	1.0339	1.0339	53.49	53.49	0.00
266	2.7751	1.0325	1.0325	52.96	52.96	0.00
267	3.0200	1.0311	1.0311	52.43	52.43	0.00
268	3.2650	1.0297	1.0297	51.91	51.91	0.00
269	0.9459	1.0222	1.0222	54.60	54.60	0.00
270	1.1046	1.0222	1.0222	54.60	54.60	0.00
271	1.4750	1.0222	1.0222	54.60	54.60	0.00
272	1.6338	1.0222	1.0222	54.60	54.60	0.00
273	1.7925	1.0222	1.0222	54.60	54.60	0.00
274	2.1630	1.0222	1.0222	54.60	54.60	0.00
275	2.6921	1.0222	1.0222	54.60	54.60	0.00
276	5.3380	1.0222	1.0222	54.60	54.60	0.00
277	10.6298	1.0222	1.0222	54.60	54.60	0.00
278	1.8822	1.0216	1.0216	54.63	54.63	1.87
279	1.7955	1.0210	1.0210	54.98	54.98	3.75
280	1.7088	1.0204	1.0204	55.66	55.66	5.65
281	1.6222	1.0198	1.0198	56.68	56.68	7.57
282	1.5355	1.0191	1.0191	58.03	58.03	9.54
283	1.4488	1.0185	1.0185	59.73	59.73	11.54
284	1.3621	1.0179	1.0179	61.77	61.77	13.60
285	1.2754	1.0173	1.0173	64.18	64.18	15.71
286	1.1888	1.0166	1.0166	66.95	66.95	17.88
287	1.1021	1.0160	1.0160	70.10	70.10	20.12

References

1. Atchity, G. J.; Ruedenberg, K., DEtermination of diabatic bases though enforcement of configurations uniformity. *Theor. Chem. Acc.* **1997**, *97*, 47-58.
2. Viel, A.; Eisfeld, W.; Evenhuis, C. R.; Manthe, U., Photoionization-induced dynamics of the ammonia cation studied by wave packet calculations using curvilinear coordinates. *Chemical Physics* **2008**, *347* (1-3), 331-339.
3. Evenhuis, C. R.; Collins, M. A., Interpolation of Diabatic potential energy surfaces. *J. Chem. Phys.* **2004**, *121*, 2515.
4. Evenhuis, C. R.; Lin, X.; Zhang, D. H.; Yarkony, D. R.; Collins, M. A., Interpolation of diabatic potential-energy surfaces: Quantum dynamics on ab initio surfaces. *J. Chem. Phys.* **2005**, *123*, 134110 (12 pages).
5. Godsi, O.; Evenhuis, C. R.; Collins, M. A., Interpolation of Multidimensional diabatic surfaces. *J. Chem. Phys.* **2006**, *125*, 104105.
6. Zhang, P.; Morokuma, K.; Wodtke, A. M., High level ab initio studies of unimolecular dissociation of the ground state N₃ radical. *J. Chem. Phys.* **2005**, *122*, 014106.
7. Nangia, S.; Truhlar, D. G., Direct Calculation of Coupled Diabatic Potential Energy Surfaces for ammonia and mapping of a 4-dimensional conical intersection seam. *J. Chem. Phys.* **2006**, *124*, 124309.
8. Lischka, H.; Dallos, M.; Szalay, P.; Yarkony, D. R.; Shepard, R., The analytic evaluation of nonadiabatic coupling terms at the MR-CI level I: Formalism. *J. Chem. Phys.* **2004**, *120*, 7322-7329.

9. Baer, M., Electronic non-adiabatic Transitions Derivation of the general adiabatic-diabatic transformation matrix. *Molec. Phys.* **1980**, *40*, 1011-1013.
10. Mead, C. A.; Truhlar, D. G., Conditions for the definition of a strictly diabatic basis. *J. Chem. Phys.* **1982**, *77*, 6090-6098.
11. Baer, M., Introduction to the theory of electronic nonadiabatic coupling terms in molecular systems. *Physics Reports* **2002**, *358*, 75-142.
12. Papas, B. N.; Schuurman, M. S.; Yarkony, D. R., *Determining quasi diabatic coupled electronic state Hamiltonians using derivative couplings. A normal equations based method.* *J. Chem. Phys.* **2008**, *129*, 124104(10 pages).
13. Zhu, X.; Yarkony, D. R., On the Determination of Optimized, Fully Quadratic, Coupled State Quasi Diabatic Hamiltonians for Determining Bound State Vibronic Spectra. *J. Chem. Phys.* **2009**, *130*, 234108 (11 pages).
14. Fogarasi, G.; Zhou, X.; Taylor, P. W.; Pulay, P., The Calculation of ab initio molecular geometries: Efficient optimization by natural internal coordinates and empirical correction by offset forces. *J. Amer. Chem. Soc.* **1992**, *114*, 8191.
15. Braams, B. J.; Bowman, J. M., Permutationally Invariant Potential Energy Surfaces in High dimensionality. *Int. Rev. Phys. Chem.* **2009**, *28*, 577-606.
16. Huang, X.; Braams, B. J.; Bowman, J. M., Ab initio potential energy and dipole moment surfaces for H₅O₂⁺. *J. Chem. Phys.* **2005**, *122*, 044308(12 pages).
17. Koziol, L.; Wang, Y. M.; Braams, B. J.; Bowman, J. M.; Krylov, A. I., The theoretical prediction of infrared spectra of trans- and cis-hydroxycarbene calculated using full dimensional ab initio potential energy and dipole moment surfaces. *Journal of Chemical Physics* **2008**, *128* (20), 204310.

18. Longuet-Higgins, H. C., The symmetry groups of non-rigid molecules. *Mol. Phys.* **1963**, *6*, 445-460.
19. Bunker, P. R., *Molecular Symmetry and Spectroscopy*. Academic Press: New York, 1979.
20. Bach, A.; Hutchison, J. M.; Holiday, R. J.; Crim, F. F., Vibrational spectroscopy and photodissociation of jet-cooled ammonia. *J. Chem. Phys.* **2002**, *116*, 4955-4961.
21. Bach, A.; Hutchison, J. M.; Holiday, R. J.; Crim, F. F., Photodissociation of vibrationally excited ammonia: rotational excitation in the NH₂ product. *J. Chem. Phys.* **2003**, *118*, 7144-7145.
22. Hause, M. L.; Yoon, Y. H.; Crim, F. F., Vibrationally mediated photodissociation of ammonia: The influence of N-H stretching vibrations on passage through conical intersections. *J. Chem. Phys.* **2006**, *125*, 174309.
23. Yarkony, D. R., Exploring Molecular Complexity: The Role of Conical Intersections in NH₃ Photodissociation. *J. Chem. Phys.* **2004**, *121*, 628-631.
24. Bonhommeau, D.; Truhlar, D. G., Mixed Quantum/Classical investigation of the photodissociation of NH₃(A) an practical method for maintaining zero-point energy in classical trajectories *J. Chem. Phys.* **2008**, *129*, 014302.
25. Bonhommeau, D.; Valero, R.; Truhlar, D. G.; Jasper, A. W., Coupled-Surface Investigation of the photodissociation of NH₃(A). Effect of exciting the symmetric and antisymmetric stretch modes. *J. Chem. Phys.* **2009**, *130*, 234303 (17 pages).
26. Leon, S. J., *Linear Algebra with Applications*. Prentice-Hall: Upper Saddle River, NJ, 2002.

27. Lengsfeld, B. H.; Yarkony, D. R., *Nonadiabatic Interactions Between Potential Energy Surfaces: Theory and Applications*. In *State-Selected and State to State Ion-Molecule Reaction Dynamics: Part 2 Theory*, Baer, M.; Ng, C.-Y., Eds. John Wiley and Sons: New York, 1992; Vol. 82, pp 1-71.
28. Yarkony, D. R., Conical Intersections: Diabolical and Often Misunderstood. *Acc. Chem. Res.* **1998**, *31*, 511-518.
29. Schuurman, M. S.; Yarkony, D. R., On the Vibronic Coupling Approximation: A generally applicable approach for determining fully quadratic quasi diabatic coupled electronic state Hamiltonians. *J. Chem. Phys.* **2007**, *127*, 094104(9 pages).
30. Lischka, H.; Shepard, R.; Pitzer, R. M.; Shavitt, I.; Dallos, M.; Müller, T.; Szalay, P. G.; Seth, M.; Kedziora, G. S.; Yabushita, S.; Zhang, Z., COLUMBUS. *Phys. Chem. Chem. Phys.* **2001**, *3*, 664-673.
31. Yarkony, D. R., *On the adiabatic to diabatic states transformation near intersections of conical intersections*. *J. Chem. Phys.* **2000**, *112*, 2111-2120.
32. Atchity, G. J.; Xantheas, S. S.; Ruedenberg, K., Potential Energy Surfaces Near Intersections. *J. Chem. Phys.* **1991**, *95*, 1862-1876.
33. Ben-Nun, M.; Martinez, T. J., Ab Initio Multiple Spawning: Photochemistry from First Principles Quantum Molecular Dynamics. *J. Phys. Chem. A* **2000**, *104*, 5161-5175.
34. Worth, G. A.; Robb, M. A.; Lasorne, B., Solving the Time dependent Schrödinger equation for nuclear motion in one step: direct dynamics on nonadiabatic systems. *Mol. Phys.* **2008**, *106*, 2077-2091.

35. Thompson, K. C.; Jordan, M. J. T.; Collins, M. A., Polyatomic Molecules potential energy surfaces by interpolation in cartesian coordinates. *J. Chem. Phys.* **1998**, *108*, 564-578.
36. McCarthy, M. I.; Rosmus, P.; Werner, H.-J.; Botschwina, P.; Vaida, V., NH₃ photodissociation. *J. Chem. Phys.* **1987**, *86*, 6693.

Chapter 3 Quasi-Diabatic Representations of Adiabatic Potential Energy Surfaces Coupled by Conical Intersections including Bond Breaking: A More General Construction Procedure and an Analysis of the Diabatic Representation

3.1 Abstract

The analytic representation of adiabatic potential energy surfaces and their nonadiabatic interactions is a key component of accurate, fully quantum mechanical descriptions of nonadiabatic dynamics. In this work we describe extensions of a promising method for representing the nuclear coordinate dependence of the energies, energy gradients and derivative couplings of N^{state} adiabatic electronic states coupled by conical intersections. The description is based on a vibronic coupling model and can describe multichannel dissociation. An important feature of this approach is that it incorporates information about the geometry dependent interstate derivative couplings into the fitting procedure so that the resulting representation is quantifiably quasi diabatic and quasi diabatic in a least squares sense. The reported extensions improve both the rate of convergence and the converged results and will permit the optimization of nonlinear parameters including those parameters that govern the placement of the functions used to describe multichannel dissociation. Numerical results for a coupled quasi-diabatic state representation of the photodissociation process $\text{NH}_3 + h\nu \rightarrow \text{NH}_2 + \text{H}$ illustrate the potential of the improved algorithm. A second focus in this numerical example is the quasi-diabatic character of the representation which is described and analyzed. Special attention is paid to the immediate vicinity of the conical intersection seam.

3.2 Introduction

For the foreseeable future, accurate fully quantum mechanical simulations of electronically nonadiabatic processes involving conical intersections will require analytic representations of the requisite electronic structure data,¹ energies, energy gradients and derivative couplings in the adiabatic representation, or the Hamiltonian matrix elements in the diabatic representation. The need to accurately sample initial distributions means that even more approximate dynamical approaches such as trajectory surface hopping,² which can be used with electronic structure data determined 'on the fly' or 'directly' as needed,³⁻⁴ can also benefit from analytic representations of electronic structure data. A principal advantage of analytic representations is that they can employ much more accurate wave functions than are currently practical in direct dynamics. Unfortunately the representation of adiabatic potential energy surfaces coupled by conical intersections obtained by *ab initio* methods is a challenging problem. The challenge is particularly daunting when chemical bonds are broken and the molecule dissociates.

The existence of conical intersections, with their singular derivative couplings in the adiabatic basis motivates the use of a quasi-diabatic state representation of the adiabatic states. The advantages of a diabatic representation are two fold. A rigorous diabatic representation solves the problem of the singular derivative couplings by requiring that the derivative coupling in the diabatic representation vanish globally (see section 3.4). The vanishing of the derivative coupling also simplifies the form the nuclear Schrödinger equation.⁵ Unfortunately the attribute *quasi* used above, which we shall omit below except as needed for emphasis, indicates that for polyatomic molecules rigorous diabatic bases do not exist.⁵⁻⁷

The determination of a quasi-diabatic representation of coupled adiabatic states data has long been a problem of considerable interest in computational nonadiabatic chemistry. For a synopsis of much of this work prior to 2008, see Ref. ⁸. The determination of a diabatic representation combines a method for constructing the diabatic state data from the adiabatic state data with a method for fitting or representing the diabatic state data. The type of *ab initio* data used to define the diabatic basis, some combination of energies, energy gradients and derivative couplings data, is also an issue. Approaches to this problem include (i) the fourfold way diabatization,⁹⁻¹¹ accompanied by fitting the resulting diabatic matrix elements;¹² (ii) diabatization by ansatz which fits the adiabatic energies using a matrix of smoothly varying functions;^{11, 13-14} (iii) Shepard interpolation of a diabatic representation based on energy gradients, derivative couplings and their derivatives;¹⁵⁻¹⁷ (iv) diabatizations based on the regularized representation¹⁸⁻¹⁹ followed by fitting the diabatic energies; (v) double many body expansions;²⁰⁻²³ (vi) the generalized adiabatic angle method;⁸ (vii) methods based on polyspherical coordinates and dynamical symmetry groups,^{1, 24} and (viii) methods based on molecular properties.²⁵⁻

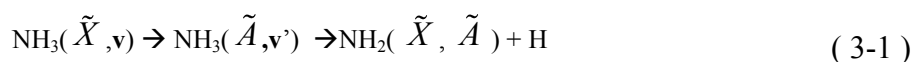
26

Recently we have introduced an approach based on a vibronic coupling model²⁷ that uses *ab initio* energies, energy gradients and derivative couplings to determine the diabatic representation.²⁸⁻³⁰ This approach has several features to its merit. It uses overcomplete sets of coordinates (see also Ref. ²³) and is therefore not tied to a specific coordinate representation. Although most of the *ab initio* data is described in a least squares sense, the ability to designate some points as nodes, points where the *ab initio* data is exactly reproduced, allows for a flexible combination of least squares fitting and

interpolation. The use of functions localized in distinct regions of nuclear coordinate space, facilitates the description of multichannel processes.²³ The incorporation of interstate derivative coupling information into the fitting procedure results in a representation that is quantifiably diabatic and diabatic in a least-squares sense. The use of derivative coupling data and intersection adapted coordinates³¹ enables a continuous and accurate description of a seam of conical intersection and its local topography. The numerical example used in this work³⁰ accurately describes twenty-four points of conical intersection on a two state seam.

In this work, we introduce an enhanced algorithm which improves both convergence and the converged result of the fitting procedure and will enable optimization of nonlinear parameters. In light of our earlier comments concerning diabatic representations, we will also investigate, from a computational perspective, the diabatic representation produced by this procedure, demonstrating in particular, its ability to accurately describe the immediate vicinity of a conical intersection.

The nonadiabatic photodissociation of ammonia,



(see Figure 3-1) is a problem that has received considerable attention for nearly three decades.^{12, 32-56} Despite this long history, important questions about the nonadiabatic dynamics, arising from vibrationally mediated photodissociation experiments,^{36, 57-58} remain unresolved.⁵⁵ Recently, using our original algorithm,³⁰ we obtained a diabatic representation of the $1,2^1\text{A}$ states of ammonia that showed considerable promise in being able to address these fundamental questions. The root mean square error for the energy data on over 2500 points was $\sim 77 \text{ cm}^{-1}$ for energies as high $50,000 \text{ cm}^{-1}$. Twenty-four

points on the seam of conical intersection were included in the representation and their locus, energy differences and branching plane parameters⁵⁹ are exactly reproduced. Using this representation a full six dimensional quantum scattering simulation of the ν_2 progression in the absorption spectrum of ground state ammonia was carried out⁶⁰ and found to be in good agreement with the available experimental data, line positions, intensities and lifetimes, and a considerable improvement over a simulation⁵⁴ using the same quantum scattering techniques but based on an alternative diabatic representation of *ab initio* data.¹² In this work the potential of the new algorithm is illustrated by improving our previous description of these coupled PESs.

Section 3.3 describes the enhanced algorithm. Section 3.4 illustrates its potential revisiting the $1,2^1A$ coupled PESs of NH_3 . In this section the properties of the diabatic representation are analyzed. Section 3.5 summarizes and concludes.

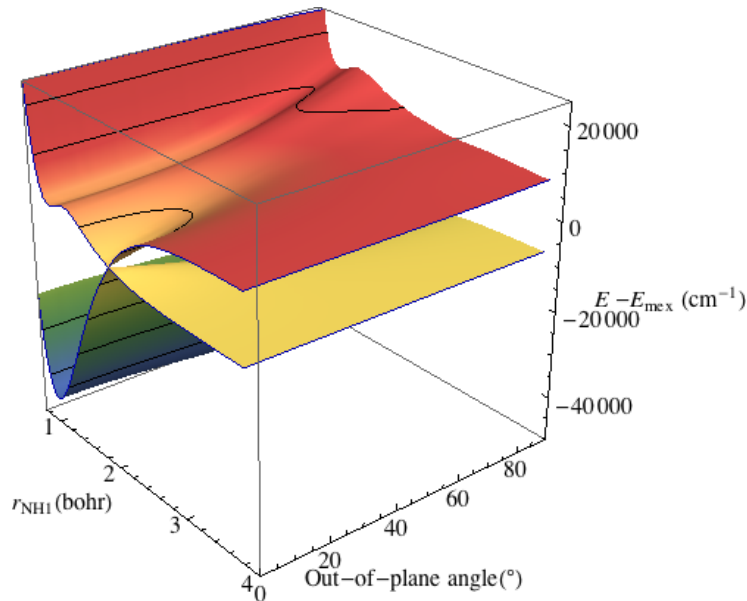


Figure 3-1. Plot of $1,2^1A$ adiabatic potential energy surfaces of NH_3 as a function of $R(\text{N-H})$ and out of plane angle(degree). The out of plane angle ϕ , ($0 < \phi < 90^\circ$) satisfies

$$\sin \phi = \frac{\vec{d}_{N-H1} \times \vec{d}_{N-H2} \cdot \vec{d}_{N-H3}}{\|\vec{d}_{N-H1} \times \vec{d}_{N-H2} + \vec{d}_{N-H2} \times \vec{d}_{N-H3} + \vec{d}_{N-H3} \times \vec{d}_{N-H1}\|} \quad \text{where } \vec{d}_{N-Hn} = \vec{r}_{N-Hn} / r_{N-Hn}$$

3.3 The Algorithm

3.3.1 General Definitions

The *ab initio* adiabatic electronic states $\Psi_J^{a,ab}(\mathbf{q}; \mathbf{R})$ are expanded in a CSF basis, $\psi_\alpha(\mathbf{q}; \mathbf{R})$, as

$$\Psi_J^{a,ab}(\mathbf{q}; \mathbf{R}) = \sum_{\alpha} c_{\alpha}^J(\mathbf{R}) \psi_{\alpha}(\mathbf{q}; \mathbf{R}) \quad (3-2)$$

and have energies $E^{a,J,(ab)}(\mathbf{R})$. Here \mathbf{R} are the $3N^{\text{at}}$ Cartesian nuclear coordinates and \mathbf{q} are the $3N^{\text{el}}$ electronic coordinates. The $E^{a,J,(ab)}(\mathbf{R})$ are determined from the electronic Schrödinger equation

$$[\mathbf{H}^{\text{CSF}}(\mathbf{R}) - \mathbf{I}E^{a,J,(ab)}(\mathbf{R})]\mathbf{c}^J(\mathbf{R}) = \mathbf{0} \quad (3-3)$$

where $\mathbf{H}^{\text{CSF}}(\mathbf{R})$ is the fixed nuclei electronic Hamiltonian, $H^e(\mathbf{q}; \mathbf{R})$, in the CSF basis.

N^{state} eigenstates of \mathbf{H}^{CSF} are represented by an $N^{\text{state}} \times N^{\text{state}}$ diabatic state Hamiltonian, \mathbf{H}^{d} in terms of which the electronic Schrödinger equation, eq. (3-3), becomes

$$[\mathbf{H}^{\text{d}}(\mathbf{R}) - \mathbf{I}E^{a,J,(m)}(\mathbf{R})]\mathbf{d}^J(\mathbf{R}) = \mathbf{0} \quad (3-4)$$

Here the superscript (m) indicates that the results come from the model Hamiltonian \mathbf{H}^{d} , rather than the *ab initio* wave functions. The diabatic states, formally the basis for \mathbf{H}^{d} , are constructed from adiabatic states,

$$\Psi_u^{\text{d}}(\mathbf{q}; \mathbf{R}) = \sum_{J=1}^{N^{\text{state}}} \Psi_J^{a,(ab)}(\mathbf{q}; \mathbf{R}) (d^{-1})_u^J(\mathbf{R}) = \sum_{J=1}^{N^{\text{state}}} \Psi_J^{a,(ab)}(\mathbf{q}; \mathbf{R}) \mathbf{d}_J^u(\mathbf{R}) \quad (3-5)$$

As discussed in Ref. ³⁰, \mathbf{H}^{d} is expanded in terms of basis matrices, $\mathbf{B}^{u,v}$, as :

$$\mathbf{H}^{\text{d}}(\mathbf{R}) = \sum_{n=1}^{N^{\text{c}}} V_n P^{(n)}(\mathbf{R}) \mathbf{B}^{u(n),v(n)} \quad (3-6)$$

where $\mathbf{B}^{u,v}$ is an $N^{\text{state}} \times N^{\text{state}}$ symmetric matrix with a 1 in the (u,v) and (v,u) elements and the remaining elements 0. For example, for $N^{\text{state}} = 2$ there are three basis matrices

$$\mathbf{B}^{1,1} = \begin{pmatrix} 1 & 0 \\ 0 & 0 \end{pmatrix} \quad \mathbf{B}^{1,2} = \begin{pmatrix} 0 & 1 \\ 1 & 0 \end{pmatrix} \quad \text{and} \quad \mathbf{B}^{2,2} = \begin{pmatrix} 0 & 0 \\ 0 & 1 \end{pmatrix} .$$

The N^c unknown coefficients of combination, the V_n , $1 \leq n \leq N^c$, are denoted the linear parameters. The advantage of \mathbf{H}^d in the form of eq. (3-6), is that makes the linear dependence of \mathbf{H}^d on the V_j explicit and easy to work with. The geometry dependence of \mathbf{H}^d is contained in the polynomials $p^{(n)}(\mathbf{R})$, symmetry adapted linear combinations of basic monomials, $g_l(\mathbf{R})$. The $g_l(\mathbf{R})$ currently in use are described in Appendix 3.6.1. As explained in Ref³⁰. $p^{(n)}(\mathbf{R}) = P^{u(n)} g^{l(n)}(\mathbf{R})$, where $P^{u(n)}$ is the appropriate group theoretical projection operator. The nonlinear parameters are contained in the $p^{(n)}$ and are denoted collectively as γ_i , $1 \leq i \leq N^l$. The nonlinear parameters are described in Appendix 3.6.1.

3.3.2 Defining equations

We now turn to the equations defining the linear and nonlinear parameters. The V_j and γ_i are chosen so that the differences between the \mathbf{H}^d determined, and *ab initio* determined, energies, energy gradients and derivative couplings (actually the interstate coupling vector which is approximately the derivative coupling times the energy difference) are minimized on a set of nuclear configurations, \mathbf{R}_n , $1 \leq n \leq N^{\text{point}}$, in a prescribed manner. The following definitions will allow us to succinctly express the conditions:

$$L_0^{I,J,(x)}(\mathbf{R}_n) \equiv E^{a,I,(x)}(\mathbf{R}_n) \quad (3-7)$$

$$L_j^{I,J,(x)}(\mathbf{R}_n) \equiv \nabla_j E^{a,I,J,(x)}(\mathbf{R}_n) \quad (3-8)$$

$$L_j^{I,J,(x)}(\mathbf{R}_n) = h_j^{a,I,J,(x)}(\mathbf{R}_n) \quad (3-9)$$

where $h_j^{a,I,J,(x)}$ is a component of the interstate coupling vector $\mathbf{h}^{a,I,J,(x)}$ defined by

$$\mathbf{h}^{a,I,J,(m)}(\mathbf{R}) = \mathbf{d}^I(\mathbf{R})^\dagger \nabla \mathbf{H}^d(\mathbf{R}) \mathbf{d}^J(\mathbf{R}) \quad (3-10)$$

and

$$\mathbf{h}^{a,I,J,(ab)}(\mathbf{R}) = \mathbf{c}^I(\mathbf{R})^\dagger \nabla \mathbf{H}^{CSF}(\mathbf{R}) \mathbf{c}^J(\mathbf{R}) \approx \mathbf{f}^{a,I,J,(ab)}(\mathbf{R}) [E^{a,J,(ab)}(\mathbf{R}) - E^{a,I,(ab)}(\mathbf{R})] \quad (3-11)$$

where $\mathbf{f}^{a,I,J,(ab)}$ is the *ab initio* derivative coupling vector. From eq. (3-4) and its derivative and eq. (3-6), eqs. (3-7), (3-8) and (3-9) become, for $x = m$

$$L_j^{I,J,(m)}(\mathbf{R}_n) = \sum_{l=1}^N V_l W_{n,I,J,j;l} \equiv (\mathbf{WV})_k = L_k^{(m)} \quad (3-12)$$

where

$$W_{n,I,J,j;l} = \mathbf{d}^{I\dagger}(\mathbf{R}_n) \mathbf{B}^{u(l),v(l)} \mathbf{d}^J(\mathbf{R}_n) [\nabla_j p^{(l)}(\mathbf{R}_n)] \quad (3-13)$$

and ∇_0 means do nothing. In eq. (3-12) and below is convenient to re-index the four indices (n,I,J,j) by k so that $L_j^{I,J,(x)}(\mathbf{R}_n)$, is replaced by $L_k^{(x)}$, and $W_{n,I,J,j;l}$ by $W_{k,l}$ for $1 \leq k \leq N^{eq}$. In eq. (3-13) at each \mathbf{R}_n , the ∇_j denote the derivatives with respect to a local, nonredundant coordinate system. The choice of local coordinates is arbitrary and different coordinates can be used for different points. This flexibility is a key aspect of the algorithm. It is also important to emphasize that eq. (3-12) is exact even though the \mathbf{d}^J depend on \mathbf{R} .

We would like to require $L_k^{(ab)} = L_k^{(m)}$ for all k , but that is not possible since $N^{eq} \gg (N^c + N^m)$. Instead we require $L_j^{(ab)} = L_j^{(m)}$ for $1 \leq j \leq N^{lsq}$ be solved in a least squares sense and the remaining $N^{ex} = N^{eq} - N^{lsq}$, equations, that is $L_j^{ab} = L_j^m$ for $N^{lsq} < j \leq N^{eq}$, be

solved exactly. Nuclear configurations whose *ab initio* data fall into the second category will be referred to as nodes. The desired solution is obtained with the help of the Lagrangian

$$\Lambda(\mathbf{V}, \boldsymbol{\gamma}, \boldsymbol{\lambda}) = \frac{1}{2} \sum_{j=1}^{N^{bq}} [L_j^{(m)} - L_j^{(ab)}]^2 + \sum_{j=N^{bq}+1}^{N^{eq}} \lambda_{j-N^{bq}} [L_j^{(m)} - L_j^{(ab)}] + \frac{t}{2} \mathbf{V}^\dagger \mathbf{V} \quad (3-14)$$

where the λ_j are the Lagrange multipliers. The final term in eq. (3-14), a damping

term, as explained previously. Requiring $G_i^V = \frac{\partial \Lambda}{\partial V_i} = 0$, for $1 \leq i \leq N^c$; $G_i^\lambda = \frac{\partial \Lambda}{\partial \lambda_i} = 0$,

for $1 \leq i \leq N^{ex}$; and $G_j^\gamma = \frac{\partial \Lambda}{\partial \gamma_j} = 0$ for $1 \leq j \leq N^{nl}$, gives through second order in

displacements, the standard Newton-Raphson equations

$$\begin{pmatrix} \Lambda^{V,V} & \Lambda^{V,\lambda} & \Lambda^{V,\gamma} \\ \Lambda^{V,\lambda} & 0 & \Lambda^{l,\gamma} \\ \Lambda^{\gamma,V} & \Lambda^{\gamma,\lambda} & \Lambda^{\gamma,\gamma} \end{pmatrix}_0 \begin{pmatrix} \delta \mathbf{V} \\ \delta \boldsymbol{\lambda} \\ \delta \boldsymbol{\gamma} \end{pmatrix} = - \begin{pmatrix} \mathbf{G}^V \\ \mathbf{G}^\lambda \\ \mathbf{G}^\gamma \end{pmatrix}_0 \quad (3-15)$$

Here $\Lambda_{i,j}^{V,V} = \frac{\partial^2 \Lambda}{\partial V_i \partial V_j}$, $\Lambda_{i,j}^{V,\lambda} = \frac{\partial^2 \Lambda}{\partial V_i \partial \lambda_j}$, and *etc.*; $\mathbf{V} = \mathbf{V}^0 + \delta \mathbf{V}$, $\boldsymbol{\lambda} = \boldsymbol{\lambda}^0 + \delta \boldsymbol{\lambda}$, and

$\boldsymbol{\gamma} = \boldsymbol{\gamma}^0 + \delta \boldsymbol{\gamma}$; and the superscript 0, which we will suppress when no confusion will

result, indicates that the quantities are evaluated at the current, as opposed to the

displaced, ‘point’. The gradients are given by

$$\begin{pmatrix} \mathbf{G}^V \\ \mathbf{G}^\lambda \end{pmatrix} = \begin{pmatrix} \mathbf{W}^{lsq^\dagger} \mathbf{W}^{lsq} + t\mathbf{I} & \mathbf{W}^{ex^\dagger} \\ \mathbf{W}^{ex} & \mathbf{0} \end{pmatrix} \begin{pmatrix} \mathbf{V} \\ \boldsymbol{\lambda} \end{pmatrix} - \begin{pmatrix} \mathbf{W}^{lsq^\dagger} \mathbf{L}^{(ab),lsq} \\ \mathbf{L}^{(ab),ex} \end{pmatrix} + \begin{pmatrix} \overline{\mathbf{G}}^V \\ \mathbf{0} \end{pmatrix} \quad (3-16)$$

and

$$G_j^\gamma = [\mathbf{L}^{(m),lsq} - \mathbf{L}^{(ab),lsq}] \frac{\partial \mathbf{W}^{lsq}}{\partial \gamma_j} \mathbf{V} + \lambda^\dagger \frac{\partial \mathbf{W}^{ex}}{\partial \gamma_j} \mathbf{V} \quad (3-17)$$

where

$$\bar{\mathbf{G}}_j^V = \mathbf{V}^\dagger \frac{\partial (\mathbf{W}^{lsq})^\dagger}{\partial V_j} (\mathbf{L}^{(m),lsq} - \mathbf{L}^{(ab),lsq}) + \mathbf{V}^\dagger \frac{\partial (\mathbf{W}^{ex})^\dagger}{\partial V_j} \boldsymbol{\lambda} \quad (3-18)$$

In eqs. (3-16), (3-17) and (3-18), we have partitioned the *exact* and *least squares* equations, writing

$$\mathbf{L}^{(ab)} = \begin{pmatrix} \mathbf{L}^{(ab),lsq} \\ \mathbf{L}^{(ab),ex} \end{pmatrix} \quad \text{and} \quad \mathbf{W} = \begin{pmatrix} \mathbf{W}^{lsq} \\ \mathbf{W}^{ex} \end{pmatrix} \quad (3-19)$$

where $\mathbf{L}^{(ab),lsq}$ (\mathbf{W}^{lsq}) is a vector (matrix) of length (size) N^{lsq} ($N^{lsq} \times N^c$) and $\mathbf{L}^{(ab),ex}$ (\mathbf{W}^{ex}) is a vector (matrix) of length (size) N^{ex} ($N^{ex} \times N^c$). Note that \mathbf{W} has an explicit γ -dependence through the $p^{(n)}$ and an implicit γ -dependence through the \mathbf{d}^J , that is:

$$\begin{aligned} \frac{\partial W_{n,I,J,j,l}}{\partial \gamma_k} &= \mathbf{d}^{I^\dagger}(\mathbf{R}_n) \mathbf{B}^{u(l),v(l)} \mathbf{d}^J(\mathbf{R}_n) \left[\frac{\partial}{\partial \gamma_k} \nabla_j p^{(l)}(\mathbf{R}_n) \right] + \\ &\left[\frac{\partial \mathbf{d}^{I^\dagger}(\mathbf{R}_n)}{\partial \gamma_k} \mathbf{B}^{u(l),v(l)} \mathbf{d}^J(\mathbf{R}_n) + \mathbf{d}^{I^\dagger}(\mathbf{R}_n) \mathbf{B}^{u(l),v(l)} \frac{\partial \mathbf{d}^J(\mathbf{R}_n)}{\partial \gamma_k} \right] \left[\nabla_j p^{(l)}(\mathbf{R}_n) \right] \end{aligned} \quad (3-20)$$

whereas, from eqs. (3-12) (3-13), \mathbf{W} , has only an implicit V -dependence through the \mathbf{d}^J , that is

$$\frac{\partial W_{n,I,J,j,l}}{\partial V_k} = \left[\frac{\partial \mathbf{d}^{I^\dagger}(\mathbf{R}_n)}{\partial V_k} \mathbf{B}^{u(l),v(l)} \mathbf{d}^J(\mathbf{R}_n) + \mathbf{d}^{I^\dagger}(\mathbf{R}_n) \mathbf{B}^{u(l),v(l)} \frac{\partial \mathbf{d}^J(\mathbf{R}_n)}{\partial V_k} \right] \left[\nabla_j p^{(l)}(\mathbf{R}_n) \right] \quad (3-21)$$

Here and below we suppress the superscripts *ex* and *lsq* when no confusion will result. The evaluation of $\partial^2 \Lambda / \partial z_i \partial z_j$ is discussed in Appendix 3.6.2. The appearance of terms like $\partial \mathbf{d}^{I^\dagger}(\mathbf{R}_n) / \partial V_k$, might appear to preclude accurate description of the immediate vicinity of a conical intersection. However we show in Appendix 3.6.3, where the evaluation of $\partial \mathbf{d}^{I^\dagger}(\mathbf{R}_n) / \partial \gamma_k$ and $\partial \mathbf{d}^{I^\dagger}(\mathbf{R}_n) / \partial V_k$ is discussed, that this is emphatically not the case, although it is by no means a trivial matter. Finally, note that $\bar{\mathbf{G}}^V$ contains only terms that arise from the implicit V -dependence of \mathbf{W} .

3.3.3 Original Algorithm

There are several ways to use these results to obtain a viable \mathbf{H}^d . Our previous work^{30, 61} has been restricted to the determination of the linear parameters, the V_i , with the γ_j fixed, using

$$\begin{pmatrix} \mathbf{W}^{lsq^\dagger} \mathbf{W}^{lsq} + t\mathbf{I} & \mathbf{W}^{ex^\dagger} \\ \mathbf{W}^{ex} & 0 \end{pmatrix} \begin{pmatrix} \mathbf{V} \\ \boldsymbol{\lambda} \end{pmatrix} = \begin{pmatrix} \mathbf{W}^{lsq^\dagger} \mathbf{L}^{(ab),lsq} \\ \mathbf{L}^{(ab),ex} \end{pmatrix} \quad (3-22)$$

which is obtained from eq. (3-16), by neglecting $\bar{\mathbf{G}}^V$, which as we note in Appendix 3.6.2 is expected to be small when an approximate solution has been achieved. While an approximation to the more complete Newton-Raphson result in eq. (3-15), eq. (3-22) is comparatively straightforward to formulate and solve. The \mathbf{V} obtained from this system of linear equations reproduce well, the *ab initio* data.^{30, 61-62} These equations must be solved iteratively since the $\mathbf{d}^J(\mathbf{R}_n)$ are required to determine the V_i and conversely.

3.3.4 Newton Raphson equations

We now turn to the use of the Newton Raphson equations. Given the occurrence of $\frac{\partial \mathbf{d}^{I^\dagger}(\mathbf{R}_n)}{\partial V_k}$ and the importance of conical intersections the full Newton-Raphson equations must be used with some care. Appendices 3.6.2, 3.6.3 and 3.6.4 address many technical issues in this regard.

(i) Linear terms, \mathbf{V}

In general, eq. (3-22) converges rapidly to a unique solution as long as N^c is relatively small. However for more elaborate representations, larger N^c , the \mathbf{V} determined from this equation provide a minimum in the root mean square energy error,

with a modest residual gradient.⁶⁰ In this work, to go beyond eq. (3-22), we introduce an economical approximation to the full second order procedure for the linear terms

$$(\mathbf{M})_0 \begin{pmatrix} \delta \mathbf{V} \\ \delta \boldsymbol{\lambda} \end{pmatrix} = - \begin{pmatrix} \mathbf{G}^V \\ \mathbf{G}^\lambda \end{pmatrix}_0 \quad (3-23)$$

where

$$\mathbf{M} = \begin{pmatrix} \boldsymbol{\Lambda}^{V,V} & \boldsymbol{\Lambda}^{V,\lambda} \\ \boldsymbol{\Lambda}^{\lambda,V} & \mathbf{0} \end{pmatrix} \quad (3-24)$$

The approximate Hessian is discussed in Appendices 3.6.2 and 3.6.3. The solution to eq. (3-23) is discussed in Appendix 3.6.4.

(ii) Nonlinear terms, γ

Finally we turn to the issue of optimizing the nonlinear parameters, parameters whose principal purpose, see Appendix 3.6.1, is to distribute the basic monomials, $g_l(\mathbf{R})$, throughout coordinate space. This is accomplished using the full Newton-Raphson equations, eqs. (3-15). Again the approximate Hessian is described in Appendices 3.6.2 and 3.6.3. Here it is only important to emphasize the need to have good starting values for the linear parameters before the nonlinear terms are optimized.

3.4 Computational Results

The coupled adiabatic potential energy surfaces considered in this study describe the $1,2^1A$ states of NH_3 . The subspace of the full 6-dimensional nuclear coordinate space described by \mathbf{H}^d is relevant to the well studied photodissociation reaction given in (3-1). This reflects the fact that the preponderance of the \mathbf{R}_n used to define \mathbf{H}^d were obtained from nonadiabatic surface hopping trajectories with initial conditions appropriate for reaction (3-1). A three dimensional plot of the adiabatic potential energy surfaces for

the $1,2^1A$ states evincing the ground state minimum, the minimum and saddle point on the 2^1A potential energy surface and the minimum energy point of conical intersection, is provided in Figure 3-1. Although at first glance this might appear to be a relatively straightforward computational problem, that turns out not to be the case. The \mathbf{H}^d must accurately describe: (i) an extended 4 dimensional seam of conical intersection, for which points well removed from the minimum energy crossing point are accessible and likely to be relevant to the nonadiabatic photodissociation; (ii) a highly anharmonic minimum for the \tilde{A} state with a low barrier separating the region of the minimum from that of the seam of conical intersections; and (iii) a ground state potential energy surface that must be well described over an energy range of ~ 6 eV while insuring that the representation is sufficiently diabatic to be suitable for quantum dynamics.

Previously we have constructed, using eq. (3-22), an \mathbf{H}^d intended for use in describing reaction (3-1).³⁰ The electronic structure description of the $1,2^1A$ states of NH_3 , multireference configuration interaction wave functions comprised of over 30×10^6 CSFs and the form of \mathbf{H}^d , which consisted of over 9000 linear terms defined by a total of over 27,000 energies, energy gradients and derivative couplings, is presented in Ref. ³⁰. This \mathbf{H}^d was shown to provide an excellent representation of the *ab initio* data from which it was constructed.³⁰ The utility of \mathbf{H}^d for describing reaction (3-1) was tested by a fully quantum mechanical, 6 dimensional simulation of the v_2 progression in the $\tilde{A} \leftarrow \tilde{X}$ absorption spectrum of NH_3 , including the line positions, intensities and line widths. Although this spectrum had proven difficult to simulate previously,⁵⁴ excellent agreement with the experimental results was found.⁶⁰

In this work our goals are two-fold, (i) to establish the utility of the Newton-Raphson approach in eq. (3-23) in systems with conical intersections, and determine the potential benefits compared to the use of eq. (3-22) and (ii) to assess and illustrate the diabaticity of the derived diabatic representation.

3.4.1 Derivative Couplings

As noted previously the goal of the transformation to diabatic states is to minimize the derivative coupling in the diabatic representation, $\langle \Psi_\alpha^d(\mathbf{q}; \mathbf{R}) | \nabla_k \Psi_\beta^d(\mathbf{q}; \mathbf{R}) \rangle_{\mathbf{q}}$, which is evaluated in terms of the residual derivative coupling as follows. Using the definition the adiabatic derivative coupling

$$f_k^{a,I,J,(ab)}(\mathbf{R}) \equiv \langle \Psi_I^{a,(ab)}(\mathbf{q}; \mathbf{R}) | \nabla_k \Psi_J^{a,(ab)}(\mathbf{q}; \mathbf{R}) \rangle_{\mathbf{q}} \quad (3-25)$$

from eqs. (3-4), (3-5) and their derivatives, we obtain

$$f_k^{a,I,J,(ab)}(\mathbf{R}) = \sum_{\alpha=1}^{N^{state}} d_\alpha^I(\mathbf{R}) \nabla_k \mathbf{d}_\alpha^J(\mathbf{R}) + \sum_{\alpha,\beta=1}^{N^{state}} d_\alpha^I(\mathbf{R}) \langle \Psi_\alpha^d(\mathbf{q}; \mathbf{R}) | \nabla_k \Psi_\beta^d(\mathbf{q}; \mathbf{R}) \rangle_{\mathbf{q}} d_\beta^J(\mathbf{R}) \quad (3-26)$$

$$\approx \sum_{\alpha=1}^{N^{state}} d_\alpha^I(\mathbf{R}) \nabla_k \mathbf{d}_\alpha^J(\mathbf{R}) = \frac{\mathbf{d}^I(\mathbf{R})^\dagger (\nabla_k \mathbf{H}^d) \mathbf{d}^J(\mathbf{R})}{E^{a,J,(m)}(\mathbf{R}) - E^{a,I,(m)}(\mathbf{R})} \equiv f_k^{a,I,J,(m)}(\mathbf{R}) \quad (3-27)$$

The approximate equality in eq. (3-27) comes from neglecting the second term in eq. (3-26), the derivative coupling due to the quasi-diabatic states Ψ_u^d . The use of eq. (3-5) to define the quasi-diabatic states guarantees that, in principle, the diabatic states can reproduce the adiabatic energies. The question is how diabatic is the transformation. This is determined from eqs. (3-26) and (3-27), from which for $1 \leq I < J \leq N^{state}$, the residual derivative coupling, $\delta f_k^{a,I,J}(\mathbf{R}) \equiv f_k^{a,I,J,(ab)}(\mathbf{R}) - f_k^{a,I,J,(m)}(\mathbf{R})$ is related to the

quasi-diabatic state coupling, $\langle \Psi_\alpha^d(\mathbf{q}; \mathbf{R}) | \nabla_k \Psi_\beta^d(\mathbf{q}; \mathbf{R}) \rangle_{\mathbf{q}}$ by the following system of linear equations

$$\begin{aligned} \delta f_k^{a,I,J}(\mathbf{R}) &= \sum_{\alpha,\beta=1}^{N^{state}} d_\alpha^I(\mathbf{R}) \langle \Psi_\alpha^d(\mathbf{q}; \mathbf{R}) | \nabla_k \Psi_\beta^d(\mathbf{q}; \mathbf{R}) \rangle_{\mathbf{q}} d_\beta^J(\mathbf{R}) \\ &= \sum_{1 \leq \alpha < \beta \leq N^{state}} [d_\alpha^I(\mathbf{R}) d_\beta^J(\mathbf{R}) - d_\beta^I(\mathbf{R}) d_\alpha^J(\mathbf{R})] \langle \Psi_\alpha^d(\mathbf{q}; \mathbf{R}) | \nabla_k \Psi_\beta^d(\mathbf{q}; \mathbf{R}) \rangle_{\mathbf{q}} \end{aligned} \quad (3-28)$$

For the $N^{state} = 2$ case considered here eq. (3-28) reduces to a simple appealing result:

$$\delta f_k^{a,1,2}(\mathbf{R}) = \langle \Psi_1^d(\mathbf{q}; \mathbf{R}) | \nabla_k \Psi_2^d(\mathbf{q}; \mathbf{R}) \rangle_{\mathbf{q}} \quad (3-29)$$

For a general case where N^{state} is arbitrary, we can rewrite the first equality in eq. (3-28) in a matrix form:

$$\Delta \mathbf{F}_k = \mathbf{D} \mathbf{F}_k^{(d)} \mathbf{D}^\dagger, \quad (3-30)$$

where

$$(\Delta \mathbf{F}_k)_{I,J} = \delta f_k^{a,I,J}(\mathbf{R}), \quad (\mathbf{F}_k^{(d)})_{\alpha,\beta} \equiv \langle \Psi_\alpha^d(\mathbf{q}; \mathbf{R}) | \nabla_k \Psi_\beta^d(\mathbf{q}; \mathbf{R}) \rangle_{\mathbf{q}}, \quad \mathbf{D}_{I,J} = d_J^I(\mathbf{R})$$

Since the diabatic-to-adiabatic transformation is an orthogonal transformation, the Frobenius norm of each component of the quasi-diabatic state coupling matrix is unchanged by the two transformations on its left and right side in eq. (3-30), giving

$$\begin{aligned} \|\Delta \mathbf{F}_k\|_F &= \|\mathbf{F}_k^{(d)}\|_F \\ \sum_{I,J}^{N^{states}} \left[\delta f_k^{a,I,J}(\mathbf{R}) \right]^2 &= \sum_{I,J}^{N^{states}} \left\langle \Psi_I^d(\mathbf{q}; \mathbf{R}) | \nabla_k \Psi_J^d(\mathbf{q}; \mathbf{R}) \right\rangle_{\mathbf{q}}^2 \end{aligned} \quad (3-31)$$

That is, for any given point and a given component, the total amount of couplings between quasi-diabatic states is the same as the total amount of residual couplings. Thus, in any scenario, the magnitude $\|\delta \mathbf{f}^{a,I,J}(\mathbf{R})\|$ is a direct measure of the quality of the quasi-

diabatic representation. For a rigorous diabatic basis, $\delta\mathbf{f}^{a,I,J}(\mathbf{R})$, would vanish globally. As noted above this is not possible here.

Two comments concerning the derivative coupling are in order. The *ab initio* determined derivative couplings cannot be described exactly in the current approach since the nonremovable part of the derivative coupling, cannot be described by a square *truncated* representation such as the one we use.⁶ This contribution becomes part of the residual coupling. As we will see below, this contribution is small compared to the removable part, where the energy separation of the adiabatic states is small. When the energy separation is large, although the residual coupling is an appreciable fraction of the actual coupling, neither is significant. In dissociation channels where the total derivative coupling can become small, as noted below, care must be taken to avoid including the nonremovable part.³⁰ The second point concerns the fact that the derivative couplings determined from \mathbf{H}^d are necessarily due to internal coordinates only. However the *ab initio* determined derivative couplings include contributions from overall rotations and translations. These contributions, are not a problem, in principle, since they can be represented as electronic matrix elements of the form $\langle \Psi_I^{a,(ab)} | O^{el} | \Psi_J^{a,(ab)} \rangle$, where O^{el} is the total electronic gradient or total orbital angular momentum operator.⁶³ One must only be careful to remove these contributions from $\mathbf{f}^{a,I,J,(ab)}(\mathbf{R})$ prior to the fitting.

3.4.2 Newton-Raphson equations

In this section we consider using eq. (3-23) to improve the result obtained from eq. (3-22). Table 3-1 reports the RMS errors in the energies, energy gradients and derivative couplings obtained using eq. (3-22) and eq. (3-23). Also tabulated are the

initial and final values of the norm of the gradient of Λ . From Table 3-1 it is seen that use of eq. (3-23) reduces the root mean square (RMS) energy (energy gradient percentage error) from 77 cm^{-1} (2.3%) to 33 cm^{-1} (1.1%) while the magnitude of the gradient, the right hand side of eq. (3-23), is reduced by a factor of 8, with, we emphasize, no change in the functional form. A reduction of the RMS energy error of this size by increasing the number of terms in the expansion is a not a simple matter. Here the percent error is defined as the magnitude of the error divided by magnitude of the *ab initio* quantity. As seen in Table 3-1 similar improvements are found for the derivative couplings whose magnitudes are within the range 1-10. The absence of improvement for the derivative couplings with magnitudes > 10 reflects the fact that the corresponding nuclear configurations are nodes, so that these derivative couplings are already fit 'exactly'. Derivative couplings with magnitudes < 1 , as we illustrate below, occur in regions where the energy separation of the adiabatic states is large and therefore are of no dynamical consequence.

A more careful analysis of the improvement is provided in Figure 3-2 which plots the magnitude of the relative error for the norm of the energy gradient for each state against the norm of that quantity at each of the ~ 2500 nuclear configurations. Figure 3-3 reports similar results for the derivative couplings. In these figures, the red (black) dots show the results for eq. (3-23) (eq. (3-22)). For clarity the data is presented twice, once with the red dots over the black dots and conversely. Despite the fact that a log scale is required to represent the range of data, the significant improvement for gradients on the order of 10^{-3} and elimination of outliers is evident.

Table 3-1. RMS errors for \mathbf{H}^d determined from eqs. (3-22) and (3-23).

	Eq. (3-22)	Eq. (3-23)
Energy (cm^{-1})	77.0	33.2
Energy Gradients (%)	2.33	1.14
Derivative Couplings(%)		
$\ f\ > 10$ (192 points)	0.594	0.570
$\ f\ > 1$ (612 points)	7.43	4.71
Norm of Lagrangian Gradient	4.29×10^{-2}	6.04×10^{-3}

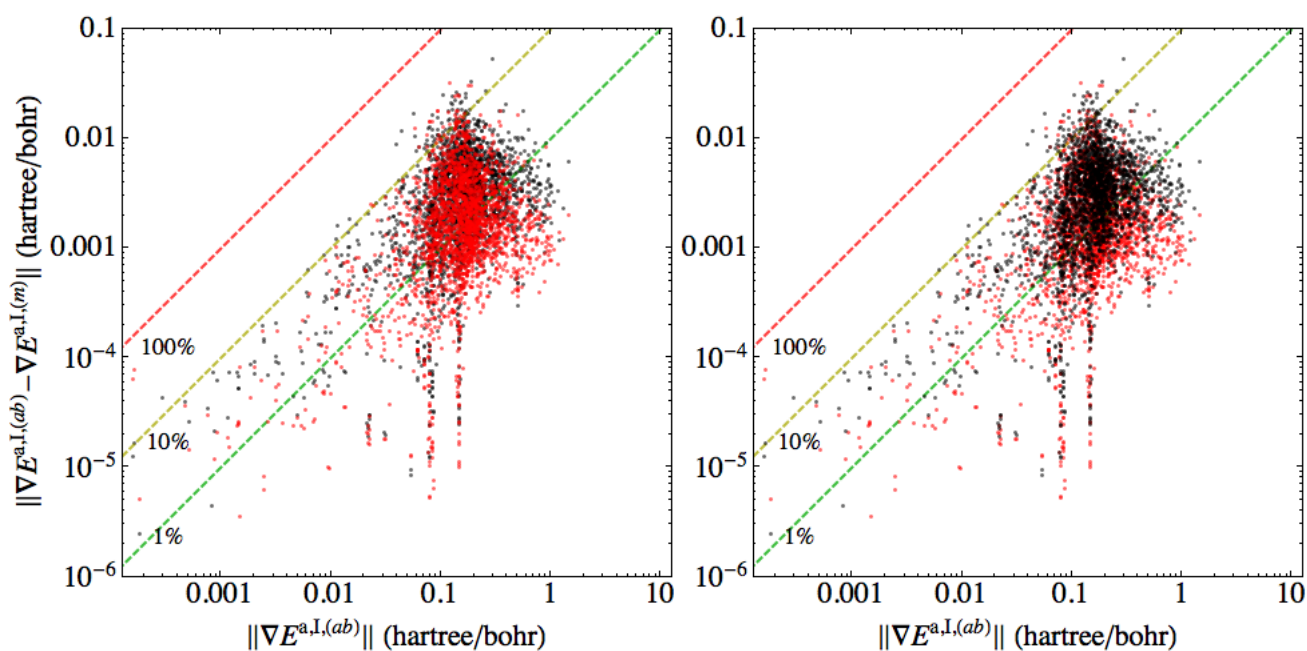


Figure 3-2. Plot comparing the accuracy of \mathbf{H}^d constructed from eq. (3-22), black dot and eq. (3-23), red dots. Magnitude of residual energy gradient plotted against the magnitude of the energy gradient. These two figure are plotted from the same data. Left: Red on top; Right: Black on top.

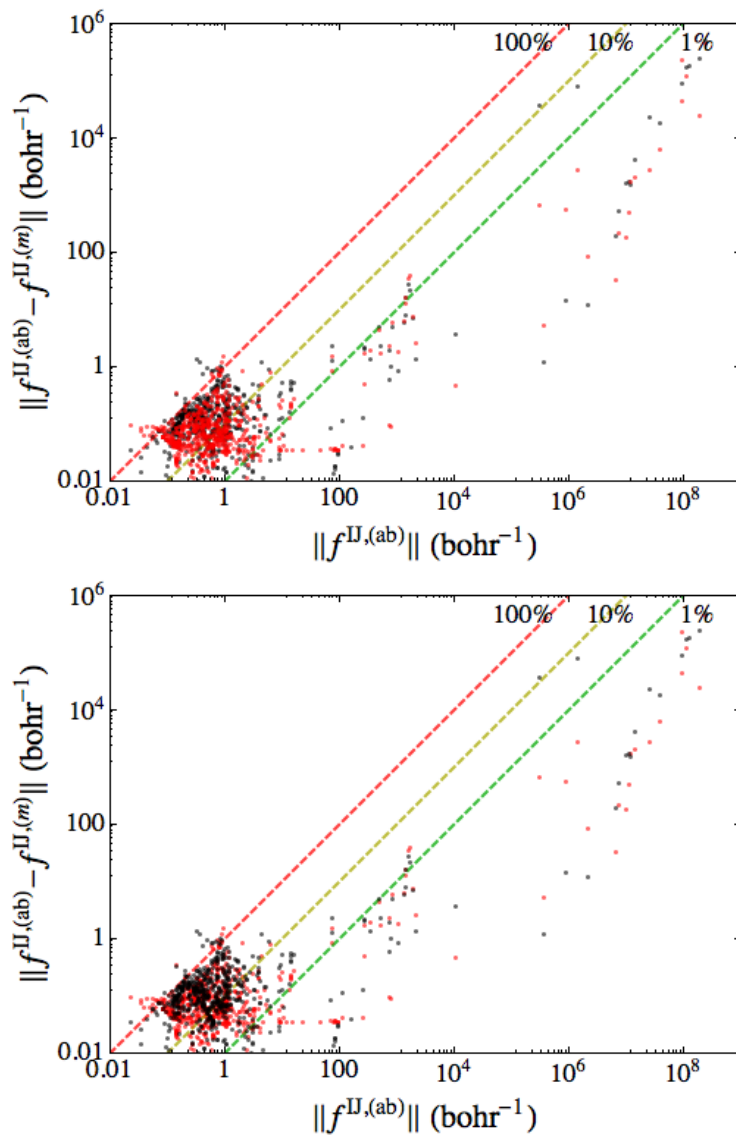


Figure 3-3. Plot comparing the accuracy of \mathbf{H}^d constructed from eq. (3-22), black dot and eq. (3-23), red dots. Magnitude of residual derivative coupling plotted against the magnitude of the derivative coupling.

Table 3-2 considers how the reduction of residual gradient in eq. (3-23) is reflected in the key stationary points on the $1,2^1A$ potential energy surfaces. These stationary points are taken as nodes so that the locations and vanishing of the gradients are not an issue. We are only concerned here with the harmonic frequencies. Table 3-2 addresses this issue, comparing the frequencies obtained from the \mathbf{H}^d determined from

eq. (3-22) and from eq. (3-23) with the *ab initio* results and reporting the corresponding unsigned error. From Table 3-2 it is seen that although some frequencies actually deteriorate slightly using eq. (3-23), the preponderance of the errors, which are generally not large to begin with, are reduced by factors of 2, 3 or more, with some of the large unsigned errors for NH₂ showing dramatic improvement.

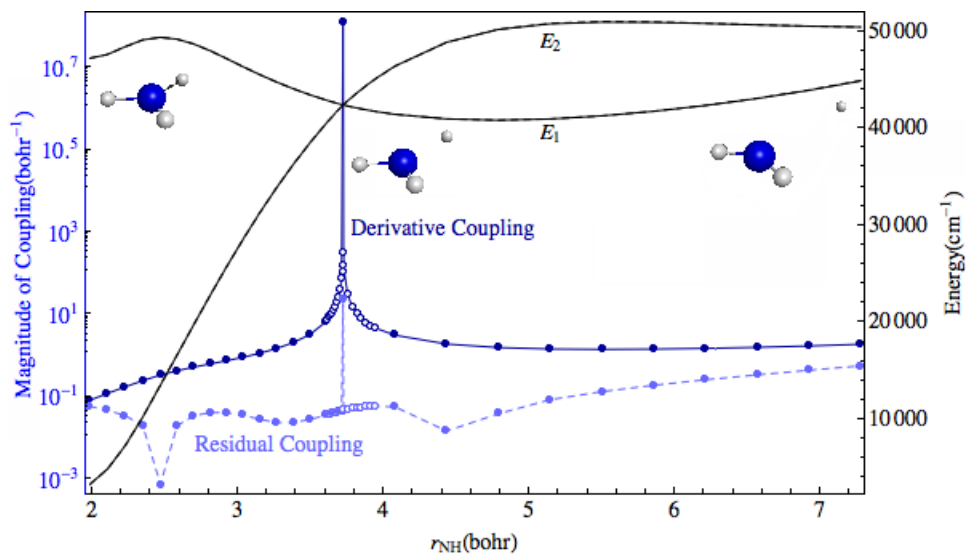
Table 3-2 \mathbf{H}^d and *ab initio* determined frequencies and their unsigned errors (Uerror) at extrema. |Err| is the magnitude of the difference between the \mathbf{H}^d and *ab initio* determined quantity. All quantities in cm⁻¹.

Extremum	Mode	<i>Ab initio</i>	Eq. (3-22)	 Err 	Eq. (3-23)	 Err
NH₃($\tilde{\chi}$ min)	1	3456.26	3447.08	9.18	3450.70	5.56
	2	1066.24	1093.12	26.88	1077.63	11.39
	3	3584.10	3581.40	2.70	3578.64	5.46
	4	1674.48	1655.33	19.15	1659.96	14.52
NH₃($\tilde{\chi}$ ts)	1	3620.10	3610.00	10.10	3609.06	11.04
	2	870.00 <i>i</i>	847.10 <i>i</i>	22.90 <i>i</i>	858.13 <i>i</i>	11.87 <i>i</i>
	3	3830.50	3825.20	5.30	3826.79	3.71
	4	1584.00	1575.50	8.50	1589.97	5.97
NH₃(\tilde{A} min)	1	2793.70	2838.70	45.00	2787.11	6.59
	2	754.10	780.70	26.60	782.55	28.45
	3	2955.80	2949.70	6.10	2953.72	2.08
	4	1334.30	1377.70	43.40	1334.47	0.17
NH₃(\tilde{A} ts)	1	2003.32 <i>i</i>	-2000.10 <i>i</i>	3.22 <i>i</i>	-2001.21 <i>i</i>	2.11 <i>i</i>
	2	475.29	508.05	32.76	463.68	11.61
	3	962.68	981.30	18.62	979.28	16.60
	4	1435.37	1419.51	15.86	1428.94	6.43
	5	3027.80	2995.81	31.99	3011.68	16.12
	6	3244.42	3231.10	13.32	3239.08	5.34
NH₂($\tilde{\chi}$ min)	1	3350.23	2934.62	415.61	3415.15	64.92
	2	1539.57	1556.79	17.22	1563.71	24.14
	3	3443.40	3427.33	16.07	3498.00	54.60
NH₂(\tilde{A} min)	1	3612.56	3796.34	183.78	3683.38	70.82
	2	978.14	935.75	42.39	992.28	14.14
	3	3924.56	4154.31	229.75	3971.20	46.64

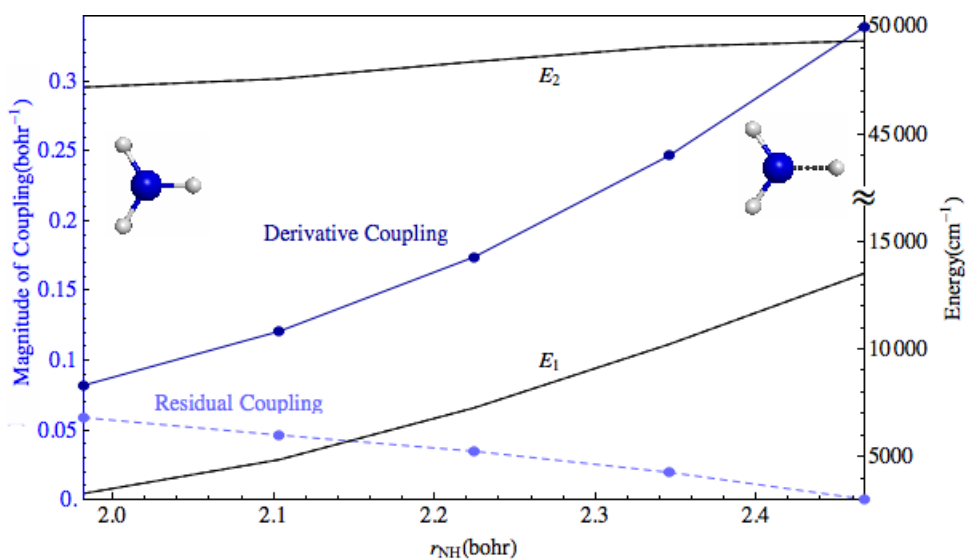
3.4.3 The Diabatic Character of the Representation

One of the principal advantages of the present approach is that it directly addresses the quality of the diabatic representation by quantifying the residual coupling. In this section, we juxtapose the residual derivative coupling with the adiabatic energies to illustrate the quality of the constructed diabatic representation. Particular attention is paid to the quality of the diabatization near conical intersections.

The quality of the diabatic representation obtained by the method used in this work is addressed in Figure 3-4 to Figure 3-7, which report the *ab initio* determined adiabatic energies $E^{a,I,(ab)}$, $E^{a,J,(ab)}$, solid lines, and \mathbf{H}^d determined adiabatic energies $E^{a,I,(m)}$, $E^{a,J,(m)}$, dashed lines, together with $\|\mathbf{f}^{a,I,J,(ab)}(\mathbf{R})\|$, $\|\delta\mathbf{f}^{a,I,J}(\mathbf{R})\|$ along several paths or in regions. In these figures the points denoted by filled (open) circles were included (not included) in the \mathbf{R}_n used to construct \mathbf{H}^d . Below we will refer to the included \mathbf{R}_n as members of the fit data set and the \mathbf{R}_n not included as interpolated points. Note that except for Figure 3-7, where differences are observed at high energies, the *ab initio* and \mathbf{H}^d determined adiabatic energies are indistinguishable on the scale of the plots.

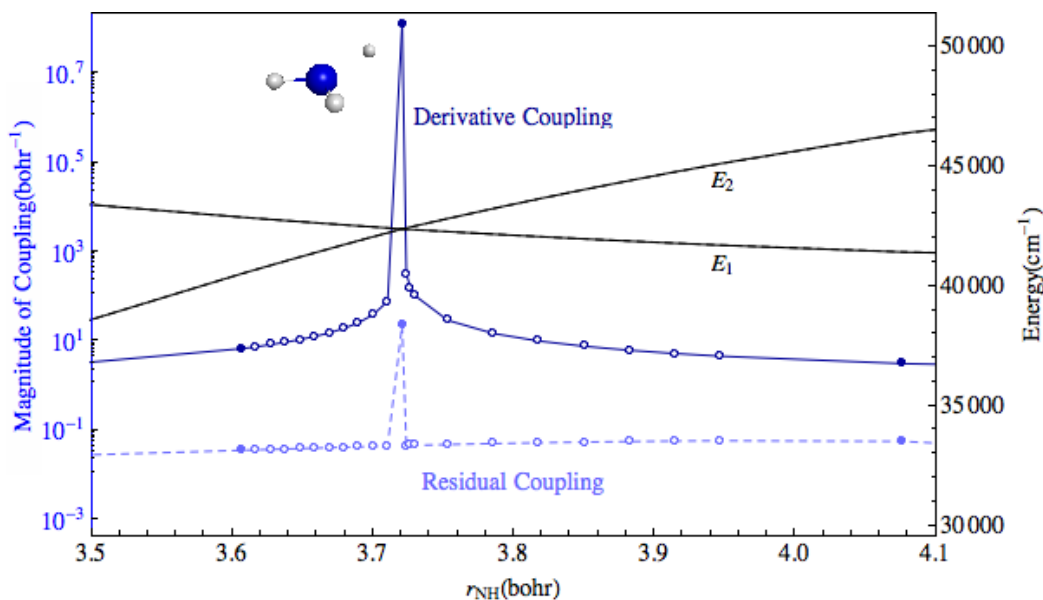


(a) Global dissociation path



(b) Path from the \tilde{A} state minimum to the \tilde{A} state saddle point

Figure 3-4. Plot of energies $E^{a,I,(ab)}$, $E^{a,J,(ab)}$ (black, solid lines) $E^{a,I,(m)}$, $E^{a,J,(m)}$ (black dashed lines) derivative couplings $\|\mathbf{f}^{a,I,J,(ab)}\|$ (dark blue, solid lines) and residual coupling $\|\delta\mathbf{f}^{a,I,J}\|$ (light blue, dashed lines) as a function of R(N-H) along a dissociative path which is the union of points connecting the \tilde{A} state minimum to the \tilde{A} state saddle point; the \tilde{A} state saddle point to the minimum energy crossing (MEX) point; and the MEX point toward the asymptote. Plate (a) reports the global path. Plates (b) and (c) report restrictions of that path to: (b) a path from the \tilde{A} state minimum to the \tilde{A} state saddle point and (c) a path near the MEX. Filled (open) circles points included (not included) in the fit data set.



(c) Path near the Minimum Energy Crossing (MEX)

Figure 3-4. Energies, derivative couplings and residual couplings along paths.(Continued)

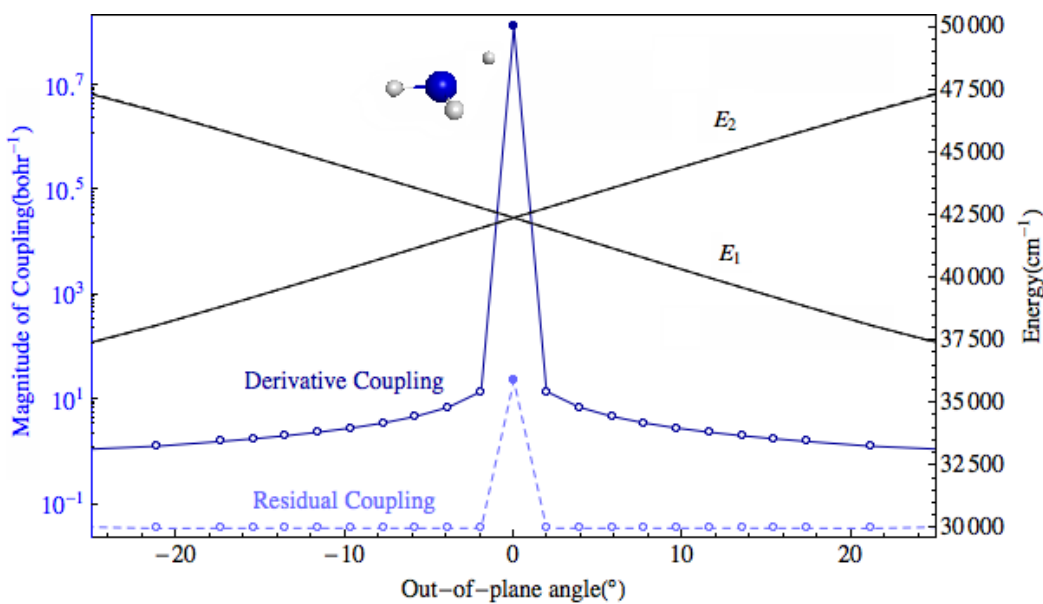


Figure 3-5. Plot of energies $E^{a,I,(ab)}$, $E^{a,J,(ab)}$ (black, solid lines) $E^{a,I,(m)}$, $E^{a,J,(m)}$ (black dashed lines), derivative couplings $\|\mathbf{f}^{a,I,J,(ab)}\|$ (dark blue, solid line) and residual coupling $\|\delta\mathbf{f}^{a,I,J}\|$ (light blue, dashed line) along a path centered at the minimum energy conical intersection as a function of the out of plane angle. Filled (open) circles are points included (not included) in the fit data set.

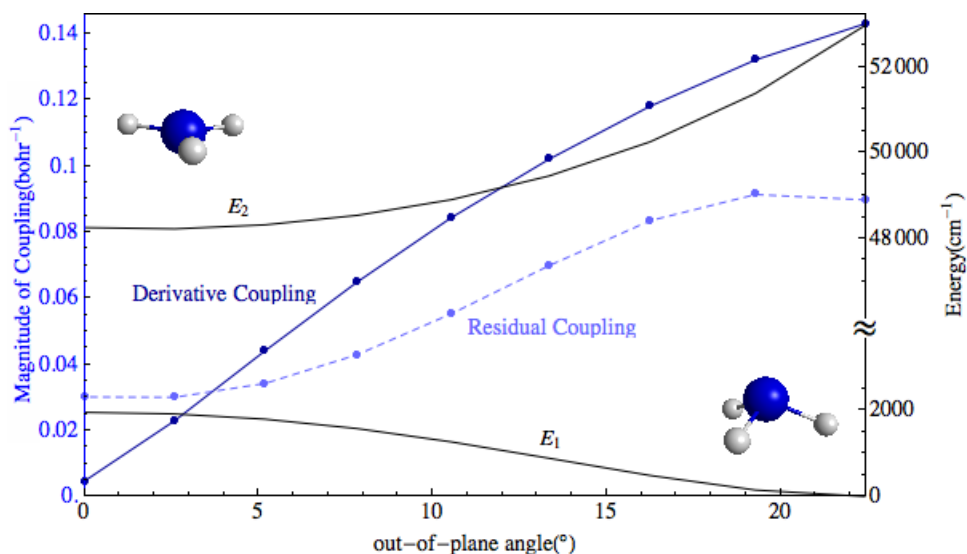


Figure 3-6. Plot of energies $E^{a,I,(ab)}$, $E^{a,J,(ab)}$ (black solid lines), $E^{a,I,(m)}$, $E^{a,J,(m)}$ (black dashed lines), derivative couplings $\|\mathbf{f}^{a,I,J,(ab)}\|$ (dark blue solid line) and residual coupling $\|\delta\mathbf{f}^{a,I,J}\|$ (light blue, dashed lines) as a function of the out of plane angle from the planar saddle point on the 1^1A potential energy surface to the ground state minimum. Filled circles points included in the fit data set.

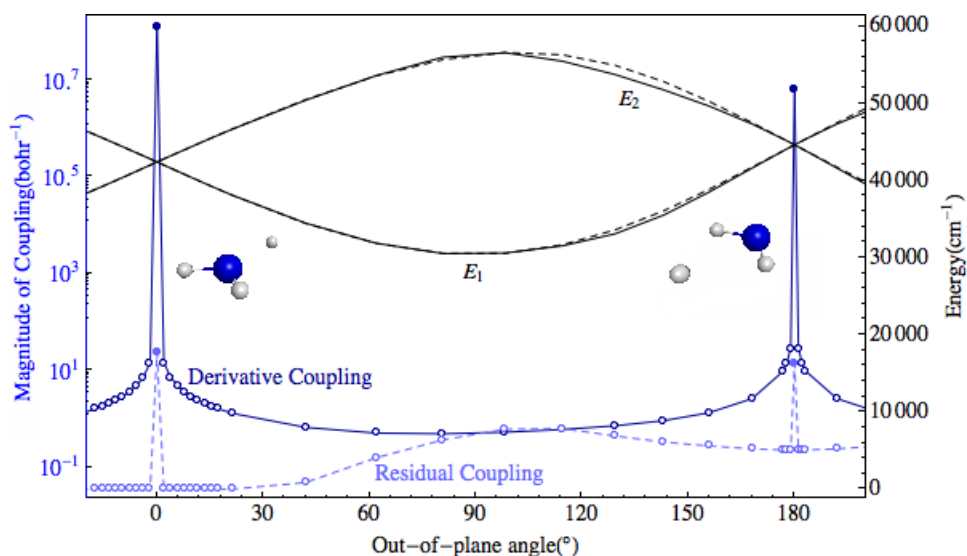


Figure 3-7. Plot of energies $E^{a,I,(ab)}$, $E^{a,J,(ab)}$ (black, solid lines) $E^{a,I,(m)}$, $E^{a,J,(m)}$ (black dashed lines), derivative couplings $\|\mathbf{f}^{a,I,J,(ab)}\|$ (dark blue, solid line) and residual coupling $\|\delta\mathbf{f}^{a,I,J}\|$ (light blue dashed lines) along a path starting from the MEX to a distinct local minimum energy conical intersection, MEX-L with a significantly different molecular structure. Filled (open) circles points included (not included) in the fit data set. The path is predominately along the out-of-plane angle, along which direction the diabatic states are coupled. Note that by moving along the mirror image of this path one can achieve a full rotation and return to the MEX .

Panels of Figure 3-4 present a path connecting the minimum energy point on the 2^1A potential energy surface to the saddle point on that surface; the saddle point to the minimum energy point on the $1,2^1A$ state conical intersection seam; and the seam point to the product channel. This path is essential for the description of the nonadiabatic photodissociation process, given by reaction (3-1). Note that the percentage error in the derivative coupling “at” the point of conical intersection is tiny with $\| \delta \mathbf{f}^{a,I,J}(\mathbf{R}) \| / \| \mathbf{f}^{a,I,J,(ab)}(\mathbf{R}) \| \sim 10^{-7}!$ Equally significant, the residual coupling remains small in the vicinity of the conical intersection. See Figure 3-4 panel (c). This is particularly gratifying since these points are interpolated points. Thus, the diabatic representation of the vicinity of the conical intersection is excellent. This is not unexpected since the points of conical intersection are treated as nodes, but the results evinced in this figure are reassuring. Focusing on the region in panel (b), the region of \tilde{A} state minimum and saddle point, the derivative coupling and the residual couplings, are seen to be small. As $R(\text{N-H})$ becomes large, a small increase in $\| \delta \mathbf{f}^{a,I,J}(\mathbf{R}) \|$ is observed which is most likely due to the nonremovable⁶ part of $\mathbf{f}^{I,J,ab}(\mathbf{R})$. $\mathbf{f}^{I,J,(m)}(\mathbf{R})$ vanishes asymptotically as required. However the nonremovable component of $\mathbf{f}^{I,J,ab}(\mathbf{R})$ persists and could lead to spurious long range coupling if it were not removed. In our surface hopping trajectories used to determine the \mathbf{R}_n no evidence of spurious exit channel hops was detected.³⁰ Figure 3-5 continues our study of the vicinity of the minimum energy conical intersection, this time as a function of the out of plane angle, starting from the (planar) minimum energy conical intersection. As in Figure 3-4, this plot indicates how accurately the conical intersection is described. Also evident in that figure is how quickly the *ab initio* derivative coupling decays as a function of the out of plane angle

and how well \mathbf{H}^d describes that change, again using interpolated points. Figure 3-6 examines another region in which nonadiabatic effects are expected to be negligible. Shown in that figure is a path connecting the C_{3v} minimum energy geometry on the ground state potential energy surface to the D_{3h} saddle point for inversion. Both the derivative coupling and the residual coupling are small as expected. Figure 3-7 presents a path, as function of the out of plane angle, connecting two points on the seam of conical intersections in distinctly different regions of nuclear coordinate space. The small residual couplings, obtained with interpolated points, in the vicinity of two distinct conical intersections is quite gratifying. These results illustrate the fact that the behavior of the derivative couplings near the minimum energy conical intersection considered in Figure 3-4 and Figure 3-5 is typical of points on the seam of conical intersection defined by \mathbf{H}^d . Taken together the results in these figures strongly support the quasi- diabatic character of \mathbf{H}^d .

Figure 3-8 presents a more global picture of the quasi diabatic representation plotting $H_{1,1}^d$, $H_{2,2}^d$ and $H_{1,2}^d$. It is interesting to observe how the region of the saddle point on the 2^1A state, a strongly avoided intersection of the 2^1A and 3^1A states, is reproduced by a single diabatic state. This region is illustrated in the figure with an arrow. Although the scale is necessarily large for $H_{1,1}^d$ and $H_{2,2}^d$ their smoothness is evident.

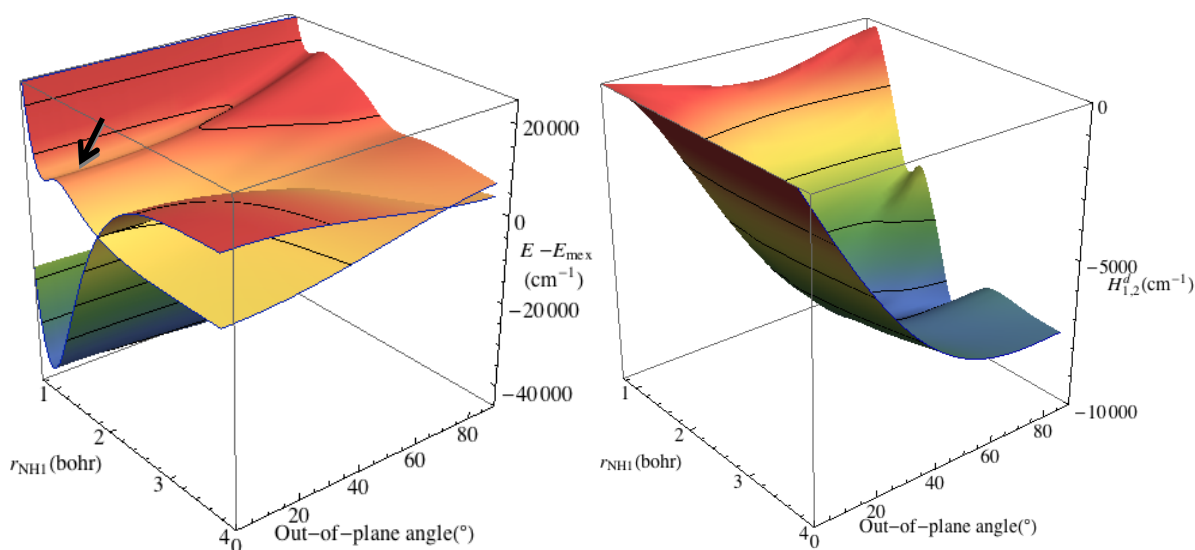


Figure 3-8. Diabatic representation as a function of R(N-H) and out-of-plane angle. Top: $H_{1,1}^d$ and $H_{2,2}^d$; Bottom: $H_{1,2}^d$

3.5 Summary and Conclusions

In this work an approximate Newton Raphson procedure is introduced which leads to a more precise quasi-diabatic representation of adiabatic potential energy surfaces coupled by conical intersections. The quasi diabatic representation uses polynomials with flexible origins to improve the description locally. The Newton-Raphson procedure will enable optimization of these origins. The properties of the derived quasi-diabatic representation are studied.

3.6 Appendices

3.6.1 Form of Single Coordinate Functions Used to Construct \mathbf{H}^d

As discussed in previous work^{28, 30} the g^I are constructed from four basic functions of the internal coordinates, w_i :

- Exponential⁶⁴ $w_1(r_{i,j}) = \exp[-s_1(r_{i,j} - r_{i,j}^{(a)})]$
- Gaussian $w_2(r_{i,j}) = \exp[-s_2(r_{i,j} - r_{i,j}^{(b)})^2]$
- Reciprocal⁶⁴ $w_3(r_{i,j}) = \exp[-s_1(r_{i,j} - r_{i,j}^{(c)})]/(r_{i,j} + r_{i,j}^{(d)})$
- Dot-Cross product¹⁵ $w_4^{i,j,k,l} = \mathbf{r}_{i,j} \times \mathbf{r}_{i,k} \cdot \mathbf{r}_{i,l} / \left| r_{i,j} r_{i,k} r_{i,l} r_{j,k} r_{j,l} r_{k,l} \right|^\alpha$

(3-32)

Gaussian functions are centered on specific origins and their values can be made to vanish quickly when stepping away from those origins. They are local basis functions that serve to describe the region near their origin. The origins, consequently, are key nonlinear parameters.

The $g_l(\mathbf{R})$ are constructed as products of the \mathbf{w} and have the following monomial form:

$$g_l(\mathbf{R}) = \prod_{m=1}^3 \prod_{1 \leq i < j \leq N^a} [w_m(r_{i,j})]^{\alpha_{m,i,j}^{(l)}} \prod_{(i,j,k,m)} [w_4^{(i,j,k,m)}]^{\beta_{i,j,k,m}^{(l)}} \quad (3-33)$$

for $1 \leq l \leq N^g$, where N^g is the size of polynomial basis. Note in eq. (3-33), (l) is a label, not an exponent, but $\alpha_{m,i,j}^{(l)}$ and $\beta_{i,j,k,m}^{(l)}$ are exponents. Here (i,j,k,m) , again a label not an exponent, denotes the allowed combinations of four atoms. The order of the monomial g_l , $o(l)$, is given by

$$o(l) = \sum_{m,i < j} \alpha_{m,i,j}^{(l)} + \sum_{m,i < j} \beta_{i,j,k,m}^{(l)} \quad (3-34)$$

The choice of $\alpha_{m,i,j}^{(l)}$ and $\beta_{i,j,k,m}^{(l)}$, which are introduced in eq. (3-32), is in principle arbitrary. Increases in $\alpha_{m,i,j}^{(n)}$ and $\beta_{i,j,k,m}^{(n)}$ are used to reduce the error in the representation of the adiabatic data, at the expense of a larger N^g . In previous work the nonlinear parameters s_j , α , $r_{i,j}^{(a(i,j))}$, $r_{i,j}^{(b(i,j))}$, $r_{i,j}^{(c(i,j))}$ and $r_{i,j}^{(d(i,j))}$, were determined by trial and error in

the range $s_j > 0$, $r_{i,j}^{(x_i,j)} > 0$ and $\alpha > 1/2$. The approach introduced here will be used, in future work, to determine optimal values of these quantities.

3.6.2 Second derivatives of Unknown Coefficients

Through straightforward but tedious algebra the first and second derivatives with respect to V_j , λ_j and γ_j can be determined by differentiating eq. (3-14). For the gradients we find

$$\frac{\partial \Lambda}{\partial x} = \left[\mathbf{L}^{(m),lsq} - \mathbf{L}^{(ab),lsq} \right]^\dagger \frac{\partial \mathbf{L}^{(m),lsq}}{\partial x} + \left[\mathbf{L}^{(m),ex} - \mathbf{L}^{(ab),ex} \right]^\dagger \frac{\partial \lambda}{\partial x} + \frac{\partial \left(\mathbf{L}^{(m),ex} \right)^\dagger}{\partial x} \lambda + t \mathbf{V}^\dagger \frac{\partial \mathbf{V}}{\partial x} \quad (3-35)$$

and then for the second derivatives

$$\begin{aligned} \frac{\partial^2 \Lambda}{\partial x \partial y} &= \frac{\partial \mathbf{L}^{(m),lsq \dagger}}{\partial y} \frac{\partial \mathbf{L}^{(m),lsq}}{\partial x} + \left[\mathbf{L}^{(m),lsq} - \mathbf{L}^{(ab),lsq} \right]^\dagger \frac{\partial^2 \mathbf{L}^{(m),lsq}}{\partial x \partial y} + \frac{\partial \mathbf{L}^{(m),ex \dagger}}{\partial x} \frac{\partial \lambda}{\partial y} + \frac{\partial \mathbf{L}^{(m),ex \dagger}}{\partial y} \frac{\partial \lambda}{\partial x} \\ &+ \left[\mathbf{L}^{(m),ex} - \mathbf{L}^{(ab),ex} \right]^\dagger \frac{\partial^2 \lambda}{\partial x \partial y} + \frac{\partial^2 \mathbf{L}^{(m),ex \dagger}}{\partial x \partial y} \lambda + t \mathbf{V}^\dagger \frac{\partial^2 \mathbf{V}}{\partial x \partial y} + t \frac{\partial \mathbf{V}^\dagger}{\partial y} \frac{\partial \mathbf{V}}{\partial x} \\ &= \frac{\partial \mathbf{L}^{(m),lsq \dagger}}{\partial y} \frac{\partial \mathbf{L}^{(m),lsq}}{\partial x} + \frac{\partial \mathbf{L}^{(m),ex \dagger}}{\partial x} \frac{\partial \lambda}{\partial y} + \frac{\partial \mathbf{L}^{(m),ex \dagger}}{\partial y} \frac{\partial \lambda}{\partial x} + \frac{\partial^2 \mathbf{L}^{(m),ex \dagger}}{\partial x \partial y} \lambda + t \frac{\partial \mathbf{V}^\dagger}{\partial y} \frac{\partial \mathbf{V}}{\partial x} \\ &+ \left[\mathbf{L}^{(m),lsq} - \mathbf{L}^{(ab),lsq} \right]^\dagger \frac{\partial^2 \mathbf{L}^{(m),lsq}}{\partial x \partial y} \end{aligned} \quad (3-36)$$

where differentiating the second equality in eq. (3-12), gives,

$$\frac{\partial \mathbf{L}^{(m)}}{\partial x} = \frac{\partial \mathbf{W}}{\partial x} \mathbf{V} + \mathbf{W} \frac{\partial \mathbf{V}}{\partial x} \quad (3-37)$$

$$\frac{\partial^2 \mathbf{L}^{(m)}}{\partial x \partial y} = \frac{\partial^2 \mathbf{W}}{\partial x \partial y} \mathbf{V} + \frac{\partial \mathbf{W}}{\partial y} \frac{\partial \mathbf{V}}{\partial x} + \frac{\partial \mathbf{W}}{\partial x} \frac{\partial \mathbf{V}}{\partial y} + \mathbf{W} \frac{\partial^2 \mathbf{V}}{\partial x \partial y} \quad (3-38)$$

Here $x, y \square (V_i, \lambda_j, \gamma_k)$. Using the results in eq. (3-36), (3-37), (3-38) and the fact that

$$\frac{\partial L_k^{(m)}}{\partial \lambda_i} = 0 \quad (3-39)$$

we obtain the following hessian matrix elements

$$\frac{\partial^2 \Lambda}{\partial \lambda_i \partial \lambda_j} = 0 \quad (3-40)$$

$$\frac{\partial^2 \Lambda}{\partial V_i \partial \lambda_j} = \frac{\partial L_j^{(m),ex\dagger}}{\partial V_i} \quad (3-41)$$

$$\frac{\partial^2 \Lambda}{\partial \gamma_i \partial \lambda_j} = \frac{\partial L_j^{(m),ex\dagger}}{\partial \gamma_i} \quad (3-42)$$

$$\frac{\partial^2 \Lambda}{\partial V_i \partial V_j} = \frac{\partial \mathbf{L}^{(m),lsq\dagger}}{\partial V_j} \frac{\partial \mathbf{L}^{(m),lsq}}{\partial V_i} + \left[\mathbf{L}^{(m),lsq} - \mathbf{L}^{(ab),lsq} \right]^\dagger \frac{\partial^2 \mathbf{L}^{(m),lsq}}{\partial V_i \partial V_j} + \frac{\partial^2 \mathbf{L}^{(m),ex\dagger}}{\partial V_i \partial V_j} \boldsymbol{\lambda} + t \delta_{ij} \quad (3-43)$$

$$\frac{\partial^2 \Lambda}{\partial V_i \partial \gamma_j} = \frac{\partial \mathbf{L}^{(m),lsq\dagger}}{\partial \gamma_j} \frac{\partial \mathbf{L}^{(m),lsq}}{\partial V_i} + \left[\mathbf{L}^{(m),lsq} - \mathbf{L}^{(ab),lsq} \right]^\dagger \frac{\partial^2 \mathbf{L}^{(m),lsq}}{\partial V_i \partial \gamma_j} + \frac{\partial^2 \mathbf{L}^{(m),ex\dagger}}{\partial V_i \partial \gamma_j} \boldsymbol{\lambda} \quad (3-44)$$

$$\frac{\partial^2 \Lambda}{\partial \gamma_i \partial \gamma_j} = \frac{\partial \mathbf{L}^{(m),lsq\dagger}}{\partial \gamma_j} \frac{\partial \mathbf{L}^{(m),lsq}}{\partial \gamma_i} + \left[\mathbf{L}^{(m),lsq} - \mathbf{L}^{(ab),lsq} \right]^\dagger \frac{\partial^2 \mathbf{L}^{(m),lsq}}{\partial \gamma_i \partial \gamma_j} + \frac{\partial^2 \mathbf{L}^{(m),ex\dagger}}{\partial \gamma_i \partial \gamma_j} \boldsymbol{\lambda} \quad (3-45)$$

where the intermediate quantities are evaluated using

$$\frac{\partial L_k^{(m)}}{\partial V_i} = \left(\frac{\partial \mathbf{W}}{\partial V_i} \mathbf{V} \right)_k + W_{k,i} \quad (3-46)$$

$$\frac{\partial L_k^{(m)}}{\partial \gamma_i} = \left(\frac{\partial \mathbf{W}}{\partial \gamma_i} \mathbf{V} \right)_k \quad (3-47)$$

Our working approximation is that we can ignore $\frac{\partial^2 L_k^{(m)}}{\partial x \partial y}$ terms because they are

multiplied by $\left[\mathbf{L}^{(m),lsq} - \mathbf{L}^{(ab),lsq} \right]$ or $\boldsymbol{\lambda}$, which are small quantities if the fit is qualitatively

correct. Thus, the working approximation for the hessian is given by equations (3-40), (3-41), (3-42) and the following approximations to eqs. (3-43), (3-44), (3-45)

$$\frac{\partial^2 \Lambda}{\partial V_i \partial V_j} \approx \frac{\partial \mathbf{L}^{(m),lsq\dagger}}{\partial V_j} \frac{\partial \mathbf{L}^{(m),lsq}}{\partial V_i} + t \delta_{ij} \quad (3-48)$$

$$\frac{\partial^2 \Lambda}{\partial V_i \partial \gamma_j} \approx \frac{\partial \mathbf{L}^{(m),lsq\dagger}}{\partial \gamma_j} \frac{\partial \mathbf{L}^{(m),lsq}}{\partial V_i} \quad (3-49)$$

$$\frac{\partial^2 \Lambda}{\partial \gamma_i \partial \gamma_j} \approx \frac{\partial \mathbf{L}^{(m),lsq\dagger}}{\partial \gamma_j} \frac{\partial \mathbf{L}^{(m),lsq}}{\partial \gamma_i} \quad (3-50)$$

3.6.3 Evaluation of $\frac{\partial \mathbf{d}^I(\mathbf{R}_n)}{\partial z_k}$

Since \mathbf{W} is given by $W_{n,l,j;l} = \mathbf{d}^{I\dagger}(\mathbf{R}_n) \mathbf{B}^{u(l),v(l)} \mathbf{d}^J(\mathbf{R}_n) [\nabla_j p^{(l)}(\mathbf{R}_n)]$ its derivative with respect to the parameter z_k requires $\frac{\partial \mathbf{d}^I(\mathbf{R}_n)}{\partial z_k}$. This is obtained from the derivative

of eq. (3-4) as follows:

$$(\mathbf{d}^I)^\dagger \left[\frac{\partial}{\partial z_k} \mathbf{H}^d(\mathbf{R}) \right] \mathbf{d}^J(\mathbf{R}) = (E^{a,J,(m)} - E^{a,I,(m)}) (\mathbf{d}^I)^\dagger \frac{\partial}{\partial z_k} \mathbf{d}^J(\mathbf{R}) \quad (3-51)$$

so

$$\frac{\partial \mathbf{d}^I(\mathbf{R})}{\partial z_k} = \sum_{K \neq I}^N \mathbf{d}^K(\mathbf{R}) \frac{\mathbf{d}^K(\mathbf{R})^\dagger \left[\frac{\partial}{\partial z_k} \mathbf{H}^d(\mathbf{R}) \right] \mathbf{d}^I(\mathbf{R})}{(E^{a,I,(m)}(\mathbf{R}) - E^{a,K,(m)}(\mathbf{R}))} \quad (3-52)$$

or

$$\frac{\partial \mathbf{d}^I(\mathbf{R})^\dagger}{\partial z_k} \mathbf{d}^K(\mathbf{R}) = \frac{\mathbf{d}^K(\mathbf{R})^\dagger \left[\frac{\partial}{\partial z_k} \mathbf{H}^d(\mathbf{R}) \right] \mathbf{d}^I(\mathbf{R})}{(E^{a,I,(m)}(\mathbf{R}) - E^{a,K,(m)}(\mathbf{R}))} \quad (3-53)$$

This is valid provided we are not near a conical intersection where

$$E^{a,I,(m)}(\mathbf{R}) = E^{a,K,(m)}(\mathbf{R}).$$

At a conical intersection of states I and J , it might appear that $\frac{\partial \mathbf{d}^I(\mathbf{R})^\dagger}{\partial z_k} \mathbf{d}^J(\mathbf{R})$ is not well defined but this is not the case. The desired derivative is obtained from the derivative of the orthogonality constraint⁶⁵, which requires that at a conical intersection \mathbf{d}^I are chosen so that the \mathbf{g} and \mathbf{h} vectors are orthogonal, that is, $\mathbf{g} \cdot \mathbf{h} = 0$, where

$$2g_k \equiv L_k^{I,I,(m)} - L_k^{J,J,(m)} \quad \text{and} \quad h_k \equiv L_k^{I,J,(m)} \quad (3-54)$$

The derivative of $\mathbf{g} \cdot \mathbf{h} = 0$ is obtained as follows

$$\begin{aligned} \frac{\partial \mathbf{h}}{\partial z_k} &= \frac{\partial (\mathbf{d}^I)^\dagger}{\partial z_k} (\nabla \mathbf{H}^d \mathbf{d}^J) + (\mathbf{d}^I)^\dagger \frac{\partial (\nabla \mathbf{H}^d)}{\partial z_k} (\mathbf{d}^J) + (\mathbf{d}^I)^\dagger \nabla \mathbf{H}^d \frac{\partial \mathbf{d}^J}{\partial z_k} \\ &= \frac{\partial (\mathbf{d}^I)^\dagger}{\partial z_k} (\mathbf{d}^J) L^{J,J,(m)} + \sum_{K \neq I,J} \frac{\partial (\mathbf{d}^I)^\dagger}{\partial z_k} (\mathbf{d}^K) L^{K,J,(m)} + (\mathbf{d}^I)^\dagger \frac{\partial (\nabla \mathbf{H}^d)}{\partial z_k} (\mathbf{d}^J) + L^{I,I,(m)} (\mathbf{d}^I)^\dagger \frac{\partial \mathbf{d}^J}{\partial z_k} \\ &\quad + \sum_{K \neq I,J} (\mathbf{d}^K)^\dagger \frac{\partial (\mathbf{d}^J)}{\partial z_k} L^{K,I,(m)} \\ \frac{\partial \mathbf{h}}{\partial z_k} &= [L^{I,I,(m)} - L^{J,J,(m)}] (\mathbf{d}^I)^\dagger \frac{\partial \mathbf{d}^J}{\partial z_k} + (\mathbf{d}^I)^\dagger \frac{\partial (\nabla \mathbf{H}^d)}{\partial z_k} (\mathbf{d}^J) + \sum_{K \neq I,J} \frac{\partial (\mathbf{d}^I)^\dagger}{\partial z_k} (\mathbf{d}^K) L^{K,J,(m)} \\ &\quad + \sum_{K \neq I,J} (\mathbf{d}^K)^\dagger \frac{\partial (\mathbf{d}^J)}{\partial z_k} L^{K,I,(m)} \\ &= 2[\mathbf{g}] (\mathbf{d}^I)^\dagger \frac{\partial \mathbf{d}^J}{\partial z_k} + (\mathbf{d}^I)^\dagger \frac{\partial (\nabla \mathbf{H}^d)}{\partial z_k} (\mathbf{d}^J) \\ &\quad + \sum_{K \neq I,J} \frac{\partial (\mathbf{d}^I)^\dagger}{\partial z_k} (\mathbf{d}^K) L^{K,J,(m)} + \sum_{K \neq I,J} (\mathbf{d}^K)^\dagger \frac{\partial (\mathbf{d}^J)}{\partial z_k} L^{K,I,(m)} \end{aligned} \quad (3-55)$$

Similarly

$$\frac{\partial \mathbf{g}}{\partial z_k} = \left[-2\mathbf{h} \frac{\partial (\mathbf{d}^J)^\dagger}{\partial z_k} (\mathbf{d}^I) \right] + \sum_{K \neq I,J} \left[\frac{\partial (\mathbf{d}^I)^\dagger}{\partial z_k} \mathbf{d}^K L^{K,I,(m)} - \frac{\partial (\mathbf{d}^J)^\dagger}{\partial z_k} (\mathbf{d}^K) L^{K,J,(m)} \right]$$

$$+\frac{1}{2}\left[(\mathbf{d}^I)^\dagger \frac{\partial(\nabla\mathbf{H}^d)}{\partial z_k}(\mathbf{d}^I) - (\mathbf{d}^J)^\dagger \frac{\partial(\nabla\mathbf{H}^d)}{\partial z_k}(\mathbf{d}^J)\right] \quad (3-56)$$

Using eqs. (3-55) and (3-56) we construct

$$\mathbf{g} \cdot \frac{\partial}{\partial z_k} \mathbf{h} + \mathbf{h} \cdot \frac{\partial}{\partial z_k} \mathbf{g} = 0 \quad (3-57)$$

which gives the desired equation for $(\mathbf{d}^I)^\dagger \frac{\partial \mathbf{d}^J}{\partial z_k}$:

$$\begin{aligned} 0 = & 2\left[\|\bar{\mathbf{g}}\|^2 - \|\bar{\mathbf{h}}\|^2\right](\mathbf{d}^I)^\dagger \frac{\partial \mathbf{d}^J}{\partial z_k} \\ & + \bar{\mathbf{g}} \cdot \left[(\mathbf{d}^I)^\dagger \frac{\partial(\bar{\nabla}\mathbf{H}^d)}{\partial z_k}(\mathbf{d}^J) + \sum_{K \neq I, J} \frac{\partial(\mathbf{d}^I)^\dagger}{\partial z_k}(\mathbf{d}^K) \bar{L}^{K, J, (m)} + \sum_{K \neq I, J} \frac{\partial(\mathbf{d}^K)^\dagger}{\partial z_k}(\mathbf{d}^J) \bar{L}^{K, I, (m)} \right] \\ & + \bar{\mathbf{h}} \cdot \left[\frac{1}{2}(\mathbf{d}^I + \mathbf{d}^J)^\dagger \frac{\partial(\bar{\nabla}\mathbf{H}^d)}{\partial z_k}(\mathbf{d}^I - \mathbf{d}^J) \right. \\ & \quad \left. + \sum_{K \neq I, J} \bar{L}^{K, J, (m)} \frac{\partial(\mathbf{d}^I)^\dagger}{\partial z_k} \mathbf{d}^K - \sum_{K \neq I, J} \bar{L}^{K, I, (m)} \frac{\partial(\mathbf{d}^K)^\dagger}{\partial z_k} \mathbf{d}^J \right] \quad (3-58) \end{aligned}$$

Note that when N^{state} is greater than 2, eq. (3-58) includes terms $(\mathbf{d}^I)^\dagger \frac{\partial \mathbf{d}^K}{\partial z_k}$ which are obtained from eq. (3-53). For clarity we note that in eq. (3-58) the dot products, $\mathbf{h} \cdot$ and $\mathbf{g} \cdot$ refer to the coordinates components, that is the gradient components of $\nabla\mathbf{H}^d$ or the vector components of $\bar{L}^{K, J, (m)}$, which come from $\nabla\mathbf{H}^d$ via eq. (3-13).

3.6.4 Formulation and solution of Eq. (3-23)

In this section we explain how terms included in eq. (3-23) are assembled and the equation subsequently solved. From eq. (3-37) we see that, the quantity required for

eq. (3-23) that is not already available from eq. (3-22) is $\frac{\partial W_{n,I,J,j;l}^x}{\partial V_k}$, $x = lsq$ or ex .

From eq. (3-21), $\frac{\partial W_{n,I,J,j;l}^x}{\partial V_k}$ is given by (where the superscript x is omitted as irrelevant)

$$\begin{aligned} \frac{\partial W_{n,I,J,j;l}}{\partial V_k} &= \sum_K \left[\frac{\partial \mathbf{d}^{I^\dagger}(\mathbf{R}_n)}{\partial V_k} \mathbf{d}^K(\mathbf{R}_n) \mathbf{d}^K(\mathbf{R}_n)^\dagger \mathbf{B}^{u(l),v(l)} \mathbf{d}^J(\mathbf{R}_n) \right. \\ &\quad \left. + \mathbf{d}^{I^\dagger}(\mathbf{R}_n) \mathbf{B}^{u(l),v(l)} \mathbf{d}^K(\mathbf{R}_n) \mathbf{d}^K(\mathbf{R}_n)^\dagger \frac{\partial \mathbf{d}^J(\mathbf{R}_n)}{\partial V_k} \right] [\nabla_j p^{(l)}(\mathbf{R}_n)] \\ &= \sum_K \left[\frac{\partial \mathbf{d}^{I^\dagger}(\mathbf{R}_n)}{\partial V_k} \mathbf{d}^K(\mathbf{R}_n) W_{n,K,J,j;l} + W_{n,I,K,j;l} \mathbf{d}^K(\mathbf{R}_n)^\dagger \frac{\partial \mathbf{d}^J(\mathbf{R}_n)}{\partial V_k} \right] \end{aligned} \quad (3-59)$$

with $\frac{\partial (\mathbf{d}^{I'})^\dagger}{\partial V_k} \mathbf{d}^J$ given by eq. (3-53) or (3-58) depending on $E^{a,I(m)}(\mathbf{R}) - E^{a,J(m)}(\mathbf{R})$.

The approximate Hessian described in Appendix 3.6.2 when used in eq. (3-23), gives an extension of the standard Gauss-Newton method to problems with constraints, being equivalent to the Gauss-Newton method when no exact equations are present. It is well known that, unlike Newton-Raphson method, Gauss-Newton method is not guaranteed to be locally convergent. Even though the convergence of Gauss-Newton method can approach quadratic when the approximate hessian is well conditioned, such a favorable situation has never been observed in the present work. Divergence has been observed when during the fitting procedure \mathbf{H}^d exhibits qualitative changes.

On the other hand, the original method (eq. (3-22)) has shown a tendency to enter small oscillations, but behave more stably when the step sizes are large. This is

caused by the fact that the $\frac{\partial (\mathbf{d}^{I'})^\dagger}{\partial V_k} \mathbf{d}^J$ described by eq. (3-53) can take large values when

states are energetically close but not yet degenerate enough to use intersection adapted

coordinates and equation (3-58). For this reason, eq. (3-22) is used at the start of the fitting procedure and eq. (3-23) used when the coefficients cease to change dramatically.

Even in this situation, however, the fitting procedure is not guaranteed to converge and can be subject to the same divergence problem of the Gauss-Newton methods. Two techniques, damping and line search, both routinely used for Gauss-Newton and Newton-Raphson methods, are applied to counter such problems.

In damping a shift is added to the hessian, so that eq (3-48) becomes

$$\frac{\partial^2 \Lambda}{\partial V_i \partial V_j} \approx \frac{\partial \mathbf{L}^{(m),lsq\dagger}}{\partial V_j} \frac{\partial \mathbf{L}^{(m),lsq}}{\partial V_i} + (\tilde{t} + t) \delta_{ij} \quad (3-60)$$

\tilde{t} is an arbitrary nonnegative number. When no exact equations are present, the method becomes equivalent to the Levenberg-Marquardt Algorithm,⁶⁶ which is the algorithm used in most nonlinear least squares fitting programs. The size of the damping parameter \tilde{t} can be adjusted dynamically during the fitting procedure. Note that \tilde{t} appears only on the left hand side of the equation while t appears on both sides. As a result, unlike the flattening term t , \tilde{t} does not affect the final converged result. Instead, \tilde{t} can be properly described as a damping parameter that only affects the rate of convergence. This method is intermediate between a Newton type method and a gradient descent method, which balances the stability of gradient descent and rapid convergence of Newton-type methods. The parameter is chosen in the range of 10^{-3} and 10^{-7} depending on the stability of the convergence procedure.

In the line search approach the program steps along the direction pointed by the solution vector of eq. (3-23), and locates the point where the norm of the gradient of Lagrangian reaches a minimum. This point is taken as the starting point for the next iteration. The line search technique ensures that the gradient of the Lagrangian will

always decrease and thus is immune to oscillations. However, the line search can be trapped in a very shallow local minimum. It is therefore only used when approaching final convergence.

As in Gauss-Newton method, because the hessian matrix is approximate, when damping term is absent convergence is not guaranteed and in general will not be reached. When a large enough damping term is present, the method has a guaranteed linear convergence. The linear convergence can be extremely slow when the hessian is ill-conditioned. However, the quality of the fit will cease to change significantly when this situation occurs and we therefore terminate the procedure at this point.

Finally note that while the line search guarantees the norm of the gradient decreases, it does not guarantee the constraints be exactly satisfied until the final convergence is reached. We therefore monitor the exact equations and will only terminate the procedure when that part error becomes sufficiently small. We are presently studying the relation between the residual norm of the gradient of the Lagrangian and the quality of the fit.

References

1. Lasorne, B.; Robb, M. A.; Meyer, H.-D.; Gatti, F., The electronic excited states of ethylene with large-amplitude deformations:
A dynamical symmetry group investigation. *Chem. Phys.* **2010**, *377*, 30.
2. Tully, J. C., Molecular Dynamics with electronic transitions. *J. Chem. Phys.* **1990**, *93*, 1061-1071.
3. Ben-Nun, M.; Martinez, T. J., Ab Initio Multiple Spawning:Photochemistry from First Principles Quantum Molecular Dynamics. *J. Phys. Chem. A* **2000**, *104*, 5161-5175.
4. Worth, G. A.; Robb, M. A.; Lasorne, B., *Mol. Phys.* **2008**, *106*, 2077.
5. Baer, M., Adiabatic and diabatic representations for atom-diatom collisions: Treatment of the three-dimensional case. *Chem. Phys.* **1976**, *15*, 49-57.
6. Mead, C. A.; Truhlar, D. G., Conditions for the definition of a strictly diabatic basis. *J. Chem. Phys.* **1982**, *77*, 6090-6098.
7. Baer, M., Introduction to the theory of electronic nonadiabatic coupling terms in molecular systems. *Physics Reports* **2002**, *358*, 75-142.
8. Mota, V. C.; Varandas, A. J. C., HN₂(2A⁺) Electronic Manifold. II. Ab Initio Based Double-Sheeted DMBE Potential Energy Surface via a Global Diabatization Angle. *J. Phys. Chem. A* **2008**, *112*, 3768–3786.
9. Nakamura, H.; Truhlar, D. G., Direct diabatization of electronic states by the fourfold way. II. Dynamical correlation and rearrangement processes. *J. Chem. Phys.* **2002**, *117*, 5576-5593.
10. Nakamura, H.; Truhlar, D. G., Extension of the fourfold way for the calculation of global diabatic potential energy surfaces of complex multiarrangement non-Born

Oppenheimer systems. Application to HNCO(S0,S1). *J. Chem. Phys.* **2003**, *118*, 6816-6829.

11. Xu, X. F.; Yang, K. R.; Truhlar, D. G., Diabatic Molecular Orbitals, Potential Energies, and Potential Energy Surface Couplings by the 4-fold Way for Photodissociation of Phenol. *J Chem Theory Comput* **2013**, *9* (8), 3612-3625.

12. Li, Z. H.; Valero, R.; Truhlar, D. G., Improved DIrect Diabatization and Coupled Potential Energy Surfaces for the dissociation of ammonia. *Theor. Chem. Acc.* **2007**, *118*, 9-24.

13. Einfeld, W.; Viel, A., Higher order (A+E)xe Pseudo Jahn-Teller coupling *J. Chem. Phys.* **2005**, *122*, 204317.

14. Viel, A.; Einfeld, W., Effects of higher order Jahn-Teller coupling on the nuclear dynamics. *J. Chem. Phys.* **2004**, *120*, 4603.

15. Godsi, O.; Evenhuis, C. R.; Collins, M. A., Interpolation of Multidimensional diabatic surfaces. *J. Chem. Phys.* **2006**, *125*, 104105.

16. Evenhuis, C. R.; Collins, M. A., Interpolation of Diabatic potential energy surfaces. *J. Chem. Phys.* **2004**, *121*, 2515.

17. Evenhuis, C.; Martínez, T. J., A scheme to interpolate potential energy surfaces and derivative coupling vectors without performing a global diabatization. *J. Chem. Phys.* **2011**, *135*, 224110.

18. Köppel, H.; Gronki, J.; Mahapatra, S., Construction Scheme for Regularized Diabatic States. *J. Chem. Phys.* **2001**, *115*, 2377.

19. Köppel, H.; Schubert, B., regularized diabatic representation. *Mol. Phys.* **2006**, *104*, 1069.

20. Thompson, T. C.; Izmirlian, G.; Lemon, S. J.; Truhlar, D. G.; Mead, C. A., Consistent Analytic Representation of the two lowest potential energy surfaces for Li₃, Na₃ and K₃. *J. Chem. Phys* **1985**, *82*, 5597.
21. Varandas, A. J. C.; Brown, F. B.; Mead, C. A.; Truhlar, D. G.; Blais, N. C., A double Many Body expansion of the two lowest energy potential energy surfaces and nonadiabatic couplings for H₃. *J. Chem. Phys.* **1987**, *86*, 6258.
22. Martínez-Núñez, E.; Varandas, A. J. C., Single-Valued DMBE Potential Energy Surface for HSO: A Distributed n-Body Polynomial Approach. *J. Phys. Chem. A* **2001**, *105*, 5923–5932.
23. Poveda, L. A.; Biczysko, M.; Varandas, A. J. C., Accurate ab initio based DMBE potential energy surface for the ground electronic state of N₂H₂. *J. Chem. Phys.* **2009**, *131*, 044309.
24. Jornet-Somoza, J.; Lasorne, B.; Robb, M. A.; Meyer, H. D.; Lauvergnat, D.; Gatti, F., A generalised 17-state vibronic-coupling Hamiltonian model for ethylene. *J Chem Phys* **2012**, *137* (8).
25. Macías, A.; Riera, A., Calculation of diabatic states from molecular properties. *J. Phys. B.* **1978**, *11*, L489-L492.
26. Dobbyn, A. J.; Knowles, P. J., A comparative study of methods for describing nonadiabatic coupling: diabatic representation of the 1Σ⁺/1Π HOH and HHO conical intersections. *Mol. Phys.* **1997**, *91*, 1107-1123.
27. Köppel, H.; Domcke, W.; Cederbaum, L. S., The Multimode Vibronic Coupling Approach. In *Conical Intersections*, Domcke, W.; Yarkony, D. R.; Köppel, H., Eds. World Scientific: New Jersey, 2004; Vol. 15, pp 323-368.

28. Zhu, X.; Yarkony, D. R., Toward the Elimination of the Electronic Structure Bottleneck in Nonadiabatic Dynamics on the Fly. Construction of Non-local, Quasi-Diabatic, Coupled Electronic State Hamiltonians based on ab initio Electronic Structure Data. *J. Chem. Phys.* **2010**, *132*, 104101 (15 pages).
29. Zhu, X.; Yarkony, D. R., On the Representation of Coupled Adiabatic Potential Energy Surfaces using Quasi-Diabatic Hamiltonians: Description of Accidental Seams of Conical Intersection. *Molec. Phys.* **2010**, *108* (19), 2611 - 2619.
30. Zhu, X.; Yarkony, D. R., On the Representation of Coupled Adiabatic Potential Energy Surfaces using Quasi-Diabatic Hamiltonians: Geometrically Distributed Expansions. *J. Chem. Phys.* **2012**, *136*, 174110.
31. Atchity, G. J.; Xantheas, S. S.; Ruedenberg, K., Potential Energy Surfaces Near Intersections. *J. Chem. Phys.* **1991**, *95*, 1862-1876.
32. Vaida, V.; Hess, W.; Roebber, J. L., The direct ultraviolet absorption spectrum of the A1A2" \leftarrow X'A1 transition of jet-cooled ammonia. *J. Phys. Chem.* **1984**, *88*, 3397-3400.
33. Walsh, A. D.; Warsop, P. A., NH₃. *Trans. Faraday Soc.* **1961**, *57*, 345.
34. Rosmus, P.; Botschwina, P.; Werner, H.-J.; Vaida, V.; Engelking, P. C.; McCarthy, M. I., NH₃ photodissociation. *J. Chem. Phys.* **1987**, *86*, 6677.
35. McCarthy, M. I.; Rosmus, P.; Werner, H.-J.; Botschwina, P.; Vaida, V., NH₃ photodissociation. *J. Chem. Phys.* **1987**, *86*, 6693.
36. Bach, A.; Hutchison, J. M.; Holiday, R. J.; Crim, F. F., Vibronic structure and photodissociation dynamics of the A state of jet-cooled ammonia. *J. Chem. Phys.* **2002**, *116*, 9315-9325.

37. Tang, S. L.; Imre, D. G., NH₃. *Chem. Phys.Lett.* **1988**, *144*, 6.
38. Henck, S. A.; Mason, M. A.; Yan, W.-B.; Lehmann, K. K.; Coy, S. L., Microwave detected, microwave-optical double resonance of NH₃, NH₂D, NHD₂ and ND₃. II Predissociation dynamics of the A State. *J. Chem. Phys.* **1995**, *102*, 4783-4792.
39. Biesner, J.; Schnieder, L.; Ahlers, G.; Xie, X.; Welge, K. H.; Ashfold, M. N. R.; Dixon, R. N., NH₃ photodissociation. *J. Chem. Phys.* **1988**, *88*, 3607.
40. Biesner, J.; Schneider, L.; Ahlers, G.; Xie, X.; Welge, K. H.; Ashfold, M. N. R.; Dixon, R. N., State Selective Photodissociation dynamics of A State ammonia. II. *J. Chem. Phys.* **1989**, *91*, 2901-2911.
41. Woodbridge, E. L.; Ashfold, M. N. R.; Leone, S. R., Photodissociation of ammonia at 193.3nm: Rovibrational state distribution of the NH₂(A₂A₁) fragment. *J. Chem. Phys.* **1991**, *94*, 4195-4204.
42. Mordaunt, D. H.; Ashfold, M. N. R.; Dixon, R. N., Photodissociation dynamics of state ammonia molecules. II. The isotopic dependence for partially and fully deuterated isotopomers. *J. Chem. Phys.* **1996**, *104*, 6472.
43. Mordaunt, D. H.; Ashfold, M. N. R.; Dixon, R. N., NH₃ photodissociation. *J. Chem. Phys.* **1996**, *104*, 6460.
44. Mordaunt, D. H.; Ashfold, M. N. R.; Dixon, R. N.; Löffler, P.; Schneider, L.; Welge, K. H., *J. Chem. Phys.* **1998**, *108*, 519-526.
45. Loomis, R. A.; Lester, M. I., OH-H₂ entrance Channel Complexes. *Annu. Rev. Phys. Chem.* **1997**, *48*, 643-673.
46. Reid, J. P.; Loomis, R. A.; Leone, S. R., NH₃ photodissociation. *J. Chem. Phys.* **2000**, *112*, 3181.

47. Reid, J. P.; Loomis, R. A.; Leone, S. R., NH₃ photodissociation. *Chem. Phys. Lett.* **2000**, *324*, 240.
48. Reid, J. P.; Loomis, R. A.; Leone, S. R., NH₃ photodissociation. *J. Phys. Chem. A* **2000**, *104*, 10139.
49. Wells, K. L.; Perriam, G.; Stavros, V. G., Time-resolved velocity map ion imaging study of NH₃ photodissociation. *J. Chem. Phys.* **2009**, *130*, 074308.
50. Dixon, R. N., NH₃. *Chem. Phys. Lett.* **1988**, *147*, 377.
51. Dixon, R. N., NH₃. *Mol. Phys.* **1996**, *88*, 949.
52. Dixon, R. N.; Hancock, T. W. R., Recoil anisotropy following molecular predissociation: NH₃* --> H + NH₂ and HFCO* --> H + FCO. *J. Phys. Chem. A* **1997**, *101*, 7567.
53. Bonhommeau, D.; Truhlar, D. G., Mixed quantum/classical investigation of the photodissociation of NH₃(A) and a practical method for maintaining zero-point energy in classical trajectories
. *J. Chem. Phys.* **2008**, *129*, 014302.
54. Lai, W.; Lin, S. Y.; Xie, D.; Guo, H., Full-dimensional quantum dynamics of -state photodissociation of ammonia: Absorption spectra. *J. Chem. Phys.* **2008**, *129*, 154311.
55. Bonhommeau, D.; Valero, R.; Truhlar, D. G.; Jasper, A. W., Coupled-Surface Investigation of the photodissociation of NH₃(A). Effect of exciting the symmetric and antisymmetric stretch modes. *J. Chem. Phys.* **2009**, *130*, 234303 (17 pages).

56. Lai, W.; Lin, S. Y.; Xie, D.; Guo, H., Non-adiabatic dynamics of A-state photodissociation of ammonia: a four-dimensional wave packet study. *J. Phys. Chem. A* **2010**, *114*, 3121.
57. Bach, A.; Hutchison, J. M.; Holiday, R. J.; Crim, F. F., Photodissociation of vibrationally excited ammonia: rotational excitation in the NH₂ product. *J. Chem. Phys.* **2003**, *118*, 7144-7145.
58. Hause, M. L.; Yoon, Y. H.; Crim, F. F., Vibrationally mediated photodissociation of ammonia: The influence of N–H stretching vibrations on passage through conical intersections. *J. Chem. Phys.* **2006**, *125*, 174309.
59. Yarkony, D. R., Conical Intersections: Diabolical and Often Misunderstood. *Acc. Chem. Res.* **1998**, *31*, 511-518.
60. Zhu, X.; Ma, J.; Yarkony, D. R.; Guo, H., Computational Determination of X State Absorption Spectrum of NH₃ and ND₃ using a Quasi Diabatic Representation of the X and A States and Full Six Dimensional Quantum Dynamics. *J. Chem. Phys.* **2012**, submitted.
61. Dillon, J. J.; Yarkony, D. R.; Schuurman, M. S., On the Construction of Quasi Diabatic State Representations of Bound Adiabatic State Potential Energy Surfaces Coupled by Conical Intersections. Incorporation of Higher Order Terms. *J. Chem. Phys.* **2011**, *134*, 044101 (11 pages).
62. Papas, B. N.; Schuurman, M. S.; Yarkony, D. R., *Determining quasi diabatic coupled electronic state Hamiltonians using derivative couplings. A normal equations based method.* *J. Chem. Phys.* **2008**, *129*, 124104(10 pages).

63. Yarkony, D. R., Nonadiabatic effect in the Vicinity of Multiple Surface crossings....H+ + NO. *J. Chem. Phys.* **1989**, *90*, 1657.
64. Braams, B. J.; Bowman, J. M., Permutationally Invariant Potential Energy Surfaces in High dimensionality. *Int. Rev. Phys. Chem.* **2009**, *28*, 577-606.
65. Yarkony, D. R., *On the adiabatic to diabatic states transformation near intersections of conical intersections.* *J. Chem. Phys.* **2000**, *112*, 2111-2120.
66. Marquardt, D., An Algorithm for Least-Squares Estimation of Nonlinear Parameters. *SIAM Journal on Applied Mathematics* **1963**, *11*, 431-441.

Chapter 4 Computational Determination of the $\tilde{A} \leftarrow \tilde{X}$ Absorption Spectra and Photodissociation Product Branching Ratios of NH_3 and of ND_3 using H^d and Full Six Dimensional Quantum Dynamics

4.1 Abstract

A recently developed method to represent adiabatic electronic states coupled by conical intersections has been used to construct a full six dimensional quasi-diabatic representation of the 1^1A and 2^1A states of NH_3 . This representation is expected to be appropriate to simulate the photodissociation of ammonia when it is excited to the 2^1A electronic state. In this work the electronic structure aspects of this quasi-diabatic representation are analyzed. This representation is then used as the basis for a simulation of the $\tilde{A} \leftarrow \tilde{X}$ absorption spectrum, dominated by a progression in the ν_2 mode, using a full six dimensional quantum mechanical treatment of the nuclear motion. Then the non-adiabatic dynamics is investigated with six-dimensional wave packet method. Results are reported for both NH_3 and ND_3 . This simulation provides the most accurate computational determination of this absorption spectrum and product $\tilde{A}^2\text{A}_1 / \tilde{X}^2\text{B}_1$ branching ratios reported to date. These results serve to validate the quasi-diabatic representation and set the stage for subsequent studies of vibrationally mediated photodissociation of NH_3 .

4.2 Introduction

It has been almost 80 years since Leifson first reported the \tilde{A} state absorption of ammonia beginning at 220 nm.¹ The diffuse character of the absorption reflects strong

predissociation. In the intervening decades this state has been probed using a plethora of experimental and theoretical techniques. It is now clear that the photochemistry of the \tilde{A} state reflects the fact that this state is quasi bound in the Franck-Condon region and that beyond a small barrier in the dissociation (N-H) coordinate a seam of conical intersections is encountered.

Over fifty years after its initial observation, Vaida *et al.*² using a cold supersonic jet, reported a progression in the umbrella mode, ν_2 , in the \tilde{A} band absorption of NH_3 . This progression reflects the change from a trigonal structure in the \tilde{X} state to a planar structure in the \tilde{A} state.³ The lifetimes of the individual levels of the ν_2 progression were subsequently measured by several groups.⁴⁻⁷ Interestingly, however, the anticipated progression in the symmetric stretch, the ν_1 mode, based on the greater N-H bond length in the \tilde{A} state when compared to the \tilde{X} state³ was not observed by Vaida *et al.* More recent vibrationally mediated photodissociation experiments have provided access to combinations of levels in the \tilde{A} state not previously seen.⁸⁻¹⁰

The lifetimes of the ν_2 levels and the absence of an observed progression in ν_1 are related to the efficiency of intramolecular vibrational energy transfer. The vibrational mediated photodissociation experiments raise further questions about intramolecular vibrational energy transfer but these experiments also address how the seam of conical intersection impacts the products of the dissociation, $\text{NH}_2(\tilde{X}^2\text{B}_1) + \text{H}$ or $\text{NH}_2(\tilde{A}^2\text{A}_1) + \text{H}$. The absence of a progression in ν_1 has been attributed to a near 3:1 degeneracy of the ν_1 and ν_2 modes¹¹ or a sufficiently low barrier to allow direct dissociation from an excited ν_1 mode.^{7, 12} This barrier to \tilde{A} state dissociation has been determined from *ab initio* calculations and inferred from experimental measurements. Computed barriers include

the early work of McCarthy *et al.*¹³⁻¹⁴ who reported a barrier of 3226 cm⁻¹ and more recent work of Bach *et al.*⁸ and of Li *et al.*¹⁵ who reported barriers of 2348 cm⁻¹ and 1750 cm⁻¹, respectively. These results should be compared with the experimental estimate of ~2100 cm⁻¹ of Henck *et al.*⁷ based on microwave detected, microwave-optical double resonance measurements and supported by the measured lifetimes of Bach *et al.*⁸ obtained from vibrationally mediated photodissociation action spectroscopy.

The final state resolved dynamics of ammonia photodissociation has been investigated experimentally by several groups.¹⁶⁻²⁶ The production of the ground state NH₂ fragment clearly indicates nonadiabatic coupling between the \tilde{X} and \tilde{A} states of ammonia. It is now well established that the nonadiabatic transition is facilitated by a seam of conical intersections encountered after the initial barrier near the Franck-Condon region is traversed.^{13-15, 27-30}

The photodissociation dynamics following \tilde{A} state absorption have been the subject of numerous computational studies as well,³¹⁻³⁷ including those of Dixon who determined the \tilde{A} state lifetimes using three³¹ and higher dimensional³² model potential energy surfaces; those of Bonhommeau *et al.*³⁶, denoted *BVTJ* below, who simulated the vibrationally mediated photodissociation spectrum measured in Crim's group,^{8-10, 38} using trajectory surface hopping techniques;^{34, 39} and those of Lai *et al.*³⁵, denoted *LLXG* below, who computed the lifetimes of the umbrella mode levels using full 6-dimensional quantum dynamics. The results in the *LLXG* work were subsequently reproduced semi-quantitatively using the same coupled potential energy surfaces by Giri *et al.*⁴⁰, denoted *GCSW* below, using the multiconfiguration time-dependent Hartree (MCTDH) method,⁴¹⁻

⁴² The quantitative differences in both energies and widths between the results of *LLXG*

and those of *GCSW* are presumably attributable to the approximate nature of aspects of the MCTDH procedure. The studies of *BVTJ*, *LLXG* and *GCSW* are notable since they employed the same full six dimensional approximate diabatic representation of the $1,2^1A$ states of NH_3 based on *ab initio* data.¹⁵ The approximate or quasi-diabatic representation was constructed using the fourfold way method of Nakamura and Truhlar.⁴³⁻⁴⁴ The use of an approximate diabatic representation is a consequence of the seam of conical intersections coupling the $1,2^1A$ adiabatic states. The qualifiers approximate or quasi in front of diabatic, which we shall omit below, remind us that rigorous diabatic states do not exist for general polyatomic molecules.⁴⁵⁻⁴⁷

The representation of *ab initio* determined adiabatic state PESs coupled by conical intersections has long been a goal of quantum chemistry. Efforts to find diabatic representations include the vibronic coupling model of Köppel, Domcke and Cederbaum;⁴⁸⁻⁵⁶ the perturbation theory based work of Mead, Truhlar and Varandas;⁵⁷⁻⁵⁸ the four-fold way diabatization schemes of Truhlar,⁴³⁻⁴⁴ based on earlier work of Ruedenberg;⁵⁹ the regularized diabatization procedure of Köppel;⁶⁰ the block diabatization method of Pacher, Cederbaum and Köppel;⁶¹⁻⁶² the generalized adiabatic angle method of Varandas⁶³⁻⁶⁴ and the Shepard interpolation based method of Collins, Evenhuis and coworkers.⁶⁵⁻⁶⁸ Approaches based on a combination of the interpolated moving least squares⁶⁹⁻⁷⁰ and the general dynamically weighted⁷¹ state averaged multiconfiguration self consistent field methods also show promise in this regard. In Chapter 2, we introduced an approach, in which a diabatic Hamiltonian, \mathbf{H}^d , is constructed with polynomial expansions of its matrix elements. In Chapter 3, this approach was generalized and given a more flexible and rigorous mathematical

framework. \mathbf{H}^d is capable of representing, *ab initio* energies, gradients and derivative couplings over a wide range of geometries including those for dissociated species and seams of conical intersections. Further since derivative couplings are included in defining the representation it is quantifiably diabatic in a least squares sense. However this method has yet to be tested in a practical calculation.

In the vibrationally mediated photodissociation experiments reported by Crim's group,^{8-10, 38} a dramatic difference in the $\text{NH}_2 \tilde{A}/\tilde{X}$ branching fraction was found depending on whether the \tilde{X} state is excited to $v_1=1$ or to $v_3=1$, prior to dissociation through the \tilde{A} state by a second photon. This difference in the branching fraction is attributed to differences in the dynamics near the $1,2^1\text{A}$ conical intersection seam noted above. The nonadiabatic dynamics study of *BVTJ*, despite a very careful analysis, was unable to explain the measured branching fractions. Further the line widths of the v_2 levels computed by *LLXG* using a full 6 dimensional quantum treatment, systematically over estimate the measured line widths of this mode and the spectral intensity distribution was poorly approximated. The lack of fully satisfactory agreement between these careful dynamics studies and the relevant experimental measurements suggests the need to reconsider the determination of the coupled diabatic state representation of the $1,2^1\text{A}$ states.

In this work then an \mathbf{H}^d developed using the methods described in Chapter 3 and appropriate for simulating NH_3 photodissociation will be analyzed. This diabatic representation will then be validated by comparing the measured line positions, intensities⁶ and lifetimes^{4, 6-8} of the umbrella vibrations with computed values based on the coupled diabatic state description of the $1,2^1\text{A}$ states of NH_3 . This simulation/analysis

of the absorption spectrum, will employ the full 6 dimensional, accurate, fully quantum mechanical treatment of the nuclear dynamics of *LLXG*. The \mathbf{H}^d produced in the pioneering work, of Li, Valero and Truhlar¹⁵ denoted *LVT* below, is, to our knowledge the only other approximate diabatic \mathbf{H}^d available for this system so that comparisons to that work are inevitable.

The computed lifetimes are sensitive to the region of the minimum and the barrier to dissociation on the \tilde{A} state. The region of the seam of conical intersections, which is responsible for the branching between \tilde{X} and \tilde{A} states of NH_2 , is very carefully described by \mathbf{H}^d .⁷² However its validation using this full dimensional quantum dynamics approach is quite costly and will be the subject of future work.

Section 4.3 reviews the form of \mathbf{H}^d , its construction and the full dimensional quantum determination of the positions, intensities and lifetimes of the ν_2 levels. Section 4.4 describes the electronic structure aspects of the representation. Section 4.5 presents and discusses the positions, intensities and lifetimes of the ν_2 levels of the \tilde{A} state. The consequent validation of \mathbf{H}^d is also discussed. Section 4.6 summarizes and discusses directions for future studies.

4.3 Theoretical Approach

4.3.1 Diabatic Representations

i. Diabatic States and the Reference Geometry

The details of constructing \mathbf{H}^d have been described in Chapter 2 and Chapter 3. Here we summarize the key points so as to be able to discuss the constructed \mathbf{H}^d .

The diabatic states $\Psi_u^d(\mathbf{q}; \mathbf{R})$ are chosen to agree with the adiabatic states $\Psi_I^{a,(ab)}(\mathbf{q}; \mathbf{R})$ at the reference point \mathbf{R}_0 .⁷³ Here $\Psi_I^{a,(ab)}$ is an adiabatic state, with energy $E^{a,I,(ab)}$, determined from *ab initio* calculations, \mathbf{q} denote the electronic coordinates and \mathbf{R} the Cartesian coordinates of the N^{at} , nuclei. This choice of diabatic representation is permitted as the diabatic states are defined up to a single arbitrary, geometry independent, unitary transformation. Since at \mathbf{R}_0 , Ψ_u^d is an adiabatic state, it carries an irreducible representation of the CNPI⁷⁴⁻⁷⁶ group. For ammonia the CNPI group is isomorphic to D_{3h} . We chose \mathbf{R}_0 to be a point with D_{3h} point group symmetry so that the CNPI symmetry of the diabatic states at \mathbf{R}_0 can be determined from the D_{3h} transformation properties of the adiabatic states at \mathbf{R}_0 .⁷⁵

Using \mathbf{H}^d the electronic Schrödinger equation is given by

$$[\mathbf{H}^d(\mathbf{R}) - \mathbf{I}E^{a,J,(m)}(\mathbf{R})]\mathbf{d}^J = \mathbf{0} \quad (4-1)$$

Here the superscript (m) indicates that the results come from the model Hamiltonian \mathbf{H}^d , rather than the *ab initio* wave functions. The diabatic states are constructed from the adiabatic states, using

$$\Psi_u^d(\mathbf{r}; \mathbf{R}) \equiv \sum_{J=1}^{N^{\text{states}}} \Psi_J^{a,(ab)}(\mathbf{r}; \mathbf{R})(d^{-1})_u^J(\mathbf{R}) = \sum_{J=1}^{N^{\text{states}}} \Psi_J^{a,(ab)}(\mathbf{r}; \mathbf{R})d_J^u(\mathbf{R}) \quad (4-2)$$

From eqs. (4-1) and (4-2) and their derivatives, with the derivation given in section 3.4.1, one obtain the derivative couplings between the quasi-diabatic states as:

$$\sum_{I,J}^{N^{\text{states}}} [\delta f_k^{a,I,J}(\mathbf{R})]^2 = \sum_{I,J}^{N^{\text{states}}} \left\langle \Psi_I^d(\mathbf{q}; \mathbf{R}) \left| \nabla_k \Psi_J^d(\mathbf{q}; \mathbf{R}) \right\rangle_{\mathbf{q}}^2, \quad (4-3)$$

where there residual coupling $\delta f_k^{a,I,J}(\mathbf{R})$ is the difference between *ab initio* derivative couplings and the couplings generated by the adiabatic-to-diabatic transformation, which is given by the fit:

$$\delta f_k^{a,I,J}(\mathbf{R}) \equiv f_k^{a,I,J,(ab)}(\mathbf{R}) - f_k^{a,I,J,(m)}(\mathbf{R})$$

Therefore norm of residual couplings $\|\delta f_k^{a,I,J}(\mathbf{R})\|$ can be used as a direct measure of the degree of diabaticity of the representation.

ii. Diabatic Hamiltonian

(a) General Form

\mathbf{H}^d is expanded in terms of basis matrices, $\mathbf{B}^{u,v}$, as :

$$\mathbf{H}^d(\mathbf{R}) = \sum_{n=1}^{N^c} V_n p^{(n)}(\mathbf{R}) \mathbf{B}^{u(n),v(n)} \quad (4-4)$$

Details of the definition have been discussed in the previous chapter, in section 3.3.1.

The polynomials $p^{(n)}(\mathbf{R})$ are symmetry adapted according to the CNPI group. The $p^{(n)}(\mathbf{R})$ are constructed from basic monomials $g_{l(n)}(\mathbf{R})$ using $\hat{P}^{\mu(n)} g_{l(n)}(\mathbf{R}) = p^{(n)}(\mathbf{R})$. \hat{P}^{μ} is a standard projection operator⁷⁷ for the μ^{th} irreducible representation of the CNPI group

$$\hat{P}^{(\mu)} = \frac{1}{O_G} \sum_x \Gamma^{(\mu)}(x) \hat{x} \quad (4-5)$$

Here O_G is the number of group elements, x , whose corresponding operator is denoted \hat{x} . Since only 1-dimensional representations will be required here, given $\Gamma^{(\mu)}(x)$ the irreducible character, and the effect of the group operations, \hat{x} , on the functions g_l , it is straightforward to evaluate $\hat{P}^{\mu(n)} g_{l(n)}$.

The projector used in eq. (4-5) depends (only) on the block of \mathbf{H}^d , and different projections are required for different blocks. For its contribution to $\mathbf{B}^{u,v}$ to be nonvanishing, a symmetry adapted $p^{(n)}$ should transform as the direct product $\mu(n) = ir(u) \times ir(v)$, where $ir(u)$ is the irreducible representation carried by Ψ_u^d . This

result, which is also used in Refs. ^{30,15}, is rigorous at \mathbf{R}_0 . Its utility is demonstrated numerically, in Sec. 4.4.

(b) Form of the monomials

As discussed in appendix 3.6.1 of the previous chapter, we use a generalization of an idea introduced by Bowman and coworkers to describe a single adiabatic potential energy surface⁷⁸ to correctly describe the bond-breaking process. Four distinct basic functions of the internal coordinates, w_i , are used, given in eq. (3-32).

The $g_l(\mathbf{R})$ are constructed as products of the w and have the monomial form given by eq. (3-33). The order of the monomial g_l , $o(l)$, is given by eq. (3-34). In this work, $\alpha_{m,i,j}^{(l)}$ and $\beta_{i,j,k,m}^{(l)}$, which are introduced in eq. (3-33), and the parameters s_j , α , $r_{i,j}^{(a)}$, $r_{i,j}^{(b)}$, $r_{i,j}^{(c)}$ and $r_{i,j}^{(d)}$, are chosen by trial and error in the range $s_j > 0$, $r_{i,j}^{(x)} > 0$ and $\alpha > 1/2$.

iii. Parametrization of H^d

The g_l from which the $p^{(n)}$ are constructed are enumerated with the help of Table 4-1. Parameters for g_l . Noting that there are three NH and three HH internuclear distances, $r_{i,j}$, there are 34 functions in that table. Denote the order of the j^{th} function in a given g_l as n_j . Then the $p^{(n)}$ are constructed from monomials, g_l , satisfying all the following constraints, on the n_j : (i) the total order is lower or equal to 4 ($\sum_{j=1}^{34} n_j \leq 4$); (ii) the maximum total order of the NH Gaussian functions is 3; (iii) the maximum total order of the HH Gaussian functions is 3; and (iv) the maximum total order of any reciprocal function is 1. Also reciprocal functions with 0 shifts in the denominator only appear in 1st order monomials. After projection and elimination of symmetry zeros, we find $N^c = 9652$.

Table 4-1. Parameters for g_l

(a) Exponential Coordinates: $w_1(r_{i,j}) = \exp[-s_1(r_{i,j} - r_{i,j}^{(a)})]$

Coordinate#	Atoms	s_1	$r_{i,j}^{(a)}$	Max Order
1	N-H	1.5	1.5	4
2	H-H	0.5	1.0	4

(b) Gaussian Coordinates: $w_2(r_{i,j}) = \exp[-s_2(r_{i,j} - r_{i,j}^{(b)})^2]$

Coordinate#	Atoms	s_2	$r_{i,j}^{(b)}$	Max Order
1	N-H	2.3	2.0	3
2	N-H	1.5	2.5	
3	N-H	1.5	3.0	
4	H-H	0.8	2.5	3
5	H-H	0.4	3.3	

(c) Reciprocal Coordinates: $w_3(r_{i,j}) = \exp[-s_1(r_{i,j} - r_{i,j}^{(c)})]/(r_{i,j} + r_{i,j}^{(d)})$ Max order=1.

Coordinate#	Atoms	s_3	$r_{i,j}^{(c)}$	$r_{i,j}^{(d)}$
1	N-H	1.25	1.0	1.0
2	N-H	1.30	2.0	0.0
3	H-H	0.5	1.0	1.0
4	H-H	0.5	1.5	0.0

(d) Scalar Triple-product Coordinates: $w_4^{i,j,k,l} = \mathbf{r}_{i,j} \times \mathbf{r}_{i,k} \cdot \mathbf{r}_{i,l} / |r_{i,j}r_{i,k}r_{i,l}r_{j,k}r_{j,l}r_{k,l}|^\alpha$ $\alpha=0.55$

iv. Determination of \mathbf{H}^d

The equations used to determine the \mathbf{V} and their solution were initially reported in Chapter 2 and later revisited in Chapter 3. Briefly the \mathbf{V} are determined by the requirement that the energies, energy gradients and the interstate coupling gradients (= derivative coupling vector times the energy difference) determined from \mathbf{H}^d agree with those determined from the *ab initio* calculations. Data at $N^{\text{point}} = 2536$ nuclear configurations, producing ~ 40000 equations, was used. The nuclear configurations were largely generated using ~ 2000 surface hopping trajectories^{39, 79} sampled from a Wigner distribution by the requirement that a fixed percentage of trajectories, here 99% (1%) remain within the region well defined (approximately defined) by the nuclear configurations. Since there are many more equations than V_n , the equations are partitioned into two groups, those solved in least squares manner and those solved exactly. The equations included in the exact block are not entirely arbitrary. For example, the energy difference at a point of conical intersection must be exactly zero to ensure that proper intersection adapted coordinates⁸⁰ can be constructed; the branching plane vectors,⁸¹ energy difference gradient and interstate coupling gradients, also need to be exactly reproduced, so that the residual coupling is finite at a point of intersection. It is, also, desirable that energies and gradients be reproduced at critical points to ensure the correct topology of \mathbf{H}^d . Nuclear configurations whose electronic structure data is exactly reproduced are called nodes.

Note from eq (3-29) that the requirement that the \mathbf{H}^d and *ab initio* determined interstate coupling gradients agree, in a least squares sense or exactly, gives \mathbf{H}^d is diabatic character.

v. *Quality of the Fit.*

There are two issues concerning the \mathbf{H}^d representation: (i) how reliably does the \mathbf{H}^d describe the *ab initio* data and (ii) how reliably does the \mathbf{H}^d representation of the NH_3 $1,2^1\text{A}$ potential energy surfaces and their interactions, describe experimentally measured observables. The first question has been addressed in Chapter 3. The second is the subject of Sec. 4.4. Here we briefly summarize from Chapter 3 how reliably the \mathbf{H}^d describes the *ab initio* data.

Over the energy range $0 - 60,000 \text{ cm}^{-1}$ the \mathbf{H}^d representation of the 1^1A (2^1A) potential energy surface has a mean unsigned[root mean square] error of 73[210] (83[284]) cm^{-1} . The representation is by construction more accurate in the range $0 - 50,000 \text{ cm}^{-1}$ where the \mathbf{H}^d representation of the 1^1A (2^1A) potential energy surface has a mean unsigned[root mean square] error of 51[82] (13[24]) cm^{-1} .

Another assay of the accuracy of the \mathbf{H}^d representation involves the energy gradients and the derivative couplings. For the preponderance of the points the energy gradient are accurate to 1% error and derivative couplings are accurate to 10%. The results for the large derivative couplings are particularly gratifying since data in the range $10^1 - 10^8$ are well reproduced, with no point in error by $> 10\%$. This is because the large derivative couplings are near points of conical intersection which are nodes in the fitting procedure. For small derivative couplings, which occur in regions of large energy separation, agreement decreases, which is not unexpected since \mathbf{H}^d provides a removable approximation to the derivative coupling while the *ab initio* values contain a small nonremovable⁴⁶ part. Up to $50,000 \text{ cm}^{-1}$, the average percentage error for energy gradients for points with magnitude of gradient higher than 10^{-4} is 2.33%. For the full

range of data the error in the norms of energy gradients is less than 10% except for a limited number of outliers. The outliers are found in the region of large gradients on repulsive walls, with high energies and the errors are only slightly over 10% and all are below 30%. Given their small number, high energies and size of their error, it is unlikely that they will affect the dynamics.

4.3.2 Quantum Dynamics

Following *LLXG*,³⁵ the non-rotating nuclear Hamiltonian for the NH₃ systems is defined in the (2+1) Radau-Jacobi coordinate system,

$$\mathbf{H}_e = \sum_{i=0}^2 \left(-\frac{1}{2\mu_i} \frac{\partial^2}{\partial r_i^2} + V_i(r_i) \right) + \sum_{i=0}^2 \frac{\hat{j}_i^2}{2\mu_i r_i^2} + \left[V(r_0, r_1, r_2, \theta_1, \theta_2, \varphi) - \sum_{i=0}^2 V_i(r_i) \right] \quad (4-6)$$

where r_1 and r_2 are two Radau radial coordinates, r_0 is Jacobi radial coordinate, μ_1, μ_2 and μ_0 are the corresponding reduced masses, θ_1 (θ_2) is the included angle between \vec{r}_1 (\vec{r}_2) and \vec{r}_0 and φ is the relative azimuthal angle between \vec{r}_1 and \vec{r}_2 in body fixed system. \hat{j}_1 and \hat{j}_2 are the angular momentum operators for r_1 and r_2 respectively, and $\hat{j}_0^2 = (\hat{j}_1 + \hat{j}_2)^2$. V is the 6 dimensional potential energy surface, and $V_i(r_i)$ are the reference potential for r_i .

The wavefunction is discretized in a mixed representation. The three radial coordinates were represented by the discrete variable representation (DVR) or potential-optimized discrete variable representation (PODVR).⁸² For the angular coordinates, finite basis representation (FBR) is used.

(i) Absorption spectrum

The parity (p) adapted wavefunction can thus be expanded on the FBR basis,

$$|\Phi\rangle^p = \sum_{i_0 i_1 i_2 j_1 j_2 m} \psi_{i_0 i_1 i_2 j_1 j_2 m}^p |i_0 i_1 i_2\rangle |j_1 j_2 m, p\rangle \quad (4-7)$$

where $\psi_{i_0 i_1 i_2 j_1 j_2 m}^p$ is the wave function in the discrete representation, i_0 , i_1 , and i_2 denote the indices of three radial coordinates, respectively. $|j_1 j_2 m, p\rangle$ are the angular FBR basis functions defined as parity-adapted products of the spherical harmonics,

$$|j_1 j_2 m, p\rangle = (2 + 2\delta_{m,0})^{-1/2} (|j_1 m\rangle |j_2 - m\rangle + p |j_1 - m\rangle |j_2 m\rangle), p = \pm 1 \quad (4-8)$$

The detailed formulation for how the Hamiltonian acts on basis set can be found in our earlier work.³⁵

To simulate the absorption spectrum, we first calculated vibrational levels of NH₃ on its ground electronic state using the iterative Lanczos algorithm⁸³⁻⁸⁴ with the basis set of 5 PODVR for r_1 and r_2 , 21 sine-DVR for $r_0 \in (1.2, 4.5)a_0$ and $j_1, j_2 = 0 : 24$. For ND₃, we have used a basis set of 5 PODVR for r_1 and r_2 , 25 sine-DVR for $r_0 \in (1.2, 4.5)a_0$ and $j_1, j_2 = 0 : 30$. 500 steps of iterations were sufficient to converge the low-lying energy levels.

The absorption spectrum was calculated assuming a Condon transition, in which the ground state vibrational eigenfunctions were placed vertically on the \tilde{A} state. The wave functions were transformed into a new grid/basis for the excited state propagation. In particular, we used 21 sine-DVR points for three radial coordinates in the region of (1.2, 4.5) a_0 and 25 FBR functions for angular coordinates in absorption spectrum calculation of NH₃, 25 sine-DVR points for three radial coordinates in the same region and 30 FBR functions for angular coordinates in calculation of ND₃. The evolution of the excited state wave packet was performed using the Chebyshev propagator.⁸⁵

The $\tilde{A} \leftarrow \tilde{X}$ absorption spectrum, $S(E)$, was obtained from the Fourier transform of the Chebyshev auto-correlation function $C_k \equiv \langle \psi_0 | \psi_k \rangle$,⁸⁶

$$S(E) = \frac{1}{\pi H^- \sin \vartheta} \sum_{k=0} (2 - \delta_{k,0}) \cos(k\vartheta) C_k \quad (4-9)$$

H^- is half-width of the Hamiltonian, $\vartheta = \arccos E$ is the Chebyshev angle, and k is the Chebyshev order. To avoid reflection at the edge of the grid, a damping function was used in Chebyshev propagation, and the damping starts at $r = 3.1a_0$ for all three radial coordinates. To obtain a convergent absorption spectrum, 5000 steps of Chebyshev propagation were carried out for both NH_3 and ND_3 .

To determine accurately the positions and widths of narrow resonances, a low-storage filter diagonalization (LSFD) method was used.⁸⁷

(ii) Non-adiabatic dynamics

For non-adiabatic dynamics simulations, the total wave function, which is expressed as a vector:

$$|\Phi\rangle = \begin{pmatrix} \Phi^A \\ \Phi^X \end{pmatrix} \quad (4-10)$$

has two components for the two electronic states. They are expanded in terms of the parity (p) adapted basis:

$$\Phi^{A/X,p} = \sum_{i_0 i_1 i_2 j_1 j_2 m} \Psi_{i_0 i_1 i_2 j_1 j_2 m}^{A/X,p} |i_0\rangle |i_1 i_2\rangle |j_1 j_2 m, p\rangle, \quad (4-11)$$

where $\Psi_{i_0 i_1 i_2 j_1 j_2 m}^{A/X,p}$ are the wave functions in the discrete representation. Here, i_0 denotes the DVR grid index for the radial coordinate r_0 , while i_1 and i_2 label the vibrational basis functions for the radial directions of r_1 and r_2 , respectively. $|j_1 j_2 m, p\rangle$ is the angular FBR basis function defined as parity-adapted products of the spherical harmonics,

$$|j_1 j_2 m, p\rangle = (2 + 2\delta_{m,0})^{-1/2} (|j_1 m\rangle |j_2 - m\rangle + p |j_1 - m\rangle |j_2 m\rangle), \quad p = \pm 1. \quad (4-12)$$

As expected, the grid needed to compute the dissociation fluxes in both the $\text{NH}_2(\tilde{X}^2B_1)$ and $\text{NH}_2(\tilde{A}^2A_1)$ channels is much larger than that needed to compute the absorption spectra. To make the basis compact, we have used non-direct basis approach⁸⁸ for the radial coordinates. In particular, different numbers of vibrational basis functions for the two non-reactive coordinates, namely r_1 and r_2 , were used in two different r_0 regions.

The photodissociation was simulated assuming a Franck-Condon model, in which the ground state vibrational eigenfunction was placed vertically on the excited state PES.

The propagation of the wave packet vector, $\Psi_k = \begin{pmatrix} \Psi_k^A \\ \Psi_k^X \\ \Psi_k \end{pmatrix}$, was performed with the

Chebyshev propagator:⁸⁵

$$\Psi_k = 2D\mathbf{H}_s\Psi_{k-1} - D^2\Psi_{k-2}, \quad k \geq 2 \quad (4-13)$$

with

$$\Psi_1 = D\mathbf{H}_s\Psi_0 \quad (4-14)$$

and

$$\Psi_0 = \begin{pmatrix} \Psi_i \\ 0 \end{pmatrix}, \quad (4-15)$$

in which Ψ_i in eq. (4-15) represents the ground state wave function obtained using the iterative Lanczos algorithm.^{84, 89} The Hamiltonian is scaled to the spectral range of (-1,1) via

$$\mathbf{H}_s = (\mathbf{H} - H^+\mathbf{I}) / H^-, \quad (4-16)$$

in which the spectral medium $H^+ = (H_{\max} + H_{\min})/2$ and half width $H^- = (H_{\max} - H_{\min})/2$ were determined by the spectral extrema, H_{\max} and H_{\min} , which can be readily estimated. Finally, the wave packets are damped near the edge of the grids in all three radial coordinates and the damping functions (D) and parameters are listed in Table 4-2.

Table 4-2. Numerical parameters (in a.u.) used in wave packet calculations.

	NH ₃	ND ₃
Grid/basis ranges and sizes	$r_0 \in (1.2, 14.0), N_0 = 100$	$r_0 \in (1.2, 14.0), N_0 = 120$
	for $1 \leq i_0 \leq 21$, DVR $r_1, r_2 \in (1.2, 4.5), N_1 = N_2 = 21$	for $1 \leq i_0 \leq 23$, DVR $r_1, r_2 \in (1.2, 4.5), N_1 = N_2 = 23$
	for $22 \leq i_0 \leq 100$, Basis $N_1 = N_2 = 5$	for $24 \leq i_0 \leq 120$, Basis $N_1 = N_2 = 6$
Largest values of j_1, j_2 and m	20	23
Damping function for r_0 ^a	$\alpha_D = 0.1, r_{0,D} = 11.1$	$\alpha_D = 0.1, r_{0,D} = 11.1$
Damping functions for r_1 and r_2 ^a	$\alpha_D = 0.1, \alpha_D = 0.1$	$\alpha_D = 0.1, \alpha_D = 0.1$
Flux position for r_0	$r_{0,f} = 10.0$	$r_{0,f} = 10.0$
Propagation steps	15000	15000

^aThe damping function is defined as $D = \exp[-\alpha_D(r - r_D)^2]$, $r \geq r_D$

Due to the excessively large grids needed to resolve the NH₂ internal state distributions, in this work, we elected to compute only the total probabilities in the *A* and *X* channels using a flux method:⁹⁰

$$P^{A/X}(E) = \frac{1}{2\pi\mu_0(H^-)^2 \sin^2 \theta} \times \text{Im} \left\langle \sum_{k=0} (2 - \delta_{k,0}) e^{-ik\theta} \Psi_k^{A/X} \left| \sum_{k'=0} (2 - \delta_{k',0}) e^{-ik'\theta} \left[\delta(r_0 - r_{0f}) \frac{\partial}{\partial r_0} \Psi_{k'}^{A/X} \right] \right. \right\rangle \quad (4-17)$$

The position of the dividing surface (r_{0f}), as given in Table 4-2, is located in the dissociation asymptote beyond the conical intersection.

4.4 Analysis of H^d: Electronic Structure

4.4.1 Electronic Structure: *ab initio* treatment

The *ab initio* electronic structure data used to construct H^d were determined from a multireference configuration interaction (MRCI) expansion comprised of over 30x10⁶ configuration state functions (CSFs), and constructed from molecular orbitals obtained from a two-state, state averaged multiconfigurational self-consistent field (SA-MCSCF) procedure based on aug-cc-pVTZ bases on N and H with an added 3s Rydberg function on nitrogen. All electronic structure calculations were carried out using the COLUMBUS electronic structure codes.⁹¹⁻⁹³

4.4.2 Electronic Structure: Spectroscopic constants

Table 4-3 reports the equilibrium structure and harmonic frequencies of the \tilde{X}^1A_1 and \tilde{A}^1A_2'' states of NH₃, the excitation energy T_e and the ground state dissociation energy, D_e and compares those quantities with the available experimental data and computational

results. Table 4-4 reports the equivalent quantities for the \tilde{X}^2B_1 and \tilde{A}^2A_1 states of NH_2 . The formats of Table 4-3 and Table 4-4 follow those of Tables 4 and 5 of *LVT* for ease of comparison. Note that since the structures reported in these tables are nodes in the fit, the *ab initio* geometries, the values of T_e and D_e as well as barrier heights reported in these tables are exactly reproduced by the \mathbf{H}^d representation. The *ab initio* and \mathbf{H}^d determined equilibrium and saddle point geometries of $\text{NH}_3(\tilde{X}, \tilde{A})$ and $\text{NH}_2(\tilde{X}, \tilde{A})$ are in very good accord with the tabulated ‘best values’, with the largest errors being 0.007 Å and 1.1°. The *ab initio* determined T_e for NH_3 (NH_2) is in error (= best – calculated) by 871 (-205) cm^{-1} compared to best value of 48071 (10978) cm^{-1} . The *ab initio* determined inversion (transition state) barrier on the 1^1A (2^1A) potential energy surface is in error by -173(195) cm^{-1} compared to the best value of 1784 (2348) cm^{-1} . The *ab initio* determined dissociation energy, D_e , of NH_3 on the ground 1^1A potential energy surface is in error by 1258 cm^{-1} compared to a best value of 40510 cm^{-1} . The dissociation energy on the excited state potential energy surface is in error by 179 cm^{-1} compared to a best value of 3416 cm^{-1} . The errors in the T_e values and barriers are less than the level spacing in ν_2 for NH_3 (\tilde{A}), (See section 4.5.2) while the error in ground state D_e is approximately the spacing of two such levels. The errors in the T_e for NH_3 and ground state D_e for NH_3 likely reflect an underestimate of the differential correlation energy of NH_3 near its equilibrium geometry. This error is then expected to decrease as the NH_3 bond is stretched. Consistent with this observation, the error in D_e for NH_3 on the excited state is small. In the *LVT* \mathbf{H}^d a correction function was introduced to make the \mathbf{H}^d determined potential energy surfaces reproduce the experimental values of D_e and T_e values exactly.

These errors in the D_e and T_e values in the \mathbf{H}^d described here should not impact the spectral simulations reported in Sec. 4.5.

Table 4-3. Spectroscopic constants and related data for \tilde{X}^1A_1 and \tilde{A}^1A_2'' states of NH_3 . Energies in cm^{-1} , distances in \AA and angles in degrees. Ordering of harmonic frequencies is that of Ref. ⁹⁴ except for C_{2v} saddle point on 2^1A potential energy surface where energy ordering is used. For C_{2v} geometries H^1, H^2 are symmetry equivalent
(a) 1^1A Surface

	\mathbf{H}^d	<i>ab initio</i>	best
<i>Equilibrium (C_{3v}, \tilde{X}^1A_1)</i>			
$r_e(\text{N-H})$	1.0154	1.0154	1.011 ^a
$\angle \text{H-N-H}$	106.35	106.35	106.75 ^a
Harmonic Frequencies			
	3447.08	3456.26	3483.1 ^a
	1093.12	1066.24	1052.8 ^a
	3581.40	3584.10	3616.0 ^a
	1655.33	1674.48	1675.7 ^a
<i>Saddle Point (D_{3h})</i>			
$r_e(\text{N-H})$	0.9979	0.9979	0.9943 ^a
Classical Barrier Height	1957.2	1957.2	1784.7 ^a
Harmonic Frequencies			
	3610.0	3620.1	3640.0 ^a
	847.1 <i>i</i>	870.0 <i>i</i>	837.4 <i>i</i> ^a
	3825.2	3830.5	3852.7 ^a
	1575.5	1584.0	1585.7 ^a
<i>Asymptote</i>			
$D_e \text{NH}_3(\tilde{X}) \rightarrow \text{NH}_2(\tilde{X}) + \text{H}$	39252.1	39252.1	40510 ^b

^aRef. ⁹⁵

^bRef. ¹⁹

Table 4-3. (Continued)

(b) 2^1A Surface

	H^d	<i>ab initio</i>	best
<i>Equilibrium (D_{3h}, \tilde{A}^1A_2'')</i>			
$r_e(\text{N-H})$	1.0485	1.0485	1.055(8) ^c
Harmonic Frequencies			
	2838.7	2793.7	2870 ^d
	780.7	754.1	892 ^d
	2949.7	2955.8	3020 ^d
	1377.7	1334.3	1110 ^d
T_e	47198.8	47198.8	48071 ^d
<i>Asymptote</i>			
$D_e \text{NH}_3(\tilde{A}) \rightarrow \text{NH}_2(\tilde{A}) + \text{H}$	3237	3236	3416
<i>Saddle Point (C_{2v})</i>			
$r_e(\text{N-H})$	1.3055	1.3054	1.298 ^d
$r_e(\text{N-H}^1)$	1.0408	1.0408	1.040 ^d
$\angle \text{H}^2\text{NH}^1$	112.5	112.5	112.4 ^d
$\angle \text{HNH}^1$	123.8	123.8	123.8 ^d
Classical Barrier Height	2152.98	2152.98	2348 ^d
Harmonic Frequencies			
	2000.10 i	2003.32 i	
	508.05	475.29	
	981.3	962.68	
	1419.51	1435.37	
	2995.81	3027.8	
	3231.1	3244.42	

^cRef. ⁹⁶^dRef. ⁸

Table 4-4. Spectroscopic constants and related data for \tilde{X}^2B_1 and \tilde{A}^2A_1 states of NH_2 . Energies in cm^{-1} , distances in Å and angles in degrees. Ordering of harmonic frequencies is that of Ref. ⁹⁴

	Hd	ab initio	best
1^1A Equilibrium (\tilde{X}^2B_1)			
$r_e(\text{N-H})$	1.0283	1.0283	1.024 ^a
$\angle\text{HNH}$	102.8	102.8	103.4 ^a
Harmonic Frequencies			
	2934.62	3350.23	3374.2 ^b
	1556.79	1539.57	1523.5 ^b
	3427.33	3443.40	3481.2 ^b
2^1A Equilibrium (\tilde{A}^2A_1)			
$r_e(\text{N-H})$	0.9987	0.9986	1.004 ^c
$\angle\text{HNH}$	145.13	145.1	144 ^c
Harmonic Frequencies			
	3796.34	3612.56	3635 ^b
	935.75	978.14	964 ^b
	4154.31	3924.56	3953 ^b
T_e	11184.01	11183.1	10977.8 ^d

^aFrom Ref. ⁹⁷ as cited in *LVT*

^bFrom Ref. ⁹⁸ as cited in *LVT*

^cRef. ⁹⁴

^dFrom *LVT*.

The **H^d** determined harmonic frequencies at the minimum and saddle point on the ground state potential energy surface of NH_3 are in good accord with the *ab initio* values. The largest error for an **H^d** determined frequency is -41 cm^{-1} compared to a measured value of 1052.8 cm^{-1} which occurs at the ground state minimum. The ω_4 harmonic frequency at the equilibrium geometry of the \tilde{A}^1A_2'' state exhibits the greatest deviation from a measured result (1110.9 cm^{-1}) being in error by over -20%. However it should be

noted that this minimum is quite shallow, complicating the determination of harmonic frequencies. For example, the -111 cm^{-1} error in ω_2 is inconsistent with the magnitude of error, $< 70 \text{ cm}^{-1}$ in the ν_2 progression discussed in Sec. 4.5. The harmonic frequencies for the asymptotic states of NH_2 are in general satisfactorily described.

4.4.3 Electronic Structure: Conical intersection seam

The seam of conical intersection is considered in Table 4-5, which reports 26 points on the seam. These points are nodes, with the \mathbf{H}^d and *ab initio* determined energy differences, and \mathbf{g} and \mathbf{h} constrained to agree. The absolute energies are seen to be in very good agreement (maximum error 65 cm^{-1}) even though, with the exception of the minimum energy crossing, they are not so constrained. At all such nuclear configurations the 1^1A and 2^1A states are degenerate to less than 1 wave number. All points on the seam have at least a plane of symmetry. This is a consequence of the fact that for planar geometries the 1^1A and 2^1A states carry $^1\text{A}'$ and $^1\text{A}''$ irreducible representations so that the \mathbf{h} vector (interstate coupling vector) must transform as A'' and there is only a single a'' coordinate. The minimum energy conical intersection, the MEX, is approximately $4808 (6154) \text{ cm}^{-1}$ below the $\tilde{\text{A}}^1\text{A}_2''$ minimum where the analogous result for *LVT* is given in parenthesis. As is the case for the saddle point on the 2^1A potential energy surface, the MEX has a single elongated NH bond. Its structure is in good accord with the result of *LVT*. (See Table 4-5.)

Table 4-5. Conical intersection seam for 1,2¹A States of NH₃.

E_1 , E_2 and $\Delta E = E_2 - E_1$ in cm⁻¹ relative to \tilde{X}^1A_1 state minimum. For C_{2v} structures H¹ and H² are symmetry equivalent. The 22 conical intersection points with energies < 50,000 cm⁻¹ are nodes, with energy difference, \mathbf{g} and \mathbf{h} fit exactly (Two such points exhibit small error in $\|\mathbf{g}\|$, less than 1%.) The *ab initio* geometries and energies are exactly reproduced by \mathbf{H}^d . Minimum energy crossing indicated by a *. $E_{\text{avg}} = (E_2 + E_1)/2$. Δ implies the difference between the \mathbf{H}^d determined and the *ab initio* result.

(a) C_{2v} Conical Intersections

rNH ¹	rNH ³	$\angle H^1NH^3$	$\angle H^1NH^2$	E_{avg}	ΔE_{avg}	$E_2 - E_1$	$\Delta(E_2 - E_1)$	$\ \mathbf{h}\ $	$\ \mathbf{g}\ $
*1.0222	1.9689	125.40	109.20	42390	0	0.0001	-5.7E-08	0.0523	0.0728
0.9243	1.9802	126.63	106.74	46472	-9	0.0017	4.3E-08	0.0536	0.0758
0.9731	1.9750	126.03	107.95	43310	-3	0.0002	5.2E-08	0.0529	0.0742
1.0691	1.9622	124.79	110.43	43071	-2	0.0001	-4.7E-08	0.0518	0.0719
1.1626	1.9461	123.49	113.02	47433	3	0.0072	6.2E-08	0.0508	0.0707
1.2970	1.9137	121.35	117.30	57246	-45	0.0001	-3.0E-09	0.049(6)	0.07(11)
1.0478	1.9691	125.41	109.18	42631	-2	0.0014	3.5E-08	0.0523	0.0729
1.4601	1.3229	156.50	46.99	71630	-14	0.0001	1.2E-07	0.07(38)	0.0(983)
1.3344	1.5875	148.02	63.95	64028	21	0.0004	1.0E-09	0.07(73)	0.09(58)
1.1656	1.7569	138.71	82.58	49623	-27	0.0013	1.0E-07	0.0730	0.086(4)
1.0805	1.8627	131.76	96.49	43916	4	0.0000	4.2E-08	0.0623	0.0798
0.9730	2.1167	118.17	123.67	43944	-22	0.0001	3.0E-08	0.0433	0.0628
1.0218	1.9782	58.63	117.26	44599	-1	0.0022	2.6E-08	0.0673	0.0655

(b) C_s Intersection Points

rNH ¹	rNH ²	rNH ³	$\angle H^1NH^3$	$\angle H^1NH^2$	E_{avg}	ΔE_{avg}	$E_2 - E_1$	$\Delta(E_2 - E_1)$	$\ \mathbf{h}\ $	$\ \mathbf{g}\ $
1.0225	1.0223	1.9681	127.42	109.14	42391	0	0.0176	1.4E-8	0.0524	0.0729
1.0217	1.0217	1.9682	120.34	109.33	42397	2	0.0449	4.5E-8	0.0525	0.0728
1.0201	1.0201	1.9662	115.14	109.73	42420	6	0.0000	-5.1E-8	0.0531	0.0727
1.0137	1.0137	1.9581	104.36	111.39	42556	23	0.0004	5.3E-8	0.0553	0.0723
0.9771	0.9760	1.9190	163.36	122.02	44824	-65	0.0001	1.9E-8	0.0625	0.069(0)
1.0742	0.9684	1.9691	125.41	109.18	43357	-6	0.0014	2.7E-8	0.0523	0.0730
1.1271	0.9155	1.9691	125.41	109.18	46358	-12	0.0022	4.3E-8	0.0524	0.0735
1.1904	1.0339	2.0693	9.08	101.83	48452	2	0.7355	-1.7E-7	0.0522	0.0349
1.0016	1.0009	2.2460	116.87	143.73	48706	-3	0.0001	-9.3E-8	0.0424	0.0388
0.9687	0.9651	2.0668	64.13	127.32	45848	5	0.0005	3.9E-8	0.0674	0.063(6)
0.9788	0.8059	1.9972	119.47	108.24	55786	27	0.0041	3.2E-8	0.053(9)	0.07(70)
1.0460	0.9954	1.8319	122.92	89.35	44825	-4	0.0607	1.0E-7	0.0692	0.0848
0.9773	0.9593	1.8520	154.96	93.72	45312	-30	0.0125	6.7E-8	0.0688	0.0831

^a Minimum energy crossing from *LVT* is R(N-H¹)=1.990, R(N-H³)=1.21 $\angle H^1NH^2 = 110^\circ$ and $\angle H^3NH^2 = 107.9^\circ$.

The electronic structure treatment in this region is not validated in the current spectral simulations which do not consider the $\text{NH}_2(\tilde{X}, \tilde{A})$ branching. This analysis will be the subject of a subsequent study. Figure 4-1 provides a 2-dimension slice from the $1,2^1A$ potential energy surfaces. Key critical points and their energies are indicated although only the approximate geometries of these structures are shown.

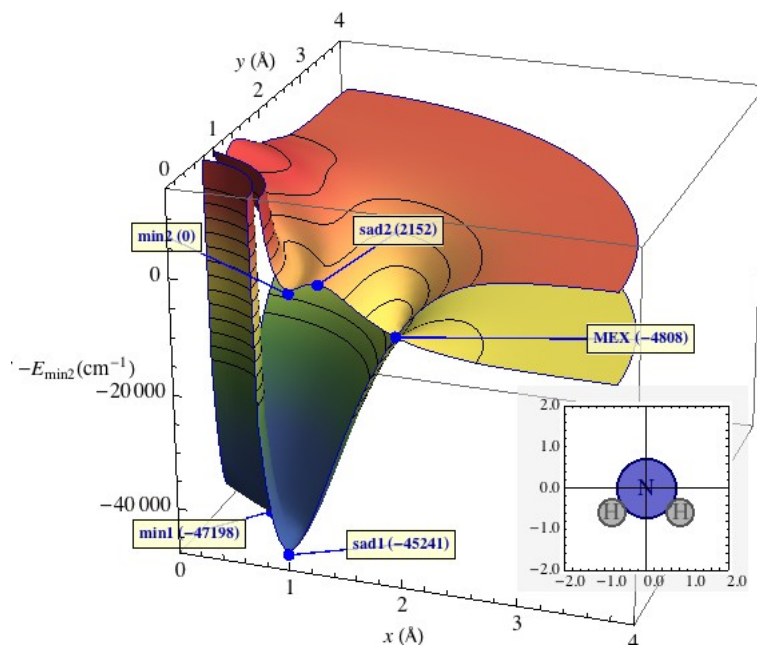


Figure 4-1. Three dimensional plot of adiabatic potential energy surfaces showing: (i) minima on ground state and excited states, (ii) a saddle points on the 1^1A and 2^1A potential energy surfaces and (iii) the minimum energy crossing on the $1,2^1A$ seam of conical intersections.

Energies in cm^{-1} . The geometry of the NH_2 used in this figure is also indicated. The x and y coordinates describe the motion of the third H in the bisector plane of the NH_2 .

4.5 Analysis of H^d : Vibrational Spectra

4.5.1 The \tilde{X}^1A_1 State

Table 4-6 reports the low-lying vibrational levels of $\text{NH}_3(\tilde{X})$ and compares them with the spectroscopic data and the equivalent theoretical treatment based on the $LVT \mathbf{H}^d$.

It should be noted that other ground state potential energy surfaces are available for NH_3 ,

for which essentially exact agreement with experimental data is possible using the computational treatment discussed in Section 4.3.2.^{95, 99} However the agreement using the potential energy surface derived from the present \mathbf{H}^d is quite reasonable, a significant improvement over that of *LVT*. The improved accuracy will be an important consideration in future studies of vibrationally mediated photodissociation.

4.5.2 The \tilde{A}^1A_2'' State

The absorption spectrum from the ground vibrational level of the \tilde{X}^1A_1 state is considered in Figure 4-2, Figure 4-3, Figure 4-4. This spectrum consists of a progression in the ν_2 mode, in agreement with experiment. There are three issues to be addressed here, the line positions, the line intensities and the line widths or lifetimes.

(i) Energy Levels

Figure 4-2 address the issue of the line positions. The experimental line positions $E^{\text{exp}}(n)$, shifted \mathbf{H}^d determined line positions $E_{\text{shift}}^m(n) \equiv E^m(n) - [E^m(0) - E^{\text{exp}}(0)]$ and the energy level error $\delta E^m(n) = E^{\text{exp}}(n) - E_{\text{shift}}^m(n)$ are reported. Here the energy of a level with n quanta in ν_2 is $E^m(n)$ and the superscript denotes the method used to compute $E(n)$ with $m=PW$ (*LVT*) if $E(n)$ is determined from the 2^1A PES constructed using the \mathbf{H}^d in this work (in *LVT*) or $m=\text{exp}$ if experimental values for $E(n)$ are used. Table 4-6 reports the unaltered $E^m(n)$. Figure 4-2 reports data for NH_3 (ND_3). Note that the $E^{PW}(n)$ in Table 4-6 reflect a systematic error due principally to the error in T_e for the $\text{NH}_3(\tilde{A})$ state noted in Sec. 4.4.2. This systematic error is eliminated in E_{shift}^{PW} . The present \mathbf{H}^d based results are quite reasonable with $-70 \text{ cm}^{-1} < \delta E^{PW}(n) < 50 \text{ cm}^{-1}$, compared to

$\Delta E^{\text{exp}}(n) = E^{\text{exp}}(n) - E^{\text{exp}}(n-1)$ in the $900 \text{ cm}^{-1} - 1000 \text{ cm}^{-1}$ range for NH_3 and with $-90 \text{ cm}^{-1} < \delta E^{\text{PW}}(n) < -10 \text{ cm}^{-1}$, compared to $\Delta E^{\text{exp}}(n)$ in the $650 \text{ cm}^{-1} - 750 \text{ cm}^{-1}$ range for ND_3 . As is evident from $|\delta E^{\text{LVT}}(n)|$ the present \mathbf{H}^{d} significantly outperforms the $\text{LVT } \mathbf{H}^{\text{d}}$.

Table 4-6. Low-lying vibrational levels of $\text{NH}_3(\tilde{X})$ obtained using the $\text{LVT } \mathbf{H}^{\text{d}}$ and the present work (PW). Energies in cm^{-1} relative to corresponding zero-point energy.

v_1	v_2^p	v_3^l	v_4^l	Exp ^a	LVT ^b	PW
0	0+	00	00	0	0	0
0	0-	00	00	0.79	0.108	0.45
0	1+	00	00	932.43	1093.05	974.36
0	1-	00	00	968.12	1099.96	997.65
0	2+	00	00	1597.47	1966.96	1679.27
0	0+	00	11	1626.28	1672.23	1622.55
0	0-	00	11	1627.37	1672.29	1623.76
0	2-	00	00	1882.18	2092.07	1918.57
0	3+	00	00	2384.15	2653.50	2420.94

^aRef. 100

^bRef. 35

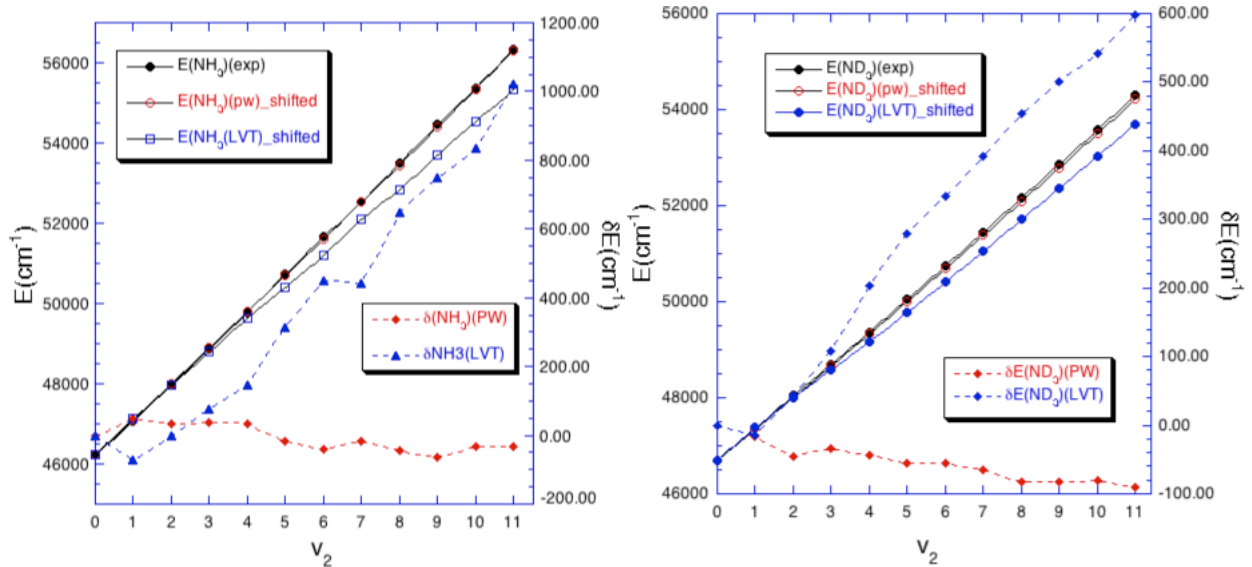


Figure 4-2. $E^{\text{exp}}(n)$, $E_{\text{shift}}^m(n) = E^m(n) - [E^m(0) - E^{\text{exp}}(0)]$ and $\delta E^m(n) = E^{\text{exp}}(n) - E_{\text{shift}}^m(n)$ for $m = \text{PW}$ and LVT for n quanta in v_2 mode of \tilde{A} state of NH_3 and ND_3 . Energies in cm^{-1} ; Left: NH_3 ; Right: ND_3 .

(ii) Intensities

Figure 4-3 report the intensities for the umbrella mode progression for NH_3 and ND_3 respectively and compare them with the measured intensities.⁶ Note that the finite temperature spectra obtained experimentally contain a temperature-dependent nuclear spin statistics¹³ and multiple J values. To simulate the finite temperatures in the jet, we have adopted the recommended temperatures of 16 K for NH_3 and 10 K for ND_3 given by Rosmus et al.¹³ The agreement is seen to be quite good. Note that the origin of the computed spectrum has been shifted so as to agree with the measured value. The maximum intensity peak $n = 6$ (9) for NH_3 (ND_3) agrees with that of the measured spectra. This represents a considerable improvement over the previous simulation by *LLXG* based on the *LVT* \mathbf{H}^d , for which the maximum intensity peaks were predicted at $n = 3$ or 4 (7 or 8), thus in disagreement with experiment.

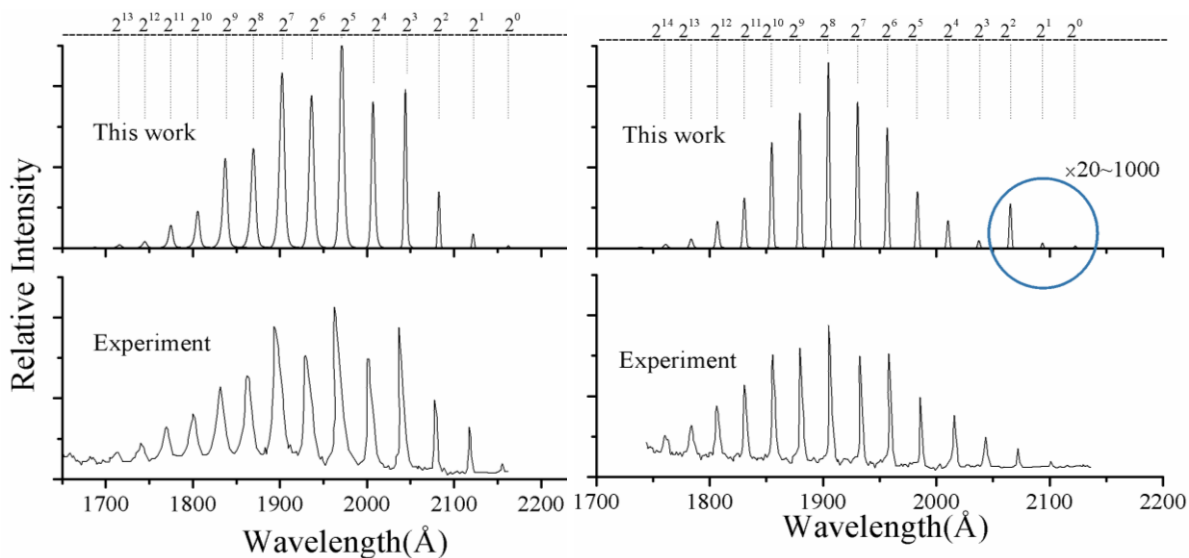


Figure 4-3. Intensities of transitions from the ground vibrational level of $\text{NH}_3(\tilde{X})$ to the 2^n level of the \tilde{A} state, compared with measured spectra from Ref. ⁶ Left: NH_3 . Right: ND_3 .

(iii) Line widths

Figure 4-4 compares the measured line widths for NH_3 with $0 \leq v_2 < 11$ with those computed from the present \mathbf{H}^d . The line widths for $0 \leq v_2 \leq 6$ are taken from the compilation in Ref. ⁸ while the remainder are taken from Ref. ⁶. For ND_3 line widths for the range $0 \leq v_2 \leq 2$ where the experimental data are most consistent,^{4, 6-7} are reported.⁷ The computed results are seen to be in very good accord with experimental results. Table 4-7 provides a more complete tabulation of the line widths. The line widths based on the present \mathbf{H}^d are seen to be in good accord with the measured results for NH_3 throughout the range of available measurements. The agreement with the ND_3 results for v_2 beyond the range in Fig. 3 is somewhat more qualitative, although based on the existing data the possibility of the experimental line widths being systematically too large for $v_2 \geq 3$ cannot be ruled out. Again the performance for the *LVT* \mathbf{H}^d whose results are also reported in Table 4-7 are seen to be less satisfactory. The most likely source of the difference in the line widths between the present \mathbf{H}^d and that developed by *LVT* is the difference in the classical barrier height which is 2153 cm^{-1} in the present work and 1774 cm^{-1} in *LVT*.

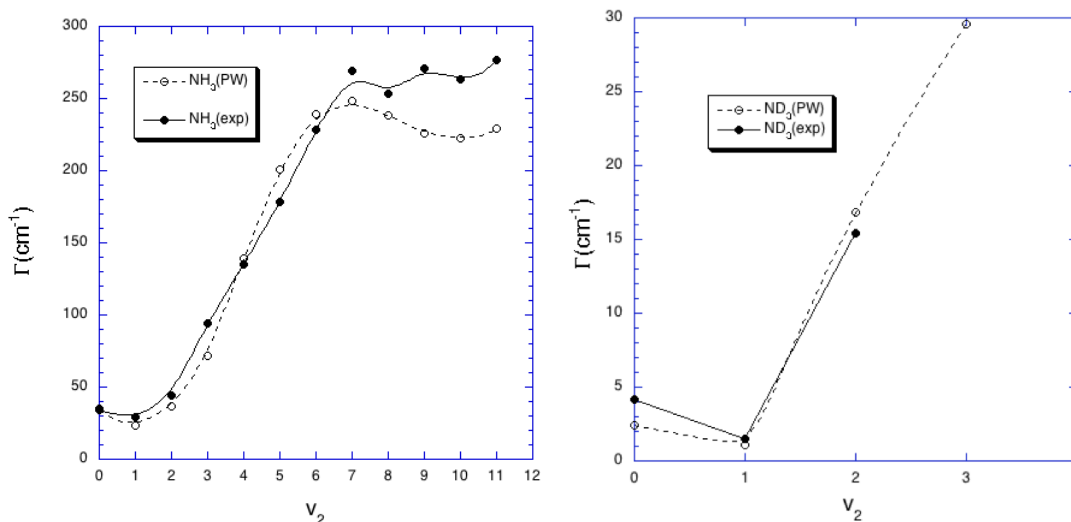


Figure 4-4. Calculated lifetimes of 2^n levels of NH_3 and ND_3 using the \mathbf{H}^d by *LVT* and present work (PW) compared with the experimental NH_3 values of Ref. ⁷ $0 \leq n \leq 3$ and Ref. ⁴ $3 < n \leq 6$ based on the compilation of Ref. ⁸ and the experimental ND_3 values of Ref. ⁷ $0 \leq n \leq 2$. Left: NH_3 ; Right: ND_3

Table 4-7. Linewidth (cm^{-1}) of NH_3 from experiment and computations based on \mathbf{H}^d obtained in the present work (PW) and \mathbf{H}^d from *LVT*, as reported in Ref. ³⁵. Experimental values taken from Ref. ⁶ except for $\nu_2 \leq 3$ for NH_3 and $\nu_2 \leq 2$ for ND_3 where values from Ref. ⁷, which are more consistent with the available experimental data are used. The $E(n)$ exhibit a systematic error owing to the error in T_e reported in Table 4-3.

(a) NH_3

Band	E(PW)	E(exp)	Γ (PW)	Γ (exp)	Γ (LVT)
0^0	45426	46222	35.3	34	103.9
2^1	46309	47057	23.1	29.2	58.8
2^2	47202	47964	36.7	44	67.4
2^3	48109	48869	72.0	794	121.2
2^4	49019	49783	139.4	132	235.1
2^5	49918	50730	201.3	178	394.4
2^6	50819	51656	238.9	228	369.7
2^7	51729	52543	248.3	269	367.1
2^8	52654	53496	238.5	253	280.8
2^9	53596	54454	225.9	271	213.4
2^{10}	54551	55380	222.3	263	146.1
2^{11}	55514	56342	229.0	277	108.5
2^{12}	56482	57300	243.8	279	16.9
2^{13}	57454	58285	263.4	293	24.5

(b) ND_3

Band	E(PW)	E(exp)	Γ (PW)	Γ (exp)	Γ (LVT)
0^0	46025	46701	2.4	4.2	11.
2^1	46676	47369	1.1	1.5	5.8
2^2	47330	48052	16.8	15.4	33.7
2^3	47988	48697	29.6	61.8	97.5
2^4	48655	49375	32.6	52.5	93.9
2^5	49331	50062	31.2	56.5	79.9
2^6	50017	50748	29.0	59.1	69.5
2^7	50710	51451	27.8	60.4	62.4
2^8	51410	52168	28.4	60.4	60.3
2^9	52116	52874	34.0	69.3	64.8
2^{10}	52826	53582	44.6	73.7	73.9
2^{11}	53540	54306	61.0	79.6	82.2
2^{12}	54258	55054	83.6	101.7	81.8
2^{13}	54977	55751	113.2	103.0	71.5

4.6 Analysis of H^{d} : Non-adiabatic Dynamics

Convergence tests have been performed with regard to the size of the grid, the propagation steps, and the position of the dividing surface. Table 4-2 lists all the numerical parameters used in the dynamic calculations. In this work, the basis set size is about 7.5×10^7 for NH_3 and 1.5×10^8 for ND_3 , which makes the propagation rather demanding.

This section focuses on non-adiabatic dynamics for photodissociation from the ground vibrational states of ammonia, which are a near degenerate tunneling pair. In Figure 4-5, the calculated percentages of the $\text{NH}_2(\tilde{A}^2A_1)$ population produced in NH_3 photodissociation are also displayed. It is clear that the percentages are essentially a monotonic function of the energy and the parity of the wavefunction has little effect on the branching ratio. Similar observations have been reported in our earlier four-dimensional quantum dynamics studies of the same process³⁷ using the PESs of Li, Valero and Truhlar,¹⁰¹ but the branching ratios are much smaller than those reported in Figure 4-5. It is currently unclear if the underestimation is due to the PESs or to the reduced dimensionality of the dynamic model. From the figure, it is evident that the \tilde{A}^2A_1 state of NH_2 cannot be accessed for the first three members of the 2^{n} progression, due to the energy constraint. All dissociation occurs non-adiabatically *via* the conical intersection. For 2^3 , the ground state $\text{NH}_2(\tilde{X}^2B_1)$ channel still dominates, but the excited $\text{NH}_2(\tilde{A}^2A_1)$ channel starts to emerge. At even higher energies, the $\text{NH}_2(\tilde{A}^2A_1)$ channel becomes increasingly important.

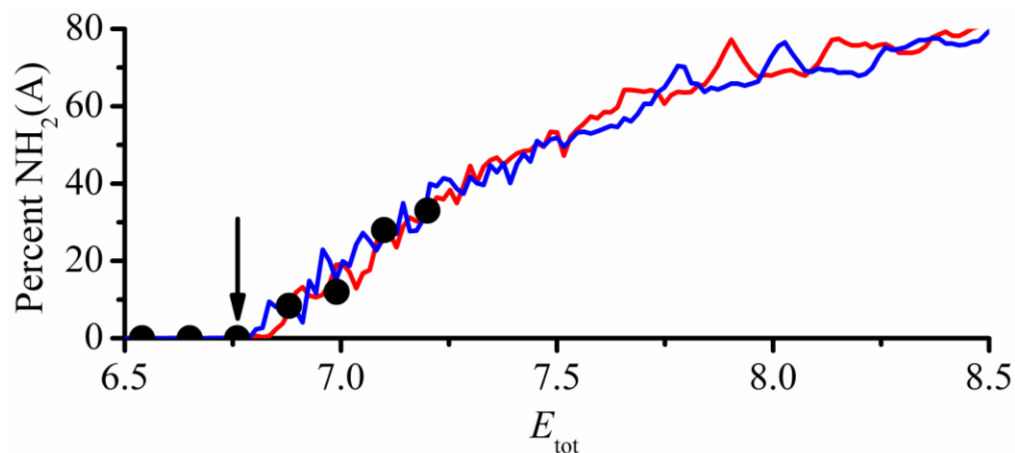


Figure 4-5 Percentage of $\text{NH}_2(\tilde{A}^2A_1)$ as a function of the total energy, relative to the \tilde{X} state minimum. The even and odd parities are represented by red and blue, respectively. The opening of the $\text{NH}_2(\tilde{A}^2A_1)$ channel is indicated in the figure by an arrow. The experimental estimates¹⁰² are given as black circles.

A similar trend is observed for the deuterated ammonia (ND_3), as shown in Fig. 4. Due to the energy constraint, the excited $\text{ND}_2(\tilde{A}^2A_1)$ channel is closed for the first four member of the 2^n progression. At higher energies, the \tilde{A}^2A_1 state percentage increases.

There has not been any accurate experimental determination of the branching ratios. In Ref. ¹⁰², the \tilde{A}/\tilde{X} branching ratios for both NH_3 and ND_3 were estimated based on the H-atom kinetic energy spectra. These experimental estimates are compared in Figs. 3 and 4 with our calculated values, and the agreement is quite good. The only exception is for the 2^6 state of ND_3 , where the experimental estimate of $\text{ND}_2(\tilde{A}^2A_1)$ is zero, while a small percentage is observed in theoretical results. The reason for this discrepancy is unclear. However, the overall good agreement provides strong evidence for the accuracy of the PESs and their couplings.

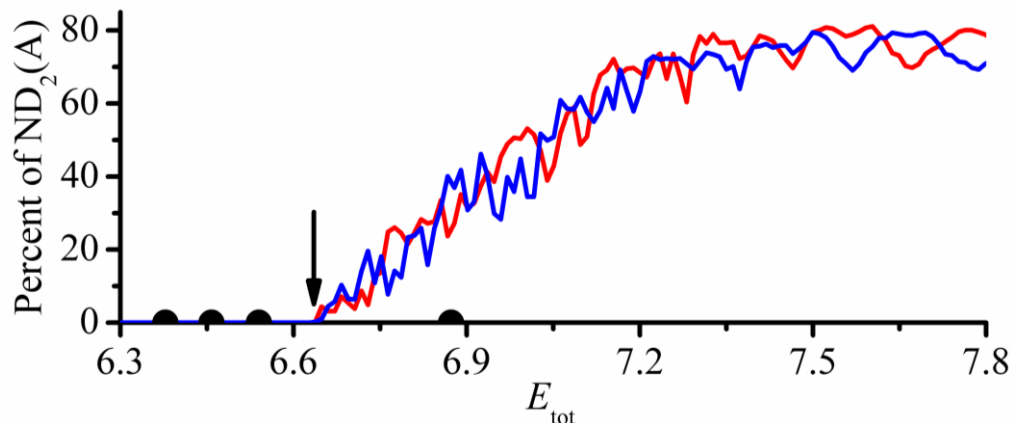


Figure 4-6. The fraction of $\text{ND}_2(\tilde{A}^2A_1)$ as a function of the total energy, relative to the \tilde{X} state minimum. The even and odd parities are represented by red and blue, respectively. The opening of the $\text{ND}_2(\tilde{A}^2A_1)$ channel is indicated in the figure by a arrow. The experimental estimates¹⁰² are given as black circles.

4.7 Summary and Conclusion

A method for determining a coupled diabatic state representation of adiabatic states coupled by conical intersections has been previously introduced. The method is notable for its use of derivative coupling and energy gradient information as well as energies to construct the diabatic representation and its combination least squares and interpolative techniques. The incorporation of energy gradient and derivative coupling information reduces the number of points at which the electronic structure data must be determined. The derivative coupling information also enables the representation to be quantifiably diabatic in a least squares sense. However a representation produced by this approach has yet to be employed in a fully quantum mechanical nuclear dynamics simulation, which provides a stringent test of the quality of the representation.

Concomitantly there have been a considerable number of computational and experimental studies of the photodissociation of the \tilde{A} state of NH_3 which exhibits both adiabatic and nonadiabatic product channels. Of particular relevance here was a full six

dimensional quantum mechanical study of the absorption from the ground vibrational level of the \tilde{X} state to the \tilde{A} state by *LLXG*. These calculations were based on a previously reported two-state diabatic Hamiltonian. However the agreement with experiment was modest at best. This shows that the non-adiabatic dynamics in this prototypical system is still not well understood.

The work reported here represents the state-of-the-art theoretical characterization of non-adiabatic dynamics in ammonia photodissociation. As argued above, a joint effort in developing accurate PESs using a high-level *ab initio* method and performing full dimensional quantum dynamic calculations using these PESs is the key to reaching an in-depth understanding of this fascinating reaction process. The excellent agreement with a wide range of experimental data, including positions, widths, and intensities of the predissociative resonances in both NH₃ and ND₃, and particularly the \tilde{A}/\tilde{X} branching ratios as reported in this work, strongly suggests that the underlying PESs and their coupling are now well described.

References

1. Leifson, S. W., *Astrophys. J.* **1933**, *63*, 73.
2. Vaida, V.; Hess, W.; Roebber, J. L., The direct ultraviolet absorption spectrum of the A1A2" \leftarrow X'A1 transition of jet-cooled ammonia. *J. Phys. Chem.* **1984**, *88*, 3397-3400.
3. Walsh, A. D.; Warsop, P. A., NH₃. *Trans. Faraday Soc.* **1961**, *57*, 345.
4. Ziegler, L. D., NH₃ lifetimes. *J. Chem. Phys.* **1985**, *82*, 664.
5. Ashfold, M. N. R.; Bennett, C. L.; Dixon, R. N., NH₃ lifetimes. *Faraday Discuss. Chem. Soc.* **1986**, *82*, 163.

6. Vaida, V.; McCarthy, M. I.; Engelking, P. C.; Rosmus, P.; Werner, H.-J.; Botschwina, P., The ultraviolet absorption spectrum of the $1A'' \leftarrow 1A_1$ transition of jet-cooled ammonia. *J. Chem. Phys.* **1987**, *86*, 6669.
7. Henck, S. A.; Mason, M. A.; Yan, W.-B.; Lehmann, K. K.; Coy, S. L., Microwave detected, microwave-optical double resonance of NH₃, NH₂D, NHD₂ and ND₃. II Predissociation dynamics of the A State. *J. Chem. Phys.* **1995**, *102*, 4783-4792.
8. Bach, A.; Hutchison, J. M.; Holiday, R. J.; Crim, F. F., Vibronic structure and photodissociation dynamics of the A state of jet-cooled ammonia. *J. Chem. Phys.* **2002**, *116*, 9315-9325.
9. Hause, M. L.; Yoon, Y. H.; Crim, F. F., Vibrationally mediated photodissociation of ammonia: The influence of N-H stretching vibrations on passage through conical intersections. *J. Chem. Phys.* **2006**, *125*, 174309.
10. Bach, A.; Hutchison, J. M.; Holiday, R. J.; Crim, F. F., Vibrational spectroscopy and photodissociation of jet-cooled ammonia. *J. Chem. Phys.* **2002**, *116*, 4955-4961.
11. Harshbarger, W. R., NH₃. *J. Chem. Phys.* **1970**, *53*, 903.
12. Tang, S. L.; Imre, D. G., NH₃. *Chem. Phys. Lett.* **1988**, *144*, 6.
13. Rosmus, P.; Botschwina, P.; Werner, H.-J.; Vaida, V.; Engelking, P. C.; McCarthy, M. I., NH₃ photodissociation. *J. Chem. Phys.* **1987**, *86*, 6677.
14. McCarthy, M. I.; Rosmus, P.; Werner, H.-J.; Botschwina, P.; Vaida, V., NH₃ photodissociation. *J. Chem. Phys.* **1987**, *86*, 6693.
15. Li, Z. H.; Valero, R.; Truhlar, D. G., Improved Direct Diabatization and Coupled Potential Energy Surfaces for the dissociation of ammonia. *Theor. Chem. Acc.* **2007**, *118*, 9-24.

16. Biesner, J.; Schnieder, L.; Ahlers, G.; Xie, X.; Welge, K. H.; Ashfold, M. N. R.; Dixon, R. N., NH₃ photodissociation. *J. Chem. Phys.* **1988**, *88*, 3607.
17. Biesner, J.; Schneider, L.; Ahlers, G.; Xie, X.; Welge, K. H.; Ashfold, M. N. R.; Dixon, R. N., State Selective Photodissociation dynamics of A State ammonia. II. *J. Chem. Phys.* **1989**, *91*, 2901-2911.
18. Woodbridge, E. L.; Ashfold, M. N. R.; Leone, S. R., Photodissociation of ammonia at 193.3nm: Rovibrational state distribution of the NH₂(A₂A₁) fragment. *J. Chem. Phys.* **1991**, *94*, 4195-4204.
19. Mordaunt, D. H.; Ashfold, M. N. R.; Dixon, R. N., Photodissociation dynamics of state ammonia molecules. II. The isotopic dependence for partially and fully deuterated isotopomers. *J. Chem. Phys.* **1996**, *104*, 6472.
20. Mordaunt, D. H.; Ashfold, M. N. R.; Dixon, R. N., NH₃ photodissociation. *J. Chem. Phys.* **1996**, *104*, 6460.
21. Mordaunt, D. H.; Ashfold, M. N. R.; Dixon, R. N.; Löffler, P.; Schneider, L.; Welge, K. H., *J. Chem. Phys.* **1998**, *108*, 519-526.
22. Loomis, R. A.; Lester, M. I., OH-H₂ entrance Channel Complexes. *Annu. Rev. Phys. Chem.* **1997**, *48*, 643-673.
23. Reid, J. P.; Loomis, R. A.; Leone, S. R., NH₃ photodissociation. *J. Chem. Phys.* **2000**, *112*, 3181.
24. Reid, J. P.; Loomis, R. A.; Leone, S. R., NH₃ photodissociation. *Chem. Phys. Lett.* **2000**, *324*, 240.
25. Reid, J. P.; Loomis, R. A.; Leone, S. R., NH₃ photodissociation. *J. Phys. Chem. A* **2000**, *104*, 10139.

26. Wells, K. L.; Perriam, G.; Stavros, V. G., Time-resolved velocity map ion imaging study of NH₃ photodissociation. *J. Chem. Phys.* **2009**, *130*, 074308.
27. Runau, R.; Peyerimhoff, S. D.; Buenker, R. J., NH₃ photodissociation. *J. Mol. Spectrosc.* **1977**, *68*, 253.
28. Manz, U.; Reinsch, E.-A.; Rosmus, P.; Werner, H.-J.; O'Neil, S. V., Dissociation of NH₃ to NH + H₂. *J. Chem. Soc. Faraday Trans.* **1991**, *87*, 1809.
29. Yarkony, D. R., Exploring Molecular Complexity: The Role of Conical Intersections in NH₃ Photodissociation. *J. Chem. Phys.* **2004**, *121*, 628-631.
30. Nangia, S.; Truhlar, D. G., Direct Calculation of Coupled Diabatic Potential Energy Surfaces for ammonia and mapping of a 4-dimensional conical intersection seam. *J. Chem. Phys.* **2006**, *124*, 124309.
31. Dixon, R. N., NH₃. *Chem. Phys. Lett.* **1988**, *147*, 377.
32. Dixon, R. N., NH₃. *Mol. Phys.* **1996**, *88*, 949.
33. Dixon, R. N.; Hancock, T. W. R., Recoil anisotropy following molecular predissociation: NH₃* --> H + NH₂ and HFCO* --> H + FCO. *J. Phys. Chem. A* **1997**, *101*, 7567.
34. Bonhommeau, D.; Truhlar, D. G., Mixed quantum/classical investigation of the photodissociation of NH₃(A) and a practical method for maintaining zero-point energy in classical trajectories
J. Chem. Phys. **2008**, *129*, 014302.
35. Lai, W.; Lin, S. Y.; Xie, D.; Guo, H., Full-dimensional quantum dynamics of -state photodissociation of ammonia: Absorption spectra. *J. Chem. Phys.* **2008**, *129*, 154311.

36. Bonhommeau, D.; Valero, R.; Truhlar, D. G.; Jasper, A. W., Coupled-Surface Investigation of the photodissociation of NH₃(A). Effect of exciting the symmetric and antisymmetric stretch modes. *J. Chem. Phys.* **2009**, *130*, 234303 (17 pages).
37. Lai, W.; Lin, S. Y.; Xie, D.; Guo, H., Non-adiabatic dynamics of A-state photodissociation of ammonia: a four-dimensional wave packet study. *J. Phys. Chem. A* **2010**, *114*, 3121.
38. Bach, A.; Hutchison, J. M.; Holiday, R. J.; Crim, F. F., Photodissociation of vibrationally excited ammonia: rotational excitation in the NH₂ product. *J. Chem. Phys.* **2003**, *118*, 7144-7145.
39. Tully, J. C., Molecular Dynamics with electronic transitions. *J. Chem. Phys.* **1990**, *93*, 1061-1071.
40. Giri, K.; Chapman, E.; Sanz, C. S.; Worth, G., A full-dimensional coupled surface study of the photodissociation dynamics of ammonia using the multiconfiguration time-dependent Hartree Method. *J. Chem. Phys.* **2011**, *135*, 044311.
41. Beck, M.; Jackle, A.; Worth, G. A.; Meyer, H.-D., The multiconfiguration time-dependent Hartree (MCTDH) method: A highly efficient algorithm for propagating wavepackets. *Phys. Rep.* **2000**, *324*, 1-105.
42. Worth, G. A.; Meyer, H.-D.; Köppel, H.; Cederbaum, L. S.; Burghardt, I., Using the MCTDH wavepacket propagation method to describe multimode nonadiabatic dynamics. *Int. Rev. Phys. Chem.* **2008**, *27*, 569-606.
43. Nakamura, H.; Truhlar, D. G., Direct diabaticization of electronic states by the fourfold way. II. Dynamical correlation and rearrangement processes. *J. Chem. Phys.* **2002**, *117*, 5576-5593.

44. Nakamura, H.; Truhlar, D. G., Extension of the fourfold way for the calculation of global diabatic potential energy surfaces of complex multiarrangement non-Born Oppenheimer systems. Application to HNCO(S0,S1). *J. Chem. Phys.* **2003**, *118*, 6816-6829.
45. Baer, M., Adiabatic and diabatic representations for atom-diatom collisions: Treatment of the three-dimensional case. *Chem. Phys.* **1976**, *15*, 49-57.
46. Mead, C. A.; Truhlar, D. G., Conditions for the definition of a strictly diabatic basis. *J. Chem. Phys.* **1982**, *77*, 6090-6098.
47. Baer, M., Introduction to the theory of electronic nonadiabatic coupling terms in molecular systems. *Physics Reports* **2002**, *358*, 75-142.
48. Köppel, H.; Domcke, W.; Cederbaum, L. S., Multimode Molecular Dynamics Beyond the Born-Oppenheimer Approximation. *Adv. Chem. Phys.* **1984**, *57*, 59-246.
49. Köppel, H.; Domcke, W.; Cederbaum, L. S., The Multimode Vibronic Coupling Approach. In *Conical Intersections*, Domcke, W.; Yarkony, D. R.; Köppel, H., Eds. World Scientific: New Jersey, 2004; Vol. 15, pp 323-368.
50. Mahapatra, S.; Worth, G. A.; Meyer, H.-D.; Cederbaum, L. S.; Köppel, H., The B2E/A2B2 photoelectron bands of allene. beyond the linear coupling scheme. ab initio dynamical study using all 15 vibrational modes. *J. Phys. Chem. A* **2001**, *105*, 5567.
51. Mahapatra, S.; Vallet, V.; Woywod, C.; Köppel, H.; Domcke, W., Multimode Jahn-Teller and Pseudo Jahn-Teller coupling effects in the photoelectron spectrum of CH3F. *Chem. Phys.* **2004**, *304*, 17-34.
52. Viel, A.; Eisfeld, W., Effects of higher order Jahn-Teller coupling on the nuclear dynamics. *J. Chem. Phys.* **2004**, *120*, 4603.

53. Einfeld, W.; Viel, A., Higher order (A+E)xe Pseudo Jahn-Teller coupling *J. Chem. Phys.* **2005**, *122*, 204317.
54. Ichino, T.; Gianola, A. J.; Lineberger, W. C.; Stanton, J. F., Nonadiabatic Effects in the photoelectron Spectrum of the pyrazolide-d3 anion. Three-state interactions in the pyrazolyl d3 radical. *J. Chem. Phys.* **2006**, *125*, 084312.
55. Papas, B. N.; Schuurman, M. S.; Yarkony, D. R., *Determining quasi diabatic coupled electronic state Hamiltonians using derivative couplings. A normal equations based method.* *J. Chem. Phys.* **2008**, *129*, 124104(10 pages).
56. Opalka, D.; Domcke, W., High-Order expansion of T2xt2 Jahn-Teller potential energy surfaces in tetrahedral molecules. *J. Chem. Phys.* **2010**, *132*, 154108 (14 pages).
57. Thompson, T. C.; Izmirlan, G.; Lemon, S. J.; Truhlar, D. G.; Mead, C. A., Consistent Analytic Representation of the two lowest potential energy surfaces for Li3, Na3 and K3. *J. Chem. Phys* **1985**, *82*, 5597.
58. Varandas, A. J. C.; Brown, F. B.; Mead, C. A.; Truhlar, D. G.; Blais, N. C., A double Many Body expansion of the two lowest energy potential energy surfaces and nonadiabatic couplings for H3. *J. Chem. Phys.* **1987**, *86*, 6258.
59. Atchity, G. J.; Ruedenberg, K., DEtermination of diabatic bases though enforcement of configurations uniformity. *Theor. Chem. Acc.* **1997**, *97*, 47-58.
60. Köppel, H.; Gronki, J.; Mahapatra, S., Construction Scheme for Regularized Diabatic States. *J. Chem. Phys.* **2001**, *115*, 2377.
61. Pacher, T.; Cederbaum, L. S.; Köppel, H., Block Diagonalization. *J. Chem. Phys.* **1991**, *95*, 6668-6680.

62. Pacher, T.; Cederbaum, L. S.; Köppel, H., Block Diagonalization Method for Quasidiabatic States. *J. Chem. Phys.* **1988**, *89*, 7367-7381.
63. Mota, V. C.; Varandas, A. J. C., HN₂(2A') Electronic Manifold. II. Ab Initio Based Double-Sheeted DMBE Potential Energy Surface via a Global Diabatization Angle. *J. Phys. Chem. A* **2008**, *112*, 3768–3786.
64. Mota, V. C.; Caridade, P. J. S. B.; Varandas, A. J. C., Toward the Modeling of the NO₂(2A₁) Manifold. *Int. J. Quant. Chem.* **2011**, *111*, 3776-3785.
65. Evenhuis, C. R.; Collins, M. A., Interpolation of Diabatic potential energy surfaces. *J. Chem. Phys.* **2004**, *121*, 2515.
66. Evenhuis, C. R.; Lin, X.; Zhang, D. H.; Yarkony, D. R.; Collins, M. A., Interpolation of diabatic potential-energy surfaces: Quantum dynamics on ab initio surfaces. *J. Chem. Phys.* **2005**, *123*, 134110 (12 pages).
67. Godsi, O.; Evenhuis, C. R.; Collins, M. A., Interpolation of Multidimensional diabatic surfaces. *J. Chem. Phys.* **2006**, *125*, 104105.
68. Evenhuis, C.; Martínez, T. J., A scheme to interpolate potential energy surfaces and derivative coupling vectors without performing a global diabatization. *J. Chem. Phys.* **2011**, *135*, 224110.
69. Dawes, R.; Passalacqua, A.; Sewell, T. D.; Wagner, A. F.; Minkoff, M.; Thompson, D. L., Interpolating moving least squares methods for fitting potential energy surfaces: using classical trajectories to explore configuration space. *J. Chem. Phys.* **2009**, *130*, 144107.

70. Dawes, R.; Thompson, D. L.; Wagner, A. F.; Minkoff, M., Interpolating moving least squares methods for fitting potential energy surfaces: A Strategy for efficient automatic data placement in high dimensions. *J. Chem. Phys.* **2009**, *128*, 84107.
71. Dawes, R.; Jasper, A. W.; Tao, C.; Richmond, C.; Mukarakate, C.; Kable, S. H.; Reid, S. A., Theoretical and Experimental Spectroscopy of the S₂ State of CHF and CDF: Dynamically Weighted Multireference Configuration Interaction Calculations for High-Lying Electronic States. *J. Phys. Chem. Lett.* **2010**, *1*, 641–646.
72. Zhu, X.; Yarkony, D. R., On the Representation of Coupled Adiabatic Potential Energy Surfaces using Quasi-Adiabatic Hamiltonians: Description of Accidental Seams of Conical Intersection. *Molec. Phys.* **2010**, *108* (19), 2611 - 2619.
73. Yarkony, D. R., Energies and derivative couplings in the vicinity of a conical intersection using degenerate perturbation theory and analytic gradient techniques. *J. Phys. Chem. A* **1997**, *101*, 4263-4270.
74. Longuet-Higgins, H. C., The symmetry groups of non-rigid molecules. *Mol. Phys.* **1963**, *6*, 445-460.
75. Bunker, P. R., *Molecular Symmetry and Spectroscopy*. Academic Press: New York, 1979.
76. Hougen, J. T., Strategies for advanced applications of permutation–inversion groups to the microwave spectra of molecules with large amplitude motions. *J. Mol. Spec.* **2009**, *256*, 170-185.
77. Tinkham, M., *Group Theory and Quantum Mechanics*. McGraw-Hill: New York, 1964.

78. Braams, B. J.; Bowman, J. M., Permutationally Invariant Potential Energy Surfaces in High dimensionality. *Int. Rev. Phys. Chem.* **2009**, *28*, 577-606.
79. Tully, J. C., Nonadiabatic Processes in Molecular Collisions. In *Modern Theoretical Chemistry*, Miller, W. H., Ed. Plenum: New York, 1976; Vol. 2, pp 217-268.
80. Atchity, G. J.; Xantheas, S. S.; Ruedenberg, K., Potential Energy Surfaces Near Intersections. *J. Chem. Phys.* **1991**, *95*, 1862-1876.
81. Yarkony, D. R., Conical Intersections: Diabolical and Often Misunderstood. *Acc. Chem. Res.* **1998**, *31*, 511-518.
82. Light, J. C.; Carrington Jr., T., Discrete-variable representations and their utilization. *Adv. Chem. Phys.* **2000**, *114*, 263-310.
83. Lanczos, C., *J. Res. Natl. Bur. Stand.* **1952**, *49*, 33.
84. Guo, H., Recursive solutions to large eigenproblems in molecular spectroscopy and reaction dynamics. *Rev. Comput. Chem.* **2007**, *25*, 285-347.
85. Guo, H., Quantum dynamics of complex-forming bimolecular reactions. *Int. Rev. Phys. Chem.* **2012**, *31*, 1-68.
86. Guo, H., A time-independent theory of photodissociation based on polynomial propagation. *J. Chem. Phys.* **1998**, *108*, 2466.
87. Chen, R.; Guo, H., Efficient calculation of matrix elements in low storage filter diagonalization. *J. Chem. Phys.* **1999**, *111*, 464.
88. Zhang, D. H.; Zhang, J. Z. H.; Bacic, Z., A time-dependent golden rule wave packet calculation for vibrational predissociation of D₂HF. *J. Chem. Phys.* **1992**, *97*, 927-933.

89. Lanczos, C., An iteration method for the solution of the eigenvalue problem of linear differential and integral operators. *J. Res. Natl. Bur. Stand.* **1950**, *45*, 255.
90. Lin, S. Y.; Guo, H., Quantum wave packet study of reactive and inelastic scattering between C(¹D) and H₂. *J. Chem. Phys.* **2003**, *119*, 11602.
91. Lischka, H.; Shepard, R.; Shavitt, I.; Pitzer, R.; Dallos, M.; Müller, T.; P.G.Szalay; Brown, F. B.; Alhrichs, R.; Böhm, H. J.; Chang, A.; Comeau, D. C.; Gdanitz, R.; Dachsel, H.; Erhard, C.; Ernzerhof, M.; Höchtl, P.; Irlle, S.; Kedziora, G.; Kovar, T.; Parasuk, V.; Pepper, M.; Scharf, P.; Schiffer, H.; Schindler, M.; Schüler, M.; Zhao, J.-G. *COLUMBUS, An ab initio Electronic Structure Program*, 5.9; 2003.
92. Lischka, H.; Dallos, M.; Szalay, P.; Yarkony, D. R.; Shepard, R., The analytic evaluation of nonadiabatic coupling terms at the MR-CI level I: Formalism. *J. Chem. Phys.* **2004**, *120*, 7322-7329.
93. Dallos, M.; Lischka, H.; Szalay, P.; Shepard, R.; Yarkony, D. R., The analytic evaluation of nonadiabatic coupling terms at the MR-CI level II; Determination of minima on the crossing seam. *J. Chem. Phys.* **2004**, *120*, 7330-7339.
94. Herzberg, G., *Electronic Spectra and Electronic Structure of Polyatomic Molecules*. Van Nostrand Reinhold: New York, 1966.
95. Huang, X.; Schwenke, D. W.; Lee, T. J., Rovibrational spectra of ammonia I. Unprecedented accuracy of a potential energy surface used with nonadiabatic corrections. *J. Chem. Phys.* **2011**, *134*, 044320.
96. Henck, S. A.; Mason, M. A.; Yan, W.-B.; Lehmann, K. K.; Coy, S. L., Microwave detected, microwave-optical double resonance of NH₃, NH₂D, NHD₂ and ND₃. I Structure and Force Field of the A State. *J. Chem. Phys.* **1995**, *102*, 4772-4782.

97. Morino, I.; Kawaguchi, K. J., *Mol. Spectrosc.* **1997**, *182*, 428.
98. Gabriel, W.; Chambaud, G.; Rosmus, P.; Carter, S.; Handy, N. C., *Mol. Phys.* **1994**, *81*, 1445.
99. Yurchenko, S. N.; Barber, R. J.; Tennyson, J.; Thiel, W.; Jensen, P., Towards efficient refinement of molecular potential energy surfaces: Ammonia as a case study. *J. Mole. Spectro.* **2011**, *268*, 123-129.
100. Yurchenko, S. N.; Zheng, J.; Lin, H.; Jensen, P.; Thiel, W., Potential-energy surface for the electronic ground state of NH₃ up to 20000 cm⁻¹ above equilibrium. *J. Chem. Phys.* **2005**, *123*, 134308.
101. Li, Z. H.; Valero, R.; Truhlar, D. G., Improved direct diabaticization and coupled potential energy surfaces for the photodissociation of ammonia. *Theo. Chem. Acc.* **2007**, *118*, 9.
102. Biesner, J.; Schnieder, L.; Ahlers, G.; Xie, X.; Welge, K. H.; Ashfold, M. N. R.; Dixon, R. N., State selective photodissociation dynamics of A state ammonia II. *J. Chem. Phys.* **1989**, *91*, 2901.

Chapter 5 Fitting Coupled Potential Energy Surfaces for Large Systems: Method and Construction of a 3-State Representation for Phenol Photodissociation in the Full 33 Internal Degrees of Freedom

5.1 Abstract

A recently reported algorithm for representing adiabatic states coupled by conical intersections using a quasi-diabatic state Hamiltonian in four and five atom systems is extended so as to be able to treat nonadiabatic processes in considerably larger molecules. The method treats all internal degrees of freedom and uses electronic structure data from *ab initio* multireference configuration interaction wave functions with nuclear configuration selection based on quasi-classical surface hopping trajectories. The method is shown here to be able to treat ~ 30 internal degrees of freedom including dissociative and large amplitude internal motion. Two procedures are introduced which are essential to the algorithm, a null space projector which removes basis functions from the fitting process until they are needed and a partial diagonalization technique which allows for automated, but accurate, treatment of the vicinity of extended seams of conical intersections of two or more states. These procedures are described in detail. The method is illustrated using the photodissociation of phenol, $C_6H_5OH(\tilde{X}^1A') + h\nu \rightarrow C_6H_5OH(\tilde{A}^1A', \tilde{B}^1A'') \rightarrow C_6H_5O(\tilde{X}^2B_1, \tilde{A}^2B_2) + H$ as a test case. *Ab initio* electronic structure data for the 1,2,3¹A states of phenol, which are coupled by conical intersections, are obtained from multireference first order configuration interaction wave functions. The design of bases to simultaneously treat large amplitude motion and dissociation is described as is the ability of the fitting procedure to smooth the irregularities in the electronic energies attributable to the orbital changes that are inherent to nonadiabatic processes.

5.2 Introduction

Using methods including Shepard interpolation¹⁻³, the permutationally invariant polynomial approach,⁴⁻⁵ and the moving least squares technique,⁶⁻⁷ the construction of fit single state potential energy surfaces (PESs), analytic representations of *ab initio* electronic energies and energy gradients, is now well-established. These single state PESs, which are essential for accurate quantum dynamics and have found wide application in more approximate quasi-classical treatments, have revolutionized adiabatic dynamics.

The situation for nonadiabatic processes involving dissociative and large amplitude motion is less sanguine. In these cases, compared to single electronic state dynamics, both the electronic structure data and the representation are more challenging to determine. Recently we have reported a procedure for representing adiabatic PESs coupled by conical intersections using a quasi diabatic representation⁸⁻⁹ in cases where molecular dissociation and/or large amplitude motion needs to be described. As in the adiabatic case, we refer to the resulting representations as fit PESs although in the nonadiabatic case interstate couplings must also be represented. This method complements other approaches aimed specifically at nonadiabatic processes which include: diabatizations based on the vibronic coupling Hamiltonian;¹⁰⁻¹⁴ the multisheeted adiabatic state method¹⁵ which extends the permutationally invariant polynomial approach to more than one PES; the Shepard interpolation/Grow method,^{3, 16-20} the four fold way;²¹⁻²⁵ the double sheeted double many body expansion;²⁶⁻²⁷ and diabatization by ansatz.²⁸⁻²⁹ Included in the final category is a recent work²⁹ which also incorporates complete nuclear permutation inversion (CNPI) symmetry.³⁰⁻³¹ CNPI symmetry is discussed in Sec. 5.4. The vibronic coupling Hamiltonian based on diabatization by ansatz and including CNPI symmetry is similar in spirit to the approach espoused herein although the present approach takes explicit account of the derivative couplings which

are not included in a diabaticization-by-ansatz approach. Our reported procedure is well-suited for tetra-atomic and penta-atomic molecules. Indeed, when applied to ammonia photodissociation, $\text{NH}_3(\tilde{X}) + h\nu \rightarrow \text{NH}_3(\tilde{A}) \rightarrow \text{NH}_2(\tilde{A}, \tilde{X}) + \text{H}$, excellent agreement with experimental data was found.³²⁻³³ Here we show that by introducing new procedures, described in Sec. 5.4, this approach can be extended to much larger molecules.

The principal alternative to the fit PESs approach is dynamics on the fly also called direct dynamics.³⁴⁻³⁸ In this approach electronic structure data is determined as required by the solution of the electronic Schrödinger equation. When compared with dynamics on the fly, the fit PES approach can: (i) utilize more accurate wave functions; (ii) provide the electronic structure information, energies, energy gradients, derivative couplings, diabatic energies and couplings, at a particular point in nuclear coordinate space in a small fraction of the time required to solve the electronic Schrödinger equation in on the fly dynamics, enabling longer and more accurate time propagations of quasi-classical trajectories with better statistics; (iii) determine the dense grids of points required for accurate quantum mechanical studies; and finally (iv) smooth out the discontinuous energy gradients that frequently accompany changing orbital spaces. The need for the final option, not available in direct dynamics, is not an uncommon occurrence in describing dissociative, multichannel, nonadiabatic processes, although flexible state averaging procedures can help in this regard.^{29, 39-40}

The urgent need for algorithms to construct fit PESs for nonadiabatic processes involving molecules larger than 4-5 atoms has been made clear in recent dynamical studies of radiationless decay of electronically excited nucleobases using *ab initio* direct dynamics methods.^{37, 41-46} For a review see Ref.⁴⁷. In these systems the use of direct dynamics limits the quasi-classical trajectory surface hopping⁴⁸⁻⁴⁹ dynamics to ~ 100 trajectories and a reliance on complete active space (CAS) based electronic structure. This results in mechanistic discrepancies. For example, a recent [2011] study of cytosine

nonadiabatic photochemical deactivation³⁷ observes: "The different results obtained by several simulations are expression of the discrepancies between the potential energy surfaces computed at diverse levels." This is not an isolated instance. Barbatti *et al.*⁴⁶ showed in a systematic treatment of radiationless decay of H9-adenine that different levels of electronic structure theory produced decidedly different nonadiabatic mechanisms with nonadiabatic dynamics based on density functional theory exhibiting significant draw backs.⁴⁶ For these molecules it is desirable to conduct more accurate nuclear dynamics using fit representations. In order to construct such representations significant algorithmic issues have to be addressed.

In this work we report an extension of our existing approach to one capable of describing radiationless decay of nucleobases and comparably sized systems. The potential of this approach is established by determining a quasi-diabatic representation of the three adiabatic states coupled by conical intersections that are encountered in the radiationless decay of phenol $C_6H_5OH(\tilde{X}^1A') + h\nu \rightarrow C_6H_5OH(\tilde{A}^1A', \tilde{B}^1A'') \rightarrow C_6H_5O(\tilde{X}^2B_1, \tilde{A}^2B_2) + H$ including *all* internal degrees of freedom. While photodissociation of phenol is of considerable interest in it own right, as evinced by the large number of recent publications,⁵⁰⁻⁶² it is chosen as a model problem here because of the level of complexity of its nonadiabatic dynamics which involves *both* dissociation and large amplitude internal motion and the fact that its electronic states are similar to those found in biomolecules, including imidazole, 9H-adenine, indole and nucleobases. These molecules have been the object of recent theoretical work using on the fly and reduced dimensionality techniques.^{44, 46, 51, 63-67} Since the goal of this work is to establish the feasibility of the fit surfaces approach in a system with the complexity of phenol, a semi-quantitative multireference first order configuration intersection (FOCI) expansion, approximately 3 million configuration state functions (CSFs) will be used to generate the *ab initio* data. Based on the treatment developed here, a more accurate description using

second order CI wave functions (estimated to include ~ 200 million CSFs) is feasible and will be the subject of a subsequent study.

In this paper we explain the computational issues associated with the extension to larger systems and how they can be addressed. Section 5.3 briefly reprises the original algorithm so as to enable a clear description of the algorithmic enhancements, which are the subject of section 5.4. Section 5.5 describes and validates the constructed representation of the 1,2,3¹A states of phenol. Particular emphasis will be paid to the simultaneous description of dissociation and large amplitude internal motion; the automated treatment of conical and avoided intersections of two or more states; and the smoothing of discontinuities arising from orbital switching. Section 5.6 summarizes and discusses directions for further studies. Technical and mathematical details are restricted to Appendices 5.7.

5.3 The algorithm

5.3.1 Definitions

In this section, we briefly recapitulates conclusions in section Chapter 3 that will be used in section 5.4. The quasi diabatic (model) Hamiltonian \mathbf{H}^d representing N^{state} adiabatic electronic states has the form

$$\mathbf{H}^d(\mathbf{R}) = \sum_{l=1}^{N^c} V_l [\bar{P}^{\kappa[u(l),v(l)]} g^{(l)}(\mathbf{R})] \mathbf{B}^{u(l),v(l)} \quad (5-1)$$

where $\mathbf{B}^{u,v}$ is an $N^{\text{state}} \times N^{\text{state}}$ symmetric matrix with a 1 in the (u,v) and (v,u) elements and the remaining elements 0; \bar{P}^{κ} is a standard group theoretical projection operator; $g^{(l)}(\mathbf{R})$, $1 \leq l \leq N^c$, are the monomial basis functions of nuclear coordinates described in detail below with N^c the total number of monomials, (including the 0th order monomial $g^{(1)} \equiv 1$); and the V_l are constants determined by the fitting procedure. Accompanying \mathbf{H}^d is an

electronic Schrödinger equation

$$\left[\mathbf{H}^d(\mathbf{R}) - \mathbf{I} E^{a,J,(m)}(\mathbf{R}) \right] \mathbf{d}^J(\mathbf{R}) = \mathbf{0} \quad (5-2)$$

which determines the adiabatic energies $E^{a,J,(m)}(\mathbf{R})$, energy gradients $E_k^{a,J,(m)}(\mathbf{R})$

$\equiv \nabla_{R_k} E^{a,J,(m)}(\mathbf{R})$ and derivative couplings $\mathbf{f}^{a,J,K,(m)}(\mathbf{R}) = \mathbf{d}^J(\mathbf{R})^\dagger \nabla_{\mathbf{R}} \mathbf{d}^K(\mathbf{R})$. The adiabatic

to diabatic state transformation is given by $\mathbf{d}^{(d)\dagger}$, where $d_{u,I}^{(d)} = d_{u,I}^I$, (Ref. 8-9) that is

$$\Psi_u^d(\mathbf{q}; \mathbf{R}) = \sum_{J=1}^{N^{state}} \Psi_J^{a,(ab)}(\mathbf{q}; \mathbf{R}) (\mathbf{d}^{(d)})_{J,u}^\dagger(\mathbf{R}) = \sum_{J=1}^{N^{state}} \Psi_J^{a,(ab)}(\mathbf{q}; \mathbf{R}) \mathbf{d}_u^J(\mathbf{R}) \quad (5-3)$$

Here $\mathbf{q}(\mathbf{R})$ denote the electronic (nuclear) coordinates, and the superscripts a , d , m and ab stand for adiabatic, diabatic, model and *ab initio* respectively. For ease of reference we define for $1 \leq j \leq N^{int} = 3N^{at} - 6$, $1 \leq n \leq N^{point}$, and $(x) = (ab)$, (m)

$$L_0^{J,J,(x)}(\mathbf{R}^n) = E^{a,J,(x)}(\mathbf{R}^n) \quad (5-4)$$

$$L_j^{J,J,(x)}(\mathbf{R}^n) = \nabla_j E^{a,J,(x)}(\mathbf{R}^n) \quad (5-5)$$

$$L_j^{J,K,(m)}(\mathbf{R}^n) = \mathbf{d}^J(\mathbf{R}^n)^\dagger \nabla_j \mathbf{H}^d \mathbf{d}^K(\mathbf{R}^n) \quad (5-6)$$

$$L_j^{J,K,(ab)}(\mathbf{R}^n) = (E^{a,K,(ab)}(\mathbf{R}^n) - E^{a,J,(ab)}(\mathbf{R}^n)) f_j^{a,J,K,(ab)}(\mathbf{R}^n) \quad (5-7)$$

where $\mathbf{f}^{a,J,K,(ab)}$ is the *ab initio* determined derivative coupling,

5.3.2 Defining equations

The residuals of the energies, energy gradients and energy difference scaled derivative couplings, eqs. (5-4), (5-5), (5-6), respectively

$$P_0^{J,J}(\mathbf{R}^n) = L_0^{J,J,(ab)}(\mathbf{R}^n) - L_0^{J,J,(m)}(\mathbf{R}^n) \quad (5-8)$$

$$P_j^{J,J}(\mathbf{R}^n) = L_j^{J,J,(ab)}(\mathbf{R}^n) - L_j^{J,J,(m)}(\mathbf{R}^n) \quad (5-9)$$

$$P_j^{J,K}(\mathbf{R}^n) = L_j^{J,K,(ab)}(\mathbf{R}^n) - L_j^{J,K,(m)}(\mathbf{R}^n) \quad (5-10)$$

will be used to determine the V_n . From eq. (5-1) and its derivative eqs. (5-4), (5-5), (5-6) become, for $x = m$, $1 \leq I \leq J \leq N^{state}$, $0 \leq j \leq N^{int}$

$$L_j^{I,J,(m)}(\mathbf{R}^n) = \sum_{l=1}^{N^c} W_{n,I,J,j;l} V_l = (\mathbf{WV})_k \equiv L_k^{(m)} \quad (5-11)$$

where

$$W_{n,I,J,j;l} = \mathbf{d}^I(\mathbf{R}^n)^\dagger \mathbf{B}^{u^{(l)},v^{(l)}} \mathbf{d}^J(\mathbf{R}^n) M_{j,l}^{u^{(l)},v^{(l)},n} \quad (5-12)$$

$$M_{j,l}^{u^{(l)},v^{(l)},n} = \nabla_j \bar{P}^{\kappa[u^{(l)},v^{(l)}]} \mathbf{g}^{(l)}(\mathbf{R}^n) \quad (5-13)$$

and ∇_0 means do nothing. Note that since the \mathbf{d}^J satisfy eq. (5-2), eq. (5-11) for $I=J$, is exact even though the \mathbf{d}^J depend on \mathbf{R} . In eq. (5-11) and below is convenient to re-index the four indices (n,I,J,j) by k so that $L_j^{I,J,(x)}(\mathbf{R}^n)$, is replaced by $L_k^{(x)}$, $P_j^{I,J}(\mathbf{R}^n)$ by P_k and $W_{n,I,J,j;l}$ by $W_{k,l}$ for $1 \leq k \leq N^{eq}$, where N^{eq} is the number of defining equations. There is one defining equation for each allowed value of (n,I,J,j) . In eq. (5-12) at each \mathbf{R}^n , the ∇_j for $j > 0$ denote the derivatives with respect to a local, nonredundant coordinate system.

Previously we have introduced three classes of \mathbf{R}^n . The \mathbf{R}^n for which the $P_k = 0$ are solved in a least squares sense. The nodes for which all the $P_k = 0$ for an \mathbf{R}^n are solved exactly and the partial nodes for which only the energy equation at an \mathbf{R}^n is solved exactly. The equations are ordered so that, the first $1 \leq k \leq N^{sq}$ $P_k = 0$ equations are solved in a least squares sense and the remaining equations $N^{sq} < k \leq N^{eq}$ are solved exactly.⁸⁻⁹ In this work neither nodes nor partial nodes are used.

The \mathbf{R}^n , $1 \leq n \leq N^{point}$, are further classified according to how they are selected. \mathbf{R}^n in the skeletal data set are selected to define the key regions of nuclear coordinate space. Enough \mathbf{R}^n must be in the skeletal set so as to enable surface hopping

trajectories^{48, 68} to be run. The quasi-classical trajectories expand the domain of definition, a generalized volume surrounding the final data set where the electronic structure data are well reproduced, to one appropriate to the problem at hand. The domain of definition is considered converged when a prescribed percentage of the trajectories (~98 % here) propagated for fixed time (here 50 ps) remain in the domain of definition. Making trajectories the arbiters of the domain of definition avoids *a priori* assumptions concerning the preeminent modes. This scheme is similar to the highly successful GROW algorithm.⁶⁹⁻⁷⁰

The \mathbf{V} are obtained as an extremum of the Lagrangian

$$\Lambda(\mathbf{V}, \boldsymbol{\lambda}) = \frac{1}{2} \sum_{j=1}^{N^{lsq}} P_j^2 + \sum_{j=1+N^{lsq}}^{N^{eq}} \lambda_{j-N^{lsq}} P_j + \frac{t}{2} \mathbf{V}^\dagger \mathbf{V} \quad (5-14)$$

where the λ_j are the Lagrange multipliers and t is a small damping factor. Requiring the

gradients to vanish, $G_i^V = \frac{\partial \Lambda}{\partial V_i} = 0$, for $1 \leq i \leq N^c$; and $G_i^\lambda = \frac{\partial \Lambda}{\partial \lambda_i} = 0$, for $1 \leq i \leq N^{ex} =$

$N^{eq} - N^{lsq}$; gives through second order in displacements, the Newton-Raphson equations

$$\begin{pmatrix} \Lambda^{V,V} & \Lambda^{V,\lambda} \\ \Lambda^{\lambda,V} & \mathbf{0} \end{pmatrix}_0 \begin{pmatrix} \delta \mathbf{V} \\ \delta \boldsymbol{\lambda} \end{pmatrix} = - \begin{pmatrix} \mathbf{G}^V \\ \mathbf{G}^\lambda \end{pmatrix}_0 \approx \begin{pmatrix} (\mathbf{W}^{lsq})^\dagger \mathbf{W}^{lsq} + t\mathbf{I} & (\mathbf{W}^{ex})^\dagger \\ \mathbf{W}^{ex} & \mathbf{0} \end{pmatrix}_0 \begin{pmatrix} \delta \mathbf{V} \\ \delta \boldsymbol{\lambda} \end{pmatrix} \quad (5-15)$$

Here $\Lambda_{i,j}^{V,V} = \frac{\partial^2 \Lambda}{\partial V_i \partial V_j} \approx (W^{lsq \dagger} W^{lsq})_{i,j}$, $\Lambda_{i,j}^{V,\lambda} = \frac{\partial^2 \Lambda}{\partial V_i \partial \lambda_j} = (W_{j,i}^{ex})^\dagger$; $\mathbf{V} = \mathbf{V}^0 + d\mathbf{V}$ and

$\boldsymbol{\lambda} = \boldsymbol{\lambda}^0 + d\boldsymbol{\lambda}$ are the improved values of coefficients and Lagrange multipliers; and the superscript 0, which we will suppress when no confusion will result, indicates that the quantities are evaluated at the current, as opposed to the displaced, ‘point’. The gradients are given by

$$\begin{pmatrix} \mathbf{G}^V \\ \mathbf{G}^\lambda \end{pmatrix}_0 = \begin{pmatrix} \mathbf{W}^{lsq \dagger} \mathbf{W}^{lsq} + t\mathbf{I} & \mathbf{W}^{ex \dagger} \\ \mathbf{W}^{ex} & \mathbf{0} \end{pmatrix} \begin{pmatrix} \mathbf{V} \\ \boldsymbol{\lambda} \end{pmatrix}_0 - \begin{pmatrix} \mathbf{W}^{lsq \dagger} \mathbf{L}^{(ab),lsq} \\ \mathbf{L}^{(ab),ex} \end{pmatrix} + \begin{pmatrix} \bar{\mathbf{G}}^V \\ \mathbf{0} \end{pmatrix}_0 \quad (5-16)$$

$$\bar{G}_j^V = \mathbf{V}^\dagger \frac{\partial (\mathbf{W}^{lsq})^\dagger}{\partial V_j} \mathbf{P}^{lsq} + \mathbf{V}^\dagger \frac{\partial (\mathbf{W}^{ex})^\dagger}{\partial V_j} \boldsymbol{\lambda} \quad (5-17)$$

$$\text{where} \quad \mathbf{L}^{(ab)} = \begin{pmatrix} \mathbf{L}^{(ab),lsq} \\ \mathbf{L}^{(ab),ex} \end{pmatrix} \quad \mathbf{W} = \begin{pmatrix} \mathbf{W}^{lsq} \\ \mathbf{W}^{ex} \end{pmatrix} \text{ and } \mathbf{P} = \begin{pmatrix} \mathbf{P}^{lsq} \\ \mathbf{P}^{ex} \end{pmatrix} \quad (5-18)$$

From eq. (5-12) the \mathbf{V} dependence of \mathbf{W} noted in eq. (5-17) is implicit being contained in the \mathbf{d}^J . The values of \mathbf{V} and $\boldsymbol{\lambda}$ need to be determined iteratively using the Newton-Raphson procedure, eq. (5-15). In order to obtain the initial values of \mathbf{V} and $\boldsymbol{\lambda}$ for the Newton-Raphson steps, $\bar{\mathbf{G}}^V$ is neglected, by neglecting the \mathbf{d}^J dependence of \mathbf{W} ,⁹ and eq. (5-15) is replaced by the much simpler iterative equation

$$\begin{pmatrix} (\mathbf{W}^{lsq})^\dagger \mathbf{W}^{lsq} + t\mathbf{I} & (\mathbf{W}^{ex})^\dagger \\ \mathbf{W}^{ex} & \mathbf{0} \end{pmatrix} \begin{pmatrix} \mathbf{V} \\ \boldsymbol{\lambda} \end{pmatrix} = \begin{pmatrix} (\mathbf{W}^{lsq})^\dagger \mathbf{L}^{(ab),lsq} \\ \mathbf{L}^{(ab),ex} \end{pmatrix} \quad (5-19)$$

which is solved to self consistency. Eq. (5-19) is much less likely to diverge than eq. (5-15), even though its convergence is also not guaranteed and when it does converge the final values of \mathbf{V} do not correspond to the optimal solution because of the approximation made to gradients. Eq. (5-19) serves as a good method for the initial few steps of the optimization procedure, and once the change in \mathbf{V} is relatively small eq. (5-15) is used to achieve correct convergence.

5.4 Treating Larger Molecules

The methodology reviewed in Sec. 5.3 was used to construct coupled PESs for the photodissociation of ammonia, $\text{NH}_3 + h\nu \rightarrow \text{NH}_3(\tilde{A}) \rightarrow \text{NH}_2(\tilde{X}, \tilde{A}) + \text{H}$.³²⁻³³ The results were quite encouraging, describing with unprecedented accuracy the lifetime of the levels

in the v_2 progression,³² and the corresponding $\text{NH}_2(\tilde{A})/\text{NH}_2(\tilde{X})$ branching ratio. However the computational effort required to handle the larger systems considered here increases with system size and additional techniques to reduce that effort and increase the generality of the approach are required. In this section we describe techniques that enable the treatment of larger systems, including: a procedure to (a) reduce N^c and introduce functions as needed by analysis of the null space, (b) use redundant coordinates with distributed origins to reduce the rate of growth of the $\mathbf{g}^{(l)}$, (c) incorporate nuclear permutation inversion symmetry in situations where the matrix elements may not be permutationally invariant and (d) treat the vicinity of a seam of conical intersection using a partially diagonalized representation.

5.4.1 Enhanced Methodology: Reduction of N^c - Preconditioning

(i) Motivation

It is difficult to anticipate how important a particular monomial $g^{(l)}$ will be in describing \mathbf{H}^d . As a result $\mathbf{W}^{lsq\dagger}\mathbf{W}^{lsq}$ appearing in eq. (5-16) and (5-19) can be ill-conditioned. To improve the conditioning and eliminate redundancies, the $g^{(l)}$ are replaced with new set $\bar{g}^{(l)} = \sum_j g^{(j)} Z_{j,l}$. Define $\bar{\mathbf{W}} = \mathbf{W}\mathbf{Z}$, then using, $\mathbf{W}^{lsq\dagger}\mathbf{W}^{lsq} = \mathbf{U}\mathbf{w}\mathbf{U}^\dagger$

where \mathbf{w} is diagonal, the conditioning requirement

$$\left(\bar{\mathbf{W}}^{lsq}\right)^\dagger \bar{\mathbf{W}}^{lsq} = \mathbf{I} = \left(\mathbf{W}^{lsq}\mathbf{Z}\right)^\dagger \mathbf{W}^{lsq}\mathbf{Z} = \mathbf{Z}^\dagger \mathbf{U}\mathbf{w}\mathbf{U}^\dagger \mathbf{Z} \quad (5-20)$$

yields $\mathbf{Z} = \mathbf{U}\mathbf{w}^{-1/2}$. Discarding the small eigenvalues and corresponding eigenvectors from \mathbf{w} yields the desired preconditioning basis reduction.

However this standard scheme has several limitations that make it unsuitable. \mathbf{W}^{lsq} depends on the \mathbf{d}^J which change every iteration of eq. (5-15). As a result \mathbf{Z} , will

have to be recomputed every iteration or some contributing components may be unintentionally discarded. Since the cost of this preconditioning is more than the cost of one iteration of the optimization procedure little is gained by this approach to preconditioning.

(ii) A \mathbf{d}^J independent, \mathbf{R}^n dependent conditioning procedure

It is desirable to choose a set of functions $g^{(l)}$ that is largely free of linear dependencies. Removing linear dependencies improves the numerical stability of the nonlinear optimization procedure, reduces the cost of determining the fit \mathbf{H}^d and improves the smoothness of the fit. To reduce the size of the basis \mathbf{g} we introduce an approximate preconditioning procedure which is independent of \mathbf{d}^J but changes with \mathbf{R}^n . In eqs. (5-1) and (5-11) the sum is over l with $(u(l), v(l))$ defining the block of \mathbf{H}^d to which each term contributes. In eqs (5-21) and (5-22) below it is convenient to reindex the sum so that each (u,v) block is separately indexed and only the l that contribute to the block are included and are denoted l' . With this reindexing the original $W_{n,l,j;l}$ becomes $W_{n,l,j;l',u,v}$. A similar reindexing of $g^{(l)}$ and $M_{j,l'}^{u,v,n}$ are suppressed. In this notation, the right null-space of \mathbf{W} has the form (using eq (5-13))

$$\sum_{l',u,v} W_{n,l,j;l',u,v} Z_{l'}^{u,v} = \sum_{l',u,v} d_u^I(\mathbf{R}^n) d_v^J(\mathbf{R}^n) M_{j,l'}^{u,v,n} Z_{l'}^{u,v} = 0 \quad (5-21)$$

If we treat \mathbf{d}^I as independent variables, then a sufficient condition for eq. (5-21) to hold for all values of \mathbf{d}^I is (for each (u,v) block)

$$\sum_{l'} \nabla_{l'} \bar{P}^{\kappa(u,v)} g^{(l')}(\mathbf{R}^n) Z_{l'}^{u,v} = \sum_{l'} M_{j,l'}^{u,v,n} Z_{l'}^{u,v} = 0 \quad (5-22)$$

Then for each block of \mathbf{H}^d , the \mathbf{d}^J -independent null space is the intersection, for each n , of the right null spaces for $\mathbf{M}^{u,v,n}$ or the null spaces of $(\mathbf{M}^{u,v,n})^\dagger \mathbf{M}^{u,v,n}$. This procedure has

the desirable properties that: it reflects the \mathbf{R}^n used in the fit-initially removing large numbers of unneeded functions and then decreasing the number of dependent functions as N^{point} grows; it treats each block of \mathbf{H}^d independently; and it can be used to eliminate functions before the fit is carried out. Because each block is treated separately in the \mathbf{d}^l -independent null-space analysis procedure, the eigenvalue decomposition(EVD) problem of a large matrix, required in our previous implementation owing to the absence of preconditioning, is reduced to a series of EVDs of smaller matrices corresponding to each block of \mathbf{H}^d . Since the cost of EVD procedure scales as $O(n^3)$, division into blocks drastically reduces the cost of the procedure. As a result, this \mathbf{d}^l -independent null-space analysis procedure proves to be a very inexpensive and efficient approach to reveal the redundancy of a polynomial basis on a given set of data. This enables us to find smaller but more efficient expansions by almost completely eliminating linear dependencies among the polynomial basis.

For the NH_3 \mathbf{H}^d , this preconditioning reduced the number of independent V_n from ~ 9800 in our previously reported expansion³³ to ~ 5000 terms, and subsequently based on the intuition afforded by the analysis, to ~ 2700 terms, in a new expansion with increased accuracy in the asymptotic region. For the phenol case this null space analysis is essential since it allows us to start processing the skeletal data with a second order expansion which otherwise would be ill-conditioned, and allows us to predetermine the impact of adding a particular $g^{(l)}$.

5.4.2 Redundant coordinates

The principal reason for using redundant coordinates is to slow the explosive growth of the monomial space $[g^{(l)}(\mathbf{R})]$ with improved accuracy that accompanies

nonredundant expansions. This can be seen as follows. For monomials of order 2 and 33 internal coordinates, there will be $\sim [33^2]/2$ second order terms. To increase the accuracy of the expansion we can either add m additional redundant variables giving $\sim [(33+m)^2]/2$ monomials or increase the order of the expansion giving $\sim [(33)^3]/3!$ terms at third order. While it is possible to manipulate the details of the growth of the expansion, the advantage of adding redundant coordinates and maintaining the low order of the expansion is clear.

The monomials in $g^{(l)}$ are based on the interatomic vectors $\mathbf{r}_{k,l} = \mathbf{R}_k - \mathbf{R}_l$ and distances $r_{k,l} = |\mathbf{r}_{k,l}|$, where $1 \leq k < l \leq N^{at}$. To facilitate the description of bond breaking we use: $g^{(l)}(\mathbf{R}) = \prod_{i=1}^{M_l} w_{m_l(i)}(\mathbf{R})$, where $w_1 = \exp(-\alpha_{k,l} r_{k,l})$; $w_2 = \mathbf{r}_{i,j} \cdot \mathbf{r}_{j,k} / (r_{i,j} r_{j,k})^\gamma$; $w_3 = \mathbf{r}_{i,j} \times \mathbf{r}_{i,k} \cdot \mathbf{r}_{i,l} / (r_{i,j} r_{i,k} r_{i,l})^\gamma$ and M_l is the degree of the monomial in w_j . w_2 describes angles (actually cosine of angles), and w_3 describes out of plane or dihedral angles. The use of scaled, dot products and scalar triple products¹ is preferred to angles since they approach zero as one bond stretches. The use of decaying exponentials, used by Braams and Bowman⁴ in describing adiabatic PESs, facilitates the description of bond breaking. Further decaying exponentials can implicitly describe Morse-like functions $[1 - \exp(-\alpha r)]^2$ which permits the representation to tacitly interpolate between data points taking anharmonicity into account. In addition to these general functions we use specially placed tanh and Gaussians, $\exp(-\alpha(r_{k,l} - c)^2)$, to divide up coordinate space into overlapping but distinct regions which are described using distinct sets of functions. $1/r_{k,l}$ functions are used to describe nuclear-nuclear repulsion. Since all functions are

ultimately based on $\mathbf{r}_{j,k}$ the $g^{(l)}$ are readily symmetry adapted in the CNPI^{30-31, 71} group. A more complete description of the $g^{(l)}$ is given in Sec. 5.5.2.

5.4.3 The diabatic representation and CNPI group symmetry

(i) A local analysis

For molecules undergoing large amplitude motion including dissociation, the appropriate group of the Schrödinger equation is the CNPI group. While the electronic energies are invariant under the group operations, the eigenfunctions are only guaranteed to carry irreducible representations of that group.^{15, 19} For the diabatic states some care is required.¹⁹ The following perturbative analysis, which is analogous to that used in the vibronic coupling problem when point group symmetry is appropriate, explains our approach.

Let \mathbf{Q}^0 be the arbitrary reference point of the expansion at which the adiabatic and diabatic representations are chosen to coincide. The electronic Hamiltonian can be expanded as

$$H^e(\mathbf{q}, \mathbf{Q}) = H^e(\mathbf{q}, \mathbf{Q}^0) + \sum_i \frac{\partial H^e(\mathbf{q}, \mathbf{Q}^0)}{\partial Q_i} \delta Q_i + 1/2 \sum_{i,j} \frac{\partial^2 H^e(\mathbf{q}, \mathbf{Q}^0)}{\partial Q_i \partial Q_j} \delta Q_i \delta Q_j + \dots \quad (5-23)$$

For $\mathbf{Q} = \mathbf{Q}^0 + \delta\mathbf{Q}$, with $\|\delta\mathbf{Q}\|$ small the adiabatic wave function $\Psi^{a,K,(ab)}(\mathbf{q}, \mathbf{Q})$ can be expanded in terms of the eigenstates at \mathbf{Q}^0 as:

$$\Psi^{a,K,(ab)}(\mathbf{q}, \mathbf{Q}) = \sum_{j=1}^{N^{ab}} \Psi^{a,j,(ab)}(\mathbf{q}, \mathbf{Q}^0) c_j^K(\mathbf{Q}) \quad (5-24)$$

where, as we use in Sec. 5.5, the $\Psi^{a,K,(ab)}(\mathbf{q}, \mathbf{Q}^0)$ and δQ_k carry 1-dimensional irreducible representations of the relevant subgroup of the CNPI group. Then the electronic Schrödinger equation becomes

$$[\mathbf{H}^e(\mathbf{Q}) - \mathbf{1}E_K(\mathbf{Q})]\mathbf{c}^K(\mathbf{Q}) = \mathbf{0} \quad (5-25)$$

where

$$H_{J,K}^e(\mathbf{q}, \mathbf{Q}) = H_{J,K}^e(\mathbf{q}, \mathbf{Q}^0) + \sum_i H_{J,K}^{e,i}(\mathbf{q}, \mathbf{Q}^0)\delta Q_i + 1/2 \sum_{i,j} H_{J,K}^{e,i,j}(\mathbf{q}, \mathbf{Q}^0)\delta Q_i\delta Q_j \quad (5-26)$$

and

$$H_{J,K}^{e,i,j,\dots}(\mathbf{q}, \mathbf{Q}^0) \equiv \left\langle \Psi^{a,J,(ab)}(\mathbf{q}, \mathbf{Q}^0) \left| \frac{\partial^n H(\mathbf{q}, \mathbf{Q}^0)}{\partial Q_i \partial Q_j \dots} \right| \Psi^{a,K,(ab)}(\mathbf{q}, \mathbf{Q}^0) \right\rangle_{\mathbf{q}} \quad (5-27)$$

Thus $H_{J,K}^{e,i,j,\dots}(\mathbf{q}, \mathbf{Q}^0)$ vanishes unless

$$\prod_m \text{irred}(\delta Q_m) = \text{irred}(\Psi^{a,J,(ab)}) \times \text{irred}(\Psi^{a,K,(ab)}) \quad (5-28)$$

While eq. (5-24) is clearly an approximation since $\Psi^{a,K,(ab)}(\mathbf{q}, \mathbf{Q}^0)$, $1 \leq K \leq N^{\text{state}}$ is not complete it is accurate near an arbitrary \mathbf{Q}^0 and correct through first order in nuclear displacements near a conical intersection.⁷² The requirement in eq. (5-28) provides an effective way of reducing the size of the polynomial expansion. Its accuracy is reflected in the size of the residual derivative coupling, which as discussed below for phenol and seen previously in Ref. ⁹ for NH_3 is acceptably small. The favorable description of the derivative coupling is obtained provided the symmetry, but not the order, of the adiabatic states established at \mathbf{Q}^0 persists. If (avoided) crossings result in changes in the CNPI symmetry of the adiabatic states it may be necessary to work with a lower symmetry subgroup of the CNPI group. It is not possible to eliminate the derivative coupling entirely, owing to its nonremovable part.⁷³⁻⁷⁴

5.4.4 Description near Conical Intersections

(i) Points of Conical Intersection. Orthogonal intersection adapted coordinates

Our description of the vicinity of a conical intersection seam exploits the simplifications obtained from orthogonal intersection adapted coordinates,⁷⁵⁻⁷⁶ based on $\mathbf{g}^{I,J}$ and $\mathbf{h}^{I,J}$ where

$$2\mathbf{g}_k^{I,J,(x)}(\mathbf{R}) = L_k^{J,J,(x)}(\mathbf{R}) - L_k^{I,I,(x)}(\mathbf{R}) \quad (5-29)$$

$$h_k^{I,J,(x)}(\mathbf{R}) = L_k^{I,J,(x)}(\mathbf{R}) \quad (5-30)$$

and we will suppress the (x) on the left hand side of eqs. (5-29) and (5-30) when no confusion will result. The local topography of points on a conical intersection seam is determined by the conical parameters, $s_w^{I,J}$, $w = x,y$ and $\mathbf{g}^{I,J}$, $\mathbf{h}^{I,J}$, where

$$2s_k^{I,J}(\mathbf{R}) = L_k^{J,J,(x)}(\mathbf{R}) + L_k^{I,I,(x)}(\mathbf{R}) \quad (5-31)$$

and

$$\mathbf{g}^{I,J} = \|\mathbf{g}^{I,J}\| \quad \text{and} \quad \mathbf{h}^{I,J} = \|\mathbf{h}^{I,J}\| \quad (5-32)$$

These parameters are continuous along the conical intersection seam, and therefore readily described by \mathbf{H}^d , provided

$$\mathbf{g}^{I,J}(\mathbf{R}) \cdot \mathbf{h}^{I,J}(\mathbf{R}) = 0. \quad (5-33)$$

This requirement is satisfied by the proper choice of a one parameter rotation of the degenerate states.⁷⁶

To evaluate the gradients in eq. (5-17) the derivatives $(\mathbf{d}^I)^\dagger \frac{\partial}{\partial V_k} \mathbf{d}^J \equiv D_k^{I,J}$ are required. Note that while $D_k^{I,J}$ bears a formal resemblance to $f_k^{I,J}$, it is not that quantity since the derivative is with respect to V_j not R_j . Away from the conical intersection seam, evaluation of $D_k^{I,J}$ this is straightforward, with

$$D_i^{I,J} = \left(\mathbf{d}^{I\dagger} \frac{\partial \mathbf{H}^d}{\partial V_i} \mathbf{d}^J \right) \left(E^{a,J,(m)} - E^{a,I,(m)} \right)^{-1}. \quad (5-34)$$

However at a conical intersection eq. (19a) is singular and eq. (5-33) is used. In that case $D_i^{I,J}$, is determined by differentiating eq. (5-33), which yields:⁹

$$\begin{aligned}
& 2 \left[- \left(\mathbf{g}^{I,J} \right)^2 + \left(\mathbf{h}^{I,J} \right)^2 \right] D_k^{I,J} \\
& = \mathbf{g}^{I,J} \cdot \left[\left(\mathbf{d}^I \right)^\dagger \frac{\partial \nabla H^d}{\partial V_k} \mathbf{d}^J + \sum_{K \neq I,J} D_k^{K,I} L^{K,J(m)} + \sum_{K \neq I,J} D_k^{K,J} L^{K,I(m)} \right] + \mathbf{h}^{I,J} . \\
& \left[\frac{1}{2} \left(\mathbf{d}^I \right)^\dagger \frac{\partial \nabla H^d}{\partial V_k} \mathbf{d}^I - \frac{1}{2} \left(\mathbf{d}^J \right)^\dagger \frac{\partial \nabla H^d}{\partial V_k} \mathbf{d}^J + \sum_{K \neq I,J} D_k^{K,I} L^{K,J(m)} - \sum_{K \neq I,J} D_k^{K,J} L^{K,I(m)} \right] \quad (5-35)
\end{aligned}$$

(ii) Near but not at Conical Intersections. Partially Diagonal Representations

For the energies to remain unchanged and diagonal when eq. (5-33) is enforced the two states must be degenerate, for both the *ab initio* data and the fit potentials. Therefore, in our previous algorithm, points of conical intersection, were at least partial nodes. For small systems like NH₃ it was possible require all located conical intersections to be nodes.

For a system the size of phenol the dimensionality of the seam space is very large, and exact reproduction of the seam cannot be achieved with a reasonable sized expansion. Further a very large number of exact equations also creates numerical problems. For points that are close to an intersection seam but not exactly degenerate, the rotation to enforce eq. (5-33) cannot be used since \mathbf{H}^d will no longer be diagonal. However proximity to a conical intersection means that rapid changes in the \mathbf{d}^J will accompany small changes in V_k making it difficult to converge eq. (5-15). In our previous work, the fitting of these near degeneracy points required us to first locate and fit a point of conical intersection in its vicinity. This proves to be expensive and inefficient in a more complex system.

With these factors in mind an alternative approach is adopted, in which we forego the requirement that \mathbf{H}^d be diagonalized by the \mathbf{d}^K . Instead we define states I, J to be quasi degenerate, elements of a (quasi) degeneracy group, provided $|\Delta E^{a,J,I,(ab)}(\mathbf{R}^n)| = |E^{a,J,(ab)}(\mathbf{R}^n) - E^{a,I,(ab)}(\mathbf{R}^n)|$ is below some preassigned value, in the case of phenol 2000 cm⁻¹. For a state pair in the same degeneracy group at a point \mathbf{R}^n eq. (5-33) is used to redefine the results of eq. (5-2) while any remaining states at that \mathbf{R}^n would satisfy eq. (

5-2). In a degeneracy group in lieu of using eq. (5-34) to evaluate $\mathbf{D}^{l,j}$, eq. (5-35) is used. Instead of simply rotating the states as in true degeneracy case, the finite energy difference is taken into account to ensure correct treatment. This approach extends the original true degeneracy treatment to an arbitrary number of degeneracy groups, each composed of an arbitrary number of states. It provides a partially diagonal representation for which the $\mathbf{D}^{l,j}$ are well behaved, facilitating convergence of eq. (5-15) and avoids the special treatment required when conical intersections are required to be nodes. Note that while a seam of conical intersections is a set of measure zero, points with quasi-degeneracy occupy a finite 'volume' in nuclear coordinate space surrounding the seam. It will not be uncommon to have more than two states be in the degeneracy group. The mathematical details of quasi degenerate spaces and the use of partially diagonalized Hamiltonians are presented in Appendices 5.7.1 and 5.7.2. In section 5.5 the numerical description of conical intersection seams using this approach will be discussed.

The treatment of an N state quasi-degeneracy is closely related to that of the corresponding N state conical intersection seam. A discussion of this will be the subject of a future publication.

5.5 1,2,3¹A States of Phenol

In this section we use the 1, 2, 3 ¹A states (also denoted the S₀, S₁, S₂ states) of phenol, pictured in Figure 5-1 below, to illustrate the use of the procedures discussed in section 5.4. An \mathbf{H}^d is constructed that reliably represents *ab initio* data on a domain of definition appropriate for nonadiabatic photodissociation dynamics for this molecule with 33 internal degrees of freedom. For this initial feasibility study the electronic structure description represents a compromise between accuracy and ease of evaluation, although we emphasize that the electronic structure treatment is in no sense minimal. In a subsequent study we will, using more accurate *ab initio* data, use the techniques

introduced here to construct an \mathbf{H}^d suitable for an accurate treatment the nonadiabatic photodissociation of phenol which has been the subject of numerous experimental and theoretical studies.^{54-56, 58-60, 77-80}

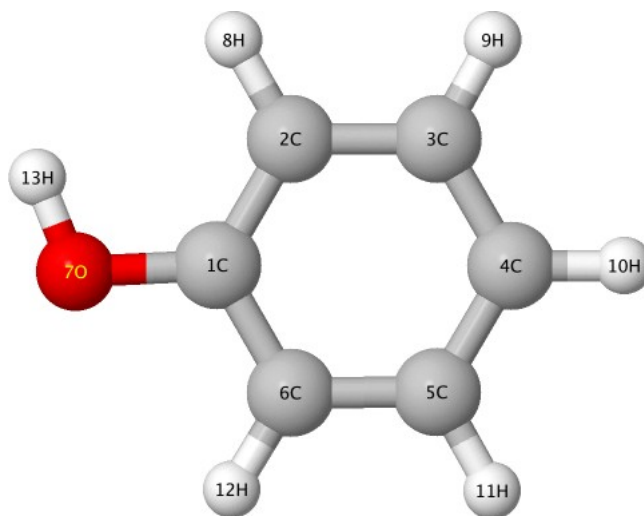


Figure 5-1. Phenol showing atom numbering used in this work

5.5.1 Electronic Structure Description

The electronic data was obtained using a FOCI wave function based on a 10 electron in 10 orbital active space. The active space includes all 7 π orbitals, σ , σ^* orbitals describing the OH bond and a Rydberg 3s orbital. There are twenty orbitals in the core. A cc-pVDZ basis augmented with an ANO 3s Rydberg function constructed specifically for phenol and benzene⁸¹ was used and gives rise to 2.7 million CSFs.

On the ground state the large amount of excess energy in the photodissociation causes the benzene ring of phenol to distort significantly. However such distortion is not observed to cause breaking of σ bonds in the benzene ring, although new bonds may be formed at some intermediate structures. Therefore we use a permutation inversion subgroup that preserves the connectivity of chemical bonds in the phenoxy moiety. Using this criterion to eliminate all unfeasible permutations, the relevant CNPI subgroup,

denoted G_4 , is generated by the inversion and a single nuclear permutation $P = (H8,H12)(C2,C6) (C3,C5)(H9,H11)$, where (a,b) denotes a transposition of atoms a and b . This group is isomorphic to C_{2v} and equivalent to that group for structures with C_{2v} point group symmetry. As observed by Dixon *et al.*⁶¹ in the Franck-Condon region, the $1,2,3^1A$ electronic states have 1A_1 , 1B_1 and 1B_2 symmetry. This symmetry will be used as described in section 5.4.3i, to reduce the number of V_j that need to be determined. In the product channel, the three electronic states have 1B_1 , 1B_2 and 1A_2 symmetry, with the 1A_2 state being highly excited. This change in symmetry requires that either we work in a lower (or no) symmetry CNPI subgroup, or obtain only an approximate fit to derivative couplings involving the 3^1A state in the asymptotic region. Since, as discussed below, in this region the 3^1A state is not germane to the nuclear dynamics the later option is chosen. Although we do not get correct couplings with the 3^1A state near C_{2v} structures in this channel, the couplings are still included in the fit and can be reproduced away from C_{2v} structures. In the more precise treatment noted above 4 states will be included in the representation which will eliminate this problem entirely. This point is discussed further below.

5.5.2 Summary of the H^d

Key parameters describing the fit representation are summarized in Table 5-1 and the functions of the internal coordinates used to construct the $g^{(l)}$ are given in Table 5-2. Referring to these tables the 51 overcomplete set of functions in Table 5-2, are constructed from 34 symmetry unique functions using the G_4 group operations. Products involving the first 47 functions in Table 5-2 are restricted to second order as discussed in section 5.4.2. The final 4 functions in Table 5-2 have the common property, denoted

partitioning in that table, of being relatively flat in two or more distinct regions, and gradually changing over between these regions. These connecting regions are often the most challenging as a result to the changing electronic structures associated with the chemical process. For these functions higher order terms are allowed.

Below we explain these restrictions and describe how the functions in Table 5-2 work together to determine a reliable representation. Reciprocal ($1/r_{k,j}$) and exponential functions, routinely used in global single surface fits, provide the foundation for the fit. They are flatter in the more chemically relevant regions but change significantly when their arguments are near 0. Therefore they are prone to produce oscillations near 0 at higher order, and their higher order terms are nearly flat in the most important regions. This limits the value of higher order terms of these monotonically decaying functions. Conversely changing the order of partitioning functions changes its rate of change between these flat areas and hence the character of this partitioning property. By allowing different types of linear combinations and higher total order of these partitioning terms, the ability to describe distinct regions, as well as the quality of description in connection regions, is improved.

Table 5-1. Important Parameters of Fitting Procedure

Number of Symmetry Unique Coordinates(functions)	34
Total Number of Coordinates(functions)	51
Number of Symmetrized Basis Matrices	21976
Number of Independent Basis Matrices	21894
Number of \mathbf{R}^n	4649
Number of Independent Equations	444776
Number of Points of Conical Intersections	73
RMS energy error (cm^{-1}) – total energy < 55000 cm^{-1}	255
Number of Skeletal \mathbf{R}^n	610

Table 5-2. Coordinate Functions Used to Construct H^d

#	Type	Atoms ²	Scaling	Note
1	Stretch	1,2	Exp ³	C-C stretch
2	Stretch	1,6	Exp	
3	Stretch	2,3	Exp	
4	Stretch	5,6	Exp	
5	Stretch	3,4	Exp	
6	Stretch	4,5	Exp	
7	Stretch	2,8	Exp	C-H stretch
8	Stretch	6,12	Exp	
9	Stretch	3,9	Exp	
10	Stretch	5,11	Exp	
11	Stretch	4,10	Exp	
12	Stretch	1,7	Exp	C-O stretch
13	Bend	1,2,3	Radius	C-C-C angle
14	Bend	1,6,5	Radius	
15	Bend	2,3,4	Radius	
16	Bend	4,5,6	Radius	
17	Bend	2,1,6	Radius	
18	Bend	3,4,9	Radius	
19	Bend	2,1,7	Radius	C-C-O angle
20	Bend	6,1,7	Radius	
21	Bend	1,2,8	Radius	C-C-H angle
22	Bend	1,6,12	Radius	
23	Bend	3,2,8	Radius	
24	Bend	5,6,12	Radius	
25	Bend	2,3,9	Radius	
26	Bend	6,5,11	Radius	
27	Bend	4,3,9	Radius	
28	Bend	4,5,11	Radius	
29	Bend	3,4,10	Radius	
30	Bend	5,4,10	Radius	
31	OOP ⁴	2,3,5,6	6R ⁴	C6 Ring torsion
32	OOP	1,2,4,6	6R	
33	OOP	1,3,4,5	6R	
34	OOP ⁵	1,2,6,7	4R ⁵	-O Wagging
35	OOP	2,1,3,8	4R	-H Wagging
36	OOP	6,1,5,12	4R	
37	OOP	3,2,4,9	4R	
38	OOP	5,4,6,11	4R	
39	OOP	4,3,5,10	4R	
40	Stretch	7,13	Exp	O-H stretch
41	Stretch	7,13	Reciprocal	O-H stretch
42	Stretch	1,13	Exp	Dissociating H with closest C
43	Stretch	2,13	Exp	Dissociating H with ortho C
44	Stretch	6,13	Exp	
45	2BDP ⁶	2,6;7,13	4R	Alignment of OH bond
46	Stretch	8,13	Exp	H-H repulsion
47	Stretch	12,13	Exp	

Table 5-2. Coordinate Functions Used to Construct \mathbf{H}^d (Continued)

#	Type	Atoms ²	Scaling	Note
48	Stretch	2,6	Gaussian ⁸	Prefulvenic bridge-partitioning ¹⁰
49	Bending	1,7,13	cos ⁷	C-O-H bending-partitioning
50	Stretch	7,13	tanh ⁹	O-H stretch – partitioning
51	OOP	7,2,6,13	4R ⁵	Ring-OH torsion-partitioning

1. Total order of all coordinates except the last 4 coordinates are restricted to two.
2. For bending coordinates, the vertex is the middle atom. For 4R out-of-plane coordinates the permutationally unique atom is the first atom. The permutationally unique atom is shown in bold face.
3. Exponential scaling takes the form of $w=\exp[-\alpha(r-r_0)]$. Here exponential factor α is determined by fitting average energy of the lowest 3 states near the 2^1A-3^1A MEX to a Morse.
4. The 6 distance (6R) scaling of out-of-plane coordinates is achieved by using all 6 pairs of internuclear distances to scale the scalar triple product coordinates. In this case all 4 atoms are permutationally equivalent (up to a sign change of the coordinate). This is used to characterize ring torsions.
5. The 4 distance (4R) scaling of out-of-plane coordinates specifies one atom to be special among the 4 atoms. This atom will not be allowed to permute with the other 3 atoms. The 3 distances launching from this atom are used to perform scaling. This is used to characterize wagging motions.
6. The bond-bond dot product coordinate is defined as the dot product between two bond vectors. This involves 4 atoms and effectively describes both the angular motion and out-of-plane torsions. This coordinate has different inversion and permutation symmetry properties when compared with the scalar triple product.
7. The cosine of bond angle is also scaled by the lengths of the two borders to ensure that the coordinate properly vanishes upon dissociation. This function serves to partition the expansion in regions where the C-O-H bond is bend and straight. The maximum order of this coordinate is 1.
8. The center of the Gaussian function is chosen as the C-C distance of the prefulvenic minimum. This function serves to partition the planar and prefulvenic regions. The maximum order is 1.
9. The *tanh* function is centered around $r_{OH}=2.25$ bohr. It serves to partition the region where the OH bond is dissociated from the region where it is bound. The maximum order of this coordinate is 1.
10. Partitioning is described in Sec. 5.5.2.

As a consequence of using gradient and derivative coupling information, data at the 4649 \mathbf{R}^n produces almost 0.5 million equations, defining $\sim 22,000 \mathbf{V}_n$. For the final set of \mathbf{R}^n , only ~ 100 functions are eliminated as linearly dependent using eq. (5-22) in Sec. 5.4.1, reflecting the ability of the null space procedure to identify and exclude superfluous functions early in the procedure. Still the resulting eq. (5-15) is large in an absolute sense, but as we demonstrate below it is quite tractable. Issues specifically related to the handling of eq. (5-15) for large data sets are discussed in Appendix 5.7.4.

From an alternative perspective, for a 33 dimensional system that experiences various large amplitude motions enabled by the large amount of excess energy available to the system from the excited state photodissociation, the representation is rather

compact. The 21894 parameters, average 3649 parameters per block (although not all blocks are of equal size). For comparison a recent state of the art representation of the ground state potential energy surface by Czako and Bowman⁸² for the $\text{Cl} + \text{CH}_4 \rightarrow \text{HCl} + \text{CH}_3$, $\text{CH}_3\text{Cl} + \text{H}$ reaction used 3262 permutation symmetry adapted polynomials to describe the ground state potential energy surface, based on energies at 16,000 points.

5.5.3 Quality of Fit: Coarse Assays

The overall RMS energy error, 255 (347) cm^{-1} for energies within 55,000 (50,000) cm^{-1} of the ground state minimum, is comparable to the RMS error for the high quality single potential energy surface result of Czako and Bowman⁸² noted above and given parenthetically. In this regard note that for energies above 50,000, 55,000, 60,000 and 70,000 cm^{-1} weighting factors of 0.5, 0.2, 0.1 and 0.05 respectively are used in constructing eq. (5-15). Figure 5-2 refines the RMS error analysis presenting the error for each state as a function of the total energy. Note that the RMS energy error for the 2^1A and 3^1A states is approximately 50 cm^{-1} for electronic energies $< 50,000 \text{ cm}^{-1}$, reducing considerably the total RMS energy error in the range 40,000 – 50,000 cm^{-1} , which is key for nonadiabatic dynamics. This in turn indicates, as will be demonstrated further below, that the low energy regions of the excited states are very well described. Discontinuities in the underlying *ab initio* data, discussed in detail in the section 5.5.7 below, are responsible for much of the RMS energy error. The expansion achieves much higher accuracy in regions where *ab initio* data is smooth. Discontinuities are frequently seen when a change in character from Rydberg states to valence states is involved. As will be discussed in detail in section 5.5.7, the fit representation provides a natural way of smoothing out these discontinuous electronic structure results. To demonstrate and study

this smoothing process no attempt was made to modify the electronic structure description to remove the discontinuities.

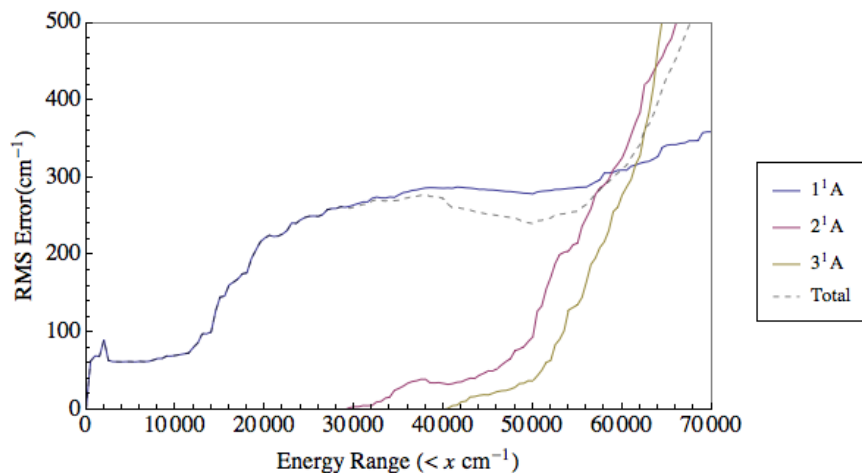


Figure 5-2. RMS energy error for 1,2,3¹A states and the total.

Figure 5-3 plots the norm of the residual energy gradient $\|\nabla(E^{a,J,(m)} - E^{a,J,(ab)})\|$ vs the norm of the *ab initio* determined energy gradient $\nabla E^{a,J,(ab)}(\mathbf{R})$. Figure 5-4 reports a similar plot for the derivative coupling. These plots demonstrate the good performance of the fitting procedure. The preponderance of the energy gradients are reproduced to better than 10% relative error for each of the three states. The outliers with larger magnitudes are on repulsive walls or represent the effects of discontinuities. Similarly the preponderance of the large derivative couplings, $\|\mathbf{f}^{a,I,J,(ab)}\| > 1$ have relative errors $< 10\%$. For those $\mathbf{f}^{a,I,J,(ab)}$ with magnitudes larger than 10^4 , the error in derivative couplings is a consequence of small errors in the location of the associated conical intersection. Errors of couplings with magnitudes beyond 10^7 will inevitably reach 100% as energy differences fall below the accuracy that can be achieved by least-squares fit. This apparent error is, however, an artifact caused by the infinity near, but not at, the fit conical intersection. The actual difference between the fit and *ab initio* result is still very small, as evidenced in Figure 5-5 and Figure 5-6, discussed in Sec. 5.5.8 below.

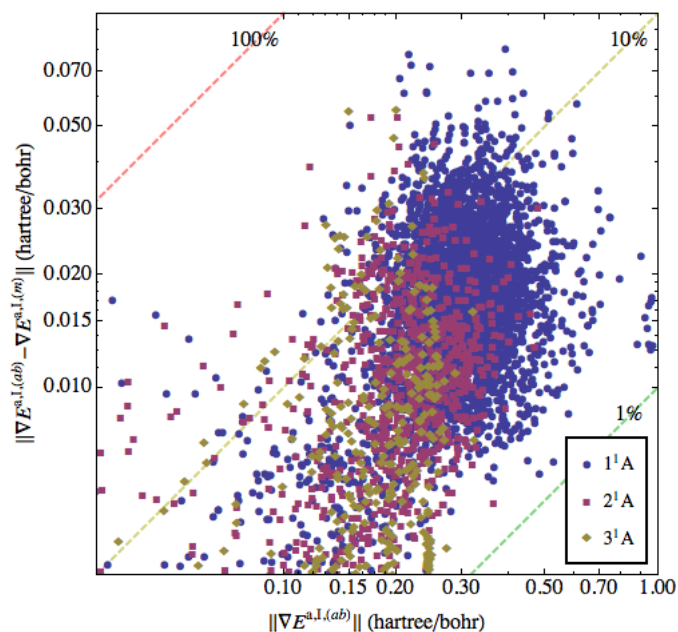


Figure 5-3. Scatter plot for energy gradients. Gradient norms are given in atomic unit. Norm of residual gradient, $\|\nabla(E^{a,J,(ab)} - E^{a,J,(m)})\|$ (ordinate) plotted against the magnitude of the *ab initio* energy gradient (abscissa).

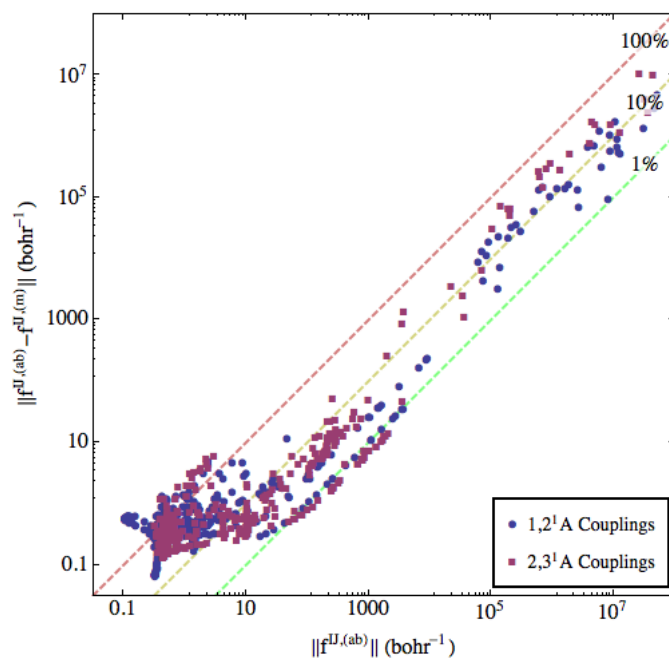


Figure 5-4. Scatter plots for derivative couplings. Coupling norms are given in atomic unit. Norm of residual coupling $\|\mathbf{f}^{a,J,I,(ab)} - \mathbf{f}^{a,J,I,(m)}\|$ (ordinate) plotted against the magnitude of the *ab initio* derivative coupling (abscissa).

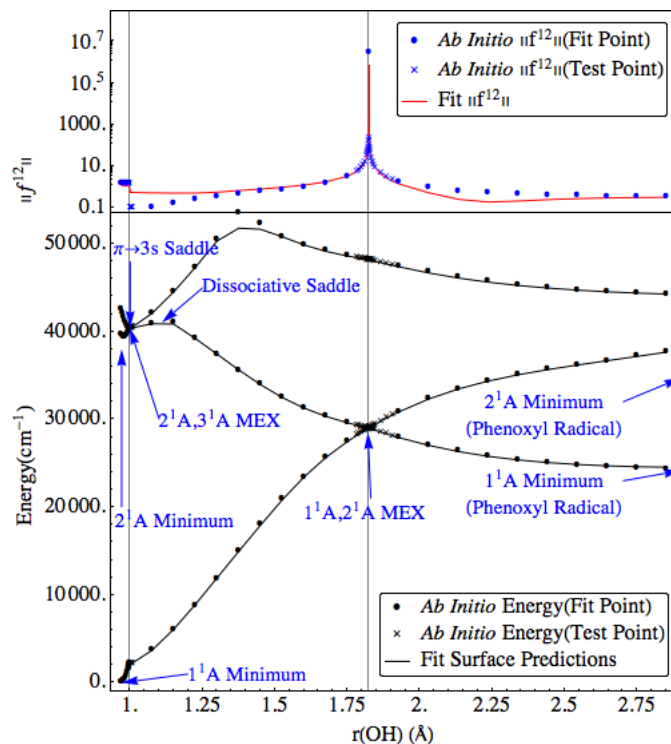


Figure 5-5. Path from ground state equilibrium to large R(O-H). Derivative couplings near the $1^1\text{A}-2^1\text{A}$ minimum energy conical intersection are also shown.

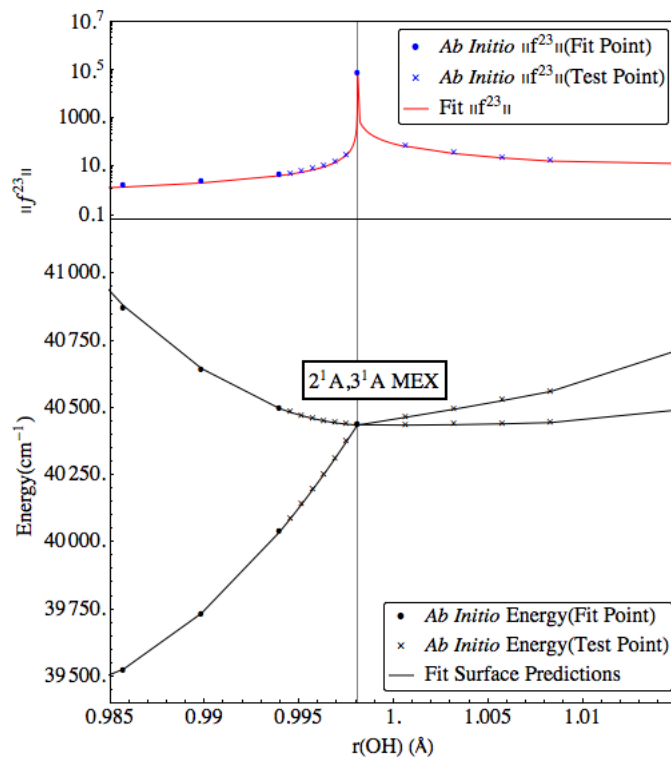


Figure 5-6. Derivative couplings near the $2^1\text{A}-3^1\text{A}$ conical intersection.

It is important to note that points with $\|\mathbf{f}^{a,I,J,(ab)}\| > 10^4$ correspond roughly to energy differences less than 1cm^{-1} . Previously such points would have been treated as nodes. However, the volume spanned by these points is extremely small. Indeed, among our numerous test trajectories, no points were found to reach such tight level of degeneracy. Most of the surface hopping events occur at geometries with $\|\mathbf{f}^{a,I,J,(ab)}\|$ between 10^1 and 10^3 , corresponding to energy differences in the range of the partial diagonal representation approach. Among all \mathbf{R}^n , 40 have $1,2^1\text{A}$ energy differences below 1cm^{-1} and 33 have $2,3^1\text{A}$ energy differences below 1cm^{-1} , all of which are part of the manually chosen skeletal points. 544 \mathbf{R}^n with small energy separations, including these 73 conical intersections are described using the partial diagonalization procedure. The majority of these points were obtained through trajectory simulations.

5.5.4 Quality of Fit: Detailed Assays

1. Extrema

Nine extrema are identified in this work. These extrema include minima on 1^1A and 2^1A potential energy surfaces in the phenolic and phenoxylic (product channel) regions; $1^1\text{A} - 2^1\text{A}$ and $2^1\text{A} - 3^1\text{A}$, minimum energy crossings and three saddle points, a saddle point to dissociation on the 2^1A state, a $\pi \rightarrow 3s$ saddle on the 2^1A state and barrier to H^{13} rotation on the 1^1A state. See Figure 5-5.

Table 5-3 reports the RMS error of 13 bond lengths, 18 bond angles and 9 torsion angles, using connectivity determined internal coordinates for the extrema noted above. These connectivity determined coordinates are tabulated Table 5-8, Table 5-9 and Table 5-10 in appendix 5.7.5. Geometries, in Cartesian coordinates, of all critical points on both *ab initio* and fit surfaces are provided in Table 5-11 in the same appendix. Their energies

are reported in Table 5-4. Both the energetics and geometries of these minima are well reproduced, despite the fact that we are treating all \mathbf{R}^n in the least squares manner as opposed to the approach used in NH_3 where such critical points were treated as nodes. It is significant to note that the errors in the fit values of excitation energies and energies at the minimum energy crossings are less than 51 cm^{-1} , which is much smaller than changes in these quantities expected when wave functions used in dynamics on the fly are replaced by the more exact wave functions practical in the fit surface paradigm.

Two extrema, both on 2^1A surface, are found in the immediate vicinity of the 2^1A - 3^1A minimum energy conical intersection: the $2^1\text{A}(\pi \rightarrow \pi^*)$ minimum and the $2^1\text{A}(\pi \rightarrow 3s)$ Rydberg saddle point. See Figure 5-5 and Figure 5-6. Both of these extrema correspond to minima on the corresponding diabatic surfaces and the intersection results from the crossing between them. The strong diabatic state coupling converts the $2^1\text{A}(\pi \rightarrow 3s)$ Rydberg diabatic surface minimum into a saddle point in adiabatic representation. As a result, the imaginary mode at saddle point is nearly identical with the derivative coupling direction at the conical intersection. It can be seen from Table 5-3 and Table 5-4 that this complex structure is well reproduced by fit.

Table 5-3. RMS Error of Fit Critical Point Geometries from *Ab Initio* Values

Critical Point	Bond Lengths(Å)	Bond Angles(°)	Torsion Angles(°)
<i>Phenol</i>			
S₀ Minimum	0.0005	0.15	0.00
S₁ Minimum	0.0005	0.09	0.00
S₀ Rotational Saddle	0.0013	0.19	0.36
S₁ π 3s Saddle	0.0002	0.07	0.00
S₁ Dissociation Saddle	0.0020	0.20	0.00
S₀-S₁ MEX	0.0011	0.07	0.00
S₁-S₂ MEX	0.0002	0.06	0.00
<i>Phenoxy Radical</i>			
S₀ Minimum	0.0021	0.13	0.00
S₁ Minimum	0.0007	0.07	0.00

Table 5-4. Energetics of Critical Points in cm^{-1}

Critical Point	<i>Ab Initio</i>	Fit (Optimized)	Error
<i>Phenol</i>			
S₀ Minimum	0.00	56.50	56.50
S₁ Minimum	38021.61	38021.15	-0.46
S₀ Rotational Saddle	1578.27	1718.51	140.24
S₁ (π 3s) Saddle	40433.20	40432.30	-0.90
S₁ Dissociation Saddle	41027.53	40976.60	-50.93
S₀-S₁ MEX	28537.27	28581.31	44.04
S₁-S₂ MEX	40436.91	40436.15	-0.76
<i>Phenoxy Radical</i>			
S₀ Minimum	24181.17	24261.88	80.70
S₁ Minimum	34738.61	34672.23	-66.38

2. Harmonic Frequencies

Harmonic frequencies at the extrema noted above are calculated from numerical Hessians for the *ab initio* and fit potential energy surfaces using forward differences of analytic energy gradients with step sizes of 0.001. The RMS errors for all 33 modes, shown in Table 5-5 are between 10 and 23 cm^{-1} . A complete tabulation of the frequencies for both *ab initio* and fit surfaces can be found in appendix 5.7.6, where it is seen that the largest error is $\sim 50 \text{ cm}^{-1}$. For the fit potential energy surfaces, it is possible to obtain much higher accuracy using centered differences, smaller step sizes, and higher order differencing schemes. By applying all three, the error in harmonic frequencies due to numerical differentiation is found to be at most 2 cm^{-1} . Due to the limited accuracy of *ab initio* energy gradients and high cost of evaluation, we did not use these techniques for the *ab initio* frequencies. Because of the demonstrated similarity between the fit and *ab initio* surfaces, the numerical error of *ab initio* frequencies is expected to be small despite the use of less expensive forward differencing method.

Table 5-5. Error in Harmonic Frequencies and Zero Point Energies

Critical Point	RMS Error	ZPE	Fit ZPE	d ZPE
S₀ Minimum	18.45	23947.50	23908.29	-39.21
S₁ Minimum	17.20	22492.03	22486.74	-5.29
S₀ Rotational Saddle	21.94	23711.61	23628.74	-82.87
S₁ ($\pi \pi^*$) Saddle	19.60	23494.80	23397.11	-97.69
S₁ Dissociation Saddle	22.52	22055.15	21984.38	-70.77
Phenoxy S₀ Minimum	13.98	20870.47	20918.73	48.25
Phenoxy S₁ Minimum	14.45	21019.65	21010.77	-8.88

It is important to note that we do not include any data points that are in close vicinity of each other. Especially, the small displacement points used to calculate harmonic frequencies for the fit surfaces are NOT used in the fitting procedure. Nevertheless, the harmonic frequencies are well reproduced, showing that the fit is not “noisy” in the vicinity of points with small gradients. This provides further evidence of the quality of the fit.

5.5.5 Determining the Domain of Definition of H^d

Even though the dimensionality of the system is extremely high, the regions, particularly on the electronically excited states, accessible to the dynamics of C₆H₅O-H photodissociation is only a small portion of the available space. It is, however, difficult to define this region without detailed knowledge of the dynamics. A manually chosen grid may not cover the relevant regions, or be too extensive to calculate owing to the inclusion of irrelevant regions.

1. Surface Hopping Quasi-classical Trajectory Simulations

In order to obtain a satisfactory yet realistic domain of definition, we employed a previously developed scheme⁸ to sample the dynamically relevant region by monitoring

surface hopping quasi-classical trajectories(QCT)⁴⁸. The trajectory simulations are performed with the Adiabatic and Nonadiabatic Trajectories 2013 (ANT2013) program suite.⁶⁸ A modified Bulirsch-Stoer method with adaptive step size⁸³ is used to perform integration.

On the ground state potential energy surface ergodicity complicates the analysis, in that, not unexpectedly, some trajectories that transition to the ground state potential energy surface, remain there for extended periods of time exploring ever increasing regions of nuclear coordinate space. These trajectories can be handled statistically. For the purpose of determining the dynamically important regions, we limit the propagation time of the trajectories to 50 ps. Illustrative of the smoothness of the fit is the fact that for all the trajectories run the maximum change in the total energy was 10^{-4} eV over the full 50 ps of propagation. The details of the use of QCT to construct the domain of definition are presented in Appendix 5.7.3. We now document properties of the domain of definition so obtained.

2. Testing the Adequacy of Domain of Definition

To ensure that the domain of definition is sufficient to describe nonadiabatic dynamics 1000 QCT are run using the \mathbf{H}^d obtained from the final data set. In general with our initial conditions the randomized trajectories have a total energy in or above the range the experimental energies (7.41-8.99 eV) defined as the sum of the laser energy and the \mathbf{H}^d determined zero point energy. See Figure 5-7. A coarse grained analysis of these trajectories is shown in Table 5-6. Key is the result that 97.4% of the trajectories stay in the domain of definition. Among all simulated trajectories, only 55(5.5%) lasted the full duration of 50ps without dissociating, showing that 50ps is a reasonable cutoff simulation

time. All of these 55 trajectories stayed within the domain of definition. Among the trajectories that reached the asymptote in the prescribed simulation time, 42.9% (56%) dissociated to $1^1\text{A}(2^1\text{A})$ in the product channel. Only 0.7% of trajectories dissociated through 3^1A surface, validating our argument that the symmetry of 3^1A surface near asymptote is not important. Note that owing to the tight tolerances used on average each trajectory required ~ 5 million H^{d} evaluations.

Table 5-6. Dynamics Summary Assay

Total Number of Trajectories	1000
Retention Ratio	97.4%
Long-living Trajectories	55(5.5%)
Average Evaluation Count	5.055×10^6
Average Total Energy	8.23eV
Percent Dissociated to 1^1A	42.9%
Percent Dissociated to 2^1A	56.4%
Percent Dissociated to 3^1A	0.7%

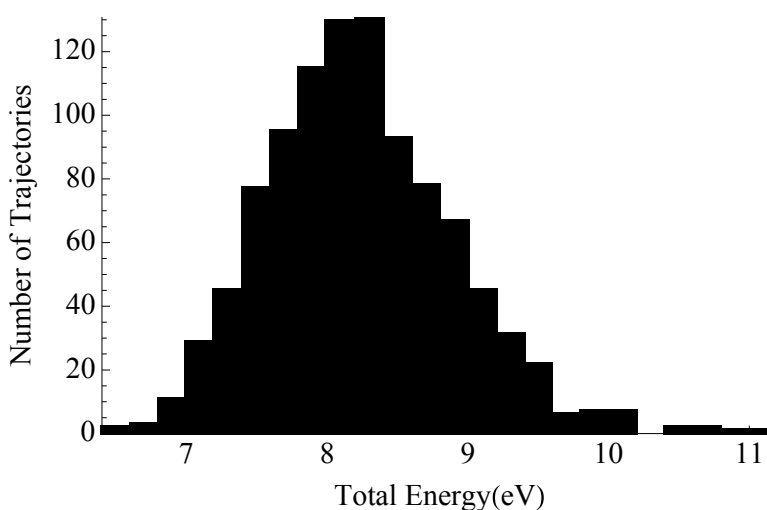


Figure 5-7. Total Energy Distribution of 1000 Test Quasi-classical Trajectories

Figure 5-8 and Table 5-7 provide a more detailed analysis of this test. Top and bottom panels of Figure 5-8 report the electronic energies for randomly chosen trajectories that dissociate on the 1^1A , 2^1A states, respectively. The trajectory terminating at the 1^1A asymptote is too long to be fully included and only the final portion of the simulation is shown. At five randomly chosen points on each of these trajectories, Table 5-7 report the H^d and *ab initio* determined energies, the energy errors, the D1 distance metric (defined and discussed in Appendix 0) and $R(OH^{13})$. The D1 distances, being < 0.15 , confirm that each trajectory stays in the domain of definition. The RMS energy errors from the 5 points, 174 and 116 cm^{-1} , respectively, are consistent with the RMS energy errors in Figure 5-2, although it is important to note here that these test points are not included among the R'' . Movies of these trajectories, available in the multimedia versions of Figure 5-8, show a more complete picture of the trajectories, including the molecular motion, the magnitude of derivative couplings, the D1 distances, the energies and the state transitions as functions of simulation time.

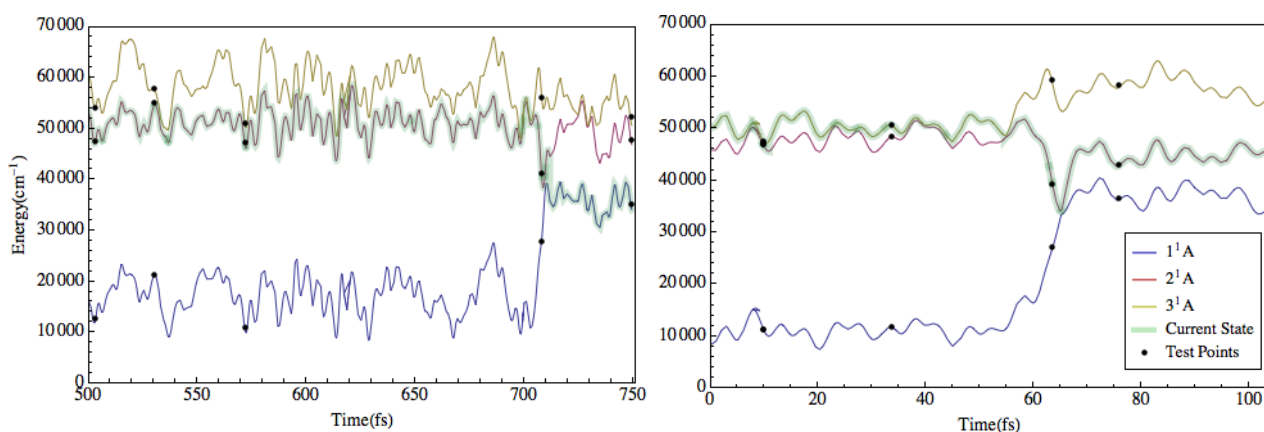


Figure 5-8. Energy profile of two sample trajectories that dissociate on 1^1A , 2^1A potential energy surfaces. Black markers denote randomly chosen points for which energies are compared with *ab initio* results. See Tables VIIa-b. Left: 1^1A Channel; Right: 2^1A Channel

Table 5-7: Fitting Error from Randomly Selected Trajectories.

A. Dissociating through 1^1A Channel(TE^a=7.96eV); RMS Error=173.84cm⁻¹

Time (fs)	Current Surface	<i>ab initio</i> Energy	Fit Energy	Error	D1 Distance	OH Distance
503.18	2	47469.1	47587.0	117.8	0.073	1.835
530.19	2	54990.7	54672.6	-318.1	0.086	1.745
571.58	2	47266.6	47192.0	-74.6	0.074	1.998
707.86	2	41201.4	41208.1	6.6	0.066	2.317
748.87	1	35112.6	34938.2	-174.4	0.074	10.336

B. Dissociating through 2^1A Channel(TE=7.40eV); RMS Error=115.8cm⁻¹

Time (fs)	Current Surface	<i>ab initio</i> Energy	Fit Energy	Error	D1 Distance	OH Distance
9.80	2	46966.6	46836.2	-130.4	0.064	1.875
9.81	2	46933.1	46805.5	-127.6	0.064	1.875
33.60	3	50567.5	50655.1	87.6	0.062	1.919
63.40	2	39363.0	39485.5	122.6	0.070	2.316
75.72	2	42957.5	42852.0	-105.4	0.079	3.829

^aFor comparison the estimated experimental total energy (TE) range is 7.41~8.99eV obtained by adding the H^d determined ground state ZPE (2.97eV) to the experimental laser energy range: 4.44~6.02eV.

Not shown are trajectories dissociating on the 3^1A state. These rare events, < 0.7% of trajectories. A randomly chosen trajectory (TE=8.77eV) in this class exhibited a larger RMS energy error, ~491 cm⁻¹. The large RMS energy errors for this channel reflect the fact, that for energies > 50,000 cm⁻¹ lower weights are used in the fit, consistent with, as the trajectory statistics demonstrate, the limited importance of this path. Also not shown are “ergodic trajectories” which remain on the 1^1A surface but never dissociate. These trajectories, only 5.5 % of total trajectories, remain in the domain of definition for 50 ps but will eventually explore regions outside the domain of

definition. The 5 point RMS energy error for the randomly chosen trajectory (TE=7.83eV) was $\sim 550 \text{ cm}^{-1}$. Should this region be proven important in the future, the quality of fit in this region can be improved in a straight forward manner by inclusion of more coordinates, similar to the treatment of OH in this work.

5.5.6 Extent of the Domain of Definition

Here we describe the extent of the final domain of definition to illustrate the range of nuclear configurations that \mathbf{H}^d must represent. The domain of definition includes motion in which the benzene ring exhibits significant deviations from harmonic motion. Figure 5-9 reports histograms showing the range of bond distances, bond angles and dihedral angles encountered. The corresponding values at the 1^1A_1 state equilibrium structure are indicated by vertical arrows. Figure 5-10 depicts phenol at the largest displacement along nine coordinates not involved in the dissociation process with energies below $50,000 \text{ cm}^{-1}$. The histogram shows that the trajectories can access a very wide range of geometries including large amplitude motions of the benzene ring particularly when propagating on the ground state, due to the large excitation energy. Most significantly, large numbers of trajectories experience excitation of OH bond torsional modes that resulted in full rotations around C-O bond. This motion is facilitated by the 2^1A potential energy surface which is lower in energy for nonplanar structures near the 2^1A - 3^1A minimum energy conical intersection region due to the a'' derivative couplings. Other than motions involving the dissociating hydrogen atom, large amplitude motion of out-of-plane bends of peripheral C-H and C-O bonds on the benzene ring and the distortion of the ring itself are also found quite frequently among the 1000 trajectories.

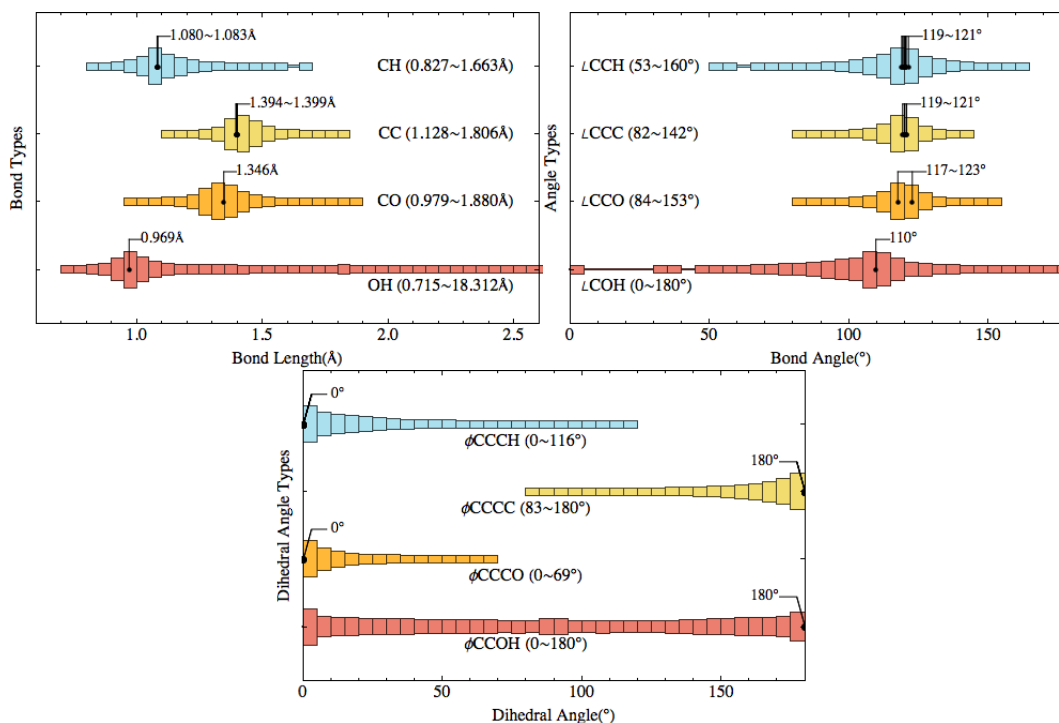


Figure 5-9. Large amplitude motion. Histogram showing displacements along bond distances, bond angles and dihedral angles for all data points used in the fit.

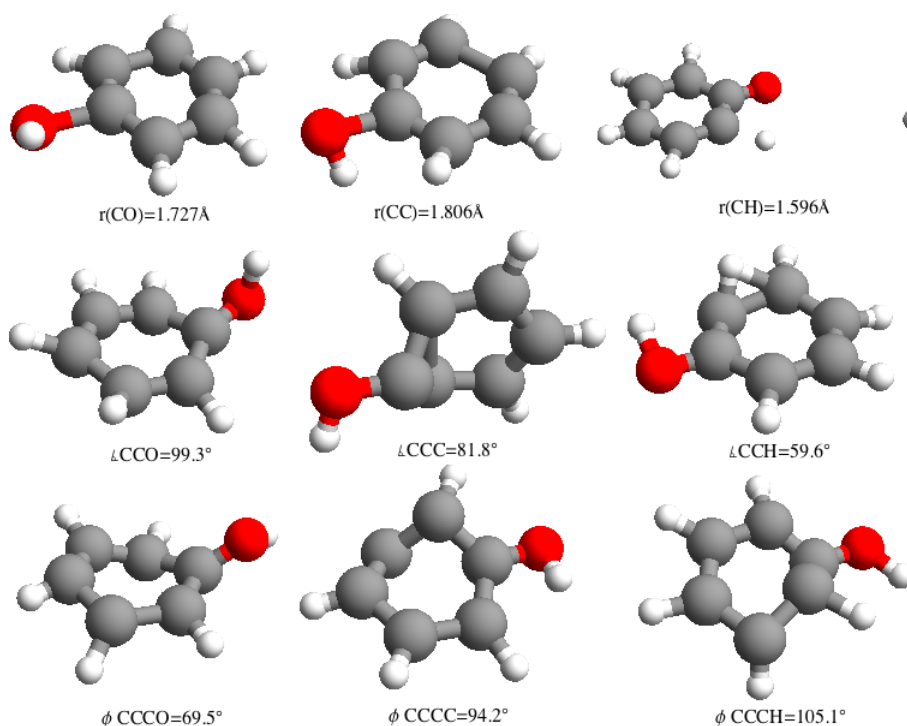


Figure 5-10. Large amplitude motion used to confirm domain of definition. Pictures of phenol showing largest displacements along 9 internal coordinates for \mathbf{R}^n with energy $<50,000\text{cm}^{-1}$. Bond stretches, bond angles and dihedral angles except those involved in the dissociation of O-H bond are included.

We also located and fit the 1^1A-2^1A intersection in the prefulvenic region⁵⁴ (See Figure 5-11), along with the linear synchronous transit path leading to it and the associated saddle point. The barrier is found to be 39072cm^{-1} above the global minimum, which is accessible at the energy level of the simulations. However, no trajectory is found to surmount this barrier to reach the prefulvenic region.

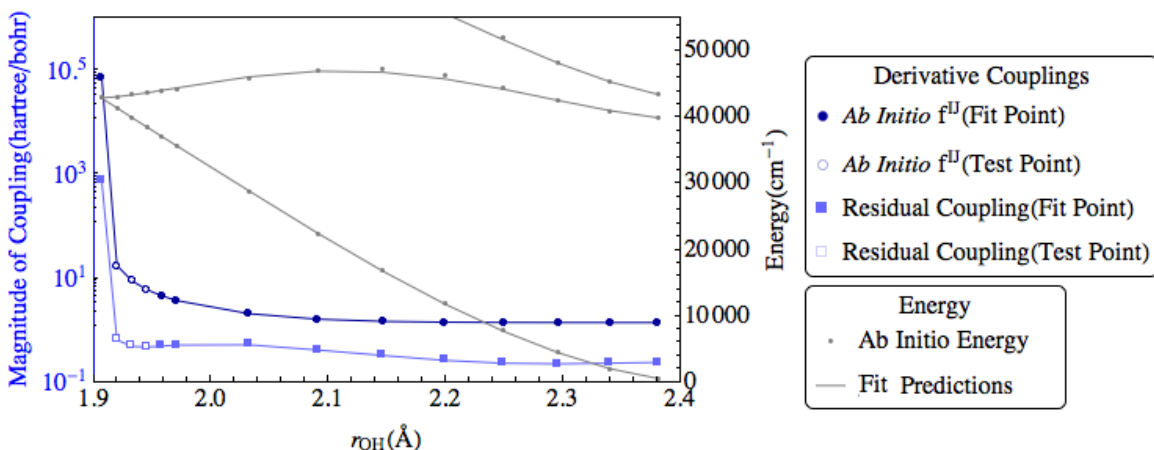


Figure 5-11. Quality of Fit Energy and Coupling on Path to Prefulvenic Intersection

5.5.7 Automatic Smoothing of Discontinuities in *Ab Initio* Data

As noted previously, discontinuities in the *ab initio* data make a significant contribution to the RMS energy error. In this section we demonstrate how the fit smooths out these discontinuities producing in effect coupled potential energy surfaces which are better than the *ab initio* data from which they are derived. In phenol the discontinuities are found to be a result of Rydberg orbital leaving the active space. In the Frank-Condon region, the 3^1A state has ($\pi \rightarrow 3s$) Rydberg character. An s-Rydberg orbital is therefore needed in the reference space to properly describe this state. However, outside the Frank-Condon region, particularly as $R(O-H)$ increases, the Rydberg state becomes a highly excited state and is not present in the reference space. As a result, the 3s Rydberg

orbital does not contribute to the $1-3^1A$ states. When this change of orbital character occurs abruptly the result is a discontinuity in the energy of all the states because of the change in the level of correlation. While it may be possible to remove this discontinuity by changing the active space or the weighting scheme, in nonadiabatic processes, such Rydberg-valence or other orbital switchings are very common and avoiding such discontinuity is often not practical. In a direct dynamics simulation, such discontinuities preclude conservation of total energy and can result in erroneous dynamics.

The fitting procedure provides a natural way of removing the discontinuity by interpolating between the two solutions and smoothing the discontinuous potential. We found that the points with large fitting error are in most cases in vicinity of such discontinuities. To illustrate this, we selected the \mathbf{R}^n with the largest fitting error, 1669 cm^{-1} . Using the trajectory that generated this point, an (extrapolated) path (a set of test points) was created by moving along the plus and minus directions of the momentum at that point in the generating trajectory. *Ab initio* data are calculated at these test points to illustrate the behavior of both *ab initio* and fit potentials around the discontinuity. The results are shown in Figure 5-12. The discontinuity is evident in the *ab initio* data, but the fit potentials are quite smooth. The orbital change that resulted in this discontinuity is shown in the inset, demonstrating that the interchange of a Rydberg orbital and a correlating orbital is the culprit. Note that none of these test points are included in the \mathbf{R}^n . The D1 distance of these points is given in the figure. All points are seen to be in the domain of definition. The smoothing functionality of fit potential is also evidenced in the tight conservation of total energy in the QCT, with variances less than 10^{-7} eV for most trajectories, and no more than 10^{-4} eV change even for propagation time as long as 50ps.

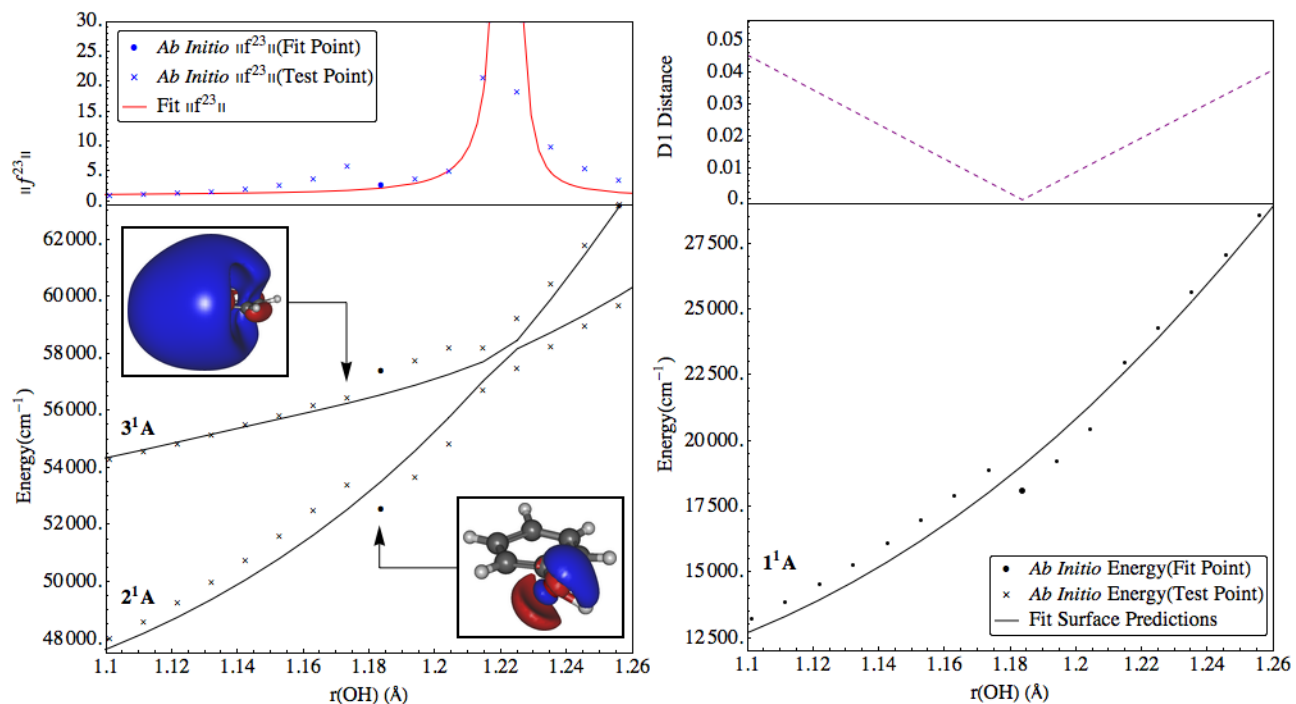


Figure 5-12. Analysis of a discontinuity in the *ab initio* data caused by a change from Rydberg to valence character of an orbital in the active space. Discontinuity occurs for $R(\text{OH}) \sim 1.185 \text{ \AA}$.

Left: Inset show the change in the orbital from Rydberg to valence character. Solid lines show fit. Small dots show *ab initio* results. The large black dot indicates the only \mathbf{R}^n included in the fit. The magnitude of the derivative coupling near the $2^1\text{A} - 3^1\text{A}$ avoided crossing is shown in upper plate. Right: The D1 distance of the remaining *ab initio* points are shown in the upper plot in plate and ground state energies from fit and *ab initio* data, including points in the fit and test points that are not used in the fit, are shown in the bottom plate.

5.5.8 Treatment of Conical Intersections

The partial diagonalization procedure introduced in this work provides an automated approach to characterizing conical intersections and their neighborhood. In this section we assess the efficacy of this approach. Figure 5-5 and Figure 5-6 address the ability of \mathbf{H}^d to correctly reproduce nonadiabatic coupling, considering the vicinity of the minimum energy $1^1\text{A}-2^1\text{A}$ and $2^1\text{A}-3^1\text{A}$ intersections, respectively. Test points (points not included in the \mathbf{R}^n) near each of the minimum energy intersections are shown. Again in these figures only the single near conical intersection point (there are no nodes in this

fit) is included in the \mathbf{R}^n . The remaining points are test points for some of which *ab initio* data were also determined. To illustrate the accuracy of the partial diagonal representation procedure, both *ab initio* and \mathbf{H}^d determined derivative couplings are reported in Figure 5-5 and Figure 5-6. The good agreement between the *ab initio* and \mathbf{H}^d derivative coupling is evident showing that fitting in the partial diagonal representation correctly reproduces quantities in adiabatic representation, while avoiding the need to require exact degeneracy of the two states in question. The relative error of derivative coupling is still around or below 1%, except for the extremely narrow area near the infinity where a very small shift in geometry of conical intersection can give rise to an artificially large relative error. It is evident, however, that the geometry error is extremely small and the fit couplings, although slightly shifted, very closely reproduced the *ab initio* values.

5.6 Summary and Conclusions

We report the extension of an algorithm for representing adiabatic states coupled by conical intersections using a quasi-diabatic state Hamiltonian useful in four and five atom systems, to treat nonadiabatic processes in considerably larger molecules. The method treats all internal degrees of freedom and is based on energies, energy gradients and derivative couplings obtained solely from *ab initio* multireference configuration interaction wave functions. The domain of definition of \mathbf{H}^d is constructed using quasi-classical surface hopping trajectories. The algorithm can simultaneously describe large amplitude motion and dissociation. These capabilities are attributable to the following procedures introduced here: (i) The representation is built up by adding data at points determined by quasi-classical surface hopping trajectories. Initially only a small fraction

of the functions ultimately required are needed. This causes significant linear dependence problems. A null space projector, which removes basis functions from the expansion until they are needed, avoids these issues and eliminates functions which are not useful in the fit. (ii) A partial diagonalization procedure allows for automated, but accurate, treatment of the vicinity of extended seams of conical intersection. (iii) The use of redundant variables limits the otherwise rapid growth of the basis functions required to describe distinct regions of nuclear coordinate space. The fitting procedure can smooth irregularities in the electronic energies attributable to the orbital changes that are frequently encountered in nonadiabatic processes producing a representation which is better than the electronic structure data from which it is derived.

The potential of this algorithm is demonstrated using the photodissociation of phenol governed by its 1^1A , 2^1A and 3^1A electronic states as a test. The results are quite encouraging as the representation was able to treat all 33 internal coordinates. This approach is expected to find application in grid based quantum dynamics such as the multiconfiguration time-dependent Hartree method,⁸⁴ where analytic representations of the coupled PESs are essential. However, since it brings more accurate electronic structure data to bear on the dynamics problem while removing the time to evaluate the electronic structure data as an issue, it will also improve the performance of trajectory based methods, including quasi-classical surface hopping methods⁴⁸ and quantum techniques including *ab initio* multiple spawning (AIMS)³⁴ and direct dynamics variational multiconfiguration Gaussian (DD-vMCG).³⁶

5.7 Appendices

5.7.1 Partial diagonalization of $\mathbf{H}^d(\mathbf{R}^n)$

In order to construct the gradients in eq. (5-17) the derivatives of the \mathbf{d}^J with respect to the V_j are required. This is numerically challenging when an \mathbf{R}^n is at or near a conical intersection, since the (near) degeneracy makes the \mathbf{d}^J sensitive functions of V_n . To remove this sensitivity the (near) degenerate eigenstates are 'rotated' to a new, nondiagonal representation. In this appendix we describe how this is accomplished. In Appendix 5.7.2 we use these results to determine $(\mathbf{d}^I)^\dagger \frac{\partial}{\partial V_i} \mathbf{d}^J$.

We define two conditions:

$$\text{for } \left| E^{a,I,(ab)}(\mathbf{R}^n) - E^{a,J,(ab)}(\mathbf{R}^n) \right| \geq t^d ; \quad (\mathbf{d}^I)^\dagger \mathbf{H}^d \mathbf{d}^J = 0 \quad (5-36)$$

$$\text{for } \left| E^{a,I,(ab)}(\mathbf{R}^n) - E^{a,J,(ab)}(\mathbf{R}^n) \right| < t^d ; \quad \mathbf{g}^{I,J} \cdot \mathbf{h}^{I,J} = 0 \quad (5-37)$$

For simplicity we say states satisfying A.1b are degenerate and form a degeneracy group. Condition (5-37) will be recognized as defining the rotation, see eq. (5-41) below, used to form the orthogonal $\mathbf{g}^{I,J}$ and $\mathbf{h}^{I,J}$ vectors at points of true degeneracy. In that case the rotated \mathbf{d}^J remain eigenstates of \mathbf{H}^d . Here, since $E^{a,J,(ab)}(\mathbf{R}^n) \square E^{a,I,(ab)}(\mathbf{R}^n)$ the rotated \mathbf{d}^J are no longer eigenstates. Since N^{state} may be greater than N_i^{deg} , the dimension of the i^{th} degeneracy group, the representation is denoted partially diagonal. Below we describe how a partial diagonalization is achieved.

At each \mathbf{R}^n all states are initially eigenstates of \mathbf{H}^d , that is they satisfy eq. (5-2). However, when their energies are closer than a preassigned t^d they are quasi degenerate and are required to satisfy (5-37). We show that these equations define the rotated \mathbf{d}^I .

Define, $d_{I,J}^{(d)} \equiv d_I^J$ where \mathbf{d}^I are the vectors of \mathbf{H}^d with phases chosen so that $\det(\mathbf{d}^{(d)}) = 1$.

Let $\mathbf{d}^{(p)}$ contain the orthonormal vectors defining the partially diagonal representation defined by (5-37). $\mathbf{d}^{(p)}$ is given by

$$\mathbf{d}^{(p)} = \mathbf{d}^{(d)} \exp \Theta , \quad (5-38)$$

where Θ is a skew symmetric matrix. Θ can be taken to be block diagonal since for \mathbf{d}^i in different degeneracy groups, (5-36) is satisfied by the original \mathbf{d}^I . Note too that Θ has $N_i^{deg}(N_i^{deg}-1)/2$ undetermined parameters which is precisely the number of equations in (5-37). However for $N_i^{deg} > 2$ it is less than straightforward to directly determine

Θ Instead we write

$$\exp \Theta = \prod_i \exp \Theta^{(i)} \quad (5-39)$$

where

$$\Theta_{M,N}^{(k)} = \delta_{I(k),M} \delta_{J(k),N} \theta^{(k)} - \delta_{I(k),N} \delta_{J(k),M} \theta^{(k)} \quad (5-40)$$

so that each $\exp \Theta^{(i)}$ is a Jacobi-type rotation with only four nonzero elements. Thus the solution is now reduced to finding a sequence of triples $\mathbf{k} = (\theta_k, I(k), J(k))$ that gives $\mathbf{d}^{(p)}$ whose vectors satisfy (5-36), (5-37). Intuitively we expect that the sequence of 2x2 Jacobi style rotations, based on the two state rotation⁷⁶

$$\tan 4\theta = \frac{2\mathbf{g}^{I,J} \cdot \mathbf{h}^{I,J}}{[|\mathbf{g}^{I,J}|^2 - |\mathbf{h}^{I,J}|^2]} \quad (5-41)$$

will do the job. We now show that this is indeed the case.

Define, for a particular I, J pair of states in the k^{th} degeneracy group, the $(n+1)^{\text{th}}$ transformation $\mathbf{d}(\theta) = \mathbf{d}^{(n)} \exp (\Theta^{(k)})$, where $\mathbf{k} = (\theta, I, J)$. The I^{th} column of $\mathbf{d}^{(n)}$ [$\mathbf{d}(\theta)$] is denoted $\mathbf{d}^{I(n)}$ [$\mathbf{d}^I(\theta)$] so that

$$\begin{aligned}\mathbf{d}^I(\theta) &= \mathbf{d}^{I,(n)} \cos\theta - \mathbf{d}^{J,(n)} \sin\theta \\ \mathbf{d}^J(\theta) &= \mathbf{d}^{I,(n)} \sin\theta + \mathbf{d}^{J,(n)} \cos\theta\end{aligned}\quad (5-42)$$

Since $\mathbf{h}^{I,J} = \mathbf{L}^{I,J,(m)}$ and $\mathbf{g}^{I,J} = [\mathbf{L}^{J,J,(m)} - \mathbf{L}^{I,I,(m)}] / 2$ (see eq.4), rotating the $\mathbf{d}^{(n)}$ rotates $\mathbf{h}^{I,J}$ and $\mathbf{g}^{I,J}$ which therefore are functions of θ . Using (5-42) we have

$$\begin{aligned}\mathbf{h}^{I,J}(\theta) &= -\mathbf{g}^{I,J,(n)} \sin 2\theta + \mathbf{h}^{I,J,(n)} \cos 2\theta \\ \mathbf{g}^{I,J}(\theta) &= \mathbf{h}^{I,J,(n)} \sin 2\theta + \mathbf{g}^{I,J,(n)} \cos 2\theta\end{aligned}\quad (5-43)$$

Then the condition (5-37), $\mathbf{h}^{I,J}(\theta) \cdot \mathbf{g}^{I,J}(\theta) = 0$ gives $\tan 4\theta$ from eq. (5-41) which defines the rotation matrix giving $\mathbf{d}^{(n+1)}$.

Since we are only rotating one pair of states at a time, when $N_i^{deg} > 2$ the rotation between I and J will change the orthogonality involving a third state K in the same degenerate block as I or J. It is, therefore not evident that this iterative procedure will eventually converge. It is not even clear that this set of equations has a valid solution.

To address this issue, we reformulate the eq. (5-37) as a minimization problem, so that the existence of a solution and convergence conditions can be more easily established. We emphasize, as noted above, that each quasi-degenerate block is treated independently of the others. If $N_i^{deg} = 2$, then that block can be constructed in 1 iteration, because the rotation satisfies the only equation in that block without affecting any other state pairs. If $N_i^{deg} \geq 3$ the problem becomes more interesting.

First examine eq. (5-43) for a pair of states I and J that are in the same quasi-degenerate block. Differentiating with respect to angle θ , we have

$$\begin{aligned}1/2 \frac{d\mathbf{h}^{I,J}(\theta)}{d\theta} &= -\mathbf{g}^{I,J,(n)} \cos 2\theta - \mathbf{h}^{I,J,(n)} \sin 2\theta \\ 1/2 \frac{d\mathbf{g}^{I,J}(\theta)}{d\theta} &= \mathbf{h}^{I,J,(n)} \cos 2\theta - \mathbf{g}^{I,J,(n)} \sin 2\theta\end{aligned}\quad (5-44)$$

Combining eqs. (5-43) and (5-44)

$$\begin{aligned}\frac{d\mathbf{h}^{I,J}(\theta)}{d\theta} \cdot \mathbf{h}^{I,J}(\theta) &= (|\mathbf{g}^{I,J,(n)}|^2 - |\mathbf{h}^{I,J,(n)}|^2) \sin 4\theta - 2 \mathbf{h}^{I,J,(n)} \cdot \mathbf{g}^{I,J,(n)} \cos 4\theta \\ \frac{d\mathbf{g}^{I,J}(\theta)}{d\theta} \cdot \mathbf{g}^{I,J}(\theta) &= -(|\mathbf{g}^{I,J,(n)}|^2 - |\mathbf{h}^{I,J,(n)}|^2) \sin 4\theta + 2 \mathbf{g}^{I,J,(n)} \cdot \mathbf{h}^{I,J,(n)} \cos 4\theta\end{aligned}\quad (5-45)$$

and

$$\frac{d\mathbf{h}^{I,J}(\theta)}{d\theta} \cdot \mathbf{h}^{I,J}(\theta) = 2\mathbf{g}^{I,J}(\theta) \cdot \mathbf{h}^{I,J}(\theta) = -\frac{d\mathbf{g}^{I,J}(\theta)}{d\theta} \cdot \mathbf{g}^{I,J}(\theta) \quad (5-46)$$

These equations give a relation between $\mathbf{g}^{I,J}$, $\mathbf{h}^{I,J}$ orthogonality and norms of $\mathbf{g}^{I,J}$ and $\mathbf{h}^{I,J}$

$$\frac{\partial}{\partial \theta} (\mathbf{g}^{I,J} \cdot \mathbf{g}^{I,J}) = -\frac{\partial}{\partial \theta} (\mathbf{h}^{I,J} \cdot \mathbf{h}^{I,J}) = 4\mathbf{g}^{I,J} \cdot \mathbf{h}^{I,J} \quad (5-47)$$

We also need the effect of a rotation on one pair of states (I,J) on the orthogonality of \mathbf{g} and \mathbf{h} vectors involving a third state K (in the same quasi-degenerate block as I and J).

Using eq. (5-41) and the fact the $\mathbf{d}^{K,(n)}$ is unchanged we have

$$\mathbf{h}^{I,K}(\theta) = (\mathbf{d}^{I,(n)\dagger} \cos \theta - \mathbf{d}^{J,(n)\dagger} \sin \theta) \nabla \mathbf{H}^d \mathbf{d}^K = \mathbf{h}^{I,K,(n)} \cos \theta - \mathbf{h}^{J,K,(n)} \sin \theta \quad (5-48)$$

$$\mathbf{h}^{J,K}(\theta) = (\mathbf{d}^{J,(n)\dagger} \cos \theta + \mathbf{d}^{I,(n)\dagger} \sin \theta) \nabla \mathbf{H}^d \mathbf{d}^K = \mathbf{h}^{J,K,(n)} \cos \theta + \mathbf{h}^{I,K,(n)} \sin \theta \quad (5-49)$$

Therefore from (5-48)

$$\begin{aligned}1/2 \frac{\partial |\mathbf{h}^{I,K}|^2}{\partial \theta} &= \mathbf{h}^{I,K} \cdot \frac{\partial}{\partial \theta} \mathbf{h}^{I,K} = (\mathbf{h}^{I,K,(n)} \cos \theta - \mathbf{h}^{J,K,(n)} \sin \theta) \cdot (-\mathbf{h}^{I,K,(n)} \sin \theta - \mathbf{h}^{J,K,(n)} \cos \theta) \\ &= -\cos 2\theta \mathbf{h}^{I,K,(n)} \cdot \mathbf{h}^{J,K,(n)} + 1/2 \left(|\mathbf{h}^{J,K,(n)}|^2 - |\mathbf{h}^{I,K,(n)}|^2 \right) \sin 2\theta\end{aligned}\quad (5-50)$$

and from (5-49)

$$\begin{aligned}1/2 \frac{\partial |\mathbf{h}^{J,K}|^2}{\partial \theta} &= (\mathbf{h}^{J,K,(n)} \cos \theta + \mathbf{h}^{I,K,(n)} \sin \theta) \cdot (-\mathbf{h}^{J,K,(n)} \sin \theta + \mathbf{h}^{I,K,(n)} \cos \theta) \\ &= \cos 2\theta \mathbf{h}^{I,K,(n)} \cdot \mathbf{h}^{J,K,(n)} + 1/2 \left(|\mathbf{h}^{I,K,(n)}|^2 - |\mathbf{h}^{J,K,(n)}|^2 \right) \sin 2\theta\end{aligned}\quad (5-51)$$

so that

$$\frac{\partial}{\partial \theta} \left(\left| \mathbf{h}^{J,K} \right|^2 + \left| \mathbf{h}^{I,K} \right|^2 \right) = 0 \quad (5-52)$$

Adding eqs. (5-47) and (5-52) gives

$$\frac{\partial S}{\partial \theta} = 4 \mathbf{g}^{I,J} \cdot \mathbf{h}^{I,J} \quad (5-53)$$

where $S = \sum_{K < L} \left| \mathbf{h}^{K,L} \right|^2$ is the sum of the norms of all \mathbf{h} vectors between states in the quasi-degenerate block of states I and J. It is important to notice that S is a block quantity, independent of the states I and J being rotated and that θ is part of the triple $\mathbf{k} = (\theta, I, J)$. For the current representation $\mathbf{d}^{(n)}$ to be converged for this block, $\mathbf{g} \cdot \mathbf{h}$ must vanish at $\theta = 0$, for all pairs in the degeneracy group. From eq.(5-52) is equivalent to the condition that S is stationary with respect to any rotation within the block. Since S is a sum of norms, it is non-negative. Being a non-negative continuous function, S is guaranteed to have a minimum. The solution to eq. (5-37) is therefore also guaranteed. However, this does not guarantee that this solution is unique, and in fact we find multiple solutions almost always exist.

We now show that the Jacobi type iteration scheme leads to a solution of eq. (5-37). We show that a rotation by $\mathbf{k} = (\theta, I, J)$ reduces the magnitude of positive semi definite S and hence moves toward the solution. From eq. (5-48), (5-49)

$$\begin{aligned} \left| \mathbf{h}^{I,K}(\theta) \right|^2 + \left| \mathbf{h}^{J,K}(\theta) \right|^2 &= \left| \mathbf{h}^{I,K,(n)} \cos \theta - \mathbf{h}^{J,K,(n)} \sin \theta \right|^2 + \left| \mathbf{h}^{J,K,(n)} \cos \theta + \mathbf{h}^{I,K,(n)} \sin \theta \right|^2 \\ &= \left| \mathbf{h}^{I,K,(n)} \right|^2 \cos^2 \theta - 2 \mathbf{h}^{I,K,(n)} \cdot \mathbf{h}^{J,K,(n)} \cos \theta \sin \theta + \left| \mathbf{h}^{J,K,(n)} \right|^2 \sin^2 \theta \\ &\quad + \left| \mathbf{h}^{I,K,(n)} \right|^2 \sin^2 \theta + 2 \mathbf{h}^{I,K,(n)} \cdot \mathbf{h}^{J,K,(n)} \cos \theta \sin \theta + \left| \mathbf{h}^{J,K,(n)} \right|^2 \cos^2 \theta \\ &= \left| \mathbf{h}^{I,K,(n)} \right|^2 + \left| \mathbf{h}^{J,K,(n)} \right|^2 \end{aligned} \quad (5-54)$$

so that any change of S comes exclusively from the I, J subspace. In the I, J subspace

$$\begin{aligned}
|\mathbf{h}^{I,J}(\theta)|^2 &= |\mathbf{h}^{I,J,(n)} \cos 2\theta - \mathbf{g}^{I,J,(n)} \sin 2\theta|^2 \\
&= |\mathbf{h}^{I,J,(n)}|^2 \cos^2 2\theta + |\mathbf{g}^{I,J,(n)}|^2 \sin^2 2\theta - 2\mathbf{h}^{I,J,(n)} \cdot \mathbf{g}^{I,J,(n)} \sin 2\theta \cos 2\theta \\
&= \frac{1}{2} \left(|\mathbf{h}^{I,J,(n)}|^2 + |\mathbf{g}^{I,J,(n)}|^2 \right) \\
&\quad + \frac{1}{2} \left(|\mathbf{h}^{I,J,(n)}|^2 - |\mathbf{g}^{I,J,(n)}|^2 \right) \cos 4\theta - \mathbf{h}^{I,J,(n)} \cdot \mathbf{g}^{I,J,(n)} \sin 4\theta
\end{aligned} \tag{5-55}$$

To simplify eq. (5-55) define C, α , so that

$$C = \sqrt{\frac{1}{4} \left(|\mathbf{h}^{I,J,(n)}|^2 - |\mathbf{g}^{I,J,(n)}|^2 \right)^2 + \left(\mathbf{h}^{I,J,(n)} \cdot \mathbf{g}^{I,J,(n)} \right)^2} \tag{5-56}$$

$$\begin{cases} \frac{1}{2} \left(|\mathbf{h}^{I,J,(n)}|^2 - |\mathbf{g}^{I,J,(n)}|^2 \right) = C \cos \alpha \\ \mathbf{h}^{I,J,(n)} \cdot \mathbf{g}^{I,J,(n)} = C \sin \alpha \end{cases} \tag{5-57}$$

giving

$$|\mathbf{h}^{I,J}(\theta)|^2 = \frac{1}{2} \left(|\mathbf{h}^{I,J,(n)}|^2 + |\mathbf{g}^{I,J,(n)}|^2 \right) + C \cos(\alpha + 4\theta) \tag{5-58}$$

The definition of 4θ in Eq. (5-41) can be rewritten

$$C \sin(4\theta + \alpha) = 0 \tag{5-59}$$

which has solutions

$$4\theta + \alpha = (2k-1)\pi \quad \text{for } k=1, 2 \tag{5-60}$$

where we have chosen the values of θ for which

$$\cos(\alpha + 4\theta) = -1 \tag{5-61}$$

From eq. (5-58) eq. (5-60), (5-61) give the solutions for which $|\mathbf{h}^{I,J}(\theta)|^2$ is minimal.

Inserting eq. (5-61) into (5-58) gives

$$\begin{aligned}
|\mathbf{h}^{I,J}(\theta)|^2 &= \frac{1}{2} \left(|\mathbf{h}^{I,J,(n)}|^2 + |\mathbf{g}^{I,J,(n)}|^2 \right) - \frac{1}{2} \sqrt{\left(|\mathbf{h}^{I,J,(n)}|^2 - |\mathbf{g}^{I,J,(n)}|^2 \right)^2 + 2 \left(\mathbf{h}^{I,J,(n)} \cdot \mathbf{g}^{I,J,(n)} \right)^2} \\
&\leq \frac{1}{2} \left(|\mathbf{h}^{I,J,(n)}|^2 + |\mathbf{g}^{I,J,(n)}|^2 \right) - \frac{1}{2} \left| |\mathbf{h}^{I,J,(n)}|^2 - |\mathbf{g}^{I,J,(n)}|^2 \right|
\end{aligned}$$

$$= \min\left(\left|\mathbf{h}^{I,J,(n)}\right|^2, \left|\mathbf{g}^{I,J,(n)}\right|^2\right) \quad (5-62)$$

where $\min()$ denotes the smaller of the two arguments. The equal sign holds only when the term $(\mathbf{h}^{I,J,(n)} \cdot \mathbf{g}^{I,J,(n)})^2 = 0$. Thus $|\mathbf{h}^{I,J}|^2$ and hence S are strictly decreasing unless $(\mathbf{h}^{I,J,(n)} \cdot \mathbf{g}^{I,J,(n)})=0$. By choosing the pairs of states I and J with the largest rotation angle every iteration, the rotation will always lower the value of S until $\mathbf{h}^{I,J} \cdot \mathbf{g}^{I,J} = 0$ holds for all pairs of states I and J , which is the desired result.

Finally we explain how the partially diagonalized representation is used in the fitting procedure. The derived transformation $\mathbf{d}^{(p)} = \mathbf{d}^{(d)} \exp(\Theta^{(m)})$ acts on the diagonal matrix $\mathbf{E}^{(m)}$, with matrix elements $E_{I,J}^{(m)} = \delta_{J,K} E^{a,J,(m)}$ forming

$$\mathbf{H}^{pd,(m)} = \exp(-\Theta^{(m)}) \mathbf{E}^{(m)} \exp(\Theta^{(m)}) \quad (5-63)$$

and also

$$d\mathbf{H}^{pd,(m)} = \exp(-\Theta^{(m)}) \begin{pmatrix} (\mathbf{d}^1)^\dagger \nabla \mathbf{H} \mathbf{d}^1 & (\mathbf{d}^1)^\dagger \nabla \mathbf{H} \mathbf{d}^2 & \dots \\ (\mathbf{d}^2)^\dagger \nabla \mathbf{H} \mathbf{d}^1 & (\mathbf{d}^2)^\dagger \nabla \mathbf{H} \mathbf{d}^2 & \dots \\ \cdot & \cdot & \cdot \end{pmatrix} \exp(\Theta^{(m)}) \quad (5-64)$$

where we have introduced the superscript (m) to indicate that model \mathbf{H}^d values are used. The same rotation procedure is also performed for the *ab initio* data to transform them into the same representation. Note that only energy gradients and derivative couplings are needed to determine the Θ , Therefore *ab initio* data can be rotated without any knowledge of \mathbf{d} . We then require

$$\mathbf{H}^{pd,(m)} = \mathbf{H}^{pd,(ab)} \quad \text{and} \quad d\mathbf{H}^{pd,(m)} = d\mathbf{H}^{pd,(ab)} \quad (5-65)$$

where the superscript (*ab*) indicates that the Θ is determined from the *ab initio* data. Note that when first part equation (5-65) holds, the *ab initio* and \mathbf{H}^d will have the same eigenvectors, therefore we have $\Theta^{(ab)} = \Theta^{(m)}$. As a result, equation (5-65) is equivalent with the corresponding equations in adiabatic representation. Thus even though the fit is done in the partially diagonal representation, the resulting \mathbf{H}^d is accurate in the adiabatic representation. The equations in (5-65) can be solved in a least square sense or exactly using Lagrange multipliers. As a result of the least squares procedure, the \mathbf{H}^d fit in adiabatic and partially diagonal representations will be different, however this difference is small when the fitting error is small.

5.7.2 Calculating $\nabla \mathbf{d}^J$ for an arbitrary number of degeneracy groups composed of an arbitrary number of degenerate states

In order to construct the gradients in eq. (5-17) the derivatives of the \mathbf{d}^J with respect to the V_j are required. Below we show how this is done when partial degeneracies may exist. It is convenient to define

$$D_i^{I,J} \equiv \mathbf{d}^{I\dagger} \frac{\partial \mathbf{d}^J}{\partial V_i} = -D_i^{J,I} \quad (5-66)$$

$$\mathbf{v}_k^{I,J} = (\mathbf{d}^I)^\dagger \frac{\partial \nabla \mathbf{H}^d}{\partial V_k} \mathbf{d}^J \quad (5-67)$$

$$E^{pd,I,J,(m)} = (\mathbf{d}^I)^\dagger \mathbf{H}^d \mathbf{d}^J \quad (5-68)$$

where we have suppressed the superscript (p) on the \mathbf{d}^J for simplicity. As we will show below, a system of linear equation for couplings $D^{I,J}_i$ can be obtained by differentiating A.1b for each pair of states *I* and *J*. There will be two cases to consider: (i) $N^{state} = N_i^{deg} > 2$; and (ii) there is more than one degeneracy group. There is clearly a relation between these quasi-degenerate groups and true *N*-state conical intersection seams. In a

future investigation the potential for the present analysis to be used to make the parametrization of an N -state conical intersection continuous along the $N^{int} - 5$ dimensional seam⁸⁵ will be considered.

(i) $\mathbf{D}^{I,J}$ between N states in a degeneracy group

For N degenerate states we have [see eq. (5-35)]

$$4\left(\left|\mathbf{h}^{I,J}\right|^2 - \left|\mathbf{g}^{I,J}\right|^2\right)D_i^{I,J} = \left(\mathbf{h}^{I,I} - \mathbf{h}^{J,J}\right) \cdot \left[\mathbf{v}_i^{I,J} + \sum_{K \neq I,J} \left(D_i^{K,I} \mathbf{h}^{K,J} + D_i^{K,J} \mathbf{h}^{K,I}\right)\right] \\ + \left[\mathbf{v}_i^{I,I} - \mathbf{v}_i^{J,J} + 2 \sum_{K \neq I,J} \left(D_i^{K,I} \mathbf{h}^{K,I} - D_i^{K,J} \mathbf{h}^{K,J}\right)\right] \cdot \mathbf{h}^{I,J} \quad (5-69)$$

If more than two states are in the degeneracy group, the $\mathbf{D}^{I,J}$ become members of a system of inhomogeneous linear equations

$$-\left(\mathbf{h}^{I,I} - \mathbf{h}^{J,J}\right) \cdot \mathbf{v}_i^{I,J} - \left(\mathbf{v}_i^{I,I} - \mathbf{v}_i^{J,J}\right) \cdot \mathbf{h}^{I,J} = 4\left[\left|\mathbf{g}^{I,J}\right|^2 - \left|\mathbf{h}^{I,J}\right|^2\right]D_i^{I,J} \\ + \sum_{K \neq I,J} D_i^{K,I} \left[\mathbf{h}^{K,J} \cdot \left(\mathbf{h}^{I,I} - \mathbf{h}^{J,J}\right) + 2\mathbf{h}^{K,I} \cdot \mathbf{h}^{I,J}\right] + \sum_{K \neq I,J} D_i^{K,J} \left[\mathbf{h}^{K,I} \cdot \left(\mathbf{h}^{I,I} - \mathbf{h}^{J,J}\right) - 2\mathbf{h}^{K,J} \cdot \mathbf{h}^{I,J}\right] \quad (5-70)$$

(ii) $\mathbf{D}^{I,J}$ between states in distinct degeneracy groups

Within a degeneracy group, the states are linear combinations of adiabatic states.

However, off-diagonal matrix elements between different groups vanish. Therefore differentiating $(\mathbf{d}^I)^\dagger \mathbf{H}^d \mathbf{d}^J = 0$ with respect to V_i gives

$$\sum_{K \sim J} D_i^{I,K} E^{pd,K,J,(m)} - \sum_{K \sim I} D_i^{J,K} E^{pd,K,I,(m)} = -\mathbf{v}_i^{I,J} \quad (5-71)$$

where the \sim implies the sum is restricted to elements of the same degeneracy group.

Eqs. (5-71) and (5-70) plus the antisymmetry of $\mathbf{D}^{I,J}$ in eq. (2-1) provides a system of linear equations for the $D_k^{I,J}$. Note that each subscript k is determined separately and if

at an \mathbf{R}^n there are only 2 nondegenerate states eq. (5-71) reduces to the standard result

$$D_i^{I,J} = \frac{v_i^{I,J}}{(E^{a,J,(m)} - E^{a,I,(m)})}$$

5.7.3 Extending the Skeletal Data

In this appendix the extension of the initial skeletal data set to a domain of definition appropriate for nonadiabatic dynamics is described. The skeletal data, 610 \mathbf{R}^n , was comprised of the nine critical points in Table 5-3 and Table 5-4, loops around them and paths between them. QCT simulations are then performed on a fit of the skeletal potentials. The initial conditions for positions and momenta are produced by sampling a quasi-classical distribution of the ground vibrational state on the ground electronic state. The trajectory is then started on the 3^1A state. This initial condition is not chosen to simulate a particular experiment, but rather to ensure coverage of the relevant area. Although the 3^1A surface has no significant transition dipole, it strongly couples with the 2^1A state, crossing with it near the Frank-Condon region. It is therefore important to correctly describe the 3^1A surface near Frank-Condon region. In order to achieve this, we initialized the test trajectories on 3^1A surface, which are found to cover a wider region of configuration space than initialization on 2^1A surface with similar energy. This produces the desired broad total energy distribution on the excited state. See Figure 5-11. The range of total energy distribution extends beyond that of the experimental conditions, which is necessary to ensure sampling of areas that will otherwise not be accessible to QCT due to the lack of tunneling effects.

As the trajectory propagates, each time an evaluation of the fit potential is made, the minimum distance to the current point from previously fit points is evaluated. We use the subset of the coordinate functions, 1-40, 42, 51 in Table 5-2, to calculate the distance,

denoted D1. D1 provides a natural way to ensure that upon dissociation the internal coordinates that are converted into translation and rotations of dissociated pieces properly vanish and do not contribute to the distance. When calculating distances, all permutation-inversions are looped over and the smallest distance among them is used. A new data point is added to the defining data set when its D1 exceeds a predetermined threshold. This threshold is dynamically adjusted: the threshold is increased when the *ab initio* data produced at new points are found to be well predicted by the existing fit and tightened when more than 5% of test trajectories produce new candidate data points, and kept constant if otherwise. Five to ten data points are selected from each trajectory that travel beyond range of existing data points, and trajectories are run until about 100 data points are chosen. *Ab initio* data are then calculated at these newly chosen points, and are subsequently incorporated into the fit. The trajectory simulations are performed again with the updated threshold. This procedure is repeated until the ratio of trajectories staying in range is satisfactory, 97% – 100 %, and the new points at threshold are well predicted by the fit. Note that if *ab initio* results of the candidate points from a trajectory are found to have been well reproduced by the fit values, that trajectory is relabeled as staying in range in the convergence analysis. About 30% of the candidate points fall into this category in the final stage of the expansion procedure. In this case the procedure converged at distance of 0.15 per coordinate, which is approximately 0.01 a.u. per coordinate distance near the Frank-Condon region.

5.7.4 Improved Least Squares Algorithm for Handling Large Systems

In this appendix we explain how eq. (5-15) based on large data sets is constructed and solved. Our previous algorithm used for tetra-atomic and penta-atomic

molecules was not particularly demanding of computational resources. For the larger systems considered here it becomes a formidable task to solve in eq. (5-15) or even store the required data. For example, for phenol, an expansion of 21,976 coefficients is used and the normal equations are constructed from 444,776 linear equations. Simply to store this (444776 x 21976) matrix requires more than 72GB of memory, and additionally the storage of the normal equations matrix, $W^{lsq\dagger}W^{lsq}$ and eigenvector matrices requires 3.6GB of memory each. This is very difficult to satisfy without parallelization on even high-end computers, and many interesting systems where the method can potentially be applied are larger than phenol. The computational cost of the construction of normal equations, as well as the diagonalization procedure required for the eigenvalue decomposition which was used in our previous works, scale as $O(n^3)$ and also becomes expensive for larger systems.

As described below, we have modified our handling of eq. (5-15) to significantly reduce memory consumption to less than 10% of that used in our previous approach, and at the same time introduce parallelism that allows the method to be used in much larger systems. In the improved algorithm, the fitting procedure is tractable on one single computation node for large problems like phenol, and even larger problems are also readily tractable with parallelization.

(i) Solution of Normal Equations

In our previous approach, solution of the normal equations is achieved by an eigenvalue decomposition procedure, which requires $O(n^3)$ computation time and an extra $O(n^2)$ memory space for the storage of eigenvectors. The use of less expensive direct methods for solving linear equations without explicit inversion was precluded by

the ill-conditioned normal equations matrix. However, after applying the preconditioning procedure in section 5.4.1, linear dependencies are largely removed from least squares block, and we apply a standard Rank-Revealing QR factorization, using the DGEQP3 subroutine in LAPACK, to remove linear dependencies among the exact equations. With linear dependencies removed, direct linear equation solvers can now be applied. This reduces the computational effort for the solution of linear equations to $O(n^2)$. Avoiding the need to store the eigenvectors required in explicit inversion techniques, reduces the memory required for the solution procedure. The cost of the solution of normal equations is found to be negligible compared to that of the construction of normal equations matrix.

(ii) Construction of Normal Equations

In the new algorithm, the storage of the matrix \mathbf{W}^{lsq} is avoided. Narrow stripes of \mathbf{W}^{lsq} that contain only equations for one data point are constructed and stored. The normal equations can be obtained by summing over contributions from these smaller matrices.

$$(\mathbf{W}^{\text{lsq}})^\dagger \mathbf{W}^{\text{lsq}} = \sum_{i=1} (\mathbf{W}_i)^\dagger \mathbf{W}_i$$

In most cases, \mathbf{W}^{lsq} is by far the largest data structure, responsible for more than 90% of the memory consumption, because the number of equations is far greater than the number of unknown coefficients. \mathbf{W}_i however, only contains a very small number of equations and takes an ignorable amount of memory. Thus by constructing normal equations one slice at a time, the memory requirement is reduced to less than 10% with no extra performance cost.

In the new fitting algorithm, the computation and summation of all matrix-matrix products $(\mathbf{W}_i)^\dagger \mathbf{W}_i$ is the only $O(n^3)$ operation in the fitting procedure and constitute most

of the computation time. Each of these pieces can be constructed independently and the summation is not sensitive to the ordering. The procedure can therefore be readily parallelized with the ScaLAPACK subroutine PDSYRK which is fully optimized and freely available on most architectures.

5.7.5 Geometries of *Ab Initio* and Fit Critical Points

Table 5-8. Bond Lengths of Critical Points. “*Ab initio*” refers to the value of internal coordinates on *ab initio* potential energy surfaces, and “Error” refers to the difference between fit and *ab initio* internal coordinates (fit minus *ab initio* coordinate value).

(a) Phenol Minima

Atoms		1 ¹ A Minimum		2 ¹ A Minimum	
		<i>Ab Initio</i>	Error	<i>Ab initio</i>	Error
C1	C2	1.3965	-0.0002	1.4316	-0.0004
C1	C6	1.3989	0.0006	1.4269	-0.0002
C1	O7	1.3457	-0.0005	1.3377	-0.0001
C2	C3	1.3983	0.0008	1.4315	0.0003
C2	H8	1.0833	0.0004	1.0807	0.0003
C3	C4	1.3950	0.0011	1.4332	0.0015
C3	H9	1.0815	0.0003	1.0789	0.0002
C4	C5	1.3992	-0.0001	1.4318	0.0009
C4	H10	1.0809	0.0000	1.0805	0.0003
C5	C6	1.3940	0.0010	1.4341	0.0005
C5	H11	1.0815	0.0000	1.0788	0.0001
C6	H12	1.0805	0.0001	1.0781	0.0001
O7	H13	0.9692	-0.0001	0.9703	-0.0003

Table 5-8. Bond Lengths of Critical Points (Continued)

(b) Phenol Saddle Points

Atoms		1^1A OH Torsional Saddle Point		2^1A $\pi \rightarrow 3s$ Rydberg Saddle Point [†]		2^1A Dissociative Saddle Point	
		<i>Ab Initio</i>	Error	<i>Ab initio</i>	Error	<i>Ab initio</i>	Error
C1	C2	1.3954	-0.0004	1.4340	-0.0002	1.4442	-0.0006
C1	C6	1.3954	-0.0004	1.4363	-0.0002	1.4454	-0.0013
C1	O7	1.3725	-0.0015	1.2740	0.0000	1.2584	0.0019
C2	C3	1.3971	0.0027	1.3706	-0.0002	1.3723	0.0006
C2	H8	1.0811	-0.0002	1.0797	0.0000	1.0773	0.0003
C3	C4	1.3976	0.0013	1.4196	0.0003	1.4176	-0.0016
C3	H9	1.0815	0.0004	1.0800	0.0001	1.0808	-0.0006
C4	C5	1.3976	0.0013	1.4159	-0.0001	1.4164	-0.0002
C4	H10	1.0812	0.0009	1.0806	-0.0002	1.0808	0.0004
C5	C6	1.3971	0.0027	1.3728	-0.0001	1.3738	0.0009
C5	H11	1.0815	0.0004	1.0791	0.0000	1.0795	0.0001
C6	H12	1.0811	-0.0002	1.0788	0.0000	1.0787	0.0009
O7	H13	0.9695	0.0007	0.9997	-0.0002	1.1085	-0.0063

[†] This saddle point on adiabatic surface is a minimum on the diabatic surface

(c) Phenol Minimum Energy Conical Intersections

Atoms		$1^1A, 2^1A$ MEX		$2^1A, 3^1A$ MEX	
		<i>Ab Initio</i>	Error	<i>Ab initio</i>	Error
C1	C2	1.4341	-0.0004	1.4337	0.0000
C1	C6	1.4364	0.0004	1.4359	-0.0003
C1	O7	1.2698	0.0014	1.2760	0.0002
C2	C3	1.3850	0.0015	1.3729	-0.0003
C2	H8	1.0799	0.0001	1.0798	0.0000
C3	C4	1.4060	0.0000	1.4201	0.0002
C3	H9	1.0818	0.0001	1.0799	0.0001
C4	C5	1.4070	0.0014	1.4163	0.0000
C4	H10	1.0811	0.0005	1.0806	-0.0001
C5	C6	1.3838	0.0009	1.3750	-0.0001
C5	H11	1.0818	0.0002	1.0791	0.0000
C6	H12	1.0807	0.0004	1.0788	0.0000
O7	H13	1.7612	0.0027	0.9981	-0.0002

Table 5-8. Bond Lengths of Critical Points(Continued)

(d) Phenoxy Radical Minima

Atoms		1 ¹ A Minimum		2 ¹ A Minimum	
		<i>Ab Initio</i>	Error	<i>Ab initio</i>	Error
C1	C2	1.4572	-0.0003	1.3986	0.0005
C1	C6	1.4572	-0.0003	1.3986	0.0005
C1	O7	1.2328	0.0060	1.3393	0.0017
C2	C3	1.3790	0.0026	1.3956	0.0010
C2	H8	1.0812	0.0006	1.0809	0.0004
C3	C4	1.4134	0.0007	1.3969	0.0001
C3	H9	1.0819	0.0001	1.0818	0.0000
C4	C5	1.4134	0.0007	1.3969	0.0001
C4	H10	1.0812	0.0003	1.0812	0.0004
C5	C6	1.3790	0.0026	1.3956	0.0010
C5	H11	1.0819	0.0001	1.0818	0.0000
C6	H12	1.0812	0.0006	1.0809	0.0004

Table 5-9. Bond Angles of Critical Points. All the bending angles of the benzene ring and one angle for each atom outside the benzene carbons are included. The second atom index in the atom list correspond to the vertex of the bond angle.

(a) Phenol Minima

Atoms			1 ¹ A Minimum		2 ¹ A Minimum	
			<i>Ab Initio</i>	Error	<i>Ab Initio</i>	Error
C2	C1	C6	119.86	0.18	122.04	0.13
C2	C1	O7	122.66	0.00	121.28	-0.13
C1	C2	C3	119.93	-0.04	118.81	0.00
C1	C2	H8	119.99	-0.08	120.25	-0.19
C2	C3	C4	120.51	-0.11	119.65	-0.11
C2	C3	H9	119.28	-0.04	120.17	0.08
C3	C4	C5	119.20	0.11	121.01	0.08
C3	C4	H10	120.39	0.10	119.39	-0.02
C4	C5	C6	120.65	0.01	119.61	-0.05
C6	C5	H11	119.31	0.20	120.22	0.10
C1	C6	C5	119.84	-0.15	118.87	-0.06
C1	C6	H12	118.87	0.11	119.08	0.00
C1	O7	H13	109.61	0.40	109.63	0.01

Table 5-9. Bond Angles of Critical Points (Continued)

(b) Phenol Saddle Points

Atoms			1^1A OH Torsional Saddle Point		2^1A $\pi \rightarrow 3s$ Rydberg Saddle Point		2^1A Dissociative Saddle Point	
			<i>Ab Initio</i>	Error	<i>Ab Initio</i>	Error	<i>Ab Initio</i>	Error
C2	C1	C6	119.98	0.16	120.62	0.05	119.38	0.27
C2	C1	O7	119.73	-0.06	122.69	-0.06	122.74	-0.45
C1	C2	C3	119.96	0.00	118.97	0.03	117.89	0.18
C1	C2	H8	119.00	-0.01	118.99	-0.15	119.42	-0.09
C2	C3	C4	120.23	-0.19	120.40	-0.09	118.10	0.33
C2	C3	H9	119.64	-0.01	119.90	0.07	122.48	-0.25
C3	C4	C5	119.58	0.22	120.72	0.07	120.70	-0.08
C3	C4	H10	120.21	-0.11	119.53	0.01	119.67	0.04
C4	C5	C6	120.23	-0.19	120.10	-0.01	119.63	0.05
C6	C5	H11	119.64	-0.01	120.07	-0.01	120.45	0.10
C1	C6	C5	119.96	0.00	119.19	-0.05	119.73	-0.02
C1	C6	H12	119.00	-0.01	117.92	0.01	119.82	-0.08
C1	O7	H13	107.75	0.54	113.55	-0.10	120.30	0.07

(c) Phenol Minimum Energy Conical Intersections

Atoms			$1^1A, 2^1A$ MEX		$2^1A, 3^1A$ MEX	
			<i>Ab Initio</i>	Error	<i>Ab Initio</i>	Error
C2	C1	C6	118.11	-0.07	120.71	0.02
C2	C1	O7	122.85	-0.13	122.62	-0.04
C1	C2	C3	120.24	0.11	118.96	0.03
C1	C2	H8	118.64	-0.07	119.03	-0.13
C2	C3	C4	120.78	-0.04	120.34	-0.07
C2	C3	H9	119.56	0.07	119.91	0.07
C3	C4	C5	119.87	-0.05	120.75	0.06
C3	C4	H10	120.01	-0.06	119.51	0.02
C4	C5	C6	120.48	0.03	120.08	-0.01
C6	C5	H11	119.75	0.02	120.08	-0.01
C1	C6	C5	120.52	0.02	119.16	-0.03
C1	C6	H12	117.88	0.10	117.97	0.00
C1	O7	H13	113.71	-0.03	113.38	-0.07

Table 5-9. Bond Angles of Critical Points (Continued)

(d) Phenoxy Radical Minima

Atoms			1 ¹ A Minimum		2 ¹ A Minimum	
			<i>Ab Initio</i>	Error	<i>Ab Initio</i>	Error
C2	C1	C6	116.91	0.19	121.14	-0.03
C2	C1	O7	121.54	-0.10	119.43	0.01
C1	C2	C3	120.90	-0.13	118.95	0.02
C1	C2	H8	117.22	0.19	119.90	0.16
C2	C3	C4	120.45	0.07	120.73	-0.01
C2	C3	H9	120.13	-0.10	119.14	0.05
C3	C4	C5	120.39	-0.06	119.49	0.02
C3	C4	H10	119.80	0.03	120.26	-0.01
C4	C5	C6	120.45	0.07	120.73	-0.01
C6	C5	H11	120.13	-0.10	119.14	0.05
C1	C6	C5	120.90	-0.13	118.95	0.02
C1	C6	H12	117.22	0.19	119.90	0.16

Table 5-10. Dihedral Angles of Phenol OH-Torsional Saddle Point. The point reported here, the OH-torsional saddle point on the ground state, is the only non-planar critical point. All the planar critical points on *ab initio* surfaces are also exactly planar in the fit due to symmetry constrains.

Atoms				Torsion Angles	
				<i>Ab Initio</i>	Error
C1	C2	C3	C4	1.60	-0.06
C1	C2	C3	H8	-0.38	0.20
C1	C2	C3	H9	-3.35	0.97
C1	C5	C6	H11	-0.58	0.17
C1	C5	C6	H12	-0.13	0.07
C2	C1	C6	C5	3.45	-0.35
C2	C1	C6	O7	-7.36	0.19
C2	C1	O7	H13	-58.23	0.02
C2	C3	C4	H10	0.89	0.07

Table 5-11. Cartesian Geometries of *Ab Initio* and Fit Critical Points.

Global Minimum of Phenol on I^1A Surface

Ab Initio

C 1	-1.71199	0.00000	-0.00355
C 2	-0.38703	0.00000	-2.28592
C 3	2.25531	0.00000	-2.27653
C 4	3.58568	0.00000	-0.00072
C 5	2.24422	0.00000	2.27787
C 6	-0.39003	0.00000	2.28562
O 7	-4.25259	0.00000	0.10850
H 8	-1.40667	0.00000	-4.06095
H 9	3.26110	0.00000	-4.05562
H 10	5.62832	0.00000	0.00218
H 11	3.24992	0.00000	4.05715
H 12	-1.44535	0.00000	4.03357
H 13	-4.94260	0.00000	-1.58804

Fit

C 1	-1.70919	0.00000	-0.00616
C 2	-0.38584	0.00000	-2.28904
C 3	2.25798	0.00000	-2.27955
C 4	3.58511	0.00000	0.00050
C 5	2.24382	0.00000	2.27902
C 6	-0.39228	0.00000	2.28726
O 7	-4.24868	0.00000	0.10736
H 8	-1.40946	0.00000	-4.06266
H 9	3.26295	0.00000	-4.05986
H 10	5.62780	0.00000	0.01070
H 11	3.25599	0.00000	4.05473
H 12	-1.44850	0.00000	4.03492
H 13	-4.95144	0.00000	-1.58367

Minimum of Phenol on 2¹A Surface

Ab Initio

C 1	-1.73357	0.00000	0.00165
C 2	-0.42173	0.00000	-2.36445
C 3	2.28335	0.00000	-2.35542
C 4	3.61539	0.00000	0.00274
C 5	2.28196	0.00000	2.35716
C 6	-0.42807	0.00000	2.36106
O 7	-4.25944	0.00000	0.10204
H 8	-1.46586	0.00000	-4.11957
H 9	3.31397	0.00000	-4.11458
H 10	5.65718	0.00000	0.00029
H 11	3.31068	0.00000	4.11711
H 12	-1.50656	0.00000	4.08948
H 13	-4.94350	0.00000	-1.59927

Fit

C 1	-1.73122	0.00000	0.00211
C 2	-0.42216	0.00000	-2.36469
C 3	2.28355	0.00000	-2.35858
C 4	3.61499	0.00000	0.00311
C 5	2.28193	0.00000	2.35970
C 6	-0.42907	0.00000	2.36286
O 7	-4.25696	0.00000	0.09932
H 8	-1.47431	0.00000	-4.11563
H 9	3.31495	0.00000	-4.11763
H 10	5.65739	0.00000	0.00164
H 11	3.31344	0.00000	4.11834
H 12	-1.50982	0.00000	4.09002
H 13	-4.93890	0.00000	-1.60230

Phenol OH-Torsional Saddle on 1¹A Surface

Ab Initio

C 1	1.70414	-0.06132	0.00000
C 2	0.38672	0.00094	-2.28343
C 3	-2.25337	0.00895	-2.28242
C 4	-3.58237	0.00868	0.00000
C 5	-2.25337	0.00895	2.28242
C 6	0.38672	0.00094	2.28343
O 7	4.28901	0.15282	0.00000
H 8	1.43947	0.02854	-4.03398
H 9	-3.26478	0.02118	-4.05823
H 10	-5.62551	0.02439	0.00000
H 11	-3.26478	0.02118	4.05823
H 12	1.43947	0.02854	4.03398
H 13	4.98958	-1.53996	0.00000

Fit

C 1	1.70195	-0.06106	0.00000
C 2	0.38780	-0.00403	-2.28463
C 3	-2.25734	0.00604	-2.28707
C 4	-3.58309	0.01092	0.00000
C 5	-2.25734	0.00604	2.28707
C 6	0.38780	-0.00403	2.28463
O 7	4.28398	0.15398	0.00000
H 8	1.44305	0.02528	-4.03317
H 9	-3.26639	0.02473	-4.06505
H 10	-5.62783	0.02903	0.00000
H 11	-3.26639	0.02473	4.06505
H 12	1.44305	0.02528	4.03317
H 13	5.00169	-1.53307	0.00000

Phenol $\pi \rightarrow 3s$ Saddle on 2^1A Surface (Minimum on Diabatic Surface)

Ab Initio

C 1	-1.71123	0.00000	-0.00999
C 2	-0.36563	0.00000	-2.36218
C 3	2.22419	0.00000	-2.32593
C 4	3.54895	0.00000	0.00671
C 5	2.22373	0.00000	2.33108
C 6	-0.37039	0.00000	2.34980
O 7	-4.11556	0.00000	0.11260
H 8	-1.42363	0.00000	-4.10679
H 9	3.26603	0.00000	-4.08079
H 10	5.59094	0.00000	0.00432
H 11	3.25837	0.00000	4.08841
H 12	-1.46491	0.00000	4.06975
H 13	-4.95751	0.00000	-1.57862

Fit

C 1	-1.70990	0.00000	-0.00937
C 2	-0.36530	0.00000	-2.36175
C 3	2.22412	0.00000	-2.32776
C 4	3.54745	0.00000	0.00625
C 5	2.22353	0.00000	2.33114
C 6	-0.37035	0.00000	2.35081
O 7	-4.11438	0.00000	0.11161
H 8	-1.42835	0.00000	-4.10324
H 9	3.26669	0.00000	-4.08249
H 10	5.58910	0.00000	0.00570
H 11	3.25845	0.00000	4.08824
H 12	-1.46548	0.00000	4.07047
H 13	-4.95221	0.00000	-1.58126

Phenol OH dissociation Saddle on 2¹A Surface

Ab Initio

C 1	-1.74067	0.00000	-0.02115
C 2	-0.35323	0.00000	-2.37127
C 3	2.23947	0.00000	-2.31989
C 4	3.56135	0.00000	0.01006
C 5	2.22368	0.00000	2.32840
C 6	-0.37230	0.00000	2.34281
O 7	-4.11706	0.00000	0.06926
H 8	-1.41214	0.00000	-4.11009
H 9	3.28534	0.00000	-4.07415
H 10	5.60366	0.00000	0.01596
H 11	3.25334	0.00000	4.08944
H 12	-1.46190	0.00000	4.06550
H 13	-5.03035	0.00000	-1.81582

Fit

C 1	-1.73865	0.00000	-0.01592
C 2	-0.35731	0.00000	-2.36835
C 3	2.23657	0.00000	-2.31907
C 4	3.55540	0.00000	0.00902
C 5	2.22057	0.00000	2.32845
C 6	-0.37702	0.00000	2.34912
O 7	-4.11906	0.00000	0.06152
H 8	-1.41044	0.00000	-4.11129
H 9	3.28156	0.00000	-4.07250
H 10	5.59840	0.00000	0.01563
H 11	3.26742	0.00000	4.07960
H 12	-1.46725	0.00000	4.07346
H 13	-5.01100	0.00000	-1.82060

Phenol I¹A,2¹A Minimum Energy Conical Intersection

Ab Initio

C 1	-1.76483	0.00000	0.05018
C 2	-0.39931	0.00000	-2.29064
C 3	2.21794	0.00000	-2.28967
C 4	3.57697	0.00000	-0.00649
C 5	2.27315	0.00000	2.31068
C 6	-0.34136	0.00000	2.36137
O 7	-4.16201	0.00000	0.15873
H 8	-1.45347	0.00000	-4.03794
H 9	3.22700	0.00000	-4.06760
H 10	5.61982	0.00000	-0.03346
H 11	3.32177	0.00000	4.06557
H 12	-1.37748	0.00000	4.12128
H 13	-5.63663	0.00000	-2.82485

Fit

C 1	-1.76777	0.00000	0.05317
C 2	-0.40153	0.00000	-2.28640
C 3	2.21857	0.00000	-2.28944
C 4	3.57945	0.00000	-0.00733
C 5	2.27414	0.00000	2.31193
C 6	-0.34211	0.00000	2.36379
O 7	-4.16796	0.00000	0.15510
H 8	-1.45710	0.00000	-4.03299
H 9	3.22712	0.00000	-4.06788
H 10	5.62312	0.00000	-0.03822
H 11	3.32430	0.00000	4.06632
H 12	-1.37407	0.00000	4.12711
H 13	-5.63460	0.00000	-2.83800

Phenol 2¹A,3¹A Minimum Energy Conical Intersection

Ab Initio

C 1	-1.71136	0.00000	-0.00965
C 2	-0.36783	0.00000	-2.36236
C 3	2.22626	0.00000	-2.32737
C 4	3.55066	0.00000	0.00665
C 5	2.22568	0.00000	2.33211
C 6	-0.37264	0.00000	2.35057
O 7	-4.11963	0.00000	0.11213
H 8	-1.42606	0.00000	-4.10704
H 9	3.26775	0.00000	-4.08237
H 10	5.59263	0.00000	0.00434
H 11	3.26038	0.00000	4.08940
H 12	-1.46705	0.00000	4.07053
H 13	-4.95464	0.00000	-1.57907

Fit

C 1	-1.71035	0.00000	-0.00908
C 2	-0.36725	0.00000	-2.36197
C 3	2.22623	0.00000	-2.32889
C 4	3.54949	0.00000	0.00614
C 5	2.22554	0.00000	2.33209
C 6	-0.37253	0.00000	2.35102
O 7	-4.11915	0.00000	0.11138
H 8	-1.42966	0.00000	-4.10403
H 9	3.26861	0.00000	-4.08366
H 10	5.59119	0.00000	0.00569
H 11	3.26035	0.00000	4.08928
H 12	-1.46738	0.00000	4.07081
H 13	-4.95093	0.00000	-1.58090

Minimum of Phenoxy Radical on 1¹A Surface

Ab Initio

C 1	-2.18997	0.00000	0.00000
C 2	-0.74940	0.00000	2.34677
C 3	1.85640	0.00000	2.31757
C 4	3.18392	0.00000	0.00000
C 5	1.85640	0.00000	-2.31757
C 6	-0.74940	0.00000	-2.34677
O 7	-4.51955	0.00000	0.00000
H 8	-1.80878	0.00000	4.09383
H 9	2.90248	0.00000	4.07428
H 10	5.22706	0.00000	0.00000
H 11	2.90248	0.00000	-4.07428
H 12	-1.80878	0.00000	-4.09383

Fit

C 1	-2.18840	0.00000	0.00000
C 2	-0.75208	0.00000	2.34876
C 3	1.85868	0.00000	2.31794
C 4	3.18814	0.00000	0.00000
C 5	1.85868	0.00000	-2.31794
C 6	-0.75208	0.00000	-2.34876
O 7	-4.52931	0.00000	0.00000
H 8	-1.80914	0.00000	4.09851
H 9	2.90283	0.00000	4.07610
H 10	5.23185	0.00000	0.00000
H 11	2.90283	0.00000	-4.07610
H 12	-1.80914	0.00000	-4.09851

Minimum of Phenoxy Radical on 2¹A Surface

Ab Initio

C 1	-2.08229	0.00000	0.00000
C 2	-0.78366	0.00000	2.30201
C 3	1.85346	0.00000	2.28008
C 4	3.18355	0.00000	0.00000
C 5	1.85346	0.00000	-2.28008
C 6	-0.78366	0.00000	-2.30201
O 7	-4.61329	0.00000	0.00000
H 8	-1.82547	0.00000	4.05889
H 9	2.86359	0.00000	4.05734
H 10	5.22678	0.00000	0.00000
H 11	2.86359	0.00000	-4.05734
H 12	-1.82547	0.00000	-4.05889

Fit

C 1	-2.08492	0.00000	0.00000
C 2	-0.78528	0.00000	2.30249
C 3	1.85372	0.00000	2.28059
C 4	3.18345	0.00000	0.00000
C 5	1.85372	0.00000	-2.28059
C 6	-0.78528	0.00000	-2.30249
O 7	-4.61918	0.00000	0.00000
H 8	-1.82202	0.00000	4.06315
H 9	2.86549	0.00000	4.05687
H 10	5.22746	0.00000	0.00000
H 11	2.86549	0.00000	-4.05687
H 12	-1.82202	0.00000	-4.06315

5.7.6 Harmonic Frequencies of *Ab Initio* and Fit Critical Points

(a) Frequencies at Phenol Minima

Mode	1 ¹ A		2 ¹ A	
	Frequency	Error	Frequency	Error
1	243.86	-5.72	160.46	-8.41
2	339.10	34.21	193.06	20.47
3	430.82	-10.02	236.57	52.02
4	436.49	7.73	360.24	-3.08
5	525.89	11.42	372.91	48.29
6	564.68	6.99	424.39	5.31
7	664.46	2.73	473.79	-24.07
8	723.49	-54.65	503.16	-14.76
9	774.93	-4.83	508.69	2.68
10	838.51	-2.77	528.16	24.19
11	876.16	-7.81	581.12	-28.54
12	889.21	8.21	602.63	-18.86
13	960.06	-6.26	683.05	1.07
14	980.43	19.06	831.64	-2.55
15	1067.69	1.10	978.35	-13.20
16	1093.14	-18.17	1017.43	-2.77
17	1145.42	-0.37	1033.97	-6.12
18	1227.13	10.56	1217.78	9.81
19	1254.32	-12.26	1235.61	10.43
20	1266.68	20.53	1265.93	3.28
21	1396.62	-15.86	1398.42	-5.14
22	1410.86	5.77	1434.07	-6.52
23	1459.39	11.27	1509.81	4.69
24	1594.84	-5.93	1555.96	-15.80
25	1639.17	-30.52	1672.64	-12.89
26	1741.49	-39.25	1707.21	-9.00
27	1764.67	-35.17	1818.67	-20.31
28	3328.84	16.27	3355.68	3.44
29	3345.88	13.89	3361.88	2.07
30	3357.33	10.15	3381.67	3.28
31	3371.09	5.37	3389.45	-3.01
32	3379.22	4.71	3402.56	-11.62
33	3803.12	-18.80	3787.09	5.05
RMSE		18.45		17.20

(b) Frequencies at Phenol Saddle Points

Mode	1^1A OH Torsional Saddle Point		2^1A $\pi \rightarrow 3s$ Rydberg Saddle Point		2^1A Dissociative Saddle Point	
	Frequency	Error	Frequency	Error	Frequency	Error
1	-485.66	54.39	-499.67	-42.23	-3394.71	26.72
2	244.87	-8.18	196.80	-24.48	188.36	-28.45
3	430.69	-17.92	452.33	-22.95	368.27	-10.51
4	435.51	14.60	478.15	-35.27	463.35	-18.44
5	537.54	-23.10	521.97	-12.11	477.85	-23.30
6	560.68	5.75	552.18	-1.75	548.63	-2.85
7	662.62	9.50	604.98	0.82	552.23	10.70
8	719.95	-32.47	670.37	6.18	610.60	11.94
9	791.15	-7.66	796.13	-3.54	670.23	-26.81
10	863.28	-20.86	823.25	0.91	809.18	-25.67
11	868.92	-13.10	871.40	14.19	821.15	-18.72
12	927.02	-16.85	938.85	-20.18	862.67	0.82
13	976.76	-41.82	1001.74	-54.99	924.13	-44.86
14	988.28	31.51	1020.36	-10.60	985.45	-34.72
15	1068.78	-4.56	1038.24	5.95	1005.06	-12.92
16	1092.12	10.29	1059.51	13.98	1034.56	-10.80
17	1142.11	3.30	1151.47	-12.71	1056.62	28.56
18	1228.55	1.88	1217.89	-24.97	1113.04	-17.62
19	1241.78	-3.06	1260.65	-16.20	1166.58	-5.11
20	1252.56	33.91	1269.19	11.17	1223.49	7.20
21	1356.43	9.33	1452.26	-30.72	1252.79	25.40
22	1367.77	8.71	1490.44	-15.42	1423.33	-17.61
23	1420.90	9.09	1520.38	-1.26	1457.82	30.75
24	1570.21	-25.42	1575.18	-17.48	1519.30	-6.49
25	1630.65	-19.33	1642.29	-10.26	1548.29	-12.55
26	1725.50	-47.87	1651.92	-5.29	1642.82	-13.63
27	1755.49	-44.15	1772.06	18.40	1671.19	-28.26
28	3341.58	4.69	3016.65	-10.43	1771.63	61.57
29	3347.79	-0.50	3372.76	-0.35	3366.00	-7.41
30	3362.43	3.56	3379.33	20.31	3378.47	9.92
31	3366.39	2.61	3388.55	12.93	3390.13	13.20
32	3376.23	6.76	3395.87	10.26	3400.11	13.88
33	3768.67	5.62	3406.44	20.48	3406.96	11.25
RMSE		21.94		19.60		22.52

(c) Frequencies at Phenoxy Radical Minima

Mode	1^1A		2^1A	
	Frequency	Error	Frequency	Error
1	197.87	-16.05	244.97	-16.30
2	392.51	-10.24	406.34	7.64
3	476.82	4.46	435.11	-9.26
4	486.59	-1.90	514.73	14.07
5	546.97	1.00	549.99	7.34
6	623.18	11.87	655.86	3.60
7	661.48	-8.69	699.51	-32.28
8	772.64	21.09	758.84	5.53
9	809.84	-3.47	834.31	1.91
10	833.38	22.80	872.28	-12.23
11	894.63	7.46	890.27	-18.53
12	977.06	-27.13	966.31	-17.71
13	984.10	-2.11	980.14	-7.00
14	1040.26	-14.10	1063.93	-7.54
15	1050.10	-1.70	1091.34	-19.07
16	1135.87	3.72	1146.26	14.98
17	1205.36	7.82	1227.81	-0.41
18	1223.49	0.25	1253.18	-5.93
19	1313.55	32.79	1310.57	25.88
20	1400.34	-0.83	1331.59	43.94
21	1514.45	-8.11	1425.57	1.31
22	1517.07	23.52	1550.33	2.21
23	1578.68	28.13	1603.60	-8.15
24	1638.52	-8.33	1688.62	8.57
25	1668.43	-10.53	1738.07	-10.69
26	3340.77	10.86	3340.88	2.11
27	3344.61	9.50	3350.21	4.09
28	3365.65	-0.43	3362.40	-6.01
29	3369.39	8.62	3370.26	2.83
30	3377.33	16.24	3376.01	7.34
RMSE		48.25		-8.88

References

1. Thompson, K. C.; Jordan, M. J. T.; Collins, M. A., Polyatomic Molecules potential energy surfaces by interpolation in local coordinates. *J. Chem. Phys.* **1998**, *108*, 8302-8316.
2. Thompson, K. C.; Jordan, M. J. T.; Collins, M. A., Polyatomic Molecules potential energy surfaces by interpolation in cartesian coordinates. *J. Chem. Phys.* **1998**, *108*, 564-578.
3. Godsi, O.; Collins, M. A.; Peskin, U., Quantum grow-A quantum dynamics sampling approach for growing potential energy surfaces and nonadiabatic couplings. *J. Chem. Phys.* **2010**, *132*, 124106.
4. Braams, B. J.; Bowman, J. M., Permutationally Invariant Potential Energy Surfaces in High dimensionality. *Int. Rev. Phys. Chem.* **2009**, *28*, 577-606.
5. Xie, Z.; Bowman, J. M., Permutationally Invariant Polynomial Basis for Molecular Energy Surface Fitting via Monomial Symmetrization. *J. Chem. Theory and Comput.* **2010**, *6*, 26-34.
6. Dawes, R.; Passalacqua, A.; Sewell, T. D.; Wagner, A. F.; Minkoff, M.; Thompson, D. L., Interpolating moving least squares methods for fitting potential energy surfaces: using classical trajectories to explore configuration space. *J. Chem. Phys.* **2009**, *130*, 144107.
7. Dawes, R.; Thompson, D. L.; Wagner, A. F.; Minkoff, M., Interpolating moving least squares methods for fitting potential energy surfaces: A Strategy for efficient automatic data placement in high dimensions. *J. Chem. Phys.* **2009**, *128*, 84107.

8. Zhu, X.; Yarkony, D. R., On the Representation of Coupled Adiabatic Potential Energy Surfaces using Quasi-Diabatic Hamiltonians: Geometrically Distributed Expansions. *J. Chem. Phys.* **2012**, *136*, 174110.
9. Zhu, X.; Yarkony, D. R., Quasi-Diabatic Representations of Adiabatic Potential Energy Surfaces Coupled by Conical Intersections including Bond Breaking. A More General Construction Procedure and an Analysis of the Diabatic Representation. *J. Chem. Phys.* **2012**, *137*, 22A511.
10. Köppel, H.; Domcke, W.; Cederbaum, L. S., Multimode Molecular Dynamics Beyond the Born-Oppenheimer Approximation. *Adv. Chem. Phys.* **1984**, *57*, 59-246.
11. Köppel, H., Diabatic Representations: methods for the construction of diabatic states. *Adv. Ser. Phys. Chem.* **2004**, *15*, 175-204.
12. Pacher, T.; Cederbaum, L. S.; Köppel, H., Block Diagonalization Method for Quasidiabatic States. *J. Chem. Phys.* **1988**, *89*, 7367-7381.
13. Pacher, T.; Cederbaum, L. S.; Köppel, H., (diabatic bases). *Adv. Chem. Phys.* **1993**, *84*, 293-391.
14. Köppel, H.; Schubert, B., regularized diabatic representation. *Mol. Phys.* **2006**, *104*, 1069.
15. Opalka, D.; Domcke, W., Interpolation of multi-sheeted multi-dimensional potential-energy surfaces via a linear optimization procedure. *J. Chem. Phys.* **2013**, *138*, 224103.
16. Collins, M. A.; Godsi, O.; Liu, S.; Zhang, D. H., An ab initio quasi-diabatic potential energy matrix for OH(Σ) + H₂. *J. Chem. Phys.* **2011**, *135*, 234307.

17. Evenhuis, C. R.; Collins, M. A., Interpolation of Diabatic potential energy surfaces. *J. Chem. Phys.* **2004**, *121*, 2515.
18. Evenhuis, C. R.; Lin, X.; Zhang, D. H.; Yarkony, D. R.; Collins, M. A., Interpolation of diabatic potential-energy surfaces: Quantum dynamics on ab initio surfaces. *J. Chem. Phys.* **2005**, *123*, 134110 (12 pages).
19. Godsi, O.; Evenhuis, C. R.; Collins, M. A., Interpolation of Multidimensional diabatic surfaces. *J. Chem. Phys.* **2006**, *125*, 104105.
20. Evenhuis, C.; Martínez, T. J., A scheme to interpolate potential energy surfaces and derivative coupling vectors without performing a global diabaticization. *J. Chem. Phys.* **2011**, *135*, 224110.
21. Nakamura, H.; Truhlar, D. G., Direct diabaticization of electronic states by the fourfold way. II. Dynamical correlation and rearrangement processes. *J. Chem. Phys.* **2002**, *117*, 5576-5593.
22. Nakamura, H.; Truhlar, D. G., Extension of the fourfold way for the calculation of global diabatic potential energy surfaces of complex multiarrangement non-Born Oppenheimer systems. Application to HNC(O)(S₀,S₁). *J. Chem. Phys.* **2003**, *118*, 6816-6829.
23. Jasper, A. W.; Kendrick, B. K.; Mead, C. A.; Truhlar, D. G., Non-Born-Oppenheimer Chemistry: Potential Surfaces, Couplings and Dynamics. In *Modern Trends in Chemical Reaction Dynamics.. Experiment and Theory (Part I)*, Yang, X.; Liu, K., Eds. World Scientific: New Jersey, 2004; Vol. 14, pp 329-392.

24. Nangia, S.; Truhlar, D. G., Direct Calculation of Coupled Diabatic Potential Energy Surfaces for ammonia and mapping of a 4-dimensional conical intersection seam. *J. Chem. Phys.* **2006**, *124*, 124309.
25. Li, Z. H.; Valero, R.; Truhlar, D. G., Improved Direct Diabatization and Coupled Potential Energy Surfaces for the dissociation of ammonia. *Theor. Chem. Acc.* **2007**, *118*, 9-24.
26. Varandas, A. J. C.; Brown, F. B.; Mead, C. A.; Truhlar, D. G.; Blais, N. C., A double Many Body expansion of the two lowest energy potential energy surfaces and nonadiabatic couplings for H₃. *J. Chem. Phys.* **1987**, *86*, 6258.
27. Mota, V. C.; Varandas, A. J. C., HN₂(2A⁺) Electronic Manifold. II. Ab Initio Based Double-Sheeted DMBE Potential Energy Surface via a Global Diabatization Angle. *J. Phys. Chem. A* **2008**, *112*, 3768–3786.
28. Einfeld, W.; Viel, A., Higher order (A+E)_g Pseudo Jahn-Teller coupling *J. Chem. Phys.* **2005**, *122*, 204317.
29. Jornet-Somoza, J.; Lasorne, B.; Robb, M. A.; Meyer, H.-D.; Lauvergnat, D.; Gatti, F., A generalised 17-state vibronic-coupling Hamiltonian model for ethylene
Author(s): ; et al.
- Source: JOURNAL OF CHEMICAL PHYSICS Volume: 137 Issue: 8 Article Number: 084304 *J. Chem. Phys.* **2012**, *137*, 084304.
30. Longuet-Higgins, H. C., The symmetry groups of non-rigid molecules. *Mol. Phys.* **1963**, *6*, 445-460.
31. Bunker, P. R.; Jensen, P., *Molecular Symmetry and Spectroscopy*. 2nd ed.; NRC Research Press: Ottawa, 1998.

32. Zhu, X.; Ma, J.; Yarkony, D. R.; Guo, H., Computational Determination of X State Absorption Spectrum of NH₃ and ND₃ using a Quasi Diabatic Representation of the X and A States and Full Six Dimensional Quantum Dynamics. *J. Chem. Phys.* **2012**, *136*, 234301.
33. Ma, J.; Zhu, X.; Guo, H.; Yarkony, D. R., First Principles determination of the NH₂/ND₂(A,X) branching ratios for photodissociation of ground state NH₃/ND₃ via full-dimensional quantum dynamics based on a new quasi-diabatic representation of coupled ab initio potential energy surfaces. *J. Chem. Phys.* **2012**, *137*, 22A541.
34. Ben-Nun, M.; Martínez, T. J., Ab Initio Quantum Molecular Dynamics. *Adv. Chem. Phys.* **2002**, *121*, 439.
35. Worth, G. A.; Robb, M. A.; Burghardt, I., A Novel Algorithm for nonadiabatic direct dynamics using variational Gaussian wave packets. *Farad. Discuss.* **2004**, *127*, 307.
36. Worth, G. A.; Robb, M. A.; Lasorne, B., Solving the Time dependent Schrödinger equation for nuclear motion in one step: direct dynamics on nonadiabatic systems. *Mol. Phys.* **2008**, *106*, 2077-2091.
37. Barbatti, M.; Aquino, A. J. A.; Szymczak, J.; Nachtigallova, D.; Lischka, H., Photodynamical simulations of cytosine: characterization of the ultrafast bi-exponential UV deactivation. *Phys. Chem. Chem. Phys.* **2011**, *13*, 6145-6155.
38. Izmaylov, A. F., Perturbative wave-packet spawning procedure for non-adiabatic dynamics in diabatic representation. *J. Chem. Phys.* **2013**, *138*, 104115.

39. Deskevich, M. P.; Nesbit, D. J.; Werner, H.-J., Dynamically weighted multiconfiguration self-consistent field: Multistate calculations for $F+H_2O \rightarrow HF+OH$ reaction paths *J. Chem. Phys.* **2004**, *120*, 7281.
40. Ramesh, S. G.; Domcke, W., A multi-sheeted three-dimensional potential-energy surface for the H-atom photodissociation of phenol. *Faraday Discuss.* **2013**, *163*, 73-94.
41. Hudock, H. R.; Levine, B. G.; Thompson, A. L.; Satzger, H.; Townsend, D.; Gador, N.; Ullrich, S.; Stolow, A.; Martínez, T. J., Ab Initio Molecular Dynamics and Time-Resolved Photoelectron Spectroscopy of Electronically Excited Uracil and Thymine. *J. Phys. Chem. A* **2007**, *111*, 8500–8508.
42. Hudock, H. R.; Martinez, T., Excited-State Dynamics of Cytosine Reveal Multiple Intrinsic Subpicosecond Pathways. *ChemPhysChem* **2008**, *9*, 2486-2490.
43. Szymczak, J. J.; Barbatti, M.; Hoo, J. T. S.; Adkins, J. A.; Windus, T. L.; Nachtigallova, D.; Lischka, H., Photodynamics Simulations of Thymine: Relaxation into the First Excited Singlet State \dagger . *J. Phys. Chem. A* **2009**, *113*, 12686–12693.
44. Barbatti, M.; Lischka, H., Nonadiabatic Deactivation of 9H-Adenine: A Comprehensive Picture Based on Mixed Quantum–Classical Dynamics. *J. Am. Chem. Soc.* **2008**, *130*, 6831-6839.
45. Nachtigallova, D.; Aquino, A. J. A.; Szymczak, J.; Barbatti, M.; Hobza, P.; Lischka, H., Nonadiatic Dynamics of Uracil: Population Split tamong Different Decay Mechanisms. *J. Phys, Chem. A* **2011**, *115*, 5247-5255.
46. Barbatti, M.; Lan, Z.; Crespo-Otero, R.; Szymczak, J. J.; Lischka, H.; Thiel, W., Critical appraisal of excited state nonadiabatic dynamics simulations of 9H-adenine. *J. Chem. Phys* **2012**, *137*, 22A514.

47. Barbatti, M.; Aquino, A. J. A.; Szymczak, J. J.; Nachtigallova, D.; Hobza, P.; Lischka, H., . J., Relaxation mechanisms of UV-photoexcited DNA and RNA nucleobase. *Proc. Natl. Acad. Sci. USA* **2010**, *107*, 21453.
48. Tully, J. C., Molecular Dynamics with electronic transitions. *J. Chem. Phys.* **1990**, *93*, 1061-1071.
49. Tully, J. C., Nonadiabatic Effects in Chemical Dynamics. *Faraday Discuss.* **2004**, *127*, 463-466.
50. Ashfold, M. N. R.; King, G. A.; Murdock, D.; Nix, M. G. D.; Olivera, T. A. A.; Sagea, A. G., $\pi\sigma^*$ excited states in molecular photochemistry. *Phys. Chem. Chem. Phys.* **2012**, *12*, , 1218-1238.
51. Devine, A. L.; Cronin, B.; Nix, M. G. D.; Ashfold, M. N. R., High Resolution photofragment translation spectroscopy studies of the near ultraviolet photolysis of imidazole. *J. Chem. Phys.* **2006**, *125*, 1184302 (9 pages).
52. King, G. A.; Oliver, T. A. A.; Nix, M. G. D.; Ashfold, M. N. R., *J. Phys. Chem. A* **2009**, *113*, 7984.
53. Daigoku, K.; Ichiuchi, S.; Sakai, M.; Fujii, M.; Hashimoto, K., *J. Chem. Phys.* **2003**, *119*, 5194.
54. Vieuxmaire, O. P.; Lan, Z.; Sobolewski, A. L.; Domcke, W., Ab initio characterization of the conical intersections involved in the photochemistry of phenol *J. Chem. Phys.* **2008**, *129*, 224307.
55. Lan, Z.; Domcke, W.; Vallet, V.; Sobolewski, A. L.; Mahapatra, S., Time-dependent quantum wave-packet description of the σ^* photochemistry of phenol. *J. Chem. Phys.* **2005**, *122*, 224315.

56. Michael G. D. Nix; Devine, A. L.; Cronin, B.; Dixon, R. N.; Ashfold, M. N. R., High resolution photofragment translational spectroscopy studies of the near ultraviolet photolysis of phenol. *J. Chem. Phys.* **2006**, *125*, 133318.
57. Devine, A. L.; Nix, M. G. D.; Cronin, B.; Ashfold, M. N. R., *Phys. Chem. Chem. Phys.* **2007**, *9*, 3749.
58. Nix, M.; Devine, A.; Dixon, R.; Ashfold, M., Observation of geometric phase effect induced photodissociation dynamics in phenol. *Chem. Phys. Lett.* **2008**, *463*, 305-308.
59. King, G. A.; Devine, A. L.; Nix, M. G. D.; Kelly, D. E.; Ashfold, M. N. R., Near-UV photolysis of substituted phenols. *Phys. Chem. Chem. Phys.* **2008**, *10*, 6417.
60. Pino, G. A.; Oldani, A. N.; Marceca, E.; Fujii, M.; Ishiuchi, S.; Miyazaki, M.; Broquier, M.; Dedonder, C.; Jouvét, C., Excited state hydrogen transfer dynamics in substituted phenols and their complexes with ammonia: pi pi*-pi sigma* energy gap propensity and ortho-substitution effect. *J. Chem. Phys.* **2010**, *133*, 124313.
61. Dixon, R. N.; Oliver, T. A. A.; Ashfold, M. N. R., Tunnelling under a conical intersection: Application to the product state distributions in the UV photodissociation of phenols. *J. Chem. Phys.* **2011**, *134*, 194303 (10 pages).
62. Xu, X. F.; Yang, K. R.; Truhlar, D. G., Diabatic Molecular Orbitals, Potential Energies, and Potential Energy Surface Couplings by the 4-fold Way for Photodissociation of Phenol. *J Chem Theory Comput* **2013**, *9* (8), 3612-3625.
63. Crespo-Otero, R.; Barbatti, M.; Yu, H.; Evans, N. L.; Ulrich, S., *Chem. Phys. Chem.* **2011**, *17*, 3365-3375.

64. Yu, H.; Evans, N. L.; Stavros, V. G.; Ulrich, S., *Phys. Chem. Chem. Phys.* **2012**, *14*, 6266-6272.
65. Barbatti, M.; Ruckebauer, M.; Szymczak, J. J.; Aquino, A. J. A.; Lischka, H., Nonadiabatic excited-state dynamics of polar π -systems and related model compounds of biological relevance. *Phys. Chem. Chem. Phys.* **2008**, *10*, 482-494.
66. Montero, R.; Conde, A.; Ovejas, V.; Fernandez-Fernandez, M.; Castano, F.; Longarte, A., Ultrafast Evolution of Imidazole after Electronic Excitation. *J. Phys. Chem. A* **2012**, *116*, 10752-10758
67. Montero, R.; Conde, A.; Ovejas, V.; Fernandez-Fernandez, M.; Castano, F.; Longarte, A., Femtosecond evolution of the pyrrole molecule excited in the near part of its UV spectrum. *J. Chem. Phys.* **2012**, *137*, 064317.
68. Li, Z. H.; Ahren W. Jasper; David A. Bonhommeau; Valero, R.; Truhlar, D. G. *ANT 2009*, University of Minnesota, Minneapolis, 2009.
69. Godsi, O.; Collins, M. A.; Peskin, U., Quantum grow-A quantum dynamics sampling approach for growing potential energy surfaces and nonadiabatic couplings. *J. Chem. Phys.* **2010**, *132*, 124106.
70. Netzloff, H.; Collins, M.; Gordon, M., Growing multiconfigurational potential energy surfaces with applications to X+H₂ (X=C,N,O) reactions. *J. Chem. Phys.* **2006**, *124*, 154104.
71. Bunker, P. R., *Molecular Symmetry and Spectroscopy*. Academic Press: New York, 1979.

72. Mead, C. A., Electronic Hamiltonian, wavefunctions and energies and derivative coupling between Born-Oppenheimer states in the vicinity of a conical intersection. *J. Chem. Phys.* **1983**, *78*, 807-814.
73. Top, Z. H.; Baer, M., *Chem. Phys.* **1976**, *15*, 49.
74. Mead, C. A.; Truhlar, D. G., Conditions for the definition of a strictly diabatic basis. *J. Chem. Phys.* **1982**, *77*, 6090-6098.
75. Atchity, G. J.; Xantheas, S. S.; Ruedenberg, K., Potential Energy Surfaces Near Intersections. *J. Chem. Phys.* **1991**, *95*, 1862-1876.
76. Yarkony, D. R., *On the adiabatic to diabatic states transformation near intersections of conical intersections.* *J. Chem. Phys.* **2000**, *112*, 2111-2120.
77. Hause, M. L.; Yoon, Y. H.; Case, A. S.; Crim, F. F., Dynamics at Conical Intersections: The influence of O-H stretching vibrations on the photodissociation phenol. *J. Chem. Phys.* **2008**, *128*, 104307(8 pages).
78. Iqbal, A.; Cheung, M.; Nix, M.; Stavros, V., Exploring the Time-Scales of H-Atom Detachment from Photoexcited Phenol-h(6) and Phenol-d(5):Statistical vs Nonstatistical Decay. *J. Phys. Chem. A* **2009**, *113*, 8157-8163.
79. Devine, A.; Nix, M.; Dixon, R.; Ashfold, M., Near-ultraviolet photodissociation of thiophenol. *J. Phys. Chem. A* **2008**, *112*, 9563-9574.
80. An, H.; Baeck, K., Quantum Wave Packet Propagation Study of the Photochemistry of Phenol: Isotope Effects (Ph-OD) and the Direct Excitation to the (1) π sigma* State. *J. Phys. Chem. A* **2011**, *115*, 13309-13315.

81. Johan Lorentzon; Per-Åke Malmqvist; Markus Fülcher; Roos, B. O., A CASPT2 study of the valence and lowest Rydberg electronic states of benzene and phenol. *Theoret. Chem. Acc.* **1995**, *91*, 91-108.
82. Czakó, G.; Bowman, J. M., Accurate ab initio potential energy surface, thermochemistry, and dynamics of the Cl(P-2, P-2(3/2)) + CH₄ -> HCl + CH₃ and H + CH₃Cl reactions. *J. Chem. Phys.* **2012**, *136*, 044307.
83. Hack, M. D.; Jasper, A. W.; Volobuev, Y. L.; Schwenke, D. W.; Truhlar, D. G., Quantum Mechanical and Quasiclassical Trajectory Surface Hopping Studies of the Electronically Nonadiabatic Predissociation of the \tilde{A} State of NaH₂. *J. Phys. Chem A* **1999**, *103*, 6309-6326.
84. Worth, G. A.; Meyer, H.-D.; Köppel, H.; Cederbaum, L. S.; Burghardt, I., Using the MCTDH wavepacket propagation method to describe multimode nonadiabatic dynamics. *Int. Rev. Phys. Chem.* **2008**, *27*, 569-606.
85. Longuet-Higgins, H. C., The intersection of potential energy surfaces in polyatomic systems. *Proc. R. Soc. Lond. A* **1975**, *344*, 147-156.

Curriculum Vitae

Xiaolei Zhu

✉ 3400 N Charles St
Remsen 315
Baltimore MD 21218

@ virtualzx@jhu.edu

☎ 410-350-6345

EDUCATION

Ph.D. , Chemistry

The Johns Hopkins University / Baltimore, MD
Advisor: David R. Yarkony

Expected Jan 2014

M.A. , Chemistry

The Johns Hopkins University / Baltimore, MD

May 2013

B.S. , Chemistry

Peking University / Beijing, China

May 2007

RESEARCH INTERESTS

Nonadiabatic processes, Potential energy surfaces, Conical intersections, Classical and Quasi-classical trajectories, Photodissociation, Photoelectron spectroscopy, Multi-reference electronic structure theories

CURRENT PROJECT

Developer and Administrator, Surfgen Project
[Github Repository: <https://github.com/virtualzx-nad/surfgen>]

A collection of programs that use *ab initio* data including derivative couplings to constructs quasi-diabatic Hamiltonians that handle arbitrary CNPI symmetry, generate the best diabatic representation in least-squares sense, and can accurately treat conical intersections seams involving any number of states. Also provides standard APIs to allow integration of fit coupled potentials into dynamics programs.

HONORS AND AWARDS

Sarah and Adolph Roseman Achievement Award

Department of Chemistry, Johns Hopkins University

May 2013

William Hooper Grafflin Fellowship

Department of Chemistry, Johns Hopkins University

June 2010

MEMBERSHIP AND AFFILIATIONS

Member, American Chemical Society

Oct 2010 - present

PUBLICATIONS

Xiaolei Zhu, and David R. Yarkony, “Fitting Coupled Potential Energy Surfaces for Large Systems: Method and Construction of a 3-State Representation for Phenol Photodissociation in the Full 33 Internal Degrees of Freedom using Multireference Configuration Interaction Determined Data”

J. Chem. Phys. **140**, 024112 (2014)

Elizabeth M.Y. Lee, **Xiaolei Zhu**, and David R. Yarkony, “On the electronic structure of the low lying electronic states of vanadium trioxide”

J. Chem. Phys. **139**, 044303 (2013)

Jianyi Ma, **Xiaolei Zhu**, Hua Guo, and David R. Yarkony, “First principles determination of the $\text{NH}_2/\text{ND}_2(\tilde{\text{A}},\tilde{\text{X}})$ branching ratios for photo-dissociation of NH_3/ND_3 via full-dimensional quantum dynamics based on a new quasi-diabatic representation of coupled *ab initio* potential energy surfaces”

J. Chem. Phys. **137**, 22A541 (2012)

Xiaolei Zhu and David R. Yarkony, “Quasi-diabatic representations of adiabatic potential energy surfaces coupled by conical intersections including bond breaking: A more general construction procedure and an analysis of the diabatic representation”

J. Chem. Phys. **137**, 22A511 (2012)

Xiaolei Zhu, Jianyi Ma, David R. Yarkony, and Hua Guo, “Computational determination of the $\tilde{\text{A}}$ state absorption spectrum of NH_3 and of ND_3 using a new quasi-diabatic representation of the X and $\tilde{\text{A}}$ states and full six-dimensional quantum dynamics”

J. Chem. Phys. **136**, 234301 (2012)

Xiaolei Zhu and David R. Yarkony, “On the representation of coupled adiabatic potential energy surfaces using quasi-diabatic Hamiltonians: A distributed origins expansion approach”

J. Chem. Phys. **136**, 174110 (2012)

Xiaolei Zhu and David R. Yarkony, “On the representation of coupled adiabatic potential energy surfaces using quasi-diabatic Hamiltonians: description of accidental seams of conical intersection”

Mol. Phys. **108**, 2611 (2010)

Xiaolei Zhu and David R. Yarkony, “Toward eliminating the electronic structure bottleneck in nonadiabatic dynamics on the fly: An algorithm to fit nonlocal, quasidiabatic, coupled electronic state Hamiltonians based on *ab initio* electronic structure data”

J. Chem. Phys. **132**, 104101 (2010)

Xiaolei Zhu and David R. Yarkony, “The Photoelectron Spectrum of Pyrrolide: Non-adiabatic Effects due to Conical Intersections”

J. Phys. Chem. C, **114**, 5312(2010)

Xiaolei Zhu and David R. Yarkony, “On the determination of optimized, fully quadratic, coupled state quasidiabatic Hamiltonians for determining bound state vibronic spectra”

J. Chem. Phys. **130**, 234108 (2009)